The characterisation and origin of the morphology of galaxies across multiple scales and epochs

Dimitrios Irodotou

Supervisors: Prof. Peter A. Thomas & Dr. Mark T. Sargent

Submitted for the degree of Doctor of Philosophy

University of Sussex

Abstract

In the widely accepted lambda cold dark matter (ΛCDM) framework, dark matter haloes acquire their initial angular momentum through tidal interactions and grow in mass and size through accretion and/or repeated mergers. Galaxies form in the centres of these haloes when the baryonic matter collapses and the subsequent formation of stars occurs. Galaxies are complex systems whose properties reveal their evolutionary history. Understanding how they acquire their properties and identifying the dynamical processes responsible is a fundamental question in modern astrophysics. In this thesis, I address these issues by studying the characterisation and origin of the morphology of galaxies across multiple scales and epochs. For that purpose, I combine observational data with various theoretical tools, as outlined below.

Determining which galaxies develop dynamical instabilities, which components are involved and how stability is restored is still an open question. Even though gaseous discs significantly contribute to the global stability, most semi-analytic models (SAMs) only identify and address stellar disc instabilities. Therefore, in Chapter 2, I introduce the new instability formulation we developed which significantly improves the predictions of the L-Galaxies SAM. The updated recipe takes into account the gravitational contribution of gas in conjunction with the stellar component and more accurately follows the physical processes responsible for bulge growth. Hence, our model produces galactic properties which are in closer agreement with observations than previous work.

There is a prominent connection between understanding the formation and evolution of galaxies and exploring how and when galactic components form. Therefore, a method that accurately identifies the constituent stellar populations and provides an additional way of exploring their properties is of great importance. Hence, in

Chapter 3, I introduced the new method we developed to identify kinematically distinct components. We applied our method to the EAGLE cosmological simulation and studied the imprint of secular and violent processes on galaxies. By creating Mollweide projections of the angular momentum map of each galaxy's stellar particles we identified a number of features which indicate distinct galactic morphologies. Thus, we were able to both classify and decompose galaxies and reproduce the observed tight relations.

Finally, in order to advance the field of structure formation and improve our theoretical tools, it is imperative to understand our models and the non-linear effects they introduce. For that reason, in Chapter 4, I investigate how AGN feedback alters stellar dynamics and affects bar formation. I re-simulated three Auriga galaxies using two different AGN feedback prescriptions in an effort to constrain their impact on the halo and galaxy properties. In addition, we use IMFIT to perform bar/bulge/disc decompositions and quantify the effect of AGN on the relative growth of each component.

Declaration

The work presented in this thesis was undertaken between October 2017 and March 2021 while the author was a PhD candidate at the University of Sussex under the supervision of Prof. Peter A. Thomas and Dr. Mark T. Sargent. I declare that no part of this work has been previously submitted for another award of the University of Sussex or any other awarding body or institution.

The following chapters of this submission consist of peer-reviewed publications:

- Chapter 2: 'Morphological evolution and galactic sizes in the L-Galaxies SA model' has been published as Irodotou et al. 2019, Monthly Notices of the Royal Astronomical Society, Volume 489, Issue 3, p.3609-3624

- Chapter 3: 'Using angular momentum maps to detect kinematically distinct galactic components' has been published as Irodotou & Thomas 2021, Monthly Notices of the Royal Astronomical Society, Volume 501, Issue 2, pp.2182-2197

The following chapter is in preparation for submission:

- Chapter 4: 'Quantifying the effects of AGN feedback on the structural and dynamical properties of disc galaxies in cosmological simulations' *in prep.*

Preface

Unless otherwise stated, all figures in this thesis have been produced by the author.

In Chapter 2, I present the peer-reviewed publication 'Morphological evolution and galactic sizes in the L-Galaxies SA model'. I undertook the vast majority of the coding, data analysis, and writing, and produced the figures. Peter A. Thomas supervised me and together we drafted the paper. Bruno M. Henriques, Mark T. Sargent, and Jessica M. Hislop provided input on content and helped with the interpretation of the results. All authors helped to proofread the text.

In Chapter 3, I present the peer-reviewed publication 'Using angular momentum maps to detect kinematically distinct galactic components'. I undertook the vast majority of the coding, data analysis, and writing, and produced the figures. Peter A. Thomas supervised me and together we drafted the paper.

In Chapter 4, I present the article in preparation for submission 'Quantifying the effects of AGN feedback on the structural and dynamical properties of disc galaxies in cosmological simulations'. I ran the new simulation variants, undertook the vast majority of the coding, data analysis, and writing, and produced the figures. Francesca Fragkoudi supervised me and together we drafted the paper. Ruediger Pakmor, Robert J.J. Grand, Dimitri A. Gadotti, and Tiago Costa provided input on content and helped with the interpretation of the results.

Acknowledgements

I would like to start by thanking my main supervisor Peter Thomas for everything I learnt whilst working with him, for sharing my excitement when things worked and also being supportive when I was confronted with obstacles. I would also like to thank my second supervisor Mark Sargent for his continuous feedback and support throughout my PhD. Finally, a huge thank you to Francesca Fragkoudi for supervising my final project and hosting me at the Max Planck Institute for Astrophysics. Without these three people this thesis would not have existed, I will always be grateful for the support and trust they put in my work. In addition, I would like to thank my collaborators for their feedback and help (in chronological order): Bruno M. B. Henriques, Robert M. Yates, Jessica M. Hislop, Christopher C. Lovell, Aswin P. Vijayan, Stephen M. Wilkins, David J. Barnes, William J. Roper, Jussi Kuusisto, Ruediger Pakmor, Robert J. J. Grand, Dimitri A. Gadotti, Tiago Costa, and the Auriga team. Finally, I would like to thank my examiners Michael Merrifield and Robert E. Smith for the interesting conversation during my viva and the constructive corrections and feedback.

My life at Sussex has been really enjoyable due to all the people I had a chance to share the 4C corridor with. Special thanks to my officemates Ciaran, Jessie, Benoit, Chris, Ian, and Will as well as to Pippa and Sunayana for the interesting discussions and support. In addition, I wish to thank all the people I was glad to share a house with (in chronological order): Damini, Sirius, Jiangtao, Eason, Gus, Maria, and my brother Thano. Lastly, I would like to thank a group of people - collectively know as the 'Greeks' - who made my life in Brighton really delightful. Many thanks to Stelio, Antonia, Thano, Gianni A., Giorgo, Gus, Gianni X., Louisa, Maria, Tasso, and Athena.

When I left to start my PhD in Brighton I left a lot of good friends and comrades

behind in Greece, who are far too many to be all listed here. Special thanks for always making time to catch up and being up for drinks every time I visited to Stelio, Gianni, Ilia, and the rest of Deka, to Natasa, Iria, Sok, Sofia, Kiki, and the rest of Sfigges, and to Aleko, Aimilio, 3 $\times$ Dimitri, Bill, and the rest with whom I started my undergraduate studies in Ioannina in 2009, when the journey towards my PhD began.

I could not thank my parents enough for financially assisting me throughout my studies as well as unconditionally supporting me and my work even though they never really understood what I was working on. I would also wish to thank my brother Thano and my cousins Thanasi and Aki for not only being my family, but my friends; we will always have each other's backs.

Finally, I wish to thank to my partner Jessie for being my number one supporter and always celebrating my successes. For proofreading pretty much everything I wrote, for being my audience when I wanted to practise a talk, and for all the constructive comments. Thank you for accepting the challenge of a long-distance relationship and being there for me for the highs and the lows.

‘If you want to go fast, go alone.
If you want to go far, go together.’
African proverb

Contents

List of Figures

List of Tables

List of Abbreviations

AGN	active galactic nuclei
BH	black hole
CALIFA	Calar Alto Legacy Integral Field Area
CGM	circumgalactic medium
CMB	cosmic microwave background
Eagle	Evolution and Assembly of GaLaxies and their Environments
ETG(s)	early-type galaxy(ies)
Flares	First Light And Reionisation Epoch Simulations
FoF	Friends-of-Friends
GAMA	Galaxy And Mass Assembly
GHASP	Gassendi HAlpha survey of SPirals
HD	hydrodynamical
ISM	interstellar medium
LITTLE THINGS	Local Irregulars That Trace Luminosity Extremes, The Hi Nearby Galaxy Survey
LTG(s)	late-type galaxy(ies)
LVHIS	Local Volume Hi Survey
MaNGA	Mapping Nearby Galaxies at Apache Point Observatory
NoR	no-radio
NoRNoQ	no-radio-no-quasar
SAMI	Sydney-AAO Multi-object Integral
SAM(s)	semi-analytic model(s)
SDSS	Sloan Digital Sky Survey
SFR	star formation rate
SMBH	supermassive black holes

SNII	type II supernova
SPARC	Spitzer Photometry & Accurate Rotation Curves
SPH	smoothed particle hydrodynamics
SSP	single stellar population
THINGS	The HI Nearby Galaxy Survey
UV	ultraviolet
VLA-ANGST	Very Large Array - survey of Advanced Camera for Surveys Nearby Galaxy Survey Treasury galaxies
WHISP	Westerbork HI Survey of Irregular and Spiral Galaxies
ΛCDM	lambda cold dark matter

Chapter 1

Introduction

In this thesis, I explore the characterisation and origin of the morphology of galaxies across multiple scales and epochs. Below, I set out the scientific topics of each chapter. The thesis is structured as follows. In Chapter 1, I provide a brief review of the cosmological and astrophysical concepts relevant to this thesis, along with an overview of the physical models and methods included in the L-Galaxies model (Henriques et al., 2015), and the Eagle (Schaye et al., 2015) and Auriga (Grand et al., 2017) simulations. In Chapter 2, we extend the L-Galaxies model to better follow gravitational instabilities and galactic sizes. In Chapter 3, we introduce a new method to identify kinematically distinct galactic components. In Chapter 4, we quantify the effects of different AGN feedback modes on the properties of stellar and gaseous components. Finally, in Chapter 5, I summarise my conclusions and reflect upon the next steps.

1.1 Background

A few years after Hubble (1929) showed that the Universe is expanding, cosmologists and astrophysicists started painting a comprehensive picture of the Universe and its structures (e.g. Blumenthal et al., 1984; Peebles, 1984), known as the ΛCDM model. The main components in this cosmological framework are the baryonic matter, cold dark matter, and dark energy. Even though the ΛCDM model has been proven to accurately predict the formation and evolution of structure in the Universe, the nature of the cold dark matter and dark energy are still unknown (Peebles and

Ratra, 2003).

Below I summarise a few key concepts of the ΛCDM model that are relevant to this thesis.

1.1.1 Cosmological background

Standard cosmology relies on the cosmological principle, which is the assumption that at large scales the Universe is homogeneous and isotropic. However, if the cosmological principle applies perfectly on all scales, the matter distribution in the Universe would also be uniform and isotropic, which would result in no structure formation (Mo et al., 2010). In order for structures to form, small deviation from a perfect homogeneity and isotropy are needed.

A successful method for generating such density perturbations comes from the inflationary theory (Guth, 1981; Albrecht and Steinhardt, 1982; Linde, 1982), in which a rapid phase of exponential expansion (i.e. inflation) produced the initial perturbations responsible for the formation of the structures we observe in the Universe today (Starobinsky, 1982). These initial perturbations in the density field grew with time, since regions with slightly higher densities than the mean density attracted the surrounding matter. Hence, over-dense regions became denser and under-dense regions became less dense.

In an expanding universe, the cosmic expansion affects the aforementioned matter flows. Once the over-densities grow enough and reach the 'turn-around' phase, they decouple from the expansion and start to collapse (Jeans, 1902; Lifshitz, 1946); this moment signals the beginning of structure formation. In the ΛCDM model, when a system collapses, its dark matter component violently relaxes and forms the so-called dark matter halo, while the baryonic gas shock heats to the virial temperature and, if cooling is adequate, later reaches the potential well of the dark matter halo.

1.1.2 Astrophysical background

1.1.2.1 Galaxy formation

The cooling of the baryonic gas is a vital step towards galaxy formation and depends on the temperature, composition, and density of the gas (Somerville and Davé, 2015). Gas in massive haloes with a virial temperatures $\gtrsim 10^7$ K is expected to be fully ionized, hence the main cooling mechanism is the Bremsstrahlung emission from free electrons. For temperatures between 10^4-10^6 K baryons can cool via excitation/de-excitation mechanisms, such as electron recombination with ions or collisional atom excitation (Rees and Ostriker, 1977). The efficiency of these phenomena depends on the chemical composition of the gas since different atoms have different excitation energies; hence they result in distinct cooling rates. Furthermore, gas with temperature $< 10^4$ K is expected to be almost neutral, thus the above processes are highly suppressed. However, heavy elements and molecules can still promote cooling if present. The former achieve this via collisional excitation/de-excitation of fine and hyperfine structure lines and the latter through rotational and/or vibrational lines. Lastly, at redshifts higher than 6, inverse Compton scattering of cosmic microwave background (CMB) (Penzias and Wilson, 1965) photons by electrons can provide an additional cooling process especially in hot haloes.

As gas cools it collapses under its own gravity and forms dense clouds which eventually turn into stars and subsequently form galaxies (commonly referred to as 'proto-galaxies'). This mechanism is usually termed the quiescent star formation and typically occurs in rotationally supported discs. In addition to that, some galaxies experience more aggressive star formation episodes; the so-called 'starbursts' (Hopkins et al., 2006). These are characterised by star formation rates per unit area several hundred times larger than that of the Milky Way (Heckman and Thompson, 2017), and usually occur near the centre of the galaxy or during mergers, since they require a lot of gas confined in small volumes.

Lastly, a process capable of suppressing the formation of stars (either by preventing gas cooling or by reheating cold gas) is energetic feedback. This energy is released during supernova explosions and/or from active galactic nuclei (AGN) as a result of gas accretion into supermassive black holes (SMBH) (Begelman, 2004).

1.1.2.2 Galactic properties

As described above, a proto-galaxy forms from gas that settles into a rotationally supported disc. In order for such a disc to form, the collapsing gas must have non-zero angular momentum. Based on the seminal work of Hoyle (1951); Peebles (1969); White and Rees (1978); Fall and Efstathiou (1980), we know that gas clouds are able to acquire their angular momenta through tidal torques from nearby (dark matter and/or baryonic) structures. In principle, this mechanism, in addition to providing the angular momentum of the gas disc, will also define its scale length, since under the assumption that the specific angular momentum of the gas is conserved throughout the collapse/cooling (Mo et al., 1998), the scale length will be proportional to the specific angular momentum.

The above simple picture is able to explain the formation of disc galaxies. However, a plethora of different morphological types exists (Hubble, 1936; Liller, 1966; van den Bergh, 1976; Kormendy and Bender, 1996; Cappellari et al., 2011b). An important aspect of the ΛCDM model is hierarchical structure formation (White and Frenk, 1991). In this framework, dark matter structures merge together and so do the galaxies residing in them. Hence, massive galaxies are built through repeated minor and/or major mergers, which leave an imprint on the merger remnant's structural and dynamical properties. In addition to mergers - which are violent phenomena - secular processes, such as disc instabilities or bar formation, can also affect the matter distribution in galaxies (Athanassoula, 2013; Kormendy, 2013; Sellwood, 2014a). Hence, violent and secular processes can alter the morphology of a galaxy.

Both violent and secular processes have the ability to redistribute stellar orbits and create central components called bulges. Mergers are expected to create 'classical bulges' which usually have ellipsoidal morphologies, are dispersion dominated systems, and have properties (e.g. Sersic index, star formation rates) similar to elliptical galaxies (Gadotti, 2012; Brooks and Christensen, 2016; Kormendy, 2016). On the other hand, secular processes give rise to 'pseudo-bulges' which have either discy or boxy morphologies, are dominated by ordered motions, and have on-going star formation (Sellwood, 2014a).

For more details on bulge formation and interactions with other galactic components (e.g. bars and black holes) I refer the reader to the following chapters.

1.2 Semi-analytic models

As described above, galaxy formation and evolution occurs within dark matter haloes. These haloes contain the vital information needed by SAMs in order to associate the dark and baryonic components of the Universe (White and Frenk, 1991). In SAMs, the evolution of dark matter is followed numerically by N-body simulations, while analytic recipes are used to capture baryonic processes, such as environmental effects, gas cooling, star formation, AGN feedback, and chemical enrichment.

1.2.1 The L-Galaxies SAM

The SAM used in this work (see Chapter 2) is the Henriques et al. (2015) version of the L-Galaxies model, which was implemented on the Millennium simulation (Springel et al., 2005b) merger trees and adopted the Planck Collaboration et al. (2014c) cosmological parameters: $\sigma_8 = 0.829$, $H_0 = 67.3$ km s^{-1} Mpc^{-1}, $\Omega_\Lambda = 0.685$, $\Omega_\mathrm{m} = 0.315$, $\Omega_\mathrm{b} = 0.0487$ ($f_\mathrm{b} = 0.155$), and $n = 0.96$. The L-Galaxies SAM has been evolving for three decades (White and Frenk, 1991; Kauffmann et al., 1993, 1999; Springel et al., 2001a; Guo et al., 2011; Henriques et al., 2015, 2020) in order to accurately model the formation and evolution of galaxies.

Below, I briefly describe the construction of merger trees (Section 1.2.1.1) and the galaxy formation processes relevant to this thesis (Section 1.2.1.2).

1.2.1.1 Dark matter trees

The first step towards modelling galaxy formation with SAMs is constructing Friends-of-Friends (FoF) group catalogues. These are created by grouping together dark matter particles with a separation less than 20 per cent of the mean inter-particle separation (Davis et al., 1985). The mass of each FoF group is defined as

$$M_{200\mathrm{c}} = \frac{4\pi}{3} 200 \rho_{\mathrm{crit.}}\ R^3_{200\mathrm{c}} = \frac{100}{G} H^2(z)\ R^3_{200\mathrm{c}} = \frac{V^3_{200\mathrm{c}}}{10G\ H(z)}\ , \tag{1.1}$$

where $\rho_{\mathrm{crit.}} = 3H^2(z)/8\pi\ G$ is the critical density, $H(z)$ is the Hubble parameter at redshift z, $R_{200\mathrm{c}}$ is the radius of a sphere containing an overdensity 200 times larger than the critical value (roughly what is expected for a virialised group, Cole and

Lacey, 1996), G is the gravitational constant, and $V_{200c} = \sqrt{G\ M_{200c}/R_{200c}}$ is the virial velocity of the halo.

The next step is identifying the substructures (i.e. dark matter subhaloes) where galaxies are assumed to reside. In the L-Galaxies project, this is performed with the Subfind algorithm (Springel et al., 2001a), which searches for gravitationally bound, locally overdense regions inside the global density field of each FoF group. Once all dark matter haloes and subhaloes have been identified at each redshift, their evolution is tracked between snapshots by linking them to their progenitors. This process creates the so-called 'merger trees' which provide necessary information regarding dark matter structures (e.g. their mass, size, and assembly history) to SAMs in order to model the formation and evolution of galaxies.

In the L-Galaxies nomenclature, the most massive subhalo in each FoF group is called the 'main halo' and the corresponding galaxy the 'central' or 'type 0' galaxy. The remaining subhaloes contain galaxies which are referred to as 'satellite' or 'type 1' galaxies if their subhaloes still exist; or as 'type 2' or 'orphan' galaxies if they have had their halo disrupted by the central halo but they have not merged with the central galaxy yet.

1.2.1.2 The formation and evolution of galaxies

In the L-Galaxies SAM, galaxy formation starts by populating each dark matter halo with gas which shock heats and then cools either immediately or more slowly via a cooling flow. The resulting cold gas disc fuels the formation of stars, which, when they die, release energy (that turns the cold gas back into a hot gas component), mass, and elements into the surrounding medium. An additional form of energetic feedback comes from black holes. Black holes grow in mass through the accretion of gas and/or mergers, and they release energy that heats up the gas. Apart from internal processes, galaxies are also subject to external effects. For example, when dark matter subhaloes merge, the satellite galaxy spirals into the central halo and merges on a dynamical friction timescale (Binney and Tremaine, 2008). During this process a number of environmental effects, such as tidal forces and ram-pressure stripping, can affect the gas and stars of satellite galaxies. A schematic representation of the aforementioned mechanisms can be seen in Fig. 1.1.

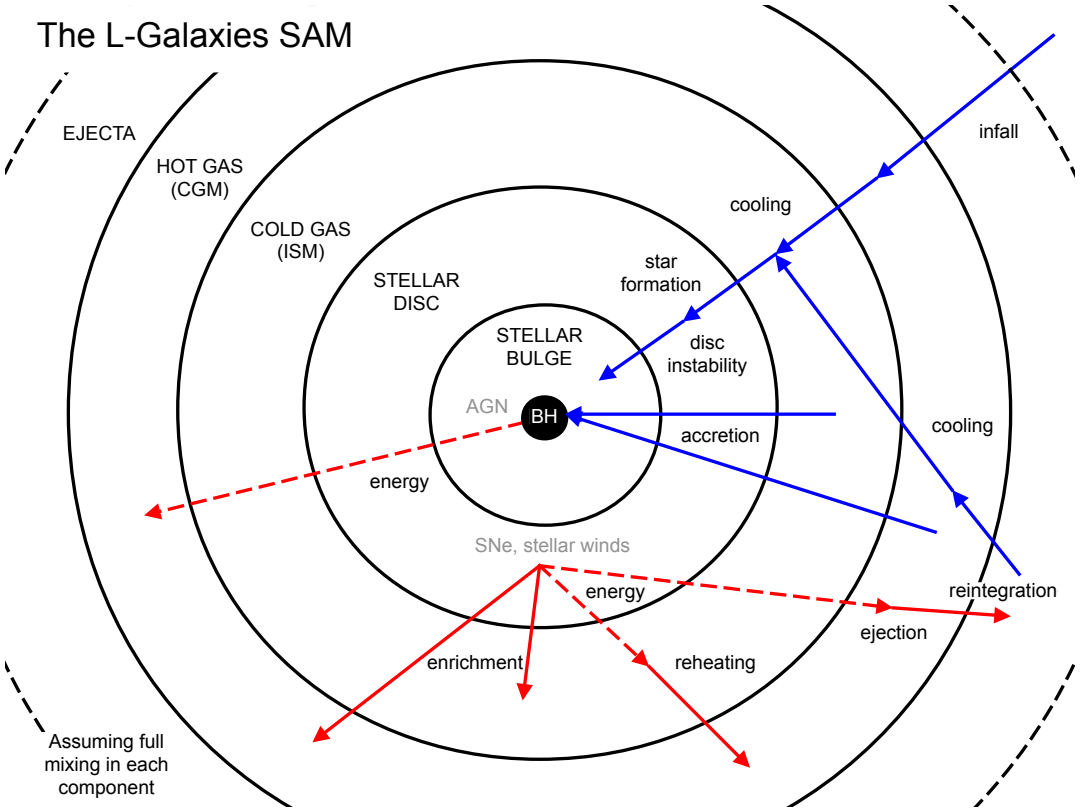

Figure 1.1: A schematic representation of the main physical processes captured by the L-Galaxies SAM. Solid and dashed lines represent the transfer of mass and energy, respectively. This schematic was provided by Rob Yates.

Below, I describe the onset of galaxy formation and the physical processes relevant to this thesis. For a complete description of the L-Galaxies SAM used in this thesis I refer the reader to Henriques et al. (2015).

1.2.1.2.1 Infall

In the L-Galaxies SAM, the formation of galaxies begins by assigning a gas component equal to the cosmic abundance of baryons ($f_{\rm b}^{\rm cos}$ = 15.5 per cent) to each subhalo. This primordial gas is expected to shock-heat as it falls into the gravitational potential well of the halo; hence it is initially placed in the hot gas component, akin to the circumgalactic medium (CGM).

As subhaloes grow in mass, additional baryonic mass is added in the same way (i.e. primordial gas in the CGM). However, in order to model the photo-heating by the ultraviolet (UV) background field, which increases the gas temperature to the point where pressure effects prevent it from accreting onto haloes, the following step

is necessary. Henriques et al. (2015) follow Gnedin (2000) who introduced a filtering halo mass below which $f_{\rm b}^{\rm cos}$ is reduced to

$$f_{\rm b}(z, M_{\rm 200c}) = f_{\rm b}^{\rm cos}\left(1 + (2^{\alpha/3} - 1)\left[\frac{M_{\rm 200c}}{M_{\rm F}(z)}\right]^{-\alpha}\right)^{-3/\alpha} , \tag{1.2}$$

where $\alpha = 2$ and $M_{\rm F}(z)$ varies from $\sim 6.5 \times 10^9$ $\rm M_\odot$ at $z = 0$, to $\sim 10^7$ $\rm M_\odot$ at $z = 8$ (Okamoto et al., 2008). Given the filtering halo masses and the fact that in this thesis (Chapter 2) we use haloes from the Millennium simulation with minimum $M_{\rm 200c} \sim 10^{10}$ $\rm M_\odot$, we expect equation (1.2) to results in $f_{\rm b}$(z,$M_{\rm 200c}$) $\sim f_{\rm b}^{\rm cos}$ since $M_{\rm 200c}/M_{\rm F}(z)$ will always be $\gtrsim 10$. Hence, the baryonic fraction will not significantly change when the L-Galaxies model is run on the Millennium simulation merger trees.

1.2.1.2.2 Cooling

Following White and Frenk (1991), Henriques et al. (2015) assume that the hot gas component is distributed similar to an isothermal sphere with density profile (as a function of radius r)

$$\rho_{\rm hot}(r) \ = \frac{M_{\rm hot}}{4\pi \ R_{\rm 200c} \ r^2} , \tag{1.3}$$

where $M_{\rm hot}$ is the hot gas mass and $R_{\rm 200c}$ is the virial radius. Following the isothermal sphere model, the hot gas' cooling time can be written as

$$t_{\rm cool}(r) = \frac{3\mu m_{\rm H} \ k_{\rm B} \ T_{\rm 200c}}{2\rho_{\rm hot}(r) \ \Lambda(T_{\rm hot}, Z_{\rm hot})} , \tag{1.4}$$

where $\mu m_{\rm H}$ is the mean particle mass, $k_{\rm B}$ is the Boltzmann constant, $T_{\rm 200c} = 35.9(V_{\rm 200c}/\ \rm km\ s^{-1})^2$ K is the virial temperature of the halo, $\rho_{\rm hot}(r)$ is the hot gas density, and Λ($T_{\rm hot}$,$Z_{\rm hot}$) is the cooling function where $Z_{\rm hot}$ and $T_{\rm hot}$ are the hot gas metallicity and temperature, respectively.

The cooling happens within a radius where the cooling time equals the halo dynamical time

$$r_{\rm cool} = \left[\frac{t_{\rm dyn,\,h} \ M_{\rm hot} \ \Lambda(T_{\rm hot}, Z_{\rm hot})}{6\pi \ \mu m_{\rm H} \ k_{\rm B} \ T_{\rm 200c} \ R_{\rm 200c}}\right]^{\frac{1}{2}} , \tag{1.5}$$

where $t_{\rm dyn,\,h} = R_{\rm 200c}/V_{\rm 200c} = 0.1H(z)^{-1}$ is the halo dynamical time (De Lucia et al., 2004), $M_{\rm hot}$ is the hot gas mass, Λ($T_{\rm hot}$,$Z_{\rm hot}$) is the cooling function, $\mu m_{\rm H}$ is the

mean particle mass, $k_{\rm B}$ is the Boltzmann constant, $T_{\rm 200c}$ is the virial temperature of the halo, and $R_{\rm 200c}$ is the virial radius.

Then, the cooling of the hot gas component can follow one of two regimes based on the ratio between $r_{\rm cool}$ and $R_{\rm 200c}$. If $r_{\rm cool} < R_{\rm 200c}$ - which is the case for massive haloes at late times - the gas cools at a rate

$$\dot{M}_{\rm cool} = M_{\rm hot} \, \frac{r_{\rm cool}}{R_{\rm 200c}} \frac{1}{t_{\rm dyn,\,h}} \, . \tag{1.6}$$

If $r_{\rm cool} > R_{\rm 200c}$ - which is the case for low-mass haloes at early times - the gas cools at a rate

$$\dot{M}_{\rm cool} = \frac{M_{\rm hot}}{t_{\rm dyn,\,h}} \, . \tag{1.7}$$

1.2.1.2.3 Star formation

At each time step, as gas cools it is assumed to settle on a thin disc and form stars (see Chapter 2). The star formation rate of that disc is given by

$$\dot{M}_{\star} = \alpha_{\rm SF} \frac{M_{\rm gas} - M_{\rm crit.}}{t_{\rm dyn.,\,disc}} \, , \tag{1.8}$$

where $\alpha_{\rm SF} = 0.055$ is the star formation efficiency, $M_{\rm gas}$ is the cold gas mass, $M_{\rm crit.}$ is the critical mass (see below) and $t_{\rm dyn.,\,disc} = R_{\star}/V_{\rm max}$ is the dynamical time of the stellar disc, where $R_{\star}$ is the stellar disc scale length and $V_{\rm max}$ is the maximum circular velocity of the halo. The threshold mass for star formation describes the critical surface density above which gas can collapse and form stars (Kauffmann et al., 1996; Kennicutt, 1998) and is defined as

$$M_{\rm crit.} = M_{\rm crit.,\,0} \left(\frac{V_{\rm 200c}}{200 {\rm km\ s^{-1}}} \right) \left(\frac{R_{\rm gas}}{10 {\rm kpc}} \right) \, , \tag{1.9}$$

where $M_{\rm crit.,\,0} = 2.4 \times 10^9$ M$_{\odot}$, $V_{\rm 200c}$ is the virial velocity of the halo and $R_{\rm gas}$ is the gas disc scale length.

1.2.1.2.4 Feedback

After an episode of star formation, a number of supernova explosions are expected. These supernovae inject energy into the surrounding cold and hot gas reservoirs, which results in mass transfer from the former to the latter component and

in an increase of the latter's temperature. The heating of the hot gas is treated by the ejection of material to an external reservoir from which gas can potentially be reincorporated, depending on the mass of the host system.

The feedback energy from supernovae is given by

$$\Delta E_{\rm SN} = \epsilon_{\rm halo} \left(\frac{1}{2} \Delta M_\star \; V_{\rm SN}^2 \right) \; , \tag{1.10}$$

where $\frac{1}{2} V_{\rm SN}^2 = \frac{1}{2} (630 \text{ km s}^{-1})^2$ is the mean energy injected per unit mass of stars formed ($\Delta M_\star$) and $\epsilon_{\rm halo}$ is the fraction of the supernovae energy that is able to affect the gas components [see equation (S17) of Henriques et al. (2015)]. The energy required to heat up the cold gas and transfer it to the hot reservoir can be written as

$$\Delta E_{\rm reheat} = \frac{1}{2} \Delta M_{\rm reheat} \; V_{\rm 200c}^2 \; , \tag{1.11}$$

where $\Delta M_{\rm reheat} = \epsilon_{\rm disc} \; \Delta M_\star$ is the cold gas mass reheated by the supernovae and added to the hot atmosphere and $\epsilon_{\rm disc}$ is a parameter that controls the efficiency of the reheat mechanism [see equation (S19) of Henriques et al. (2015)].

If $\Delta E_{\rm reheat} > \Delta E_{\rm SN}$ the maximum mass transferred is $\Delta M_{\rm reheat} = \Delta E_{\rm SN} / \frac{1}{2} V_{\rm SN}^2$. Otherwise, a mass $\Delta M_{\rm eject}$ is transferred from the hot gas to the ejecta component based on the relation

$$\frac{1}{2} \Delta M_{\rm eject} \; V_{\rm 200c}^2 = \Delta E_{\rm SN} - \Delta E_{\rm reheat} \; . \tag{1.12}$$

In the Henriques et al. (2015) version of the L-Galaxies model the black hole recipe follows that of Croton et al. (2006), where central galaxies' black holes grow in mass during mergers by acquiring the black hole of the satellite along with a fraction of cold gas, and by accreting gas from the hot gas component. Hence, due to the former mechanism the black hole mass of the merger remnant is given by

$$M_{\rm BH,\,f} = M_{\rm BH,\,1} + M_{\rm BH,\,2} + \frac{f_{\rm BH} (M_{\rm sat.}/M_{\rm cen.}) M_{\rm cold}}{1 + (V_{\rm BH}/V_{\rm 200c})^2} \; , \tag{1.13}$$

where $M_{\rm BH,\,1}$ and $M_{\rm BH,\,2}$ are the black hole masses of the progenitors, $f_{\rm BH}$ is a parameter that sets the fraction of the accreted cold gas, $M_{\rm cen.}$ and $M_{\rm sat.}$ are the baryonic masses of the central and satellite galaxy, respectively, $M_{\rm cold}$ is their total cold gas mass, $V_{\rm BH}$ is a parameter that controls the virial velocity at which the efficiency saturates, and $V_{\rm 200c}$ is the virial velocity of the central halo.

As described above, black holes are assumed to accrete gas from the hot atmosphere, which triggers the radio mode feedback. In this mode, the black hole accretion rate can be written as

$$\dot{M}_{\rm BH} = k_{\rm AGN} \left(\frac{M_{\rm hot}}{10^{11} {\rm M}_\odot} \right) \left(\frac{M_{\rm BH}}{10^{8} {\rm M}_\odot} \right) \ , \tag{1.14}$$

where $k_{\rm AGN} = 5 \times 10^{-3}$ M$_\odot$ yr^{-1} is a parameter that controls the efficiency of the accretion, $M_{\rm hot}$ is the mass of hot gas, and $M_{\rm BH}$ is the black hole mass. This growth rate produces feedback and deposits energy into the hot gas atmosphere in a rate

$$\dot{E}_{\rm radio} = \eta \ \dot{M}_{\rm BH} \ c^2 \ , \tag{1.15}$$

where $\eta = 0.1$ is the efficiency parameter and c is the speed of light. This energy is supposed to suppress the cooling of the hot gas, thus results in an effective cooling rate

$$\dot{M}_{\rm cool,\,eff.} = \max \left[\dot{M}_{\rm cool} - 2\dot{E}_{\rm radio}/V^2_{\rm 200c}, 0 \right] \ . \tag{1.16}$$

1.3 Hydrodynamical simulations

Hydrodynamical (HD) simulations differ from SAMs since they self-consistently model the evolution of gaseous, stellar, and dark matter components (Vogelsberger et al., 2020). This allows the investigation of the hydrodynamical and kinematic properties of these components, which makes HD simulations an ideal tool to study galactic dynamics and morphology. However, even though HD simulations spatially resolve the aforementioned components, there is a resolution limit below which a subgrid model, akin to a SAM, is required in order to model the small scale physics (e.g. star formation, AGN feedback, and cooling). An additional limitation is the much smaller sample size compared to SAM as well as the limited ability to investigate modifications to the physics.

1.3.1 The EAGLE simulation

The hydrodynamical simulation used in this work (see Chapter 3) is the 'Evolution and Assembly of GaLaxies and their Environments' (EAGLE) simulation (Schaye et al., 2015; Crain et al., 2015), which adopted the Planck Collaboration et al.

(2014a) cosmological parameters: $\sigma_8 = 0.8288$, $h \equiv H_0 \ / \ (100 \text{ km s}^{-1} \text{ Mpc}^{-1}) = 0.6777$, $\Omega_\Lambda = 0.693$, $\Omega_\text{m} = 0.307$, $\Omega_\text{b} = 0.04825$, and $n = 0.9611$. We use the Ref-L100N1504 simulation with boxsize $(100 \text{ cMpc})^3$, 1504^3 dark matter and initially an equal number of baryonic particles with masses $9.70 \times 10^6 \text{ M}_\odot$ and $1.81 \times 10^6 \text{ M}_\odot$, respectively, and softening length $\epsilon_\text{prop} = 0.7$ pkpc.

Below, I briefly describe the generation of the initial conditions (Section 1.3.1.1), the gravity and hydrodynamical solver (Section 1.3.1.2 and Section 1.3.1.3, respectively), and the subgrid model (Section 1.3.1.4) of the EAGLE simulation used in this thesis (Chapter 3).

1.3.1.1 Initial conditions

As discussed in Section 1.1.1, all structures in the Universe result from Gaussian density fluctuations generated during inflation (Guth, 1981). In order for cosmological simulations to accurately model galaxy formation and evolution, they require initial conditions that produce these perturbations, which are imposed on top of a homogeneous expanding background assuming a flat ΛCDM universe. In EAGLE, the initial conditions are created by the Gaussian white noise field code PANPHASIA (Jenkins, 2013), which as a first step generates the initial positions and velocities for dark matter particles (Jenkins, 2010). These particles are then split into a pair of dark matter and gas particle with a mass ratio given by $\Omega_\text{b}/(\Omega_\text{m}$ - $\Omega_\text{b})$, and their properties are integrated forward in time (see below).

1.3.1.2 Gravity solver

In a system of N particles the gravitational force acting on a particle i can be written as

$$\mathbf{F}(\mathbf{r}_i) = \sum_{j=1, j\neq i}^{N-1} \frac{G \ m_i \ m_j}{|\mathbf{r}_i - \mathbf{r}_j|^3} (\mathbf{r}_i - \mathbf{r}_j) \ , \tag{1.17}$$

where G is the gravitational constant, m_i and m_j are the masses and $\mathbf{r}_i$ and $\mathbf{r}_j$ are the position vectors of particle i and j, respectively. This gives rise to a gravitational peculiar (i.e. the mean density is subtracted) potential at position $\mathbf{r}$ which satisfies the Poisson equation

$$\nabla^2 \Phi(\mathbf{r}) = 4\pi \ G \ \alpha^2 (\rho(\mathbf{r}) - \bar{\rho}) \ , \tag{1.18}$$

where α is the expansion factor, $\bar{\rho}$ is the mean density of the Universe and ρ is the density at position $\mathbf{r}$.

In practise, following the particle-particle method and calculating equation (1.17) when N is very large can be a highly computationally demanding process. An alternative method is the tree-PM algorithm (Xu, 1995; Bode et al., 2000), in which the gravitational force acting on each particle is the sum of long and short range forces (separated by a spatial force-split parameter). The EAGLE project uses the N-body/hydrodynamical code GADGET (Springel, 2005) as a gravity solver, which treats the long range forces by mapping the density field on a mesh and solving equation (1.18) in Fourier space; while for the short range forces uses an octree algorithm (e.g. Barnes and Hut, 1986). This algorithm uses a tree-like hierarchy of cubic nodes where by 'walking' the tree, the total force acting on a particle is calculated by summing up the walked nodes.

1.3.1.3 Hydrodynamical solver

In most galaxy formation simulations, dark matter and stellar particles are supposed to be collision-less, while gas is assumed to form an inviscid fluid. In order to describe the state of that fluid, EAGLE follows the smoothed particle hydrodynamics (SPH) method (Gingold and Monaghan, 1977), in which a set of tracer particles are used to discretize the fluid and smoothing functions are invoked to interpolate the quantities (e.g. density and pressure) at any point in space.

In the SPH scheme, interpolating a property of the fluid from gas particles' properties requires a kernel function. EAGLE follows the ANARCHY implementation (Schaller et al., 2015) in which the kernel function is given by

$$W(r,h) = \frac{21}{2\pi\ h^3} \begin{cases} \left(1-\frac{r}{h}\right)^4 \left(1+4\frac{r}{h}\right) & \text{if } 0 \leq r \leq h \\ 0 & \text{if } r > h\ , \end{cases}$$

where $r = |\mathbf{r}_i - \mathbf{r}_j|$ is the separation between particle i and j and h is the smoothing length which is obtained by the relation

$$N_{\rm ngb}\ = \frac{4\pi}{3} h_i^3\ \sum_j W_{ij}(h_i)\ , \tag{1.19}$$

where $N_{\rm ngb} = 48$ and $W_{ij}(h_i) \equiv W(r, h_i)$. Then, the density of a gas particle i is

given by

$$\rho_i = \sum_j m_j \; W_{ij}(h_i) \; . \tag{1.20}$$

In practice, a weighted density is needed both for the calculation of vital thermodynamical quantities (e.g. entropy, internal energy, and pressure) and for the SPH equations of motion. The weighted density ($\bar{\rho}_i$) is given by writing the entropic function $P = A \; \rho^\gamma$ in the following form

$$\bar{P}_i = A_i \left(\frac{1}{A_i^{1/\gamma}} \sum_{j=1} m_j \; A_j^{1/\gamma} \; W_{ij}(h_i) \right)^\gamma = A_i \; \bar{\rho}_i^\gamma \; . \tag{1.21}$$

In order to fully follow the gas flow, apart from the density and the weighted pressure and density [given by equation (1.20) and equation (1.21), respectively], one needs to integrate forward in time the positions and velocities of the gas particles. EAGLE uses the pressure-entropy formulation of Hopkins (2013) in order to derive the equations of motion which can be written as

$$\frac{d\mathbf{v}_i}{dt} = -\sum_j m_j \left[\frac{A_j^{1/\gamma}}{A_i^{1/\gamma}} \frac{\bar{P}_i}{\bar{\rho}_i^2} \Omega_{ij} \; \nabla_i W_{ij}(h_i) + \frac{A_i^{1/\gamma}}{A_j^{1/\gamma}} \frac{\bar{P}_j}{\bar{\rho}_j^2} \Omega_{ji} \; \nabla_j W_{ij}(h_j) \right] \; , \tag{1.22}$$

where

$$\Omega_{ij} = 1 - \frac{1}{A_i^{1/\gamma}} \left(\frac{h_i}{3\rho_i} \frac{\partial \bar{P}_i^{1/\gamma}}{\partial h_i} \right) \left(1 + \frac{h_i}{3\rho_i} \right) \; , \tag{1.23}$$

is a term accounting for the gradients in the smoothing length.

The final aspect of the ANARCHY implementation is the addition of artificial viscosity and conduction in order to capture shocks and the mixing of gas phases, respectively. For a complete description of these processes I refer the reader to Schaller et al. (2015) and Schaye et al. (2015).

1.3.1.4 The formation and evolution of galaxies

The EAGLE subgrid model was based on the GIMIC (Crain et al., 2009) and OWLS (Schaye et al., 2010) projects and includes cooling, star formation, stellar and AGN feedback, and mergers and accretion of gas onto supermassive black holes.

1.3.1.4.1 Cooling

Radiative cooling is a fundamental process in SPH galaxy formation simulations since it describes how gas particles radiate away their energies and collapse in order to form stars. The EAGLE simulation follows the study of Wiersma et al. (2009) which uses CLOUDY (Ferland et al., 1998) to specify the gas cooling rates based on the contributions of eleven elements[1] as a function of density, temperature, and redshift.

1.3.1.4.2 Star formation

In general, star formation occurs in cold, high density gas. However, the resolution limitations in large cosmological simulations result in unresolved interstellar gas phases. Therefore, it is necessary to both identify the cold gas and use a threshold as a proxy for the gas density above which a cold phase is expected to exist.

To identify the cold gas, an equation of state $P_{\rm eos} \propto {\rho_{\rm gas}}^{4/3}$ with $\rho_{\rm gas} = 0.1$ cm^{-3} and a temperature floor of $T_{\rm eos} = 8000$ K is used. To identify the high density gas, the Schaye (2004) metallicity-dependent threshold is used

$$n_\star(Z) = \min\left[0.1\left(\frac{Z}{0.002}\right)^{-0.64}, 10\right] \text{cm}^{-3}\,, \tag{1.24}$$

where Z is the metallicity (i.e. the fraction of the gas mass in elements heavier than helium) of the gas. An additional density threshold is imposed to prevent star formation in low over-density (δ) environments particularly at high redshifts. Hence, star formation is only allowed in regions where: (a) $\log_{10}(T) < \log_{10}(T_{\rm eos}) + 0.5$, (b) equation (1.24) is met, and (c) $\delta > 57.7$.

Following Schaye and Dalla Vecchia (2008), after identifying the star forming gas particles they are stochastically allowed to turn into stellar particles during a time step Δt with probability $\min(\dot{m}_\star\, \Delta t/m_{\rm g}, 1)$ where the star formation rate $\dot{m}_\star$ is given by

$$\dot{m}_\star = m_{\rm g}\; A(1\ \text{M}_\odot\ \text{pc}^{-2})^{-n}\left(\frac{\gamma}{G} f_{\rm g}\; P\right)^{(n-1)/2}\,, \tag{1.25}$$

where $m_{\rm g}$ is the gas particle mass, $A = 1.515 \times 10^{-4}$ M$_\odot$ yr^{-1} kpc^{-2}, $n = 1.4$, $\gamma = 5/3$ is the ratio of specific heats, G is the gravitational constant, $f_{\rm g} = 1$ is the gas

[1]Hydrogen, helium, carbon, nitrogen, oxygen, neon, magnesium, silicon, sulphur, calcium, and iron.

mass fraction, and P is the total pressure.

1.3.1.4.3 Feedback

Energetic feedback in cosmological simulations usually occurs due to stellar and/or black hole activity (i.e. supernova and AGN feedback, respectively). The stellar feedback prescription follows Dalla Vecchia and Schaye (2012) in which a stellar particle is assumed to explode as a type II supernova (SNII) releasing energy; hence heating the surrounding gas particles. The expected number of gas particles heated per stellar particle is given by

$$\langle N_{\rm heat} \rangle \approx 1.3 f_{\rm th} \left(\frac{\Delta T}{10^{7.5} K} \right)^{-1} , \tag{1.26}$$

where $f_{\rm th}$ is a parameter setting the probability that a gas particle neighbouring the supernova is heated (Schaye et al., 2015; Crain et al., 2015) and $\Delta T = 10^{7.5}$ is the temperature jump of gas particles that receive the energy.

The supermassive black hole model is implemented following Booth and Schaye (2009) and Rosas-Guevara et al. (2015). Black holes are seeded at the centre of every halo with a mass greater than 10^{10} $\rm M_\odot$ h^{-1} by converting the densest gas particle into a collision-less black hole (BH) particle with mass 10^5 $\rm M_\odot$ h^{-1}. Black holes can grow in mass by merging with other black holes or by accreting surrounding gas at a rate which is the minimum of the Eddington rate

$$\dot{m}_{\rm Edd.} = \frac{4\pi \ G \ m_{\rm BH} \ m_{\rm pr.}}{\epsilon_{\rm r} \ \sigma_{\rm T} \ c} , \tag{1.27}$$

and

$$\dot{m}_{\rm accr.} = \min \left(\dot{m}_{\rm Bondi} \left[(c_{\rm s}/V_\phi)^3 / C_{\rm visc.} \right] , \dot{m}_{\rm Bondi} \right) , \tag{1.28}$$

where $\dot{m}_{\rm Bondi}$ is the Bondi and Hoyle (1944) accretion rate[2]

$$\dot{m}_{\rm Bondi} = \frac{4\pi \ G^2 \ m_{\rm BH}^2 \ \rho}{(c_{\rm s}^2 + u^2)^{3/2}} , \tag{1.29}$$

where G is the gravitational constant, $m_{\rm BH}$ is the black hole mass, $m_{\rm pr.}$ is the proton mass, $\epsilon_{\rm r} = 0.1$ the radiative efficiency, $\sigma_{\rm T}$ is the Thomson cross section, c is the speed

[2]Which describes a spherically symmetric accretion onto a point mass which is travelling through a homogeneous medium.

of light, c_s is the sound speed of the gas, V_ϕ is the rotation speed of the gas around the black hole [see equation (16) of Rosas-Guevara et al. (2015)], $C_{\rm visc.} = 2\pi$ is a parameter related to the viscosity of the accretion disc, ρ is the gas density, and u is the relative velocity of the BH and the gas.

Once the accretion rate has been calculated, it is possible to define the feedback energy that the black hole will release. In each time step, a black hole increases its feedback energy by

$$\epsilon_r \ \epsilon_f \ \dot{m}_{\rm accr.} \ c_s^2 \ \Delta t = 0.015 \dot{m}_{\rm accr.} \ c_s^2 \ \Delta t \ . \tag{1.30}$$

This energy accumulates in an energy reservoir until there is enough energy to heat at least one gas particle by a temperature of $10^{8.5}$ K.

1.4 Magnetohydrodynamical simulations

Magnetohydrodynamical simulations capture the evolution of magnetic fields along with the hydrodynamical properties of the gas component (Vogelsberger et al., 2020). In order to do that, the magnetic fields are initialized with a certain magnetic seed at high redshift and evolved by ideal magnetohydrodynamics equations (Pakmor and Springel, 2013).

1.4.1 The Auriga simulation

The magnetohydrodynamical simulation used in this work (see Chapter 4) is the Auriga simulation (Grand et al., 2017), which is a suite of cosmological zoom-in simulations of Milky-Way mass haloes. We use the level-4 resolution (based on the Aquarius project nomenclature, Springel et al., 2008) which corresponds to dark matter and baryonic particles masses of 3×10^5 $M_\odot$ and 5×10^4 $M_\odot$, respectively. The gravitational co-moving softening length for stellar and dark matter particles is set to 500 cpc h^{-1}. This is equal to the minimum co-moving softening length allowed for gas cells, while their maximum physical softening length can not exceed 1.85 kpc.

Below, I briefly describe the generation of the initial conditions (Section 1.4.1.1), the gravity and magnetohydrodynamical solver (Section 1.4.1.2 and Section 1.4.1.3,

respectively), and subgrid model (Section 1.4.1.4) of the AURIGA simulation used in this thesis (Chapter 4).

1.4.1.1 Initial conditions

The dark matter haloes used for the AURIGA suite of zoomed re-simulations were selected from a dark matter only simulation of co-moving size $(100 \text{ cMpc})^3$ from the EAGLE project (Schaye et al., 2015). Once the initial distribution of dark matter particles is identified (Jenkins, 2010), each particle is split into a pair of dark matter and gas particle following the cosmological baryon mass fraction.

1.4.1.2 Gravity solver

The AURIGA simulations are performed with the N-body/magnetohydrodynamical code AREPO (Springel, 2010; Pakmor et al., 2011, 2016; Weinberger et al., 2020) which for gravitational forces uses the TreePM method. As described in Section 1.3.1.2, this method employs a Fast Fourier Transform method to account for long range forces, while short range forces are treated with an octree algorithm (Barnes and Hut, 1986).

1.4.1.3 Magnetohydrodynamical solver

The AREPO code solves the equations of ideal magnetohydrodynamics (Pakmor and Springel, 2013; Weinberger et al., 2020) by utilising an unstructured mesh constructed from a Voronoi tessellation (Springel, 2010) to perform finite-volume discretization of the state of the fluid. The mesh can be transformed[3] at any time-step in order to ensure that each cell contains a target mass. This feature ensures that denser regions are resolved with more cells than low density regions.

For each cell, the primitive variables (gas density, velocity, and magnetic field strength) are used to estimate the spatial gradients of the corresponding variable and linearly extrapolate it from the center of mass of a cell to the centers of all its interfaces. Then, fluxes between the interfaces are calculated by locally solving the

[3] A cell is merged with its neighbours or split into two cells if it contains less than half or more than twice the target mass, respectively.

Riemann problem as described in Pakmor and Springel (2013) and Pakmor et al. (2016).

1.4.1.4 The formation and evolution of galaxies

The AURIGA subgrid model includes magnetic fields, gas cooling and heating from a UV background, star formation, and stellar and AGN feedback.

1.4.1.4.1 Cooling

The cooling model follows Vogelsberger et al. (2013) and incorporates primordial and metal-line cooling with self-shielding corrections along with a spatially uniform UV background (Faucher-Giguère et al., 2009a). Similar to the EAGLE model (see Section 1.3.1.4.1), the cooling rates are obtained based on CLOUDY cooling tables. However, instead of following the element-by-element method of Wiersma et al. (2009), Vogelsberger et al. (2013) based their implementation on the cooling rates derived for a solar composition gas, which scale linearly with the total metallicity.

1.4.1.4.2 Star formation

In AURIGA, the interstellar medium (ISM) is described by the Springel and Hernquist (2003) model. In this model, the star-forming gas is treated as a two phase medium, where a cold phase consisting of dense clouds is embedded in a hot medium. Gas cells that enter the star-forming regime (i.e. have densities higher than $n = 0.13$ cm^{-3}) are stochastically turned into stellar particles with probability that exponentially scales with time in units of the star formation timescale (set to $t_{\rm sf} = 2.2$ Gyr).

The resulting stellar particle has mass which depends on the mass of the star forming gas cell. If the mass of the gas cell is less than twice the target cell mass (see Section 1.4.1.3) $m_{\rm target} = 5 \times 10^4$ M$_\odot$ then all the gas mass is converted into a stellar particle and the gas cell is removed. Otherwise, a mass equal to $m_{\rm target}$ is converted and the gas cell survives with reduced mass.

1.4.1.4.3 Feedback

As is common in simulations with baryonic mass resolution similar to or lower than the AURIGA simulations (i.e. $> 10^4$ $M_\odot$), each stellar particle is assumed to represent a single stellar population (SSP) characterised by a given age and metallicity. Each SSP has a distribution of stellar masses which is given by a Chabrier (2003) initial mass function, which allows for the number of SNII events to be inferred from the number of stars with masses between 8-100 $M_\odot$ in each SSP.

SNII events are assumed to be instantaneous and are implemented by probabilistically converting a star-forming gas cell into a wind particle (Vogelsberger et al., 2013) which is launched in an isotropically random direction with velocity equal to 3.45 times the local 1D dark matter velocity dispersion (Okamoto et al., 2010). The wind particle is decoupled from magnetohydrodynamical forces (i.e. only interacts gravitationally) and travels until either: (a) it reaches a gas cell with density less than 5 per cent of the star formation density threshold, or (b) it exceeds the maximum travel time. Once either of the above criteria is met it deposits its metals, momentum, mass, and energy (equally split into kinetic and thermal, Marinacci et al., 2014) in the gas cell in which it is located.

The AGN feedback model in the AURIGA simulation incorporates a radio and a quasar mode, which are both active at all times. For a detailed description of the AGN seeding and feedback recipe we refer the reader to Section 4.2.2.

Chapter 2

Morphological evolution and galactic sizes in the L-Galaxies SA model

In this chapter we update the L-Galaxies semi-analytic model (SAM) to better follow the physical processes responsible for the growth of bulges via disc instabilities (leading to pseudobulges) and mergers (leading to classical bulges). We address the former by considering the contribution of both stellar and gaseous discs in the stability of the galaxy, and we update the latter by including dissipation of energy in gas-rich mergers. Furthermore, we introduce angular momentum losses during cooling and find that an accurate match to the observed correlation between stellar disc scale length and mass at $z \sim 0.0$ requires that the gas loses 20 per cent of its initial specific angular momentum to the corresponding dark matter halo during the formation of the cold gas disc. We reproduce the observed trends between the stellar mass and specific angular momentum for both disc- and bulge-dominated galaxies, with the former rotating faster than the latter of the same mass. We conclude that a two-component instability recipe provides a morphologically diverse galaxy sample which matches the observed fractional breakdown of galaxies into different morphological types. This recipe also enables us to obtain an excellent fit to the morphology–mass relation and stellar mass function of different galactic types. Finally, we find that energy dissipation during mergers reduces the merger remnant sizes and allows us to match the observed mass–size relation for bulge-dominated systems.

2.1 Introduction

In the widely accepted lambda cold dark matter (ΛCDM) scenario the baryonic matter collapses into the centres of dark matter haloes, where it tends to form rotationally supported discs (Blumenthal et al., 1984; Peebles, 1984). In this framework, dark matter haloes acquire their angular momentum through tidal interactions (Peebles, 1969; White, 1984; Barnes and Efstathiou, 1987), and the associated gas discs were originally assumed (Fall and Efstathiou, 1980) to obtain the same specific angular momentum. Eventually, the collapsed gas will form stars and subsequently galaxies (White and Rees, 1978). While these dark matter structures evolve over time, they grow in mass and size through accretion and/or repeated mergers (Lacey and Cole, 1993). Since galaxy formation occurs within haloes, these phenomena also affect the properties of the associated galaxies.

This galaxy formation paradigm has been successfully captured by semi-analytic models (SAMs), which utilize N-body simulations of dark matter to obtain information about haloes' properties, substructures and merger history, while analytic recipes infer the properties of galaxies hosted within those structures.

2.1.1 Mergers and disc instabilities

In the hierarchical picture of structure formation, galaxy mergers have the ability to redesign the morphology of the progenitors (Toomre and Toomre, 1972; Barnes and Hernquist, 1996; Hopkins et al., 2010a). In particular, major mergers (Kauffmann et al., 1993; Baugh et al., 1996) or multiple minor mergers (Bournaud et al., 2007) are considered to be the natural culprits for converting the stellar orbits from circular to random, hence forming spheroid-like components (i.e. classical bulges) and dispersion-supported galaxies.

In addition to mergers, internal secular processes (see Sellwood, 2014b, for a review), such as the formation and evolution of bars, (Combes et al., 1990a; Raha et al., 1991; Martinez-Valpuesta et al., 2006) are also known to be drivers of galactic evolution. Bars induce torques into discs that cause considerable outward angular momentum transfer and redistribution/migration of stellar material (e.g. Hohl, 1971; Debattista et al., 2006; Minchev and Famaey, 2010). Furthermore, they funnel gas

to the centre of the galaxy (Combes and Sanders, 1981; Pfenniger and Norman, 1990; Englmaier and Shlosman, 2004), thus enhancing central star formation (Hawarden et al., 1986; Friedli and Benz, 1995; Jogee, 2006; Holmes et al., 2015).

In specific cases (Governato et al., 2009; Hopkins et al., 2009a; Stewart et al., 2009; Guedes et al., 2013) mergers may as well constitute a mechanism able to trigger gravitational instabilities (e.g. Toomre, 1964; Ostriker and Peebles, 1973; Efstathiou et al., 1982) and create inner disc structures (Aguerri et al., 2001; Eliche-Moral et al., 2006, 2011) or starbust activity (Mihos and Hernquist, 1994). These secular processes will culminate in the formation of a component called pseudo-bulge (see Kormendy and Kennicutt, 2004, and references therein).

Since both stellar and gaseous discs contribute to the stability of the galaxy (e.g. Jog and Solomon, 1984b,a; Bertin and Romeo, 1988; Wang and Silk, 1994; Elmegreen, 1995; Jog, 1996; Rafikov, 2001; Romeo and Wiegert, 2011), various theoretical and/or observational studies analysed local instabilities (Toomre, 1964) of composite discs. This dictates that modelling attempts should also follow the same path.

2.1.2 Bulges: classical and pseudo

Numerous authors have investigated whether the aforementioned bulge formation scenarios lead to different bulge types with distinct intrinsic properties (e.g. Fisher and Drory, 2016). Although some more recent studies (e.g. Athanassoula, 2005; Fragkoudi et al., 2015; Sachdeva and Saha, 2018) divide bulges into more categories, most authors distinguish two major types: pseudo and classical. In fact, Andredakis and Sanders (1994); Andredakis et al. (1995); Carollo (1999) studied early- and intermediate-type spiral galaxies and concluded that bulges fall into two categories: those that can be described by an exponential profile and those by an $r^{1/4}$ profile. More recently, Fisher and Drory (2008) analysed the Sérsic index of pseudo- and classical bulges and found that 90 per cent of the former have $n_{\rm b} < 2$ and all of the latter $n_{\rm b} > 2$. Moreover, Courteau et al. (1996) used a bulge-to-disc decomposition to calculate the ratio between bulge and disc scale lengths and concluded that their observations (correlated B/D scale lengths) strongly support a secular evolution model in which bulges with exponential surface brightness profiles emerge via disc

instabilities. Additionally, Fisher (2006) and Fisher et al. (2009) compared the profile of star formation in pseudo- and classical bulges and concluded that their stars are formed via different mechanisms.

It becomes apparent that there is a lot of evidence suggesting that this dichotomy can reveal a diversity in bulge properties. This motivated us to investigate these two distinct bulge types (see Section 2.2.3) and study their scaling relations (see Section 2.3.6.3 and Section 2.6.2).

2.1.3 Previous modelling work

2.1.3.1 The angular momentum of baryons

The majority of analytic and semi-analytic models of galaxy formation (e.g. Somerville and Primack, 1999; Cole et al., 2000; Monaco et al., 2007; Guo et al., 2011; Croton et al., 2016; del P. Lagos et al., 2018) follow Fall and Efstathiou (1980) and compute disc sizes based on the assumptions that (a) the cold gas disc inherits the specific angular momentum of the dark matter halo in which it forms, and (b) the gas conserves its angular momentum while cooling (e.g. Cole et al., 1994; Dalcanton et al., 1997; Mo et al., 1998). Even though modelling explicitly these processes in SAMs remains a challenging task, in this work we attempt to include this phenomenon (i.e. angular momentum losses during cooling) in the L-Galaxies model (see Section 2.2.1 and Section 2.5.1) and investigate its direct impact on galactic properties (see Section 2.3).

2.1.3.2 Disc instabilities

In the L-Galaxies[1] SAM, stellar disc instabilities are identified by the Efstathiou et al. (1982) criterion, which describes baryonic discs whose self-gravity dominates; thus are unstable to global perturbations (i.e. growth of bar-like modes). Their work was limited to idealized systems, which are significantly different than those found in nature or in more detailed simulations (see e.g. Athanassoula, 2008; Sellwood, 2014b; Fujii et al., 2018, for a discussion on this topic). However, the work of Efstathiou et al. (1982) provides a simple instability criterion which is suitable to be used by

[1] http://galformod.mpa-garching.mpg.de/public/LGalaxies/

SAMs where discs are formed under similar assumptions (see Section 2.2.1).

Determining which systems develop instabilities (e.g. De Lucia and Helmi, 2008; Cook et al., 2010), which galactic components are involved in them (e.g. Croton et al., 2016; Gargiulo et al., 2017) and how stability is restored (Bower et al., 2006; Monaco et al., 2007; De Lucia and Helmi, 2008; Gargiulo et al., 2015) are still open questions. It is known that gaseous discs have an influential role in galactic dynamics which becomes apparent when one considers their contribution to disc stability. Nevertheless, past modelling works have relied on a one-component stability criterion (e.g. Cole et al., 2000; De Lucia et al., 2006; Guo et al., 2011; Henriques et al., 2015).

2.1.4 The L-Galaxies model

The most recent version of the L-Galaxies model (Henriques et al., 2015, hereafter HWT15) invokes a simple argument to address disc instabilities and identify the stellar mass that has to be put into the bulge. It only takes into account the stability of the stellar disc and, as a consequence, underestimates disc instabilities and fails to reproduce the observed morphological fraction of galaxies (see Section 2.3.4). In this work we extend the Efstathiou et al. (1982) criterion to include cases where both stars and gas are present and investigate the contribution of gas in galactic stability.

Furthermore, the half-mass radius of classical bulges is calculated via energy conservation and the virial theorem, as described in Guo et al. (2011). This approach overestimates the size of bulges, which can be remedied by considering dissipation during gas-rich mergers (see Section 2.2.3.1 and Section 2.3.6.2).

2.1.5 Outline of the chapter

This chapter is organised as follows. In Section 2.2, we briefly describe a few vital processes regarding the L-Galaxies model's approach to simulate the formation and evolution of galaxies. In addition, we present the new merger remnant size and disc instability recipes we included in our model. Section 2.3, contains the results and Section 2.4, our conclusions.

2.2 The model

The L-Galaxies SAM has been well-described in the literature and we refer the reader to HWT15 for more details. Here, we briefly explain some key processes that are relevant to the purpose of this study and introduce angular momentum losses during cooling, and the updated disc instability and merger remnant size recipes.

We use merger trees derived from the Millennium simulation (Springel et al., 2005b), which has been shown to produce accurate properties for galaxies with stellar masses $> 10^9$ $M_\odot$ (see Guo et al., 2011, for more details). The cosmological parameters used throughout this work are adopted from Planck Collaboration et al. (2014c): $\sigma_8 = 0.829$, $H_0 = 67.3$ km s^{-1} Mpc^{-1}, $\Omega_\Lambda = 0.685$, $\Omega_\mathrm{m}= 0.315$, $\Omega_\mathrm{b}= 0.0487$ ($f_\mathrm{b}= 0.155$), and $n = 0.96$.

2.2.1 Formation and properties of gaseous and stellar discs

As haloes form and grow, they are assigned a cosmic abundance of diffuse primordial gas, which is assumed to be shock heated to the virial temperature (Rees and Ostriker, 1977; Silk, 1977; White and Rees, 1978). That gas will either cool immediately and be added to the cold gas disc of the central galaxy, or form a quasi-static hot atmosphere and accrete onto the disc at a slower pace (see section S1.4 of HWT15).

Hitherto the L-Galaxies model followed the two core assumptions of Fall and Efstathiou (1980); namely: (a) baryons and dark matter acquire identical specific angular momentum distributions, and (b) the former conserve their angular momentum while cooling. In this work, we assume that the initial (i.e. when the cold gas disc is formed from the hot component) specific angular momentum of the cold gas is a fraction $f = 0.8$ of the specific angular momentum of the halo within which it is embedded (see also Section 2.5.1). As discussed by Dutton and van den Bosch (2012) angular momentum losses during cooling results from the fact that the mass in ΛCDM haloes is more centrally concentrated than the angular momentum and the fact that cooling is an inside-out process (i.e. inner regions cool before the outer ones). Previous studies (Dutton and van den Bosch, 2012; Jiang et al., 2018) reported that the average value of the angular momentum retention factor is ~ 0.6. We choose a slightly higher value since these simulations include additional mech-

anisms, such as dynamical friction, which can further reduce the specific angular moment of baryons. In addition, our choice of $f = 0.8$ provides an excellent fit[2] to the galactic morphologies as we discuss in Section 2.3.4. Finally, we note that the angular momentum loss should be transmitted to the dark matter but this effect will be relatively small and we choose to neglect it.

As discussed in Guo et al. (2011), there are three mechanisms capable of altering the angular momentum vector of the gaseous disc, namely the addition of gas by cooling, the removal of gas through star formation, and the accretion from minor mergers. These can be expressed mathematically by the following formula

$$\begin{aligned}\delta\vec{J}_{\mathrm{d,\,gas}} &= \delta\vec{J}_{\mathrm{gas,\,cooling}} + \delta\vec{J}_{\mathrm{gas,\,SF}} + \delta\vec{J}_{\mathrm{gas,\,acc.}} \\ &= f\frac{\vec{J}_{\mathrm{DM}}}{M_{\mathrm{DM}}}\dot{M}_{\mathrm{cool}}\ \delta t \\ &- \frac{\vec{J}_{\mathrm{d,\,gas}}}{M_{\mathrm{d,\,gas}}}((1-R_{\mathrm{ret.}})\dot{M}_{\star}\ \delta t + \delta M_{\mathrm{reheat}}) \\ &+ \frac{\vec{J}_{\mathrm{DM}}}{M_{\mathrm{DM}}}M_{\mathrm{gas,\,sat.}}\ ,\end{aligned} \tag{2.1}$$

where the factor $f = 0.8$ accounts for angular momentum losses during cooling, $\dot{M}_{\mathrm{cool}}$ is the cooling rate [see equations (S6) and (S7) of HWT15], δt is the time interval, (1 - $R_{\mathrm{ret.}}$) $\dot{M}_{\star}$ is the formation rate of long lived stars [see equation (S14) of HWT15], $\delta M_{\mathrm{reheat}}$ is the cold gas reheated into the hot atmosphere as a result of star formation activity [see equation (S18) of HWT15] and $M_{\mathrm{gas,\,sat.}}$ is the cold gas mass of the merging satellites.

Following Mo et al. (1998), we assume that the gaseous and stellar discs are infinitesimally thin, in centrifugal equilibrium and have exponential surface density profiles, hence their scale lengths can be written as

$$R_{\mathrm{d,\,gas}} = \frac{|\vec{J}_{\mathrm{d,\,gas}}|}{2V_{\mathrm{max}}\ M_{\mathrm{d,\,gas}}}\ , \tag{2.2}$$

$$R_{\mathrm{d},\star} = \frac{|\vec{J}_{\mathrm{d},\star}|}{2V_{\mathrm{max}}\ M_{\mathrm{d},\star}}\ , \tag{2.3}$$

[2]The exact value of f required to reproduce the observed morphologies is potentially affected by the last term in equation (3.10) since its simplistic assumption for the orientation of satellite's specific angular momentum can lead to the overprediction of the specific angular momentum of the gaseous disc.

where $\vec{J}_{\rm d,\,gas}$, $M_{\rm d,\,gas}$ and $\vec{J}_{\rm d,\star}$, $M_{\rm d,\star}$ are the angular momentum and mass of the gaseous and stellar disc, respectively, and $V_{\rm max}$ is the maximum circular velocity of their host halo which is used as a proxy for the rotation velocity of both discs.

2.2.2 Disc instabilities

Disc instabilities describe systems where the attraction due to self-gravity overcomes the centrifugal force due to rotation. In our updated instability recipe we treat galactic discs as two-component systems where the contribution of each disc (i.e. stellar and gaseous) to the stability of the whole galaxy is mass weighted. We extend the simple criterion of Efstathiou et al. (1982) and combine both discs in an approach similar to the one used by authors who combined the Toomre (1964) local instability criteria (e.g. Wang and Silk, 1994; Romeo and Wiegert, 2011). Our new galactic instability criterion can be written as $\epsilon_{\rm total} < 1$, where

$$\epsilon_{\rm total} \equiv \frac{M_{\rm d,\star}\ \epsilon_\star + M_{\rm d,\,gas}\ \epsilon_{\rm gas}}{M_{\rm d,\,total}}\ . \tag{2.4}$$

Here $M_{\rm d,\,total}$, $M_{\rm d,\star}$, and $M_{\rm d,\,gas}$ are, respectively, the total disc mass, the mass in stars, and the mass of gas in the disc, and

$$\epsilon_i = c_i \left(\frac{G\ M_{{\rm d},\,i}}{{V_{\rm c}}^2\ R_{{\rm d},\,i}} \right)^{\frac{1}{2}}\ , \tag{2.5}$$

where the index $i = \star$ or gas, $V_{\rm c}$ is the rotational velocity which for both discs is approximated by the circular velocity of their host halo, and $M_{{\rm d},\,i}$ and $R_{{\rm d},\,i}$ are the mass and scale length of the i component, respectively. $c_\star = 1.1$ and $c_{\rm gas} = 0.9$ are constants that reflect the stability criteria for isolated stellar (Efstathiou et al., 1982) and gaseous (Christodoulou et al., 1995) discs, respectively.

If the galaxy is unstable then we adopt the following two-step procedure:

(i) If $\epsilon_{\rm gas} > 1$, then we transfer mass from the gas disc to the stellar disc, thus lowering $\epsilon_{\rm gas}$ until, either the combined system becomes stable, $\epsilon_{\rm total} = 1$, or $\epsilon_{\rm gas} = 1$. When making this transfer, we assume that a small fraction of the gas makes its way onto the central black hole in accordance with equation (S23) of HWT15 (and setting the factor $M_{\rm sat.}/M_{\rm cen.} = 1$ in that equation).

(ii) If the system remains unstable, then we transfer stars from the stellar disc to the bulge until $\epsilon_{\rm total} = 1$.

We expect that disc instability will occur mostly in the inner regions of the galaxy in which stars have low angular momentum. For that reason, when transferring stars from the disc to the bulge, we assume that they carry no angular momentum with them.[3] In our model, that then results in an increased specific angular momentum of the stars left behind and [see equation (2.3)] a proportional increase in the disc scale length.

2.2.3 Formation and properties of classical and pseudo-bulges

In the L-Galaxies model bulges form through three distinct mechanisms: major mergers, minor mergers, and disc instabilities. Major and minor mergers are assumed to produce classical bulges, while disc instabilities lead to the formation of bar-related pseudo-bulges.

2.2.3.1 Classical bulges

Whenever two or more dark matter haloes merge, so do their associated galaxies but on a longer time-scale determined by two-body relaxation. In our model, we characterize as central galaxies those that dwell in the potential minimum of the most massive subhaloes (hereafter the main halo) and as satellite galaxies those that reside inside the non-dominant subhaloes that are bound to the main halo.

We distinguish a major from a minor merger based on the ratio of the total baryonic mass (stars + gas), M_1 and M_2, of the satellite and central galaxy, respectively. In major mergers ($M_1/M_2 > 0.1$, see HWT15 for more details) the discs of the progenitors are dismantled and both the pre-existing stars and those formed during the merger become part of the resulting bulge-dominated galaxy. In minor mergers, the bulge of the descendant accretes all the stars of the less massive progenitor, while stars formed during this process remain in the remnant's disc. The mass of those stars is calculated by using the 'collisional starburst' formulation of Somerville et al. (2000)

$$M_{\star,\,\mathrm{burst}} = \alpha_{\mathrm{SF},\,\mathrm{burst}} \left(\frac{M_1}{M_2}\right)^{\beta_{\mathrm{SF},\,\mathrm{burst}}} M_{\mathrm{d,\,gas}} \ , \tag{2.6}$$

[3] A later version of the L-Galaxies model, in development, will have spatially-resolved discs and be able to investigate this in more detail.

where $\alpha_{\rm SF,\,burst}$ and $\beta_{\rm SF,\,burst}$ are free parameters and $M_{\rm d,\,gas}$ is the total gas disc mass of both galaxies combined.

Galaxy mergers are considered to play a fundamental role in the production of elliptical galaxies, hence having a model able to evaluate the size of the remnant and reproduce its scaling relations across cosmic time is crucial. The HWT15 version of the model calculated the half-mass radius of the remnant using energy conservation arguments, where the final binding energy was equated to the self-binding energies of the two progenitors plus their orbital energy [see equation (S34) of HWT15]. Several authors have argued that this simple picture leads to unrealistic sizes, especially at the low-mass end (Covington et al., 2008; Hopkins et al., 2009c, 2010b; Shankar et al., 2010; Covington et al., 2011; Shankar et al., 2013; Porter et al., 2014). This problem mainly arises from the fact that the above approximation does not take into account gas dissipation during mergers, where gas clouds collide and radiate away their kinetic energies. In cases where the gas makes up a significant fraction of the total mass of the progenitors this phenomenon would result in smaller and denser remnants. We follow Covington et al. (2008, 2011) and Tonini et al. (2016) and include a term to account for radiative losses. In this picture the energy conservation formula is given by

$$E_{\rm final} = E_{\rm initial} + E_{\rm orbital} + E_{\rm radiative}\ , \tag{2.7}$$

where for major mergers each energy term can be explicitly written as

$$E_{\rm final} = -G\left[\frac{(M_{\star,\,1} + M_{\star,\,2} + M_{\star,\,\rm burst})^2}{R_{\rm final}}\right]\ , \tag{2.8}$$

$$E_{\rm initial} = -G\left(\frac{M_1^2}{R_1} + \frac{M_2^2}{R_2}\right)\ , \tag{2.9}$$

$$E_{\rm orbital} = -G\left(\frac{M_1\ M_2}{R_1 + R_2}\right)\ , \tag{2.10}$$

$$E_{\rm radiative} = -C_{\rm rad.}\ E_{\rm initial}\left(\frac{M_{\rm gas,\,1} + M_{\rm gas,\,2}}{M_1 + M_2}\right)\ , \tag{2.11}$$

where $M_{\star,\,\rm i}$, $M_{\rm i}$, $M_{\rm gas,\,i}$, and $R_{\rm i}$ are the total stellar mass (disc + bulge), total baryonic mass (stars + gas), gas mass, and stellar half-mass radius of the i progenitor, $R_{\rm final}$ is the stellar half-mass radius of the remnant, $C_{\rm rad.}$ is a parameter which defines the efficiency of the radiative process (see discussion below) and $M_{\star,\,\rm burst}$ is the mass of the new stars formed during the merger which is given by equation (2.6).

For minor mergers we follow Guo et al. (2011) and assume that the total stellar mass of the satellite galaxy is merged with the bulge of the central galaxy, therefore

$$E_{\rm final} = -G\left[\frac{(M_{\rm b,\,1} + M_{\star,\,2})^2}{R_{\rm final}}\right] \ , \tag{2.12}$$

$$E_{\rm initial} = -G\left(\frac{M_{\rm b,\,1}^2}{R_{\rm b,\,1}} + \frac{M_{\star,\,2}^2}{R_2}\right) \ , \tag{2.13}$$

$$E_{\rm orbital} = -G\left(\frac{M_{\rm b,\,1}\ M_{\star,\,2}}{R_{\rm b,\,1} + R_2}\right) \ , \tag{2.14}$$

$$E_{\rm radiative} = -C_{\rm rad.}\ E_{\rm initial}\left(\frac{M_{\rm gas,\,1} + M_{\rm gas,\,2}}{M_1 + M_2}\right) \ , \tag{2.15}$$

where $M_{\rm b,\,1}$ and $R_{\rm b,\,1}$ are the stellar mass and half-mass radius of the bulge of the more massive progenitor and $M_{\star,\,2}$ and R_2 are the total stellar mass and half-mass radius of the minor progenitor. Equation (2.7) indicates that galaxies with higher gas fractions will experience more dissipation during mergers, and since lower mass galaxies have low-mass progenitors which have higher cold gas fractions at all redshifts, early-wet mergers will produce more compact remnants than late-dry mergers (e.g. Robertson et al., 2006a,b; Dekel and Cox, 2006).

Covington et al. (2008) calibrated their model using the N-Body/SPH code GADGET (Springel et al., 2001b) to simulate mergers of isolated, low-redshift, gas-rich, identical disc galaxies, finding $C_{\rm rad.} \simeq 1$. However, a higher value of $C_{\rm rad.} = 2.75$ was found for disc-dominated galaxies that have recently experienced a major merger (Covington et al., 2011). In addition, Porter et al. (2014) used 68 hydrodynamical simulations of major and minor binary mergers (see Johansson et al., 2009) of galaxies with either mixed or spheroid-spheroid morphologies. They found that the morphology, the mass ratio, and the gas content could cause the $C_{\rm rad.}$ parameter to vary significantly, from 0.0 (dissipationless) for minor or major mergers where one or both of the progenitors are bulge-dominated; to 2.5 for major mergers between disc-dominated galaxies. In this work we adopt the value $C_{\rm rad.} = 1.0$ in concordance with previous modellers.

2.2.3.2 Pseudo-bulges

Galaxy-galaxy interactions have a pivotal role in regulating galactic evolution; however, internal processes, such as disc instabilities, are of similar importance since they are responsible for the emergence of pseudo-bulges.

In order to determine the half-mass radius of the resulting pseudo-bulge we distinguish between two cases; the first is when the disc already possesses a bulge and then becomes unstable. We follow Guo et al. (2011) and assume that the unstable mass merges into the existing bulge, thus the final bulge's half-mass radius is given by

$$C\frac{G\ M_{\rm final}^2}{R_{\rm final}} = C\frac{G\ M_{\rm old}^2}{R_{\rm old}} + C\frac{G\ M_{\star,\,\rm unstable}^2}{R_{\rm b}} + \alpha_{\rm inter}\frac{G\ M_{\rm old}\ M_{\star,\,\rm unstable}}{R_{\rm old}+R_{\rm b}}\ , \tag{2.16}$$

where $M_{\rm final}$ and $R_{\rm final}$ are the mass and half-mass radius of the final bulge, $M_{\rm old}$ and $R_{\rm old}$ are the mass and half-mass radius of the existing bulge, $M_{\star,\,\rm unstable}$ is the mass occurred from equation (2.4), C is a structural parameter relating the binding energy of a galaxy to its mass and radius and $\alpha_{\rm inter}$ is a parameter quantifying the effective interaction energy deposited in the stellar components. Guo et al. (2011) and Henriques et al. (2015) used $\alpha_{\rm inter}/C = 4$ as it led to bulge sizes in adequate agreement with SDSS galaxies. However, we set $\alpha_{\rm inter}/C = 1.5$ in order to be consistent with the results of Boylan-Kolchin et al. (2005) who found that $1.3 < \alpha_{\rm inter}/C < 1.7$. The half-mass radius of the unstable material $R_{\rm b}$ is taken from

$$\begin{aligned} M_{\star,\,\rm unstable} &= 2\pi\ \Sigma_{\star,\,0}\ R_{\rm d,\,\star} \\ &\quad \times \left[R_{\rm d,\,\star} - (R_{\rm b} + R_{\rm d,\,\star})\exp(-R_{\rm b}/R_{\rm d,\,\star})\right]\ , \end{aligned} \tag{2.17}$$

where $\Sigma_{\star,\,0}$ and $R_{\rm d,\,\star}$ are the central surface density and the exponential scale length of the disc. If the galaxy had no bulge prior to the instability incident we assume that the half-mass radius of the newly formed bulge is equal to $R_{\rm b}$.

Finally, in the L-Galaxies SAM the specific angular momentum of bulges is only altered during mergers, since we assume that during instabilities the unstable stellar mass transfers negligible angular momentum from the disc to the bulge (as in Guo et al., 2011; Henriques et al., 2015). We assume that the accreted specific angular momentum matches that of the halo within which the satellite galaxy is orbiting, such that the specific angular momentum of the merger remnant can be written as

$$j_{\rm b} = \frac{j_{\rm b,\,old}\ M_{\rm old} + j_{\rm halo}\ M_{\star,\,\rm sat.}}{M_{\rm b}}\ , \tag{2.18}$$

where $j_{\rm b,\,old}$ and $M_{\rm old}$ are the specific angular momentum and mass of the existing bulge, $j_{\rm halo}$ is the specific angular momentum of the halo, $M_{\star,\,\rm sat.}$ is the stellar mass of the satellite and $M_{\rm b}$ is the remnant's new mass.

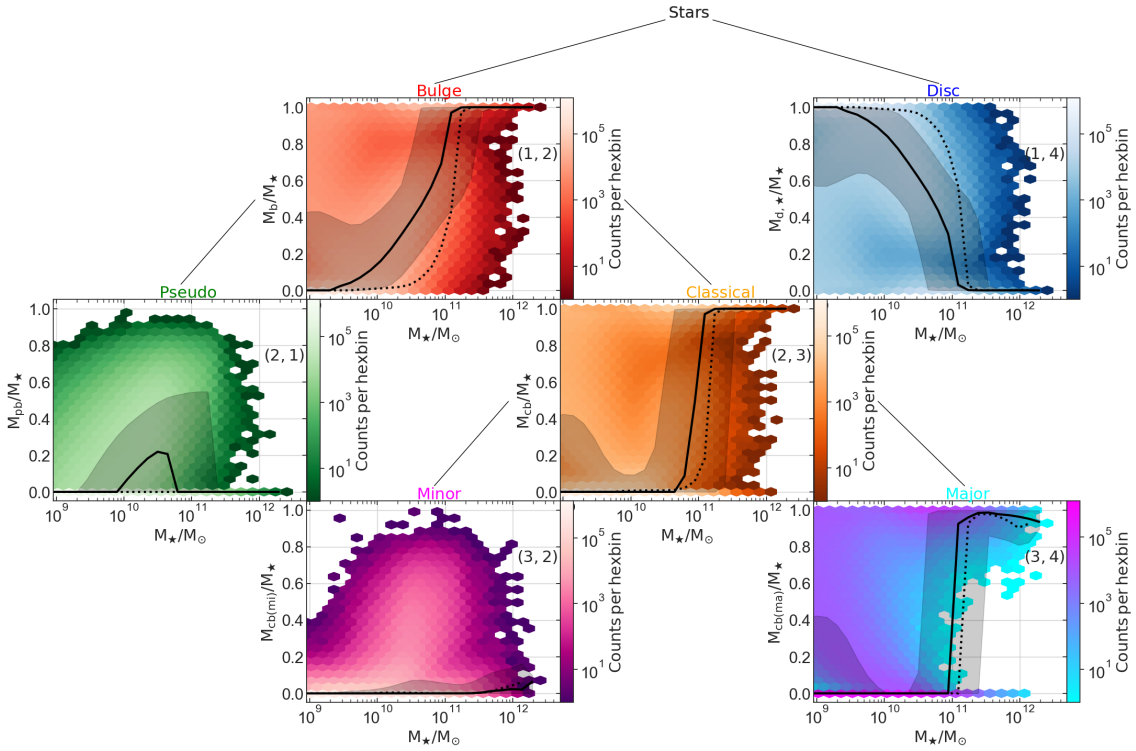

Figure 2.1: Decomposition of the total stellar mass of each galaxy at redshift $z \sim 0.0$. Each panel contains a hexagonal binning plot of the component-to-total stellar mass ratio as a function of the total stellar mass along with our (black solid) and HWT15 (black dotted) median lines and our 16th-84th percentile range (black shaded regions). The black straight lines that connect the panels represent the divisions described in the tree chart in Section 2.3.1 and the (row, column) positioning of each component in the figure corresponds to: (1,2) – bulge; (1,4) – disc; (2,1) – pseudo-bulge; (2,3) – classical-bulge; (3,2) – through minor mergers; (3,4) – through major mergers.

2.3 Results

2.3.1 Stellar mass assembly channels

One feature of our model is its ability to follow the formation and evolution of classical and pseudo-bulges by separately tracking each channel that contributes to their mass budget. This allows us to gain insight into the behaviour of each component and answer questions such as: how often do disc galaxies host classical as opposed to pseudo-bulges; how is the mass of disc- and bulge-dominated galaxies distributed; and how structurally different are galaxies that host classical or pseudo-bulges.

We follow the stellar mass transferred between galaxies in minor and major mergers, and the stellar mass transferred between galactic components during disc

instability events. We split the total stellar mass into six categories, some of which are subsets of others:

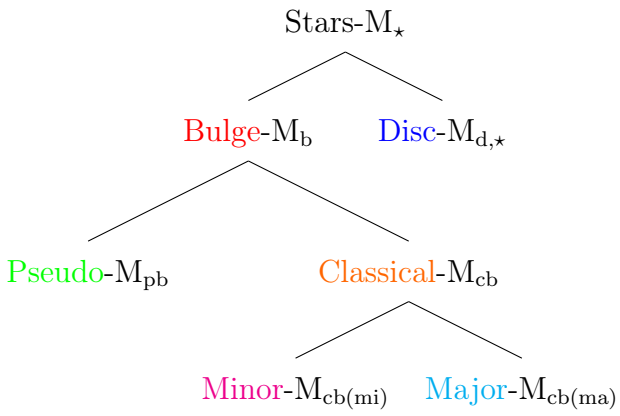

In the L-Galaxies model stars can be found in the two main galactic components, namely the stellar disc (d,⋆) and the bulge (b). Tracking the two widely accepted bulge formation paths allows us to further divide the bulge mass into the mass created via disc instabilities and the one accreted through mergers, hence leading to the formation of pseudo-bulges (pb) and classical bulges (cb), respectively. Finally, the population of classical bulges can be dichotomized into those produced through major mergers [cb(ma)] and those through minor mergers [cb(mi)]. This decomposition is shown in Fig. 2.1 which contains the ratio between the stellar mass of each of the above six components and the total stellar mass of each galaxy.

As can be seen in Fig. 2.1, the L-Galaxies model produces pure disc- (1,4) with masses up to $M_\star \sim 3 \times 10^{11}$ $M_\odot$ and pure bulge-dominated galaxies (1,2) of all masses. The corresponding median lines suggest that the most massive galaxies are bulge-dominated (e.g. Baldry et al., 2004; Wilman and Erwin, 2012; Nair and Abraham, 2010), while the majority of normal galaxies are disc-dominated (e.g. Fukugita et al., 2007; Bamford et al., 2009; Nair and Abraham, 2010); a behaviour which is consistent with observational studies.

The large scatter in (2,1) suggests that in a few galaxies pseudo-bulges dominate the total stellar mass budget, hence leading to the development of lenticular galaxies (Kormendy and Kennicutt, 2004; Kormendy and Cornell, 2004; Weinzirl et al., 2009; Vaghmare et al., 2013). Interestingly, there are a some extreme cases where the pseudo-bulge-to-total stellar mass ratio is as high as 0.9. This is in agreement with

the recent work of Saha and Cortesi (2018) who proposed disc instabilities as a mechanism responsible for the production of field S0 galaxies.

From the behaviour of our data in panels (2,1) and (2,3) and the corresponding median lines, we can say that most of the bulge mass in galaxies with masses between 10^{10} $M_\odot < M_\star < 10^{11}$ $M_\odot$ is in pseudo- and not classical bulges. At $\sim 10^{11}$ $M_\odot$ the secular evolution scenario cannot compete with the violent one and as a consequence major mergers (3,4) begin to destroy the progenitors and form bulge-dominated systems (2,3).

Finally, we note that minor mergers (3,2) never make a significant contribution to the total stellar mass due to the adopted merger mass ratio threshold.[4] High-resolution simulations (e.g. Stewart et al., 2008; Hopkins et al., 2010a) indicate that mergers with mass ratios 0.1 and below are very rare and have relatively little impact on the total stellar mass of the remnant galaxy. In addition, in cases where a minor merger triggers disc instabilities, we assume that the newly formed pseudo-bulge will contain both the unstable and the previously existing bulge mass. Thus, the stellar mass accreted from that minor merger is now considered to be part of the pseudo-bulge.

The most notable discrepancies between the HWT15 (dotted lines) and the presented version of the L-Galaxies SAM appear in panels (1,2), (1,4), and especially (2,1). These three panels highlight the importance of gas in disc instabilities since it enhances the formation of bar-related pseudo-bulges (Bournaud and Combes, 2002; Seo et al., 2019) and reduces the unrealistic population of high mass disc-dominated galaxies seen in HWT15.

2.3.2 Stellar mass evolution of galactic components

Fig. 2.2 illustrates how the contribution of each component to the total stellar mass fluctuates within each galactic mass range at different redshifts.

At $z \sim 0.0$ at the lowest masses about 80 per cent of stars lie in discs with most of the rest in merger-driven bulges. At 10^{10} $M_\odot$ minor mergers begin to initiate the formation of classical bulges and for total stellar masses above 10^{11} $M_\odot$ major mergers become the dominant mechanism that affects galactic morphology. This

[4]Set to 0.1 by HWT15 to ensure that the majority of high-mass galaxies were bulge-dominated.

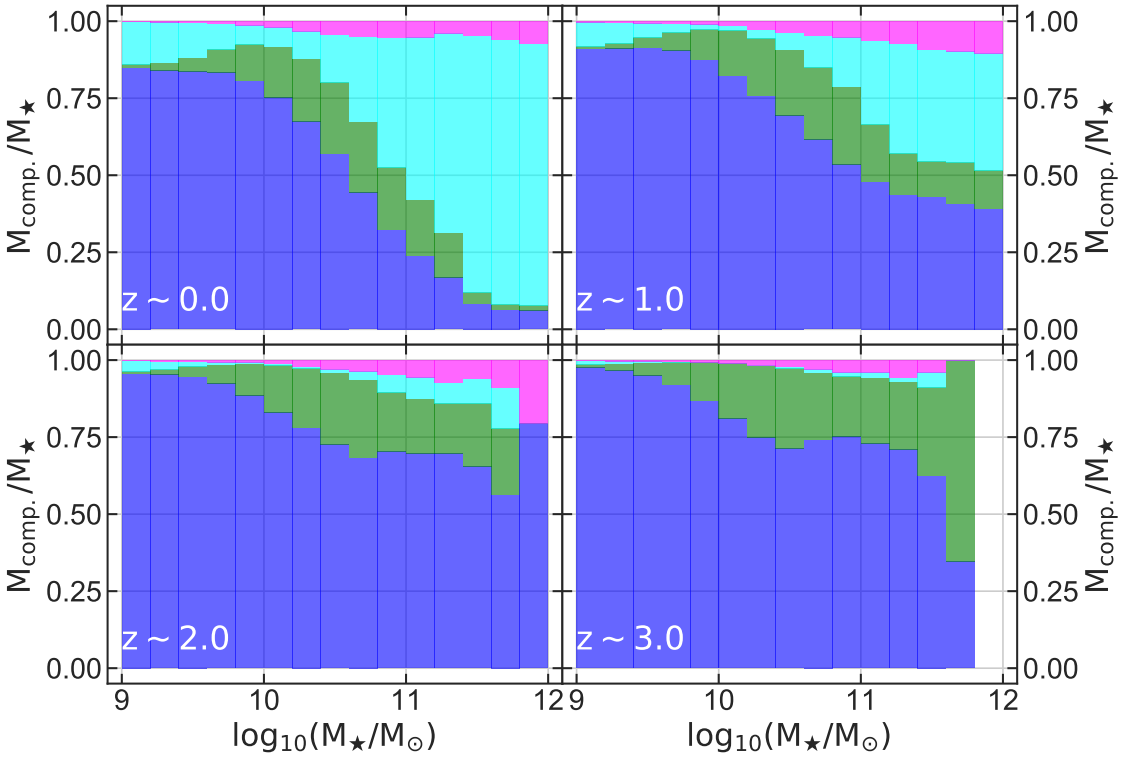

Figure 2.2: Relative contribution of each component to the total stellar mass (i.e. the mass summed over all galaxies in a given stellar mass bin) at redshifts $z \sim 0.0$, 1.0, 2.0, and 3.0. Colours are the same as in Fig. 2.1: blue – disc; green – pseudo-bulge; cyan –classical bulge through major mergers; magenta – classical bulge through minor mergers.

behaviour follows from a hierarchical galaxy assembly scenario in which mergers give rise to the formation of the most massive system. Pseudo-bulges never dominate but are most important between 10^{10} $M_\odot$ and $10^{11.5}$ $M_\odot$, accounting for about 20 per cent of the total over this range.

As pointed out by few authors (e.g. Bell et al., 2004; Conselice et al., 2005; Ilbert et al., 2010), the massive end of the galaxy mass function at $z < 0.8$ is dominated by galaxies with early-type morphologies, which is consistent with our results. Furthermore, studies which focused on the evolution of the merger rate of galaxies (e.g. Le Fèvre et al., 2000; Bell et al., 2006; Lotz et al., 2008) concluded that the majority of them have experienced major mergers since $z \sim 1$, and this event has severely affected their morphology (van Dokkum, 2005). In galaxies produced by the L-Galaxies model we can also notice that classical bulges, both via major and minor merger, have a significant contribution to the total stellar mass at $z \leq 1$, while the disc component becomes increasingly important at higher redshifts.

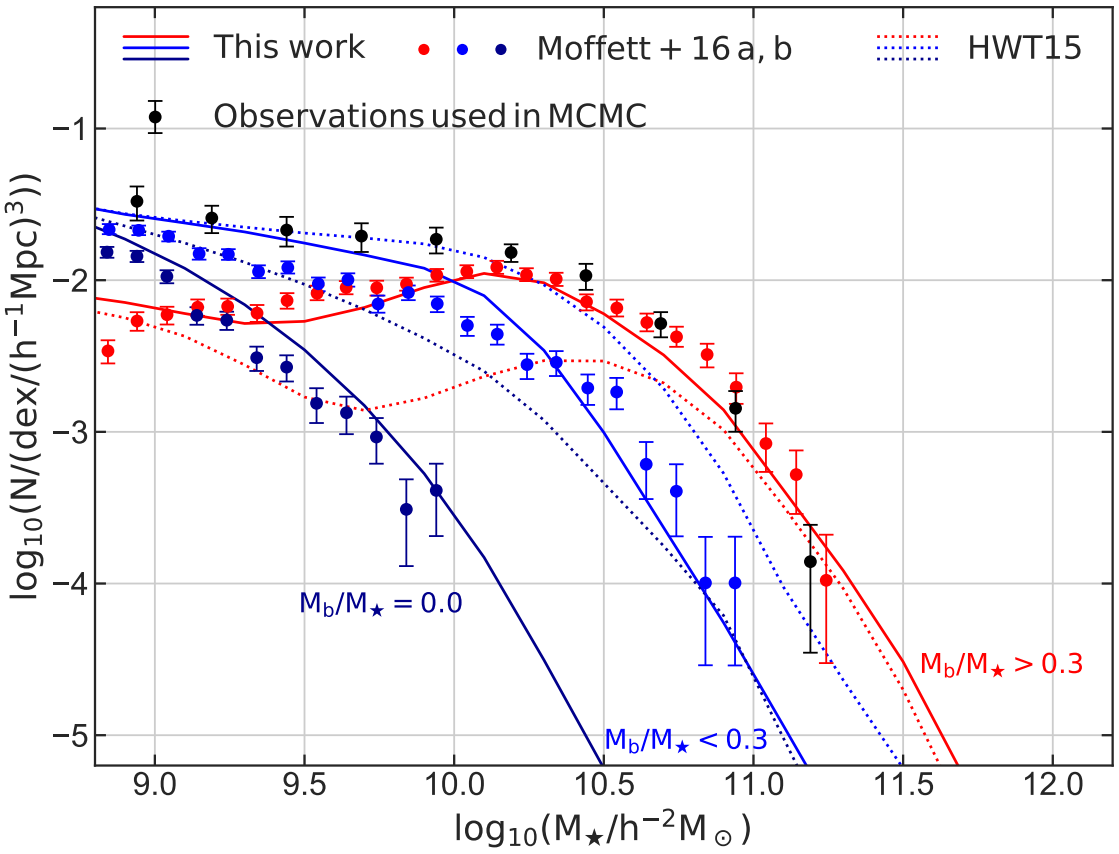

Figure 2.3: Total stellar mass function at redshift $z \sim 0.0$ for different galactic types. Blue, red and darkblue lines represent disc-dominated galaxies, systems with $M_\mathrm{b}/M_\star > 0.3$ and pure disc galaxies, respectively. Blue and red circles represent observational data from Moffett et al. (2016a), while darkblue from Moffett et al. (2016b). Solid and dotted lines show results from this work and HWT15, respectively.

Finally, we see a notable evolution in the contribution of pseudo-bulges in the total stellar mass, which is linked to the high gas content of high-redshift galaxies. This evolution is consistent with simulations (e.g. Agertz et al., 2009; Forbes et al., 2014) and is captured by our modified disc instability recipe which takes into account the contribution of the gaseous disc in the galactic stability.

2.3.3 Stellar mass functions

As discussed in Section 2.2.2, stellar and gaseous discs are able to trigger instabilities that can significantly redistribute galactic material. Hence, stellar mass functions of disc and bulge stars allow us to illustrate the influence of our new approach on galaxies produced by the L-Galaxies model (see also Fig. 2.13).

In Fig. 2.3, we split our galaxies into different morphological types according to their bulge mass fractions and plot their total stellar mass functions. We compare with the Moffett et al. (2016b) sample of single-component pure disc systems and the disc-(Sab-Scd/Sd-Irr) and spheroid-dominated (E/S0-Sa) galaxies selected by Moffett et al. (2016a). The choice of a bulge-to-total mass ratio of 0.3 to distinguish disc- and spheroid-dominated systems in our model was motivated by various studies of the B/T ratio of S0 galaxies (e.g. Laurikainen et al., 2005, 2010; Barway et al., 2016) which found that the mean value is ~ 0.25. In addition, Weinzirl et al. (2009) found that, in their sample, the fraction of spiral galaxies with $B/T > 0.4$ is 8 per cent. Hence, our B/T threshold lies between these observed values.

The updated L-Galaxies model shows an impressive agreement with the behaviour denoted by the observational data for all galaxy samples[5]. On the other hand, it is clear that the HWT15 model has a strong tendency to form more disc-dominated systems and bulgeless galaxies at higher masses. On that account, the instability recipe described in Section 2.2.2 prevents the formation of disc-dominated galaxies and restricts the abundance of purely disc systems by redistributing the stellar mass between galactic components. Hence, it directly affects the galactic morphology and allows us to better match the observed behaviours in Fig. 2.3.

2.3.4 Galactic morphology

In the L-Galaxies SAM galaxy mergers are dichotomized into major and minor. If the total baryonic mass (stars + gas) of the more massive progenitor exceeds that of the less massive by at least an order of magnitude, then this incident is characterized as minor; in any other case the merger is treated as a major. In this work, we adopt the same mass ratio threshold ($R_{\rm merger} \equiv M_{\rm sat.}/M_{\rm cen.} = 0.1$)[6] as in HWT15 in order to distinguish those two regimes. This division regulates the type of the remnant galaxy (i.e. bulge- or disc-dominated).

This categorization is depicted in the left-hand panel of Fig. 2.4 which represents

[5]We note that we do not attempt to calculate the errors on our model (e.g. Smith, 2012) and perform a detailed comparison with the observations since we are interested in broadly matching their predictions rather than perfectly fitting the data.

[6]Chosen by HWT15 to ensure that the majority of galaxies above $10^{11.5}$ $M_\odot$ are bulge-dominated.

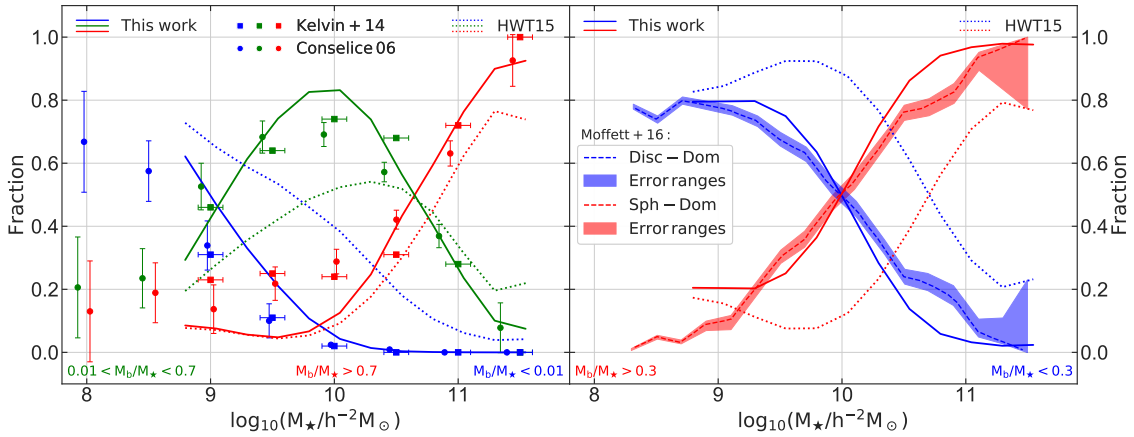

Figure 2.4: Fraction of different morphological types as a function of total stellar mass at redshift $z \sim 0.0$. *Left-hand panel:* Red, green, and blue lines show the fraction of bulge-dominated, normal spiral and pure disc galaxies, respectively. Red, green, and blue filled circles are observational data from Conselice (2006) that show the elliptical, spiral and irregular galaxies, respectively. Red, green, and blue squares are S0-Sa + Sab-Scd, LBS + E and Sd-Irr galaxies, respectively from Kelvin et al. (2014). *Right-hand panel:* Red lines represent systems with $M_{\rm b}/M_{\star} > 0.3$ while blue lines represent disc-dominated. Observational data points from Moffett et al. (2016a) are represented by dashed lines along with the corresponding errors. In both panels solid and dotted lines show results from this work and HWT15, respectively.

the fraction of different galaxy types as a function of their total stellar mass. We split our galaxy sample into three categories based on their bulge-to-total stellar mass ratio. In Fig. 2.4 the red solid line shows the fraction of bulge-dominated galaxies, akin to ellipticals ($M_{\rm b}/M_{\star} > 0.7$), blue solid line shows the fraction of normal spirals ($0.01 < M_{\rm b}/M_{\star} < 0.7$) and green solid line represents disc-dominated galaxies, akin to extreme late-types ($M_{\rm b}/M_{\star} < 0.01$). Similar approaches for proxies for the morphology of simulated galaxies have been used by several authors (e.g. Bertone et al., 2007; Lagos et al., 2008; Guo et al., 2011; Gargiulo et al., 2015). From an observational point of view, Weinzirl et al. (2009) measured the B/T ratio of 143 bright, high-mass spirals and concluded that $\sim$ 66 per cent, $\sim$ 26 per cent, $\sim$ 8 per cent, and 100 per cent of their galaxies have $B/T \leq 0.2$, $0.2 < B/T \leq 0.4$, $0.4 < B/T \leq 0.75$, and $B/T \leq 0.75$, respectively: throughout this work we use $M_{\rm b}/M_{\star} < 0.3$ (i.e. $M_{\rm d}/M_{\star} > 0.7$) for disc-dominated and $M_{\rm b}/M_{\star} > 0.7$ for bulge-dominated galaxies.

The observational data have been taken from Conselice (2006), who used a sample of $\sim$ 22 000 galaxies at $z < 0.05$ to plot the morphological fraction as a function

of stellar mass. In addition, Kelvin et al. (2014) analysed a sample of 2711 local ($0.025 < z < 0.06$) galaxies taken from the Galaxy And Mass Assembly (GAMA) survey. They visually divided their sample into five categories, namely LBS, E, S0-Sa, Sab-Scd, and Sd-Irr; however, in order to make the comparison with our data more efficient we combined the LBS with E galaxies and the S0-Sa with Sab-Scd galaxies (see table 1 of Kelvin et al., 2014). We also include the HWT15 data (dotted lines) for comparison with the previous version of the model.

Both observational surveys indicate that the fractional contribution of galaxies with stellar masses between 10^9 $M_\odot$ $< M_\star <$ 10^{11} $M_\odot$ is dominated by spirals, although by $M_\star \sim 10^{10.5}$ $M_\odot$ spirals and ellipticals represent about 50 per cent each. At stellar masses higher than that, almost all galaxies have turned into ellipticals. These behaviours are also fairly well represented by our galaxies over the whole stellar mass range. However, despite the new instability recipe the L-Galaxies model fails to match the fraction of bulge dominated galaxies for masses below $\sim 10^{10}$ $M_\odot$. Tidally induced bars (e.g. Ruiz et al., 2015; Łokas et al., 2016; Peschken and Łokas, 2019) may represent a mechanism capable of altering this behaviour by further transferring mass to the bulge; and we plan to test this effect in future work.

In the right-hand panel, we present the fraction of our disc-dominated galaxies ($M_\mathrm{b}/M_\star < 0.3$) and systems with $M_\mathrm{b}/M_\star > 0.3$ and compare with the fraction found by Moffett et al. (2016a) who selected 4971 disc-(Sab-Scd/Sd-Irr) and 1692 spheroid-dominated (E/S0-Sa) galaxies. We use the same selection criteria as those described in the previous section since we compare with the same survey. Our results suggest that the point indicating the transition between the numerical dominance of disc- and spheroid-dominated galaxies is in strong agreement with Moffett et al. (2016a) and shows a clear improvement over the HWT15 version of the L-Galaxies SAM.

2.3.5 Mass-specific angular momentum relation

Angular momentum is one of the most fundamental galactic properties; it can dictate the galactic size and morphology, and also provides a vital constraint on theories of galaxy formation (e.g. Mo et al., 1998; Romanowsky and Fall, 2012; Obreschkow and Glazebrook, 2014; Sweet et al., 2018; Posti et al., 2018a). The correlation of

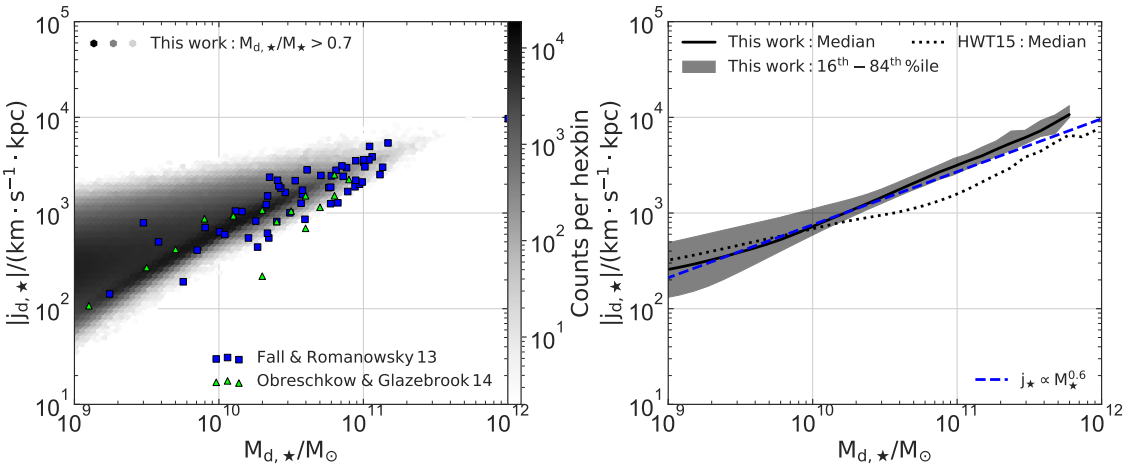

Figure 2.5: Mass-specific angular momentum relation for disc-dominated galaxies at redshift $z \sim 0.0$. *Left-hand panel:* Disc stellar mass versus specific angular momentum compared with Obreschkow and Glazebrook (2014) and Fall and Romanowsky (2013) observations. *Right-hand panel:* The median and 16th-84th percentile range (black shaded region) of the aforementioned relation compared with the Fall (1983) relation. Black solid and dotted lines show results from this work and HWT15, respectively.

the specific angular momentum with stellar mass, $j \propto M^{2/3}$, was introduced 35 yr ago by Fall (1983).

We show this relation in Fig. 2.5 for our disc-dominated galaxies ($M_{\rm d,\star}/M_\star > 0.7$). We also include results from Obreschkow and Glazebrook (2014) who analysed 16 nearby spiral galaxies of the The HI Nearby Galaxy Survey (THINGS) sample (Walter et al., 2008b), and Fall and Romanowsky (2013) who focused on 64 galaxies from type Sa to Sm from the Kent (1986, 1987, 1988) datasets, and find that our simulated galaxies follow closely the Fall (1983) relation and are in very good agreement with the observations. We also notice that for disc masses $\sim 10^{10}$ $M_\odot$ and above the differences between this work and HWT15 are mostly due to the new disc instability recipe since the formation of pseudo-bulges, which is expected to happen in this mass regime [see panel (2,1) in Fig. 2.1], increases the specific angular momenta of stellar discs (see also Section 2.5.2).

In Fig. 2.6 we calculate the total specific angular momentum of each galaxy as $j_\star = (j_{\rm d,\star}\ M_{\rm d,\star} + j_{\rm b}\ M_{\rm b})/(M_{\rm d,\star} + M_{\rm b})$ and plot it as a function of the total stellar mass. The different colours represent the $M_{\rm b}/M_\star$ ratio of the corresponding galaxy. We compare our results with Fall and Romanowsky (2018) who presented their sample of 57 spirals, 14 lenticulars, and 23 ellipticals. The behaviour of our data

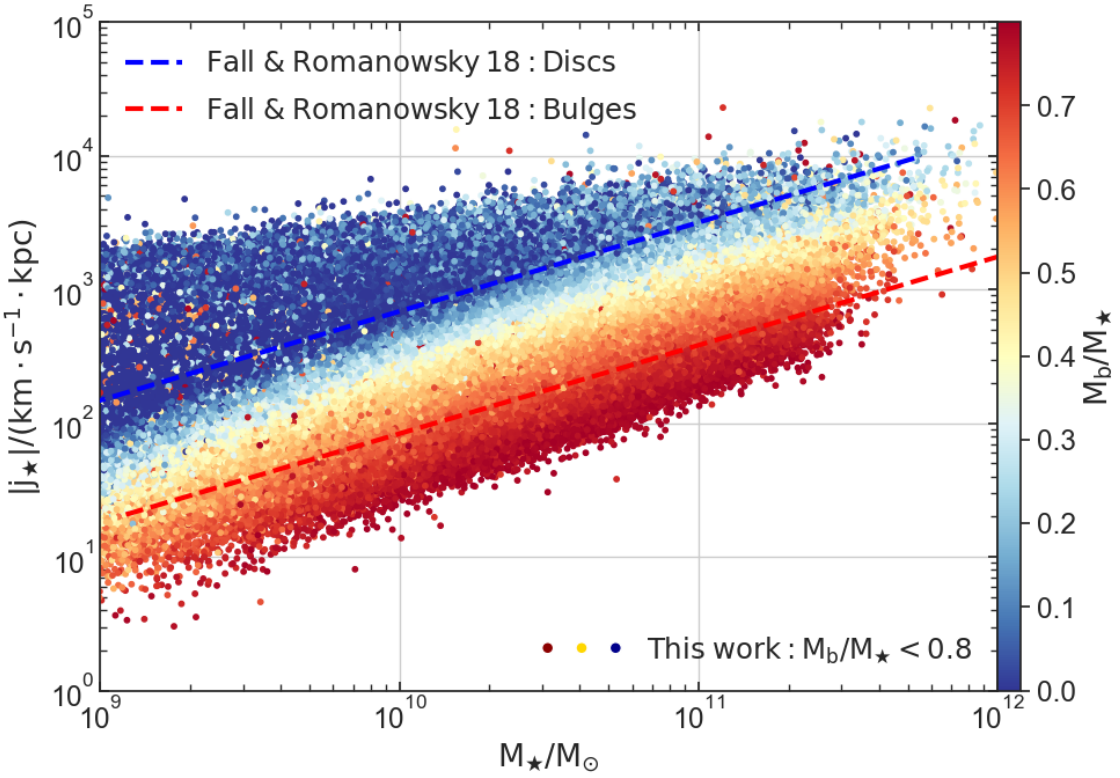

Figure 2.6: Total stellar mass versus total specific angular momentum for $M_{\rm b}/M_\star < 0.8$ galaxies at redshift $z \sim 0.0$, compared with Fall and Romanowsky (2018) fit lines for discs and bulges. The colour of the symbols indicate different $M_{\rm b}/M_\star$ values.

indicate that the more disc-dominated galaxies (i.e. lower $M_{\rm b}/M_\star$ values) rotate faster than the bulge-dominated, hence we find an impressive agreement with the observed trends.

2.3.6 Mass-size relations

Galactic mass and size are amongst the most fundamental properties and modelling their relation remains an important task for SAMs (e.g. Stevens et al., 2016; Zoldan et al., 2018; del P. Lagos et al., 2018).

2.3.6.1 Disc-dominated galaxies

In Fig. 2.7 we present the stellar half-mass radius as a function of the total stellar mass for disc-dominated galaxies. In this work we define them as those that have $M_{\rm d,\star}/M_\star > 0.7$. We compare our galaxies with the following works:

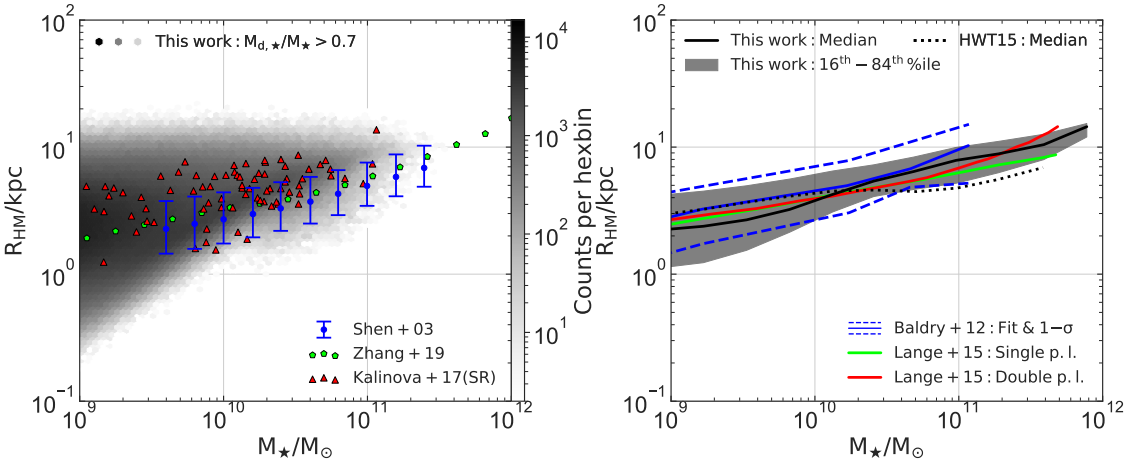

Figure 2.7: Mass-size relation for disc-dominated galaxies at redshift $z \sim 0.1$. *Left-hand panel:* Total stellar mass versus stellar half-mass radius compared with Shen et al. (2003); Zhang and Yang (2019), and Kalinova et al. (2017). *Right-hand panel:* The median and 16th-84th percentile range (black shaded region) of the aforementioned relation compared with Baldry et al. (2012) and Lange et al. (2015) fit lines. Black solid and dotted lines show results from this work and HWT15, respectively.

(i) Shen et al. (2003): selected galaxies with concentration index ($c \equiv R_{90}/R_{50}$) $c < 2.86$ from 140 000 SDSS DR1 (York et al., 2000) galaxies at $z < 0.3$.

(ii) Zhang and Yang (2019): selected 424 363 galaxies with $c < 2.85$ from the New York University Value-Added Galaxy Catalog at $z < 0.2$ (Blanton et al., 2005).

(iii) Kalinova et al. (2017): selected slow-rising class galaxies (akin to late-type) based on the shapes and amplitude of the circular velocity curve of 238 CALIFA galaxies at $z < 0.03$ (Falcón-Barroso et al., 2017).

(iv) Baldry et al. (2012): selected late-type galaxies based on colour-magnitude diagrams of 5210 GAMA galaxies at $z < 0.06$ (Driver et al., 2011).

(v) Lange et al. (2015): selected late-type galaxies by visually classifying GAMA II galaxies in the redshift range $0.01 < z < 0.1$ (Liske et al., 2015).

As explained in Section 2.2.1, we assume that the cold gas loses a fraction of its specific angular momentum to the dark matter halo during the cooling process, hence the cold gas discs are expected to be more compact than those produced by HWT15: this trait is then inherited by the stellar discs. This behaviour is present at the low-mass end of Fig. 2.7; however for stellar masses above $\sim 10^{10}$ $M_\odot$, disc

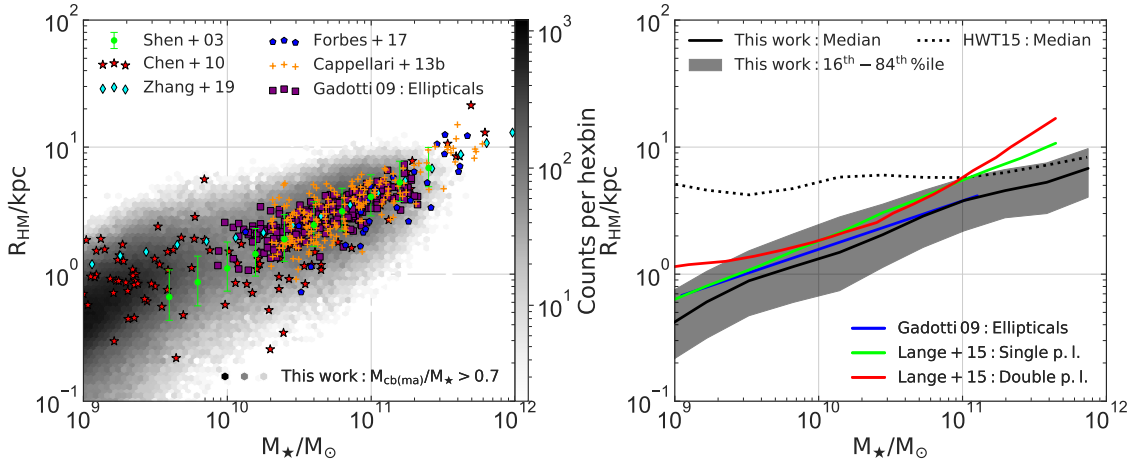

Figure 2.8: Mass-size relation for bulge-dominated galaxies at redshift $z \sim 0.1$. *Left-hand panel:* Total stellar mass versus stellar half-mass radius compared with Shen et al. (2003); Chen et al. (2010); Zhang and Yang (2019); Forbes et al. (2017); Cappellari et al. (2013), and Gadotti (2009). *Right-hand panel:* The median and 16th-84th percentile range (black shaded region) of the aforementioned relation compared with Gadotti (2009) and Lange et al. (2015) fit lines. Black solid and dotted lines show results from this work and HWT15, respectively.

instabilities begin to redistribute stellar material between the disc and the bulge, and create a significant population of pseudo-bulges, as indicated in panel (2,1) of Fig. 2.1. This mechanism causes the expansion of the disc[7] and produces discs larger than the HWT15 at intermediate and higher masses (see also Section 2.5.1). For those reasons, our results show a steeper relation that is in better agreement with the observational data and provide a significant improvement over past modelling attempts (e.g. top panel of Fig. 2 of Guo et al., 2011).

2.3.6.2 Bulge-dominated galaxies

The HWT15 model gives sizes of bulge-dominated galaxies that are too large for a given mass. That motivated us to introduce energy dissipation in gas-rich mergers, as described in Section 2.2.3.1. The result of that is shown in Fig. 2.8 where we show the total stellar mass versus stellar half-mass radius for galaxies with $M_{\rm cb(ma.)}/M_\star > 0.7$. This sample contains galaxies which composed most of their stellar mass through major mergers, akin to ellipticals. We compare with the following observa-

[7]During instabilities low angular momentum material is moved inwards and higher angular momentum material is transferred outwards. Hence, while the inner parts of the disc grow denser, the outer parts expand and become more diffuse (see Section 2.2.2).

tional datasets:

(i) Shen et al. (2003): selected galaxies with $c > 2.86$ from 140 000 SDSS DR1 (York et al., 2000) galaxies at $z < 0.3$.

(ii) Chen et al. (2010): selected about 100 early-type galaxies that populate the red sequence in the Virgo cluster from SDSS DR5 (Adelman-McCarthy et al., 2007).

(iii) Zhang and Yang (2019): selected 424 363 galaxies with $c > 2.85$ from the New York University Value-Added Galaxy Catalogue at $z < 0.2$ (Blanton et al., 2005).

(iv) Forbes et al. (2017): selected galaxies from the SLUGGS survey which targeted 25 nearby (D $\leq$ 25 Mpc) massive early-type galaxies in different environments (Brodie et al., 2014).

(v) Cappellari et al. (2013): selected 260 early-type galaxies from the ATLAS^{3D} project at $z = 0$ (Cappellari et al., 2011a).

(vi) Gadotti (2009): selected galaxies with $c > 2.5$ from the SDSS DR2 (Abazajian et al., 2004).

(vii) Lange et al. (2015): selected early-type galaxies by visually classifying GAMA II galaxies in the redshift range $0.01 < z < 0.1$ (Liske et al., 2015).

The updated merger remnant size recipe introduced in this work gives more compact remnant sizes at the low-mass end compared to HWT15 which over-predicted the size of the smallest galaxies. We can clearly see that our median line agrees well with a single power law for masses below 10^{10} M$_\odot$, as indicated by Lange et al. (2015). However, at the high-mass end we do not see the sharp upturn in size indicated by their double power-law model. We note that there is an increase in intracluster light in the most massive haloes that we do not include when calculating the size of the central galaxies.

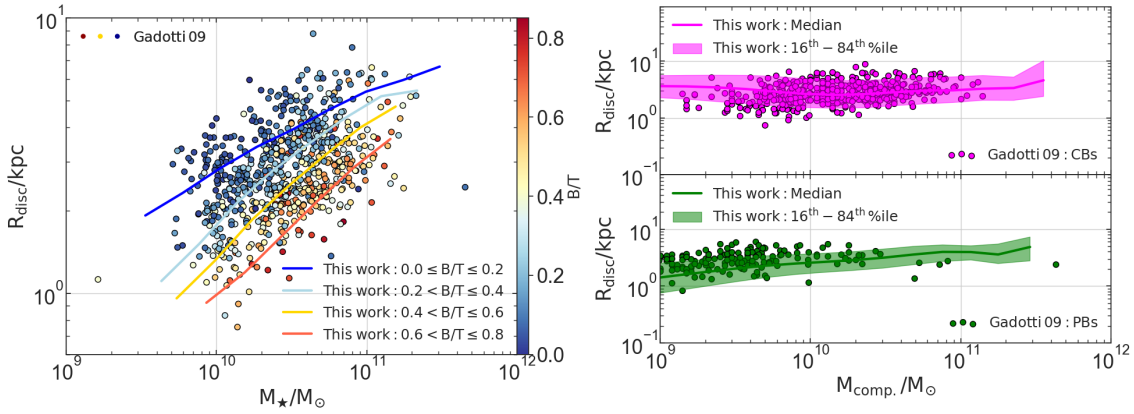

Figure 2.9: Disc scale length as a function of mass at redshift $z \sim 0.05$. *Left-hand plot:* Total stellar mass versus disc scale length compared with Gadotti (2009) galaxies coloured by different B/T ratios. *Right-hand plot:* Classical and pseudo-bulge mass against disc scale length compared with Gadotti (2009) classical and pseudo-bulges, respectively.

2.3.6.3 The dependence of disc scale length on morphology

In Fig. 2.9 we present three different versions of the disc scale length versus mass relation. The left-hand panel contains our median lines for four different bulge-to-total stellar mass ratios and Gadotti (2009) galaxies colour coded by their B/T luminosity ratio. The L-Galaxies model shows adequate agreement with the observed behaviour at all masses, which indicates that the disc scale lengths decrease as the B/T ratio increases.

For the right-hand panel we selected galaxies with classical bulges through minor mergers and galaxies with pseudo-bulges and plotted their disc scale lengths as a function of the mass of these bulges. Gadotti (2009) fitted different profiles in each galaxy image in his sample and used a bulge profile which is described by a Sersic (1968) function; when n = 4 the profile is a de Vaucouleurs (1948), while n = 1 corresponds to an exponential bulge (i.e. pseudo-bulge). We find a strong agreement with the observed trends which suggests that, as expected, galaxies with more extended discs tend to host more massive pseudo-bulges. This slope appears to be steeper for galaxies with pseudo- instead of classical bulges, and, as we discussed in Section 2.2.2, bar formation is expected to expand the outer parts of the disc (e.g. Kormendy and Kennicutt, 2004).

2.4 Conclusions

This chapter addresses some deficiencies in the otherwise very successful Henriques et al. (2015) SAM with regard to bulge formation via disc instabilities and merger remnant sizes. In making the latter change, we drew inspiration from the work of Covington et al. (2008, 2011) and Tonini et al. (2016). The main changes are:

(i) the specific angular momentum of accreted gas is reduced to 0.8 times that of the dark matter halo;

(ii) an improved disc instability recipe that considers both the gas and the stars, rather than just the latter;

(iii) the introduction of dissipation in gas-rich mergers.

Our main conclusions are as follows:

(i) The updated disc instability recipe allows us to have an impressive agreement with the observed fraction of different galactic morphologies and the stellar mass functions of different galactic types.

(ii) The stellar half-mass radius and specific angular momentum of disc-dominated galaxies is in great agreement with the observed relations due to the reduction of the initial angular momentum of the gas disc.

(iii) Highly dissipative mergers result in more compact remnants which match the observed mass–size relation of bulge-dominated galaxies.

(iv) The tight relation between the stellar disc scale length and mass is still present after the assumption that the gas loses 20 per cent of its initial specific angular momentum during cooling.

2.5 Sanity checks

2.5.1 Angular momentum

As discussed in Section 2.1.3.1, the assumptions under which the L-Galaxies and the majority of SAMs calculate disc sizes and specific angular momenta have been

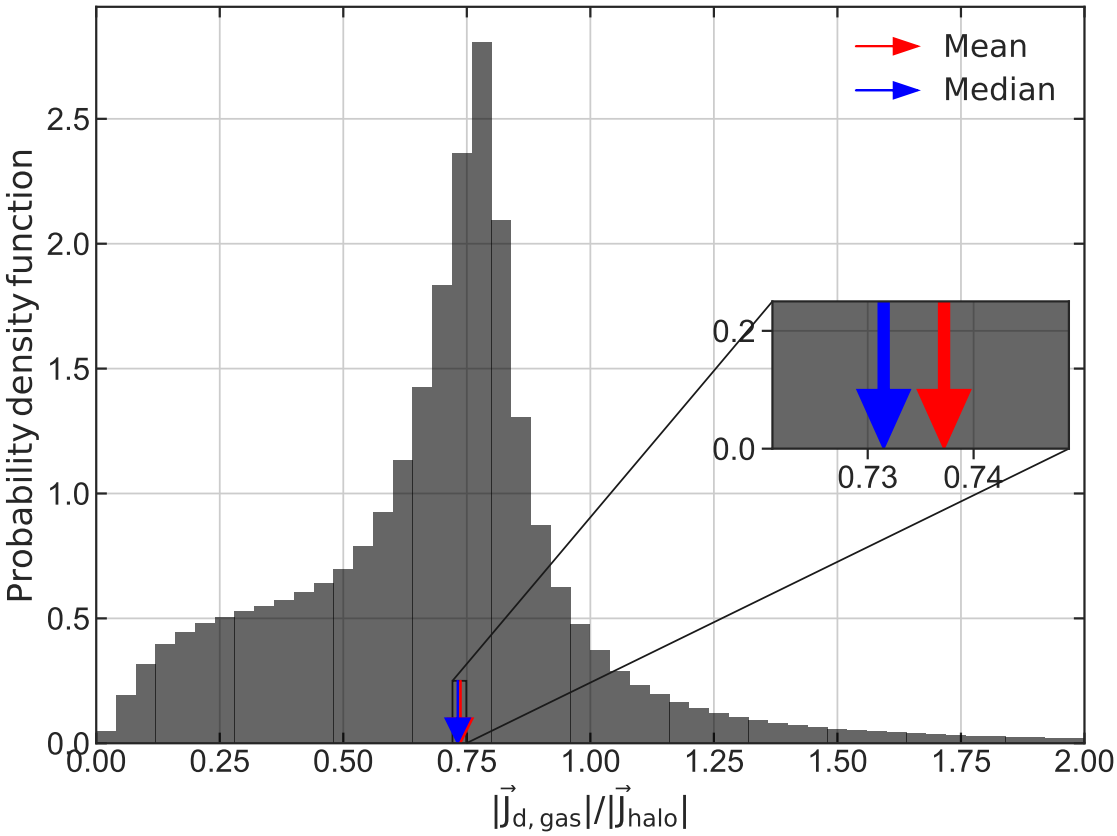

Figure 2.10: Probability density function of the ratio between the specific angular momentum of the gas disc and that of the halo at redshift $z \sim 0.0$. The red (blue) arrow indicates that the mean (median) value for the galaxies in our sample is 0.737 (0.731).

criticized by simulators who studied the connection between the dark matter halo and its baryons. These studies have found that the specific angular momentum of the latter is notably lower than that of the former (e.g. Katz and Gunn, 1991; Navarro and White, 1993, 1994; Navarro et al., 1995; Navarro and Steinmetz, 1997; Cole et al., 2000; Kaufmann et al., 2007; Zavala et al., 2008; Kimm et al., 2011; Danovich et al., 2015; Stevens et al., 2017). This motivated us to include the factor f in equation (3.10) and, as discussed in Section 2.2.1, in this work we assumed that during cooling the gas disc loses 20 per cent of its specific angular momentum.

In Fig. 2.10 we show the probability density function of the ratio between the specific angular momentum of the gas disc and that of the halo. In the L-Galaxies model, we follow the changes in the total angular momentum vector of the gas disc during each time step from a variety of physical processes, as equation (3.10) denotes. Hence, the current value of that ratio represents the angular momentum accumulated over cosmic history, and does not directly measure the instantaneous

rate of accretion of angular momentum. Thus, even though f equals 0.8 for cooling gas, a slight bias to lower specific angular momenta and a galaxy-to-galaxy scatter emerges from the other mechanisms that affect the angular momentum of each galaxy.

Furthermore, we investigate how the baryonic specific angular momentum relates to halo properties. Fig. 2.11 shows the ratio of stellar-to-halo and gas-to-halo specific angular momentum as a function of halo mass. Our results indicate that the stellar specific angular momentum is lower than that of the cold gas, which is in turn slightly lower than that of the halo. This behaviour is consistent with the one found by previous simulations (Teklu et al., 2015; Jiang et al., 2018). We find a slight decrease in the aforementioned ratios as halo mass increases (see also Section 2.5.2 for the effect of disc instabilities and angular momentum losses on discs), which is in broad agreement with the trends reported in recent theoretical studies (e.g. Posti et al., 2018c). We also notice that the scatter seen in Fig. 2.10 is also prominent in the y-axis histogram in the bottom panel of Fig. 2.11 where the use of a log scale for the normalization shows that it spans a wide range of values.

2.5.2 Stellar disc

In this section we reproduce Fig. 2.5 and Fig. 2.7 for different flavours of the L-Galaxies model in order to evaluate the effect of disc instabilities and angular momentum losses on stellar discs. In Fig. 2.12 we show the median lines for the mass versus specific angular momentum (top panel) and the mass-size relation (bottom panel) for this version of the model, the HWT15, this model (i.e. with the disc instability recipe described in Section 2.2.2) with $f = 1.0$ and this model (i.e. with the angular momentum losses described in Section 2.2.1) with the old disc instability recipe (i.e. from HWT15). In both panels we see that at the low mass end ($< 10^{10}$ $M_{\odot}$) the solid black and the blue line converge since angular momentum losses produce more compact and slowly rotating discs. On the other hand, for stellar masses $\sim 10^{10}$ $M_{\odot}$ and above, where the formation of pseudo-bulges is expected to happen [see panel (2,1) in Fig. 2.1], we see a drastic change in the properties of stellar discs since disc instabilities increase their size and specific angular momentum. Hence, the solid black line now follows closely the red one. In general, the

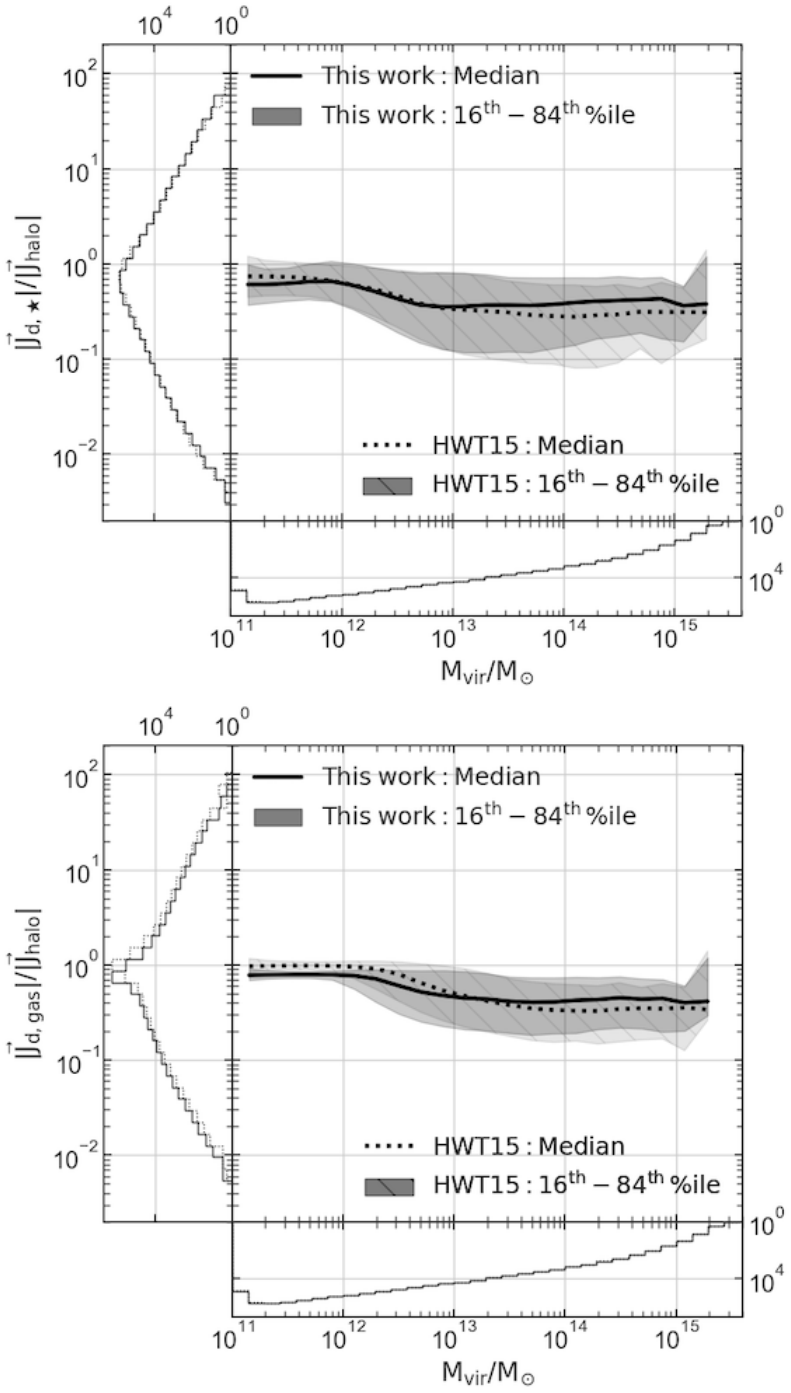

Figure 2.11: Baryonic-to-halo specific angular momentum ratio as a function of halo mass at redshift $z \sim 0.0$. *Top panel:* The median and 16th-84th percentile range of the stellar-to-halo specific angular momentum as a function of halo mass. *Bottom panel:* The median and 16th-84th percentile range of the gas-to-halo specific angular momentum as a function of halo mass. In both panels, the panels attached to the axes are the histograms of the corresponding property. Black solid lines and shaded regions show results from this work, while black dotted lines and diagonally hatched regions from HWT15.

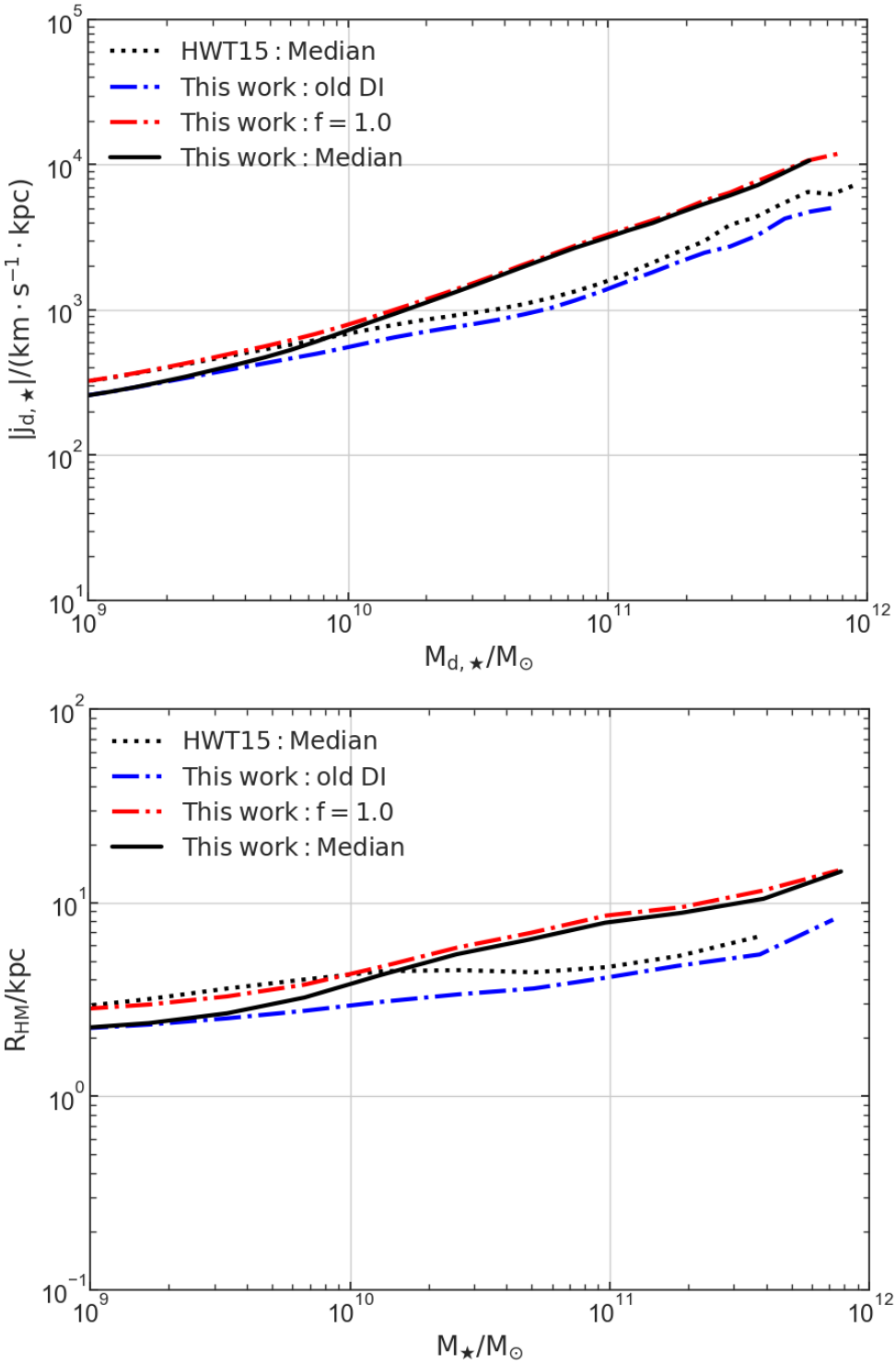

Figure 2.12: *Top panel:* Stellar mass versus specific angular momentum for disc-dominated galaxies at redshift $z \sim 0.0$. *Bottom panel:* Mass-size relation for disc-dominated galaxies at redshift $z \sim 0.1$. In both panels solid and dotted black lines show results from this work and HWT15, respectively, and the dash-dotted red and blue lines show our model (i.e. new disc instability recipe) with $f = 1.0$ and our model (i.e. $f = 0.8$) with the old disc instability recipe (i.e. from HWT15), respectively.

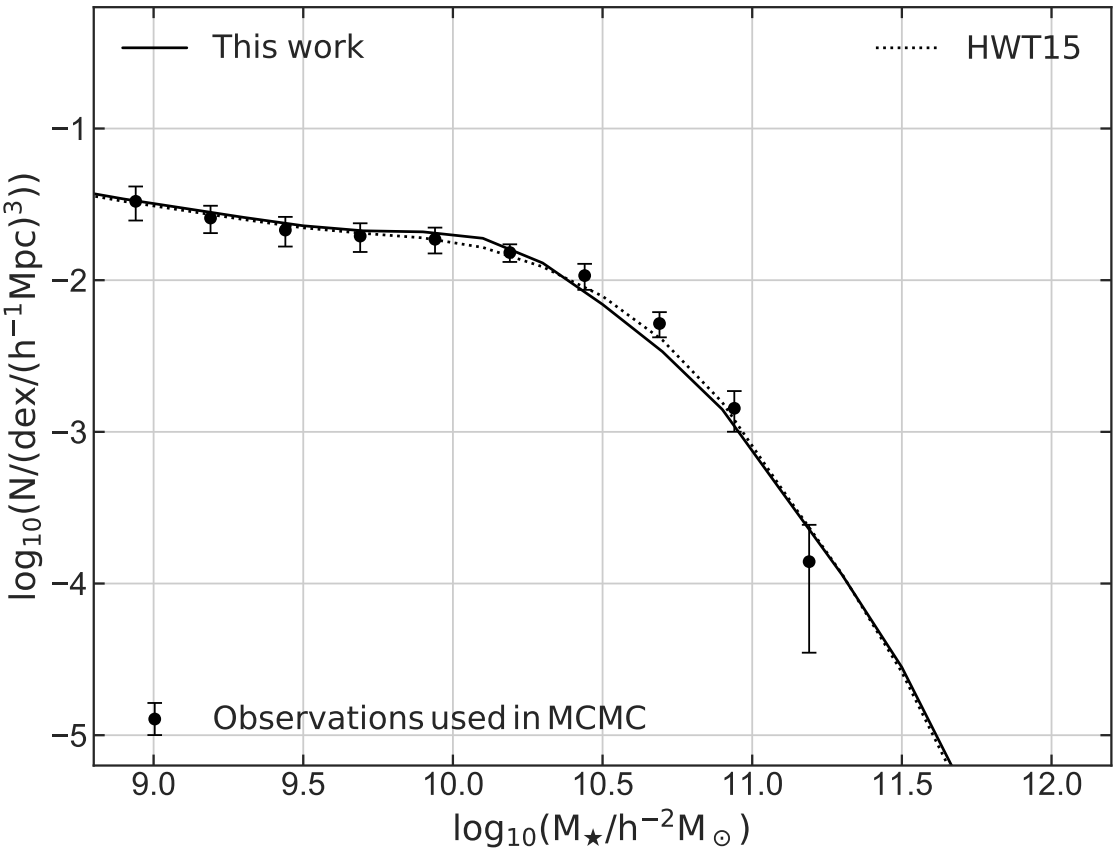

Figure 2.13: Total stellar mass functions at redshift $z \sim 0.0$. Solid and dotted lines show results from this work and HWT15, respectively, and black circles represent the combined observational data used to constrain the MCMC in HWT15.

conclusions drawn from Fig. 2.12 support the arguments put forward in Section 2.3.5 and Section 2.3.6.1, where we argued that the steepening of the median line at the high-mass end in Fig. 2.5 and Fig. 2.7 is due to our new instability recipe.

2.5.3 Stellar mass function

Fig. 2.13 shows the total stellar mass function. The black circles represent the observational data used by HWT15 to constrain the MCMC. Instead of running a new MCMC analysis and readjusting the free parameters of the L-Galaxies model, we chose to follow HWT15 results. Hence, even though we have significantly altered the L-Galaxies model we see that our stellar mass function is in close agreement with the one produced by them.

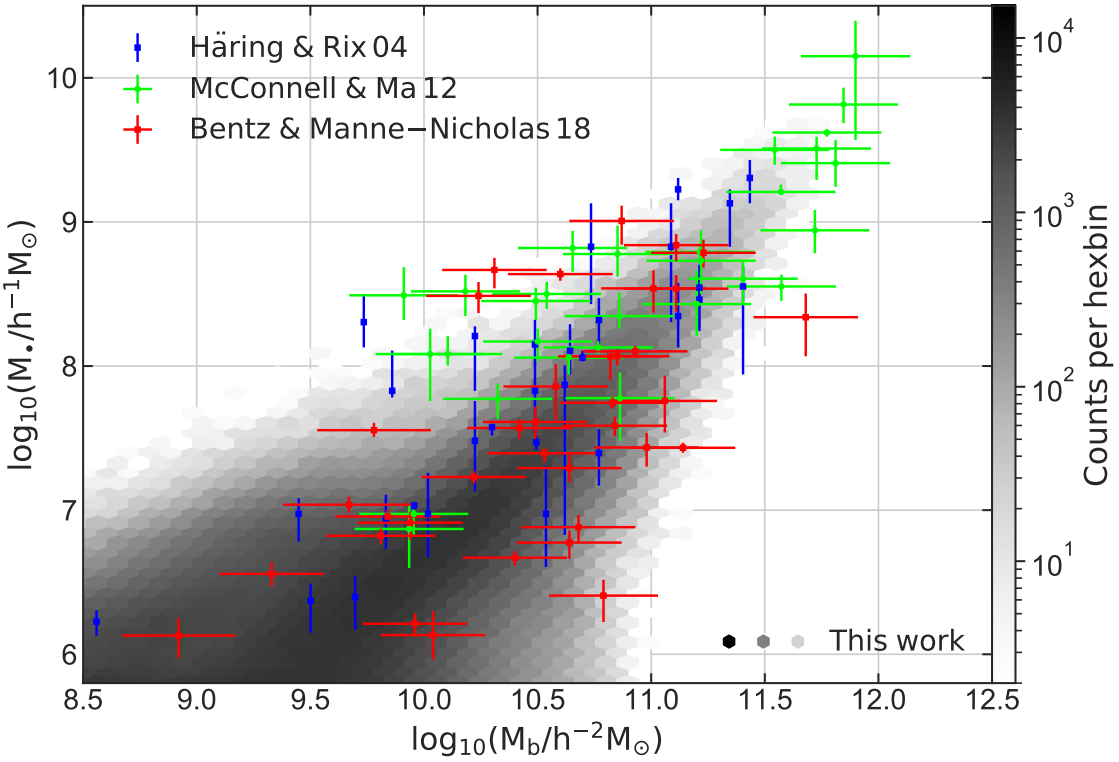

Figure 2.14: Black hole-bulge mass relation at redshift $z \sim 0.0$. Black hexagons represent our galaxies; blue, green, and red circles are observations from Häring and Rix (2004), McConnell and Ma (2013) and Bentz and Manne-Nicholas (2018), respectively.

2.5.4 Black hole-bulge mass relation

In this work, we updated the processes responsible for the growth of bulges via mergers and disc instabilities; where the latter mechanism feeds a percentage of the unstable cold gas into the central supermassive black hole. Hence, Fig. 2.14 provides a sanity check for our new model since it illustrates that the L-Galaxies model is still able to reproduce the tight black hole-bulge mass relation and shows an impressive agreement with the observational data at all masses.

We compare our simulated data with a sample of 30 nearby galaxies introduced by Häring and Rix (2004), 72 galaxies compiled by McConnell and Ma (2013) and 37 galaxies selected by Bentz and Manne-Nicholas (2018) from the Hubble Space Telescope images and deep, ground-based near-infrared images. Even though for 10^9 $M_\odot < M_b < 10^{10.5}$ $M_\odot$ the L-Galaxies model predicts a large scatter in black hole masses, the majority of our galaxies form at all masses an almost linear relation in logspace (i.e. a power law in linear-space) between black hole and bulge mass, as expected (e.g. Beifiori et al., 2012; Graham, 2012; McConnell and Ma, 2013).

2.6 Supplementary results

2.6.1 The Tully–Fisher relation

The Tully–Fisher relation (Tully and Fisher, 1977) describes an empirical correlation between the intrinsic luminosity and the emission-line width of rotating spiral galaxies. A more useful form for our purposes has been proposed by McGaugh et al. (2000) that relates the total baryonic mass and the rotation velocity.

In this work we adopt, for simplicity, as the typical rotation velocity for both the gaseous and the stellar disc, the maximum circular velocity of the surrounding dark matter halo ($V_{\rm max}$). This assumption is in agreement with Tissera et al. (2010) who found that the maximum circular velocities of dark matter haloes are very similar to the maximum rotation velocities of discs. In the top panel of Fig. 2.15 we compare gas-dominated (i.e. $M_{\rm d,\,gas} > M_\star$) galaxies produced by the L-Galaxies model with the dataset used by McGaugh (2012) which consist of gas dominated galaxies from Begum et al. (2008), Stark et al. (2009), and Trachternach et al. (2009). Furthermore, in the bottom panel we investigate the baryonic Tully-Fisher relation of disc-dominated galaxies (i.e. $M_{\rm d,\star}/M_\star > 0.7$), where we include observations from Avila-Reese et al. (2008) (normal, non–interacting disc galaxies compiled from the literature and homogenized in Zavala et al., 2003) and Torres-Flores et al. (2011) (spiral and irregular galaxies from Gassendi HAlpha survey of SPirals, GHASP; Epinat et al., 2008a,b).

As shown in both panels of Fig. 2.15, our galaxies follow a tight relation that is in close agreement with the observational data. However, in the bottom panel we notice that some of the galaxies with the highest circular velocities appear to be less massive than those observed by Avila-Reese et al. (2008) and Torres-Flores et al. (2011). This results from the fact that for baryonic masses $\log_{10}((M_\star + M_{\rm d,\,gas})/{\rm M}_\odot) > 10$ our galaxies split into two groups, where the lower one represents extremely gas poor quiescent galaxies whose contribution to the total baryonic mass is not significant.

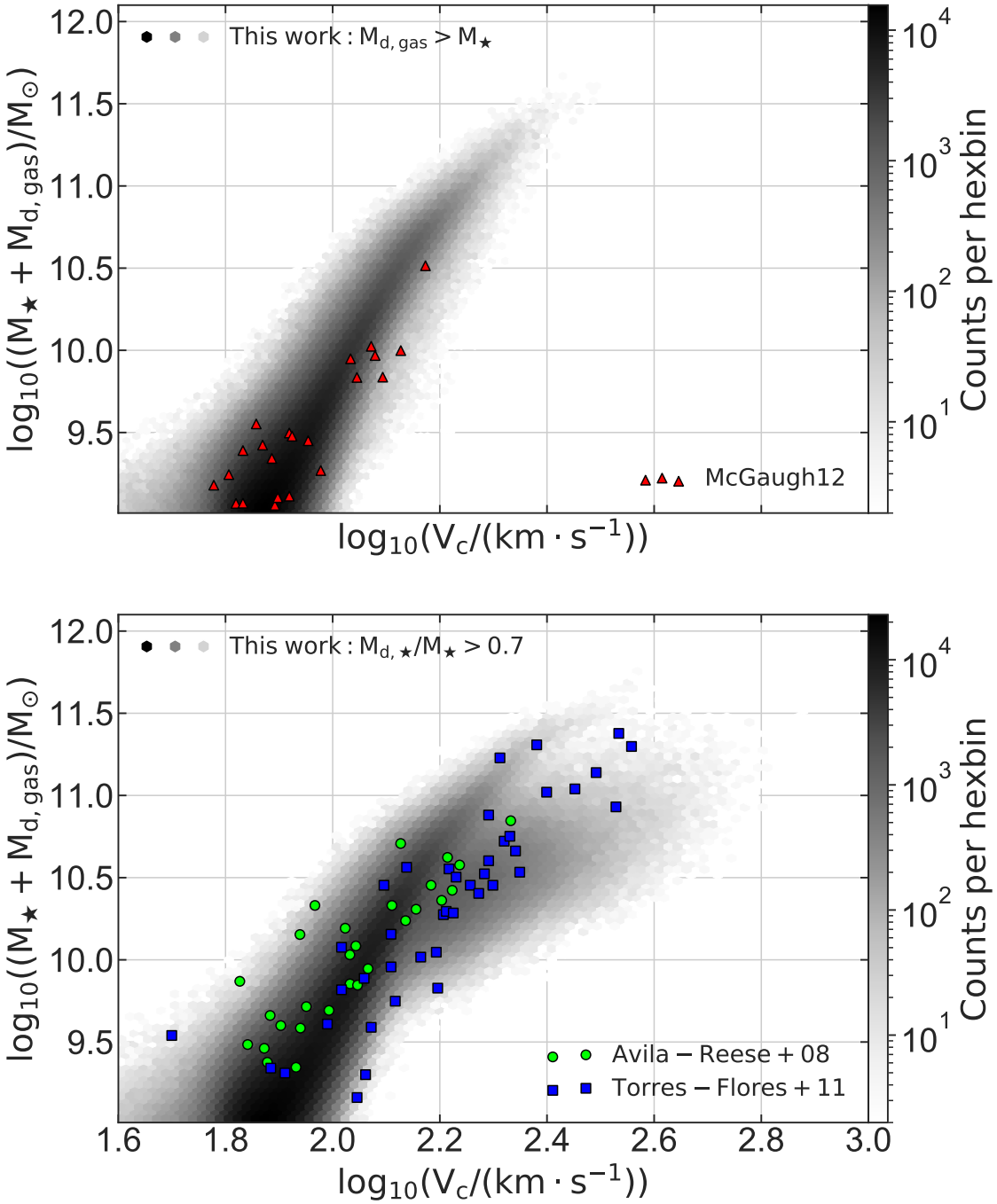

Figure 2.15: Baryonic Tully–Fisher relation at redshift $z \sim 0.0$. *Top panel:* Gas-dominated galaxies compared with a dataset from McGaugh (2012). *Bottom panel:* Disc-dominated galaxies compared with Avila-Reese et al. (2008) and Torres-Flores et al. (2011).

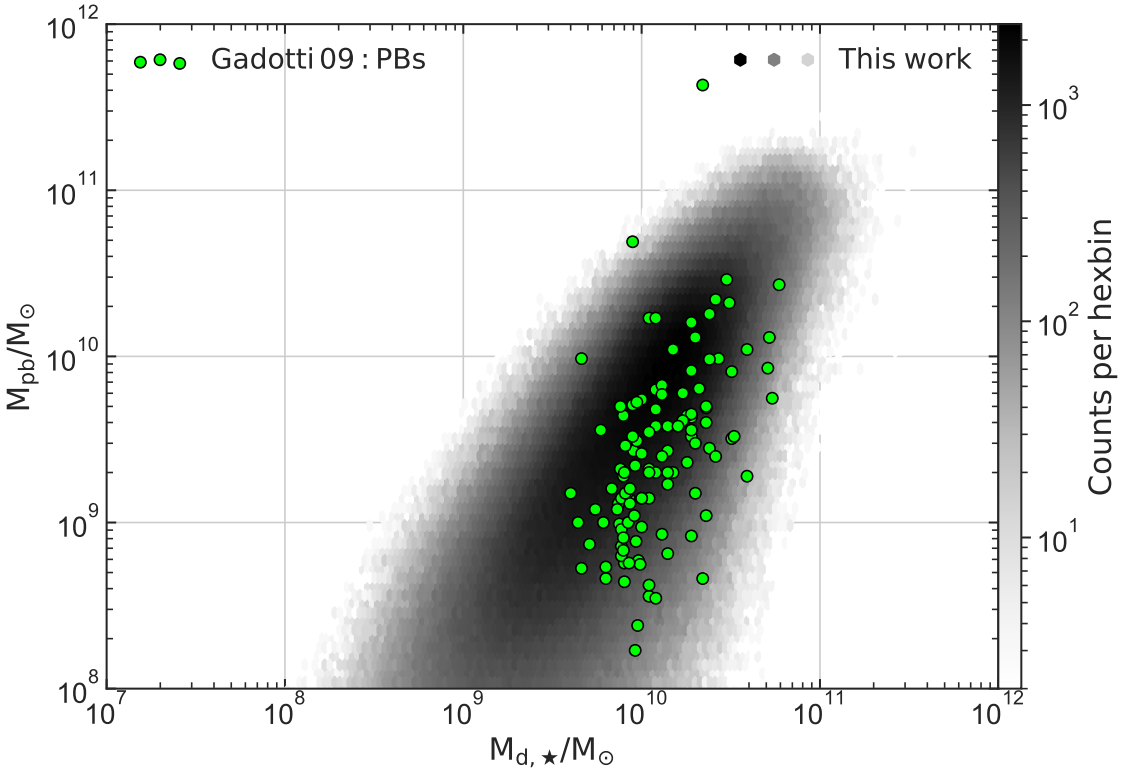

Figure 2.16: Pseudo-bulge mass as a function of disc mass at redshift $z \sim 0.0$ compared with Gadotti (2009) data.

2.6.2 A mass–mass relation

In the Efstathiou et al. (1982) criterion, more massive discs are more unstable. Hence, we expect a tight relation between the disc mass and pseudo-bulge mass to be present in our model. Interestingly, a similar trend appears to exist in real galaxies.

In Fig. 2.16, we plot the pseudo-bulge mass as a function of the disc mass. Our data suggest that since more massive discs are more unstable they will be able to create more massive pseudo-bulges. In the Gadotti (2009) galaxies the same trend is observed as more massive discs host more massive pseudo-bulges. However, their slope appears to be slightly steeper than the one produced by the L-Galaxies model.

Chapter 3

Using angular momentum maps to detect kinematically distinct galactic components

In this chapter we introduce a physically motivated method of performing disc/spheroid decomposition of simulated galaxies, which we apply to the EAGLE sample. We make use of the Hierarchical Equal Area isoLatitude Pixelation (HEALPIX) package to create Mollweide projections of the angular momentum map of each galaxy's stellar particles. A number of features arise on the angular momentum space which allows us to decompose galaxies and classify them into different morphological types. We assign stellar particles with angular separation of less/greater than 30° from the densest grid cell on the angular momentum sphere to the disc/spheroid components, respectively. We analyse the spatial distribution for a subsample of galaxies and show that the surface density profiles of the disc and spheroid closely follow an exponential and a Sersic profile, respectively. In addition discs rotate faster, have smaller velocity dispersions, are younger and are more metal rich than spheroids. Thus, our morphological classification reproduces the observed properties of such systems. Finally, we demonstrate that our method is able to identify a significant population of galaxies with counter-rotating discs and provide a more realistic classification of such systems compared to previous methods.

3.1 Introduction

Exploring how and when galactic components form is an essential step towards understanding the formation and evolution of galaxies. Hence, a method that not only accurately identifies the constituent stellar populations but provides an additional way of exploring their dynamics is of great importance. The plethora of methods as presented below shows the usefulness of decomposing either observed or simulated galaxies, and the purpose of this work is to introduce a pioneering method of detecting kinematically distinct components and exploring their properties.

Photometric decompositions have been long used for splitting distinct stellar populations. A central component ('bulge') is separated from an extended one ('disc') with the use of different photometric profiles; however different methods can lead to variations in the contributions from each component (Cook et al., 2020). Various software packages (e.g. GIM2D, GALFIT, BUDDA, and IMFIT, see Simard et al., 2002; Peng et al., 2002; de Souza et al., 2004; Erwin, 2015, respectively) allow the fit of a single- or double-component models and provide a plethora of profiles (e.g., Nuker law, Sérsic (de Vaucouleurs) profile, exponential, Gaussian or Moffat/Lorentzin functions). This allows some of these codes to perform multicomponent decomposition and identify – in addition to a disc and a bulge – nuclear rings, lenses, and bars.

Many methods of bulge/disc decomposition in simulated galaxies have been proposed. One method assumes that the bulge has zero net angular momentum, hence estimates the disc-to-total (D/T) ratio by assigning to the bulge the sum of the mass of the counter-rotating particles multiplied by 2. This method has been extensively used (e.g. Crain et al., 2010; Clauwens et al., 2018; Trayford et al., 2019) even though it contains a crude assumption regarding bulge kinematics. A different method (Abadi et al., 2003) follows a kinematic decomposition in order to estimate the D/T ratio of simulated galaxies by analysing the circularity of the orbits of stellar particles. This is defined (for a given stellar particle) as the ratio between the component of the angular momentum which is normal to the rotation plane and the maximum angular momentum for a stellar particle with the same binding energy (i.e. if on a circular orbit in the rotation plane). Many authors combined this idea with additional (spatial and/or binding energy) criteria in order to assign

stellar particles to disc, bulge, and inner/outer halo components (Tissera et al., 2012; Cooper et al., 2015; Pillepich et al., 2015; Monachesi et al., 2019; Rosito et al., 2019). These attempts to more accurately identify distinct components unavoidably increase the complexity and free parameters of the decomposition. Finally, Gargiulo et al. (2019) introduced a hybrid technique that combines spatial and kinematic criteria in order to study bulges. However, as noted by Joshi et al. (2020), this method (i.e. the circularity parameter) does not always agree with visual classifications of morphology.

A new era of decomposition software utilizes machine-learning techniques to train neural networks to identify the correct profiles for each component (e.g. Dimauro et al., 2018). For example, a method introduced by Domínguez Sánchez et al. (2018) classified Sloan Digital Sky Survey (SDSS) morphology based on Convolution Neural Networks, while Du et al. (2020) introduced a machine-learning algorithm to identify kinematic structures in IllustrisTNG galaxies.

Lastly, citizen-based projects like Galaxy Zoo (Masters and Galaxy Zoo Team, 2020) follow a different path by allowing volunteers to perform the decomposition (Lingard et al., 2020).

The aim of this chapter is to present a new decomposition method and compare galactic and component properties with local ($z \sim 0.1$) observational data. Our method not only provides a physically motivated spheroid/disc decomposition framework, but is also able to identify (in some cases multiple) kinematically distinct components based on their detailed representation on the angular momentum sphere. This gives one the unique ability of visually inspecting the angular momentum space of galaxies and utilizing this information to study the imprint of secular (Kormendy and Kennicutt, 2004) and violent (Toomre, 1977) processes on the constituent stellar components.

This chapter is organized as follows. In Section 3.2 we describe our sample and introduce our method. In Section 3.3 we present a sample of angular momentum maps drawn from the EAGLE simulation and characterize the main morphological types. A detailed analysis of our spheroid-disc decomposition is presented in Section 3.4, a discussion regarding counter-rotating discs is presented in Section 3.5, and our conclusions are summarized in Section 3.6.

3.2 Methodology

In Section 3.2.1 we describe how we select galaxies for our study, and in Section 3.2.2 we describe the decomposition into spheroid and disc components on the basis of the angular momentum distribution of the stellar particles.

3.2.1 The galaxy sample

We apply our method to the RefL0100N1504 flavour of the EAGLE simulation (Schaye et al., 2015; Crain et al., 2015). We define galaxies as gravitationally bound substructures within Friends of Friends (FoF) structures (i.e. they consist of particles that share the same subgroup and group number, The EAGLE team, 2017), where the former are identified by the SUBFIND algorithm (Springel et al., 2001a). We focus on galaxies with stellar masses $M_{30} > 5 \times 10^9$ M$_\odot$ where M_{30} represents the stellar mass within a 30 kpc spherical aperture and we exclude all particles with separation more than 30 kpc from the galactic centre (defined as the position of the most bound particle). This guarantees that even the least massive galaxy is resolved with more than 3000 stellar particles. Although our method can be used for lower particle numbers, it will become less reliable as the particle number significantly drops below 3000, due to numerical effects which will lead to scattering of orbits.

3.2.2 Decomposition

The HEALPIX[1] sphere (Gorski et al., 1999; Górski et al., 2002) is hierarchically tessellated into curvilinear quadrilaterals where the area of all grid cells at a given resolution is identical. We set $n_{\rm side} = 2^4$ which is a parameter that represents the resolution of the grid[2] (i.e. the number of divisions along the side of a base-resolution pixel). This results in 3072 HEALPIX grid cells ($N_{\rm gc} = 12n_{\rm side}^2$) available over the sky which roughly corresponds to the same number of stellar particles our least massive galaxy has. In practice, our decomposition method follows the steps:

[1] https://healpix.sourceforge.io

[2] We performed tests for $n_{\rm side} = 2^i$ where $i = 4, 5, 6$ and there is no significant change in the D/T ratios and the results presented in this work.

(i) We define the angular momentum vector of a stellar particle i as

$$\boldsymbol{j}_i = m_i(\boldsymbol{r}_i - \boldsymbol{r}_{\rm mb}) \times (\boldsymbol{v}_i - \boldsymbol{v}_{\rm CoM}) \ , \tag{3.1}$$

where m_i is its mass, $\boldsymbol{r}_i$ is its position vector, $\boldsymbol{r}_{\rm mb}$ is the position vector of the most bound particle[3] (defined by SUBFIND), $\boldsymbol{v}_i$ is the velocity vector of the particle, and $\boldsymbol{v}_{\rm CoM}$ is the velocity vector of the centre of mass defined as the collection of all stellar, gas, black hole, and dark matter particles that belong to same galaxy as particle i and are within a 30 kpc spherical aperture centred on the potential minimum. We define the total stellar angular momentum vector as

$$\boldsymbol{J}_\star = \sum_{i=1}^{N} \boldsymbol{j}_i \ , \tag{3.2}$$

where the summation goes over all stellar particles belonging to the corresponding galaxy.

(ii) We convert the angular momentum unit vector of all stellar particles from Cartesian to spherical coordinates (we use $\alpha \in [-180°, 180°]$ as the azimuth angle and $\delta \in [-90°, 90°]$ as the elevation angle) which we provide to HEALPIX in order to generate the pixelization of the angular momentum map.

(iii) We smooth the angular momentum map with a top-hat filter of angular radius 30° and then identify the densest grid cell [i.e. the coordinates ($\alpha_{\rm den.}$, $\delta_{\rm den.}$) of the grid cell on the angular momentum sphere that contains most stellar particles].

(iv) We calculate the angular separation of each stellar particle from the centre of the densest grid cell as

$$\Delta\theta_i = \arccos\big(\sin(\delta_{\rm den.})\sin(\delta) + \cos(\delta_{\rm den.})\cos(\delta)\cos(\alpha_{\rm den.} - \alpha)\big) \ , \tag{3.3}$$

where the index i goes over all stellar particles belonging to the corresponding galaxy.

[3]We prefer to use the most bound particle instead of the centre-of-mass since during mergers galaxies may develop tail-like features, due to the gravitational pull exerted on each other, which can lead to miscalculating the location of the actual centre of the galaxy.

(v) We assign to the disc component all stellar particles that satisfy

$$\Delta\theta_i < 30^\circ \ , \tag{3.4}$$

and the remaining particles to the spheroid. Hence, we directly select stellar particles based on their orbital plane. The choice of 30° was motivated by the visual inspection of the angular momentum maps (see Section 3.3) and the work of Peebles (2020) who showed that for an axisymmetric disc with a flat rotation curve the eccentricity of a particle's orbit can be written as

$$\epsilon = 0.8\cos(\theta) \ , \tag{3.5}$$

where θ is the angle that quantifies the tilt of the orbit with respect to the disc plane. For our 30° criterion this results in particles with minimum value of $\epsilon \sim 0.7$, a limit commonly used for disc particles (e.g. Scannapieco et al., 2009; Marinacci et al., 2014). In addition, our 30° criterion results in good agreement and tight correlations with other commonly used morphological parameters (see Section 3.4.2 for more details).

(vi) Our method by construction will assign particles to the disc component even for the most idealized dispersion-supported system (i.e. a systems whose particle's angular momenta will be perfectly uniformly distributed on the HEALPix sphere). That is because, even for an isotropic distribution over the sky, there will be a small fraction of particles whose angular momentum lies within 30° of the nominal (directed) rotation axis. The following expression for the D/T ratio accounts for this 'artificial' increase of the disc component

$$D/T_{\Delta\theta<30^\circ} = \frac{1}{1-\chi}\left(\frac{N_{\Delta\theta<30^\circ}}{N_{\rm all\,sky}} - \chi\right) \ , \tag{3.6}$$

where $N_{\Delta\theta<30^\circ}$ and $N_{\rm all\,sky}$ are the number of stellar particles within 30° of the direction of the rotation axis and the whole sky, respectively, and

$$\chi = \frac{1-\cos(30^\circ)}{2} \ . \tag{3.7}$$

Finally, we note that in this work we prefer not to limit the spatial extent of the spheroid (i.e. not split it into what is usually termed as a stellar halo and a bulge), since as recently discussed by Clauwens et al. (2018) and Gargiulo et al. (2019) there

is no physical criterion that determines the boundary between a bulge and a halo. In addition we do not attempt to split the disc into a cold and warm (thin and thick) component (Obreja et al., 2018). However, in a future work we intend to explore the imprint of such components on the angular momentum maps.

3.3 Morphological classification

In Section 3.3.1 we present angular momentum maps of the 100 most massive central EAGLE galaxies and classify them into distinct categories, and in Section 3.3.2 we study in more detail the maps of an example representative of each category, and compare three different methods of decomposing disc and bulge.

3.3.1 Distinct categories

Fig. 3.1 displays on a Mollweide, equal-area projection the angular momentum maps of the 100 most massive central (see The EAGLE team, 2017) galaxies. For visual purposes, all particles have been rotated so that $\boldsymbol{J}_\star$ points towards the reader (see Section 3.7). Several distinct categories of structure are visible:

(i) *Rotationally supported systems:* the simplest behaviour is a single cluster of dense grid cells (e.g. galaxy 39, 85, and 100), usually closely aligned with the total angular momentum of the galaxy, $\boldsymbol{J}_\star$. These are well-ordered disc-dominated galaxies. Interestingly, the majority of these (e.g. galaxy 25, 57, and 94) also show a slight antipolar excess of counter-rotating particles – we discuss this further in Section 3.5 below.

(ii) *Dispersion-supported systems:* these do not show a single, dominant density peak in the angular momentum map. There are a variety of morphologies:

  (a) *Double-peak systems:* there are several examples of systems with two, distinct density peaks in the angular momentum maps, either relatively isolated (e.g. galaxy 18, 40, and 87), or buried within a great circle of orbits (e.g. galaxy 2, 46, and 70). For these galaxies, there is no well-defined, ordered rotation; hence they represent dispersion-dominated systems. Where two density peaks are visible, these tend to be opposite

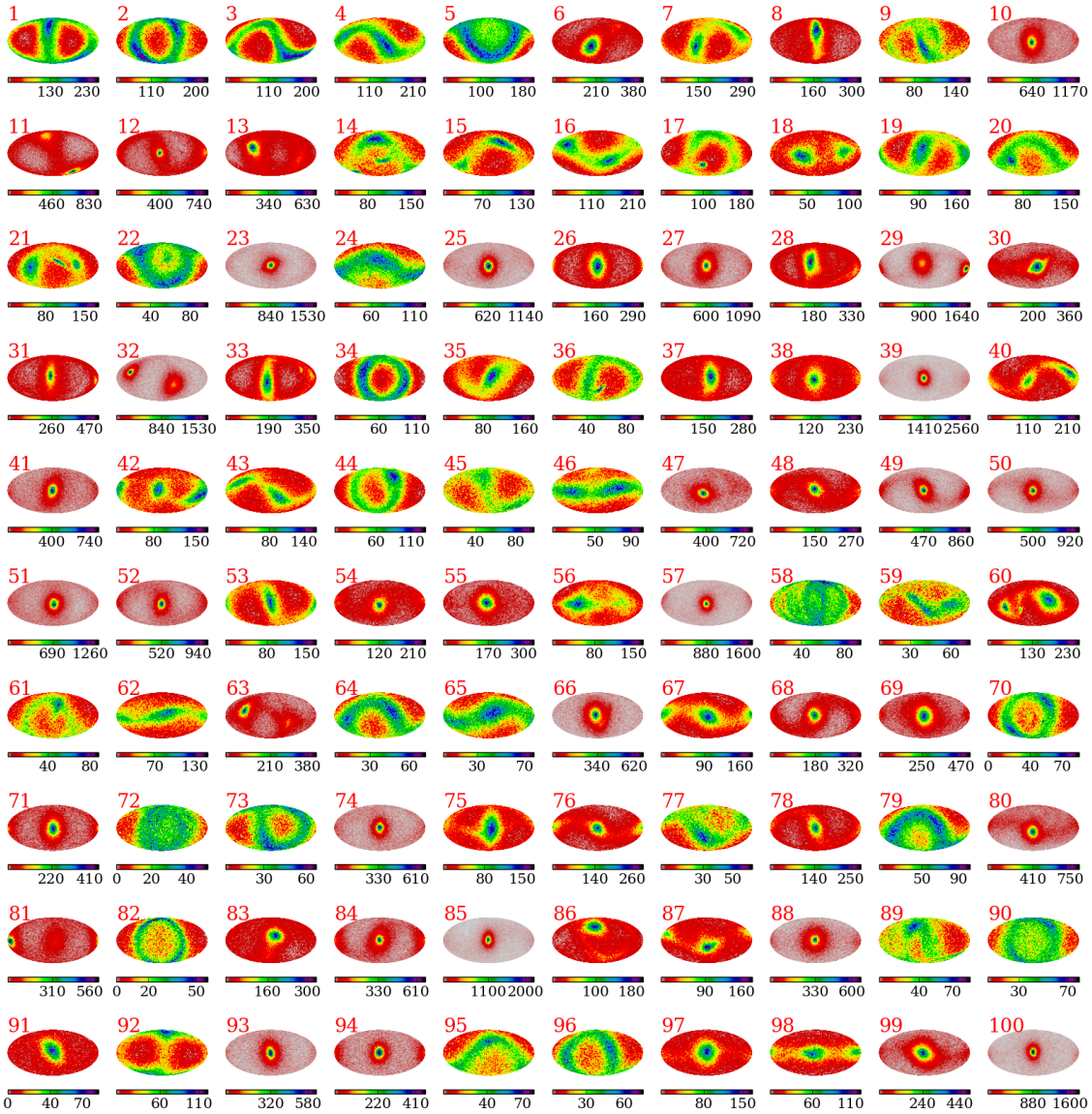

Figure 3.1: A sample of the 100 most massive central galaxies in RefL0100N1504. In each panel, the red number on the top left corner refers to the galaxy's group number and the colour bar represents the number of particles per grid cell. Note that for visual purposes the galaxies have been rotated based on the process described in Section 3.7.

each other on the sky: in such an orientation the minor axes align and the mixing and precession of orbits in the merger remnant is heavily suppressed. They are likely the result of either a merger of progenitors with opposite angular momentum (Bender, 1988; Krajnović et al., 2015) or the accretion of counter-rotating gas which settles and forms stars with angular momentum in the opposite direction (Vergani et al., 2007; Coccato et al., 2013; Algorry et al., 2014).

(b) *Great circle systems:* galaxies with a ring (great circle) of high-density points in the map (e.g. galaxy 34, 82, and 96); depending on the orientation of the galaxy it can appear as a horizontal S-shaped (e.g. galaxy 3, 19, and 65) or as a U (e.g. galaxy 5, 22, and 77) or upside down U (e.g. galaxy 20, 64, and 79). It is interesting to note that this great-circle structure is much more common than having orbits that are more uniformly distributed (e.g. galaxy 58, 72, and 90) across all directions in space. This is anticipated since mergers are not expected to mix orbits up evenly in phase space. Instead, realistic merger remnants have angular momentum distributions that are composed of varying contributions from different orbital families, such as short- and long-axis tube orbits (Valluri and Merritt, 1998; Deibel et al., 2011). Some of the dispersion-dominated systems (e.g. galaxy 5, 22, and 34) have a uniform density of orbits around a great circle, which reflects that for every direction in space there are roughly equal numbers of stellar particles with positive and negative angular momenta; others show a clear density peak (e.g. galaxy 20, 44, and 61) which suggests a relatively minor merger.

(iii) *Multiple-peak (merging) systems:* a very few systems show three or more density peaks (e.g. galaxy 14, 21, and 60). These are unlikely to be stable and may represent the early stages of mergers of a third galaxy onto a double-peaked system. It is beyond the scope of this work to study the formation path and evolution of such systems and their components, however we plan to do so in a future work.

3.3.2 Detailed kinematics

The first and fifth columns of Fig. 3.2 and Fig. 3.3 display on a Mollweide projection the angular momentum maps of galaxies representative of each one of the categories and subcategories identified in Section 3.3.1. In addition, for each galaxy it shows the grid cell density as a function of the angular separation from the densest grid cell (second and sixth columns) and from the angular momentum vector (third and seventh columns), and the distribution of the orbital circularity parameter (fourth and final columns). We follow Thob et al. (2019) and defined the latter for a given stellar particle i as

$$\epsilon_i = \frac{L_{\perp,\,i}}{L_{\perp,\,\mathrm{max}}(E < E_i)} \,, \tag{3.8}$$

where $L_{\perp,\,i}$ is the component of the angular momentum which is perpendicular to the rotation plane and $L_{\perp,\,\mathrm{max}}(E < E_i)$ is the maximum value of the same component achieved by any stellar particle with binding energy less than that of particle i. The red and blue hatched regions represent the distribution of the circularity parameter for bulge and disc particles defined as $\epsilon < 0.7$ and $\epsilon > 0.7$, respectively (Grand et al., 2017; Rosas-Guevara et al., 2020a). The $D/T_{\Delta\theta<30^\circ}$ ratio for each galaxy in the second/sixth columns results from the method introduced in this work which assigns to the disc component stellar particles with $\Delta\theta < 30^\circ$and the remaining to the spheroid. The $D/T_{\mathbf{J}_\mathrm{b}=0}$ ratio shown for each galaxy in the third/seventh columns follows the assumption that the bulge has zero net angular momentum, hence its mass equals the mass of all counter-rotating particles multiplied by 2, and the remaining stellar particles are assigned to the disc component. Finally, the $D/T_{\epsilon>0.7}$ ratio produced for each galaxy following equation (3.8) is shown in the fourth/final columns.

(i) *Galaxy 39:* the majority of stellar particles have angular momenta well aligned both with the densest grid cell (second column) and the galactic angular momentum vector (third column). As discussed in Section 3.3.1 galaxy 39 is a rotationally supported galaxy since its ordered motion results in a relatively high $D/T_{\Delta\theta<30^\circ}$ ratio (0.49). This value is quite close to the $D/T_{\mathbf{J}_\mathrm{b}=0}$ and the $D/T_{\epsilon>0.7}$ ratios (0.46 and 0.44, respectively).

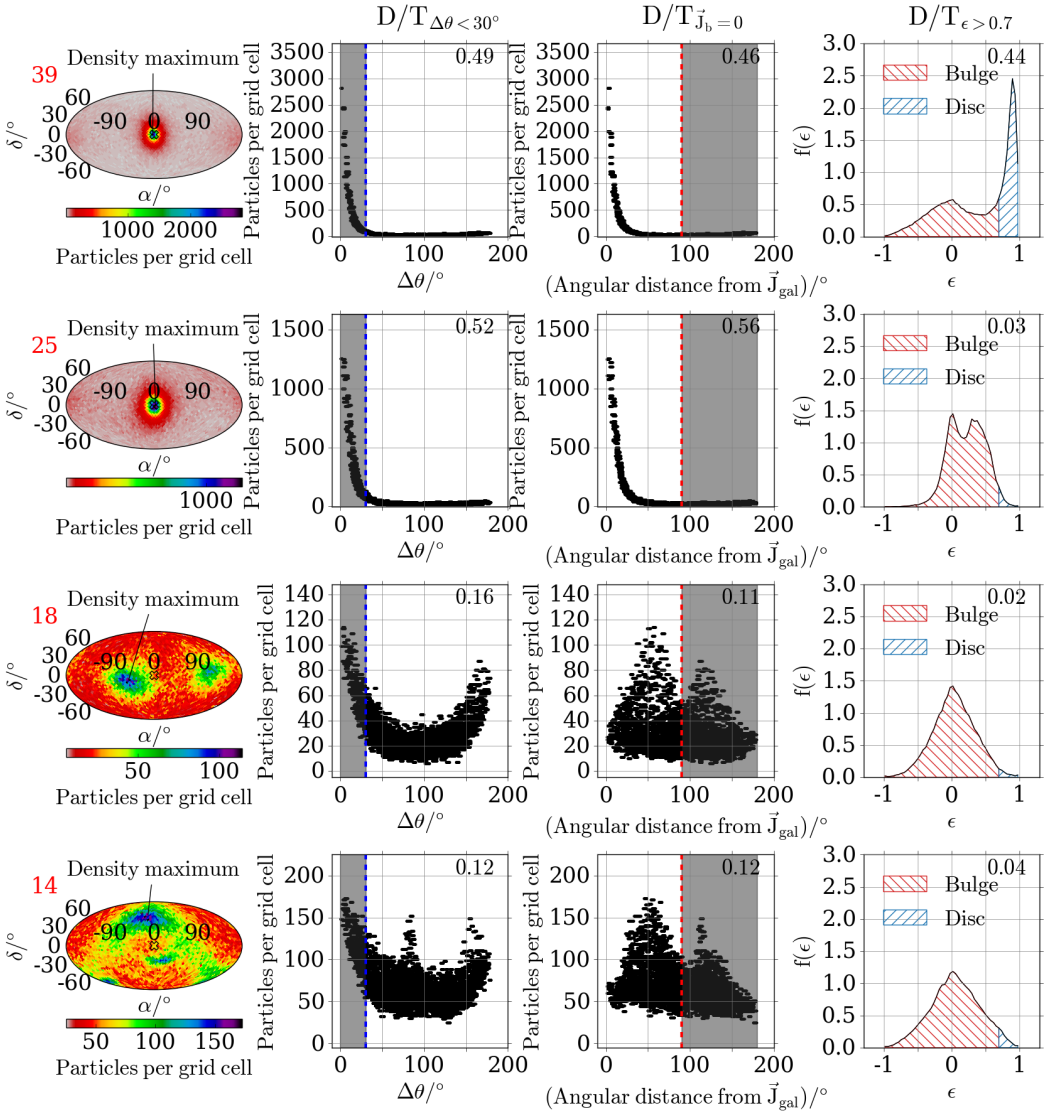

Figure 3.2: A sample of four galaxies drawn from the different morphological classifications described in Section 3.3.1. The first column for each galaxy displays on a Mollweide projection the angular momentum maps, where the red number on the top left corner in each row refers to each galaxy's group number and the black line points to the densest grid cell. As in Fig. 3.1 the galaxies have been rotated so that $\boldsymbol{J}_\star$ (hollow X symbol) points towards the reader. The second column contains the number of particles in each grid cell as a function of the angular separation from the densest grid cell (as defined by equation (3.3)). The blue dashed vertical line marks $\Delta\theta = 30°$ and the gray shaded region highlights all stellar particles that belong to the disc component (i.e., have $\Delta\theta < 30°$). The third column shows the number of particles in each grid cell as a function of the angular separation from the angular momentum vector. The red dashed vertical line marks angular distance of 90° and the gray shaded region highlights all counter-rotating stellar particles. The fourth column contains the PDF of the stellar mass-weighted distribution of the orbital circularity of its stellar particles. The red and blue hatches represent stellar particles with $\epsilon < 0.7$ and $\epsilon > 0.7$, respectively to account for a bulge and disc component. The text on the top right corner of the latter three columns represents for each galaxy an estimate of the D/T ratio based on three different methods (see text for more details).

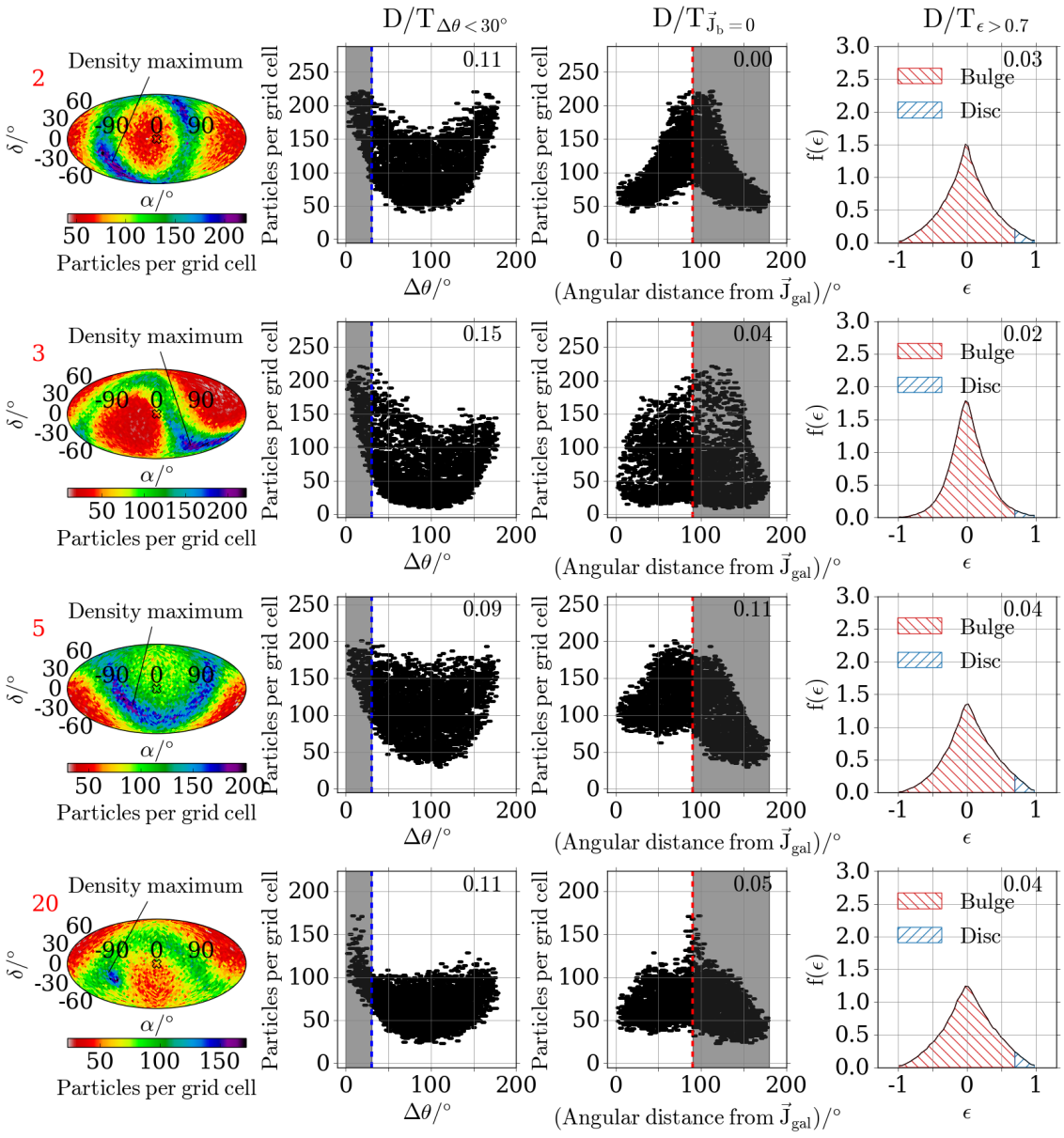

Figure 3.3: Same as Fig. 3.2 but for dispersion-supported systems.

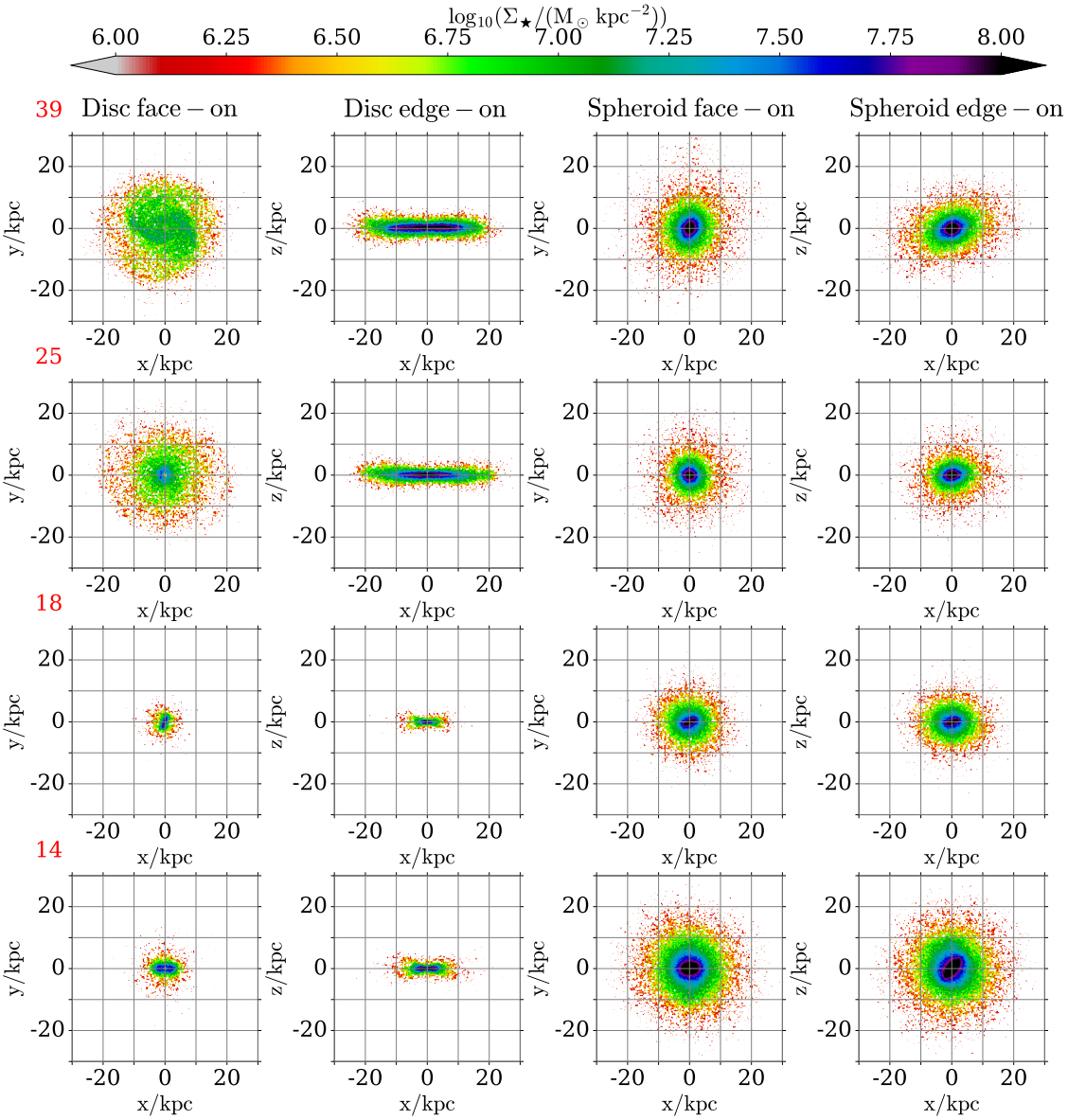

Figure 3.4: The stellar surface density of the components identified by our method for the sample of the four galaxies shown in Fig. 3.2. The red number on the top left corner in each row refers to each galaxy's group number. The face-on and edge-on projections for the disc and spheroid are shown as indicated at top of each column.

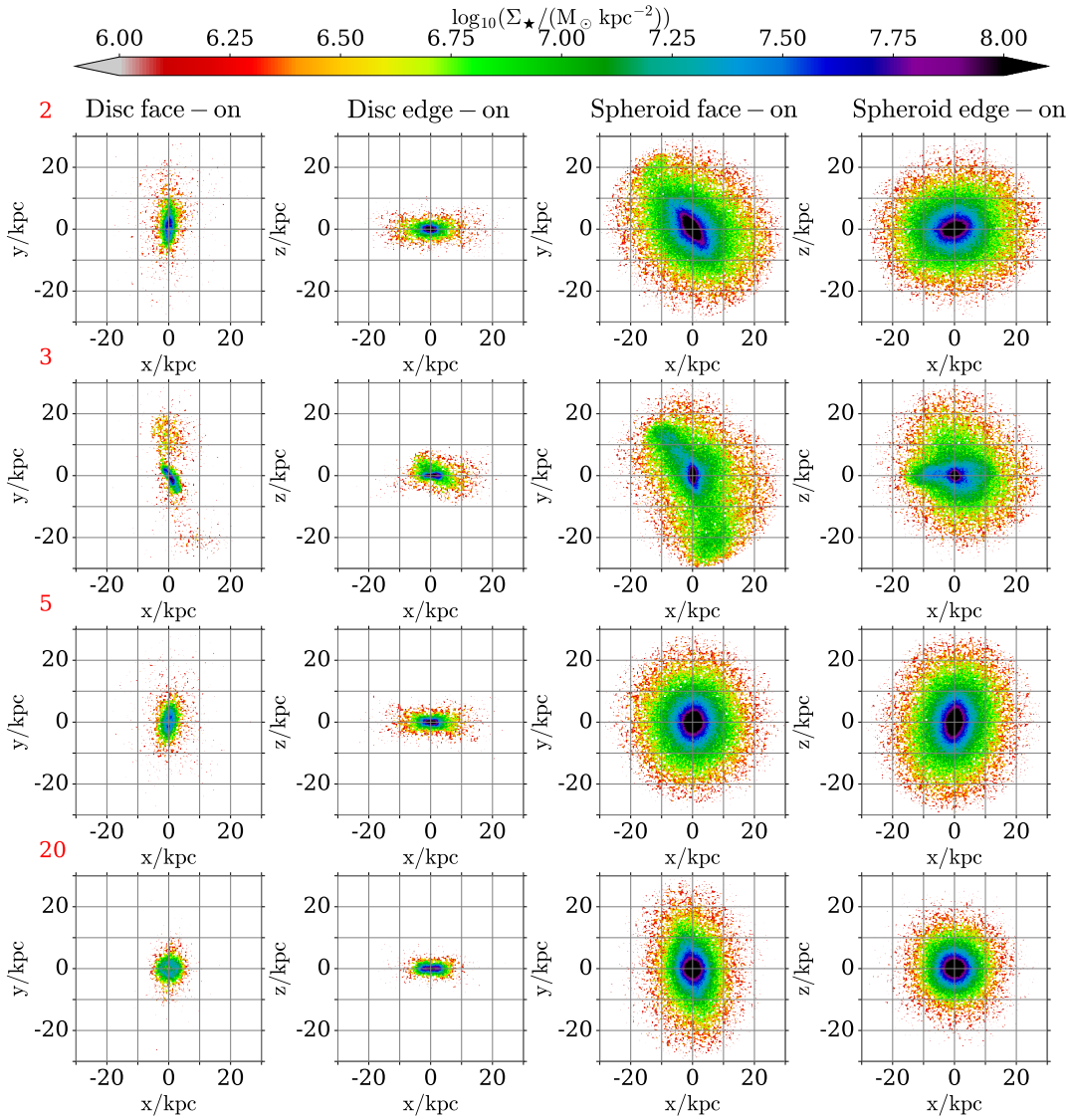

Figure 3.5: Same as Fig. 3.4 but for the galaxies presented in Fig. 3.3.

(ii) *Galaxy 25:* an interesting example of a disc-dominated galaxy which has orbits in a plane, but they are not circular. This is reflected in its relatively high $D/T_{\Delta\theta<30^\circ}$ (0.52) and $D/T_{\mathbf{J}_\mathrm{b}=0}$ (0.56) ratios, but a considerably lower $D/T_{\epsilon>0.7}$ ratio (0.03). Even though a well-ordered component appears as a second peak in the distribution of ϵ, the strict criterion of $\epsilon > 0.7$ fails to include to the disc component stellar particles with non-circular orbits. Hence, galaxy 25 (and of course others similar in nature) would have been misclassified by that method (see also discussion in Section 3.4.2).

(iii) *Galaxy 18:* the two density peaks on the angular momentum map are almost counter-rotating with respect to each other as can be seen on the $\Delta\theta$-density

plane (second column). However, the picture is different when the angular separation is calculated from the angular momentum vector (third column) and not from the densest grid cell. Since neither of the structures are aligned with $\boldsymbol{J}_\star$, particles from both clusters of dense grid cells will contaminate the counter-rotating (grey shaded) region. This results in an artificial overestimation of the number of counter-rotating particles, hence a lower $D/T_{\mathbf{J}_\mathrm{b}=0}$ and $D/T_{\epsilon>0.7}$ ratios compared to $D/T_{\Delta\theta<30^\circ}$. We discuss the effect of including counter-rotating particles in the definition of the disc component in Section 3.5.

(iv) *Galaxy 14:* there is a clear advantage of our method compared to the other ones presented in Fig. 3.2, which do not have the ability to identify three kinematically distinct components. The three distinct peaks on the $\Delta\theta$-density plane are not present in the last two panels corresponding to galaxy 14 on the fourth row.

(v) *Galaxy 2:* a perfect example of a balance between equal numbers of rotating and counter-rotating stellar particles. Galaxies with almost zero net rotation can be the result of either two counter-rotating structures or a uniform distribution of stellar orbits. Hence, in order to understand their formation one first must accurately identify their distinct kinematic components. If the mechanism behind the formation of such galaxy is a merger of two counter-rotating galaxies (Hopkins et al., 2009b; Lagos et al., 2018b) or accretion of counter-rotating gas, then the remnant disc should include both disc structures instead of none. Both $D/T_{\mathbf{J}_\mathrm{b}=0}$ and $D/T_{\epsilon>0.7}$ values are quite close to zero since these methods only use information regarding the total angular momentum of the galaxy. The inability of angular momentum based decomposition methods to reveal the true nature of such galaxies has been previously reported by Clauwens et al. (2018). However, our method is capable of identifying the two counter-rotating structures in opposite parts of the angular momentum sphere (embedded within a great circle), hence providing a more realistic D/T estimate – see also discussion in Section 3.5 where we investigate the inclusion of counter-rotating particles in our definition of D/T.

(vi) *Galaxies 3, 5, and 20:* these all represent dispersion-supported system as

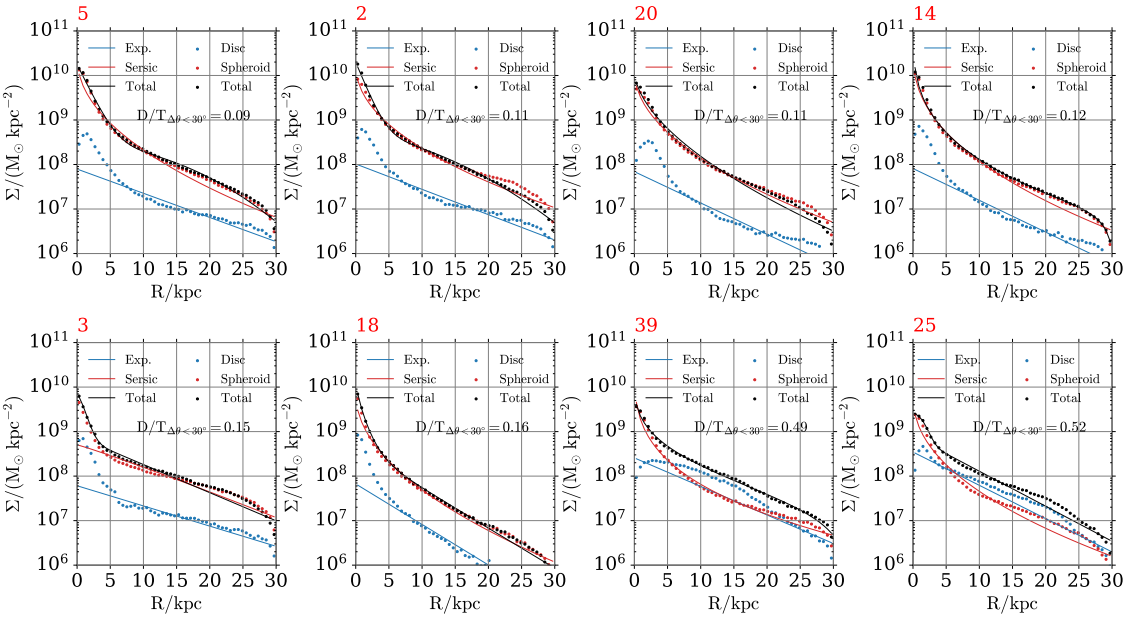

Figure 3.6: Face-on stellar surface density profiles for the sample of the eight galaxies shown in Fig. 3.2 and Fig. 3.3 sorted based on their $D/T_{\Delta\theta<30^\circ}$ values. These galaxies represent a diverse subsample as indicated by each galaxy's $D/T_{\Delta\theta<30^\circ}$ ratio. The red number on the top left corner in each panel refers to each galaxy's group number. The black symbols represent the total stellar surface density and the black curve the two-component fit which consists of a Sersic and an exponential profile (see the text for more details). The blue and red symbols represent, respectively, the disc and spheroid components' stellar surface densities which are fit with an exponential (blue curve) and a Sersic (red curve) profile, respectively.

discussed in Section 3.3.1 and are similar in nature to galaxy 2, but with more asymmetry and a variety of strengths for the main density peak(s).

In summary, all galaxies apart from galaxy 39 and 25 have relatively similar D/T ratios; however the imprint they leave on the angular momentum maps are far from similar. This means that their formation histories and the mechanisms that gave rise to these features were not identical. Identifying these kinematically distinct components gives one the ability to isolate and study them in more detail, in an attempt to understand galaxy formation and evolution, as we briefly do below.

3.3.3 Morphology of the individual components

Fig. 3.4 and Fig. 3.5 shows the face-on and edge-on projection of the disc and spheroid components identified by our method (see Section 3.2.2) for the sample of galaxies presented in Fig. 3.2 and Fig. 3.3, respectively. Galaxies 39 and 25 which

are rotationally supported galaxies, have prominent spiral arms (face-on projections) and a well-defined thin discs (edge-on projections) akin to grand-design spiral galaxies. Galaxy 18, which showed as a double peak in Fig. 3.2, is seen to contain a very compact and elongated disc, similar to the dispersion-supported systems. The triple-peak nature of Galaxy 14 shows as a small subclump within the spheroid, but Galaxy 3 shows a much stronger asymmetry, suggestive of a more significant merger, but not evident in the kinematic analysis – that shows the importance of using more than one technique to characterize the structure of galaxies.

Investigating further the morphology of each component we explore their stellar mass distributions. Fig. 3.6 shows the stellar surface density radial profiles for the total stellar mass (black points) and for the disc (blue points) and spheroid (red points) components for the sample of the eight galaxies shown in Fig. 3.2 and Fig. 3.3 and sorted based on their $D/T_{\Delta\theta<30^{\circ}}$ values. These galaxies represent a blend of disc-dominated ($D/T_{\Delta\theta<30^{\circ}} > 0.5$) and spheroid-dominated ($D/T_{\Delta\theta<30^{\circ}} < 0.5$) galaxies. We perform a two-component fit of the face-on total stellar surface density by using a non-linear least-square method to fit a double Sersic (1968) profile (black line) which consists of a 1D Sersic function and a fixed $n = 1$ exponential profile

$$\Sigma(r) = \Sigma_{0,\,\mathrm{s}}\ \exp\left[-b_n\left(\frac{r}{R_{\mathrm{eff.}}}\right)^{1/n}\right] + \Sigma_{0,\,\mathrm{d}}\ \exp\left[-\left(\frac{r}{R_{\mathrm{d}}}\right)\right]\ , \tag{3.9}$$

where r is the projected 2-D radius, $\Sigma_{0,\,\mathrm{s}}$ and $\Sigma_{0,\,\mathrm{d}}$ are the central surface densities of the spheroid and disc, respectively, b_n is the Sersic coefficient parameter, n is the Sersic index, $R_{\mathrm{eff.}}$ is the effective radius that encloses half of the projected total stellar mass and R_{d} is the disc scale length (see also Section 3.8 for more details). In addition, we fit independently the disc with an exponential profile (blue curve) and the spheroid with a Sersic profile (red curve).

Even though we do not restrict the physical extent of our components, we see a clear trend which holds for all galaxies in Fig. 3.6 and shows that the spheroid component dominates the mass budget in the central regions even for the disc-dominated galaxies; while we notice a drop in disc's surface density in the central regions. This is in agreement with previous works (e.g. Obreja et al., 2013; Breda et al., 2020) who argued that disc components exhibit central intensity depression which lowers their contribution to the stellar mass. This drop indicates that it is easier for particles to scatter away from small $\Delta\theta$ near the centre (i.e. based on our

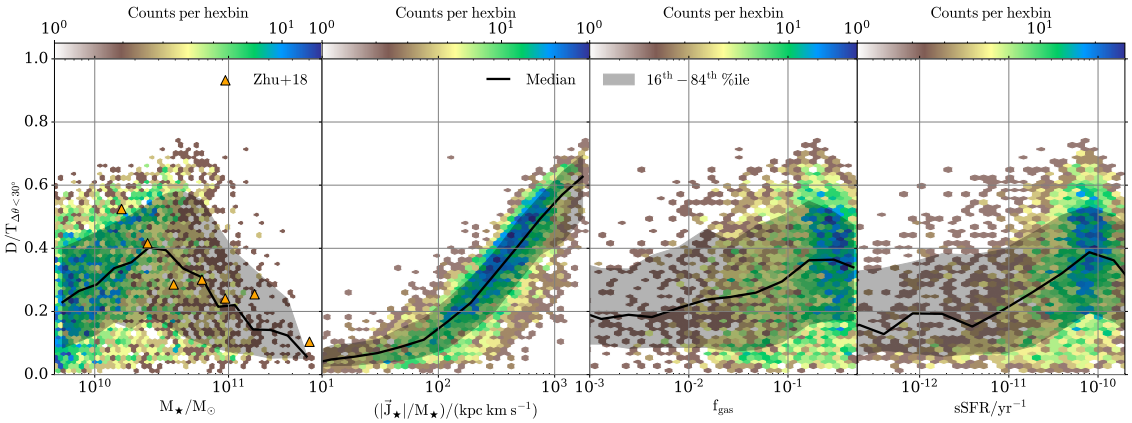

Figure 3.7: The $D/T_{\Delta\theta<30^\circ}$ ratio as a function of *first panel:* stellar mass, *second panel:* stellar specific angular momentum, *third panel:* gas fraction, and *fourth panel:* specific star formation rate. In each panel, the black line and shaded region represent the median and 16th-84th percentile range, respectively. The orange triangles in the first panel represent galaxies from Zhu et al. (2018).

method they do not have disc-like kinematics). In most cases, there is an increase in disc's surface density between 3 and 7 kpc (right after the aforementioned drop) which partially exists due to contamination between the components.

In galaxy 25, we see that at $r \sim 20$ kpc, there is a prominent bump which appears both in the total (black points) and the disc (blue points) surface densities. This excess of stellar mass is related to spiral arms and reinforces our finding that galaxy 25 has spiral arms which our method correctly associates with its disc component (see Fig. 3.4). In general, the majority of spheroids tightly follow a Sersic profile especially in the central regions, while discs are well fitted by an exponential profile (even when they are subdominant components) particularly at their outskirts, as expected.

3.4 Results

Having detailed the methodology and classification of our components, we present in this section relations between $D/T_{\Delta\theta<30^\circ}$ and galactic/component properties for EAGLE galaxies selected as described in Section 3.2.1.

3.4.1 Correlations with galactic properties

In this work, we use the information depicted on angular momentum maps to estimate the relative mass contribution of each component to the total stellar mass. Hence, in this section we use the $D/T_{\Delta\theta<30^\circ}$ ratio and study its correlations with galactic properties.

Fig. 3.7 shows, from left to right, the dependence of the $D/T_{\Delta\theta<30^\circ}$ ratio on stellar mass, stellar specific angular momentum, gas fraction (gas to gas + stellar mass), and specific star formation rate (sSFR). In the first panel, we compare with the Zhu et al. (2018) (300 nearby Calar Alto Legacy Integral Field Area (CALIFA) Sánchez et al., 2012, galaxies) data set as presented in Tacchella et al. (2019) (see their Section 3.2). Intermediate-mass ($2 \times 10^{10} \lesssim M_\star/\mathrm{M}_\odot \lesssim 4 \times 10^{10}$) galaxies have the highest $D/T_{\Delta\theta<30^\circ}$ ratios while as we move to higher or lower masses, galaxies tend to be more spheroid-dominated - in agreement with the observational data. A similar behaviour has been reported before for the EAGLE (see e.g. Fig. 4 of Clauwens et al., 2018) and the IllustrisTNG (see e.g. Fig. 3 of Tacchella et al., 2019) simulations. In addition, observational studies (e.g. Moffett et al., 2016b; Thanjavur et al., 2016) have also reported broadly similar relations.

In addition, we see a tight (positive) correlation between the $D/T_{\Delta\theta<30^\circ}$ ratio and the specific angular momentum of the galaxy, which indicates that the higher the disc contribution to the total stellar mass is the faster the galaxy is rotating (Duckworth et al., 2020). This is an expected behaviour since our method by construction will assign higher $D/T_{\Delta\theta<30^\circ}$ ratios to galaxies with higher angular momenta.

Lastly, we find a weak trend between both the gas fraction and sSFR with $D/T_{\Delta\theta<30^\circ}$, showing that more gas-rich and star-forming galaxies have preferentially more prominent disc components. These conclusions are in agreement with Lagos et al. (2018a) who found that (at fixed stellar mass) passive galaxies have lower spin parameters than star-forming ones.

3.4.2 Correlations with other methods

Even though it was originally assumed that early-type galaxies (ETGs) and (classical) bulges are solely pressure-supported systems, it was later revealed that they often do have some rotation (e.g. Bertola and Capaccioli, 1975; Kormendy and Illing-

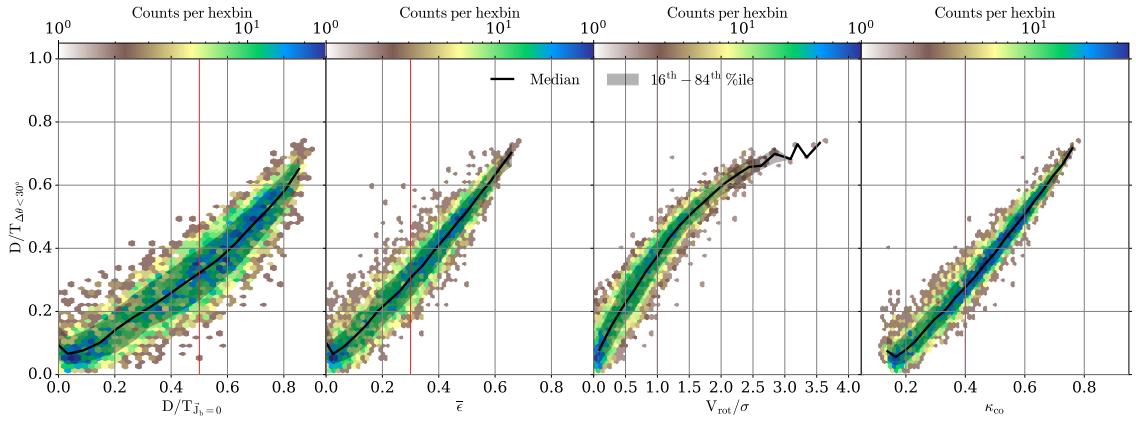

Figure 3.8: The $D/T_{\Delta\theta<30^\circ}$ ratio as a function of *first panel:* $D/T_{\mathbf{J}_\mathrm{b}=0}$ ratio, *second panel:* average circularity parameter ($\overline{\epsilon}$), *third panel:* ratio between rotation and dispersion velocities ($v_\mathrm{rot.}/\sigma$), and *fourth panel:* corotation fraction ($\kappa_\mathrm{co.}$). In each panel, the black line and shaded region represent the median and 16th-84th percentile range, respectively. The red vertical lines represent the limits usually used (see e.g. Correa et al., 2017; Thob et al., 2019) to dichotomise galaxies into late-type and early-type (values higher and lower than the red lines, respectively).

worth, 1982; Davies et al., 1983; Scorza and Bender, 1995; Emsellem et al., 2011). In general, galactic spheroids and ETGs are dominated by stars in low angular momentum orbits, while late-type galaxies (LTGs) are populated by stars performing ordered rotational orbits. Theoretical studies usually use the D/T ratio to distinguish between ETGs and LTGs, hence the method used to perform the decomposition should be able to accurately capture the distinct kinematic components.

For that reason, we compare in Fig. 3.8 the $D/T_{\Delta\theta<30^\circ}$ ratio with, from left to right, the $D/T_{\mathbf{J}_\mathrm{b}=0}$ ratio, the average circularity parameter ($\overline{\epsilon}$), the ratio between rotation and dispersion velocities ($v_\mathrm{rot.}/\sigma$), and the fraction of stellar particles' kinetic energy invested in corotation ($\kappa_\mathrm{co.}$ introduced by Correa et al., 2017). We find positive correlations between our method and the aforementioned ones, with the $D/T_{\mathbf{J}_\mathrm{b}=0}$ ratio showing the most scatter and $\kappa_\mathrm{co.}$ and $v_\mathrm{rot.}/\sigma$ the least. The latter curves over towards high $v_\mathrm{rot.}/\sigma$ values in disc-dominated systems, as has been recently reported by Thob et al. (2019).

We note that the $D/T_{\Delta\theta<30^\circ}$ value where the demarcation (red) lines meet the median (black) lines lies lower than the 0.5 value used by some other methods (e.g. Rosito et al., 2018; Tissera et al., 2019; Rosito et al., 2019) to separate disc-dominated from bulge-dominated galaxies; and it is closer to that of, for example, Lagos et al. (2008); Weinzirl et al. (2009); Gargiulo et al. (2015); Pedrosa and Tissera

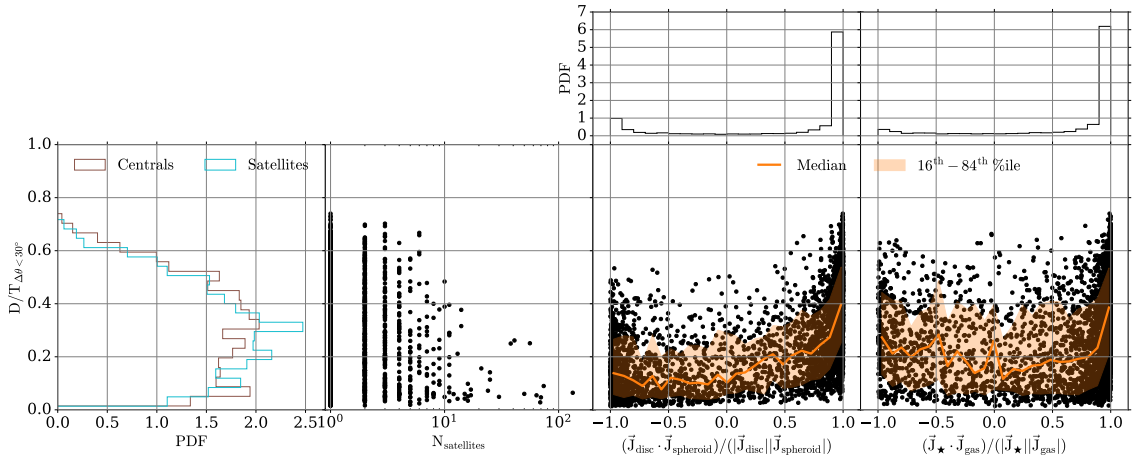

Figure 3.9: *First panel:* the $D/T_{\Delta\theta<30^\circ}$ ratio PDF for central (brown) and satellite (cyan) galaxies and the $D/T_{\Delta\theta<30^\circ}$ ratio as a function of *second panel:* number of satellites (i.e. number of galaxies that share the same group number), *third panel:* misalignment between the angular momentum of the disc and the spheroid components, and *fourth panel:* misalignment between the angular momentum of the stellar and the gaseous components. In the last two panels, we attached two panels on top showing the PDF of the x-axis data. In addition, the orange lines and shaded regions represent the median and 16th-84th percentile range, respectively.

(2015); Irodotou et al. (2019); Obreschkow et al. (2020); Zanisi et al. (2020). Finally, we note that, even though the four methods form tight relations with $D/T_{\Delta\theta<30^\circ}$, on some occasions we see a mismatch between the predictions which can lead in miss-classifications. These disagreements are responsible for the dispersion seen in Fig. 3.8 and are more prominent in the second panel, where a few (~ 20) galaxies with $2 < \bar{\epsilon} < 3$ appear well above the median and the 16th-84th percentile range. Such case is galaxy 25 (presented in Section 3.3.2) which has $\bar{\epsilon} \sim 0.2$ and $D/T_{\Delta\theta<30^\circ} \sim 0.5$: hence the former method classifies it as an ETG and the latter as disc-dominated.

The fact that our method not only identifies such discrepancies, but also provides a deeper insight and is able to explain them, is what makes it unique. In addition, it differs from some previous methods since it does not contain any a priori assumptions regarding the kinematics of the components (e.g. that stellar particles counter-rotating with respect to the total angular momentum are bulge particles) hence, provides a more physically-motivated way of identifying kinematically distinct components.

3.4.3 Correlations with environment

Dense environments are prone to frequent mergers (Naab et al., 2014; Tacchella et al., 2019) which are the natural culprits for converting ordered motion to random orbits and lowering the angular momentum of the remnant (Hopkins et al., 2010a; Lagos et al., 2018b; Jackson et al., 2020); this will also affect the $D/T_{\Delta\theta<30^\circ}$ ratios.

To study this effect, Fig. 3.9 shows, from left to right, the probability density function (PDF) for central and satellite galaxies (i.e. galaxies with subgroup number zero and greater than zero, respectively, based on the EAGLE nomenclature, McAlpine et al., 2016) and the dependence of the number of satellites, the misalignment between the angular momentum of the disc and the spheroid components, and of the stellar and the gaseous (defined following equation (3.1) and equation (3.2) but using gas particles instead of stellar) components on the $D/T_{\Delta\theta<30^\circ}$ ratio. Central and satellite galaxies share relatively similar distributions of $D/T_{\Delta\theta<30^\circ}$ ratios with preferred values between 0.2 and 0.5. However, there is a clear trend between the $D/T_{\Delta\theta<30^\circ}$ ratios and the number of satellites which indicates that the more satellites a central galaxy has the more dominating its spheroid component is (i.e. lower $D/T_{\Delta\theta<30^\circ}$ values); the well-known morphology-density relation. As far as the misalignment between the disc and spheroid components is concerned, the median line reveals a weak trend (which becomes more significant as the angular momentum vectors align) which indicates that aligned/counter-rotating components exist in more disc-/spheroid-dominated galaxies. Similar behaviour is present for the stellar and gaseous components, but with an additional weak trend as the two become more anti-aligned. The alignment (or not) between disc and spheroid, and stellar and gaseous components is linked to environmental effects (Scannapieco et al., 2009; Sales et al., 2012; Aumer et al., 2014; Garrison-Kimmel et al., 2018; Park et al., 2019), and we intend to further investigate this behaviour in a future work.

3.4.4 Mass-specific angular momentum relation

The angular momentum of a galaxy determines its size and morphology, and contains information regarding its formation path (Cortese et al., 2016; Posti et al., 2018b; Sweet et al., 2018). The relative contribution of the disc and spheroid components to the total mass has been shown to dictate where a galaxy lies on the mass-specific

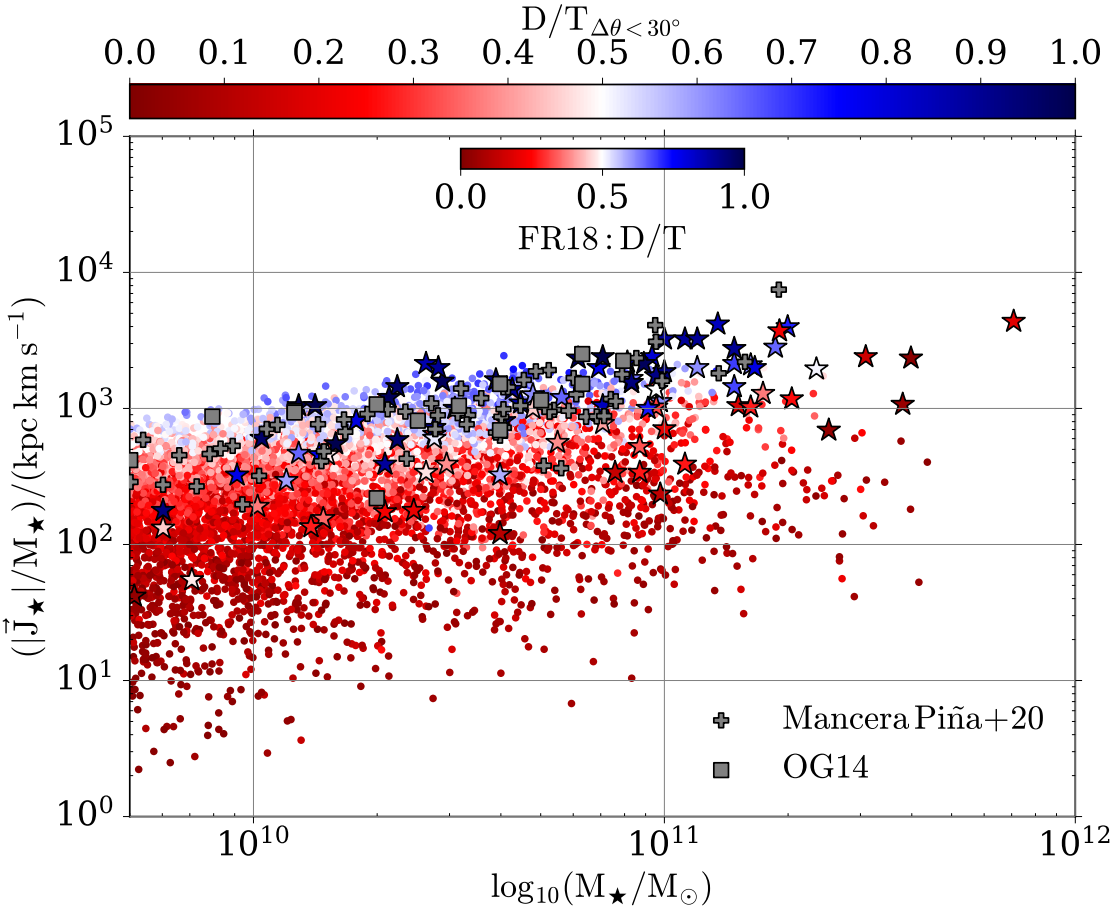

Figure 3.10: The stellar specific angular momentum as a function of the stellar mass colour-coded by the $D/T_{\Delta\theta<30°}$ ratio. The grey squares and crosses represent galaxies from Obreschkow and Glazebrook (2014) and Mancera Piña et al. (2020), respectively, and the stars represent galaxies from Fall and Romanowsky (2018) colour-coded by their D/T ratio.

angular momentum plane (Romanowsky and Fall, 2012; Fall and Romanowsky, 2018; Tabor et al., 2019).

Fig. 3.10 shows the stellar specific angular momentum as a function of the stellar mass colour-coded by the $D/T_{\Delta\theta<30°}$ ratio of each galaxy. We compare our results with the following observational data sets:

(i) Obreschkow and Glazebrook (2014): a sample of 16 nearby spiral galaxies from the The HI Nearby Galaxy Survey (THINGS) (Walter et al., 2008a) selected based on their Hubble types T (from Sab to Scd) which were taken from the HyperLeda database (Paturel et al., 2003).

(ii) Fall and Romanowsky (2018): a sample of 57 spirals, 14 lenticulars and 23 ellipticals decomposed following a 2D decomposition of r-band images with a

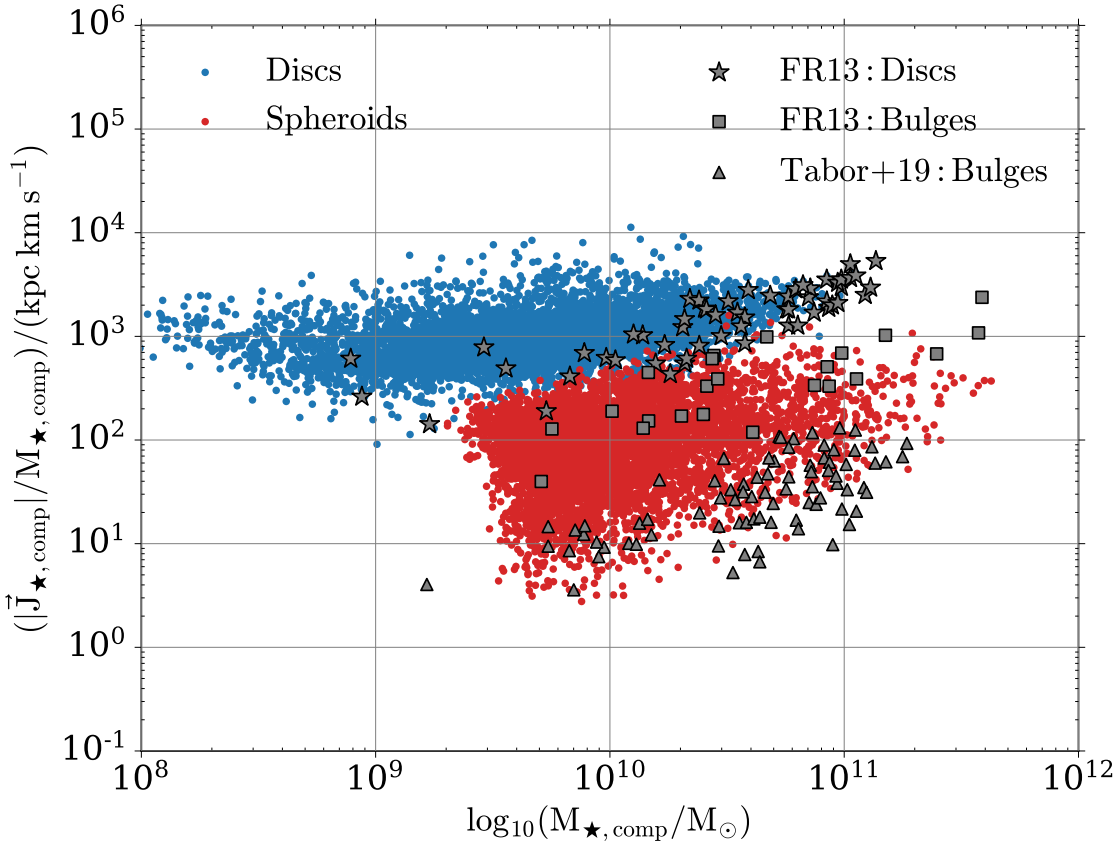

Figure 3.11: The component specific angular momentum as a function of the component stellar mass. The grey stars and squares represent discs and bulges, respectively, from Fall and Romanowsky (2013), and the grey triangles represent bulges from Tabor et al. (2019).

simple exponential and de Vaucouleurs profiles (Kent, 1986, 1987, 1988).

(iii) Mancera Piña et al. (2020): a large sample of nearby disc galaxies which contains 90 galaxies from the Spitzer Photometry & Accurate Rotation Curves (SPARC) (Lelli et al., 2016), 30 from the Ponomareva et al. (2016) sample, 16 from the Local Irregulars That Trace Luminosity Extremes, The Hi Nearby Galaxy Survey (LITTLE THINGS) (Hunter et al., 2012), 14 from the Local Volume Hi Survey (LVHIS) (Koribalski et al., 2018), 4 from the Very Large Array survey of Advanced Camera for Surveys Nearby Galaxy Survey Treasury galaxies (VLA-ANGST) (Ott et al., 2012) and 3 from the Westerbork HI Survey of Irregular and Spiral Galaxies (WHISP) (van der Hulst et al., 2001).

We match extremely well both the tight mass-angular momentum relation and the $D/T_{\Delta\theta<30^{\circ}}$ dependent vertical colour gradient which implies that for a fixed stellar mass disc-dominated galaxies have higher angular momenta than spheroid-

dominated ones.

Fig. 3.11 shows the specific angular momentum separately for the disc (red) and spheroid (blue) components as a function of their stellar mass. We compare our results with the following observational data sets:

(i) Fall and Romanowsky (2013): a sample of nearby bright galaxies of all types introduced in Romanowsky and Fall (2012).

(ii) Tabor et al. (2019): a sample of ETGs from the Mapping Nearby Galaxies at Apache Point Observatory (MaNGA) (Bundy et al., 2015; Drory et al., 2015) selected from the Galaxy Zoo 2 catalogue (Willett et al., 2013) as objects with 'smooth' vote fraction > 0.7.

We find an adequate agreement both with Fall and Romanowsky (2013) and Tabor et al. (2019) data sets. Similar to the disc-dominated galaxies in Fig. 3.10, the disc components follow a tight relation which is more constrained than the one spheroids follow. The wide scatter in the spheroid specific angular momentum can be also seen in the observational data where the two surveys cover different locations on the plot. This behaviour potentially reflects selection effects which bias the Tabor et al. (2019) sample in favour of low angular momentum objects since they studied ETGs, whereas Fall and Romanowsky (2013) analysed galaxies of different morphological types (Romanowsky and Fall, 2012). Furthermore, disagreements between the two surveys are also expected since they deduced D/T ratios following different techniques.

3.4.5 The baryonic Tully-Fisher and Faber-Jackson relations

The Tully and Fisher (1977) and Faber and Jackson (1976) relations reflect fundamental correlations between the stellar mass and kinematics of rotationally supported LTGs and pressure-supported ETGs, respectively. Given the similarities between the disc and spheroid components with LTGs and ETGs, respectively, we explore if our kinematically distinct components follow the aforementioned relations.

Fig. 3.12 shows the baryonic (McGaugh et al., 2000) Tully-Fisher (left column) and Faber-Jackson (right column) relations for each galaxy (top row) and for the disc

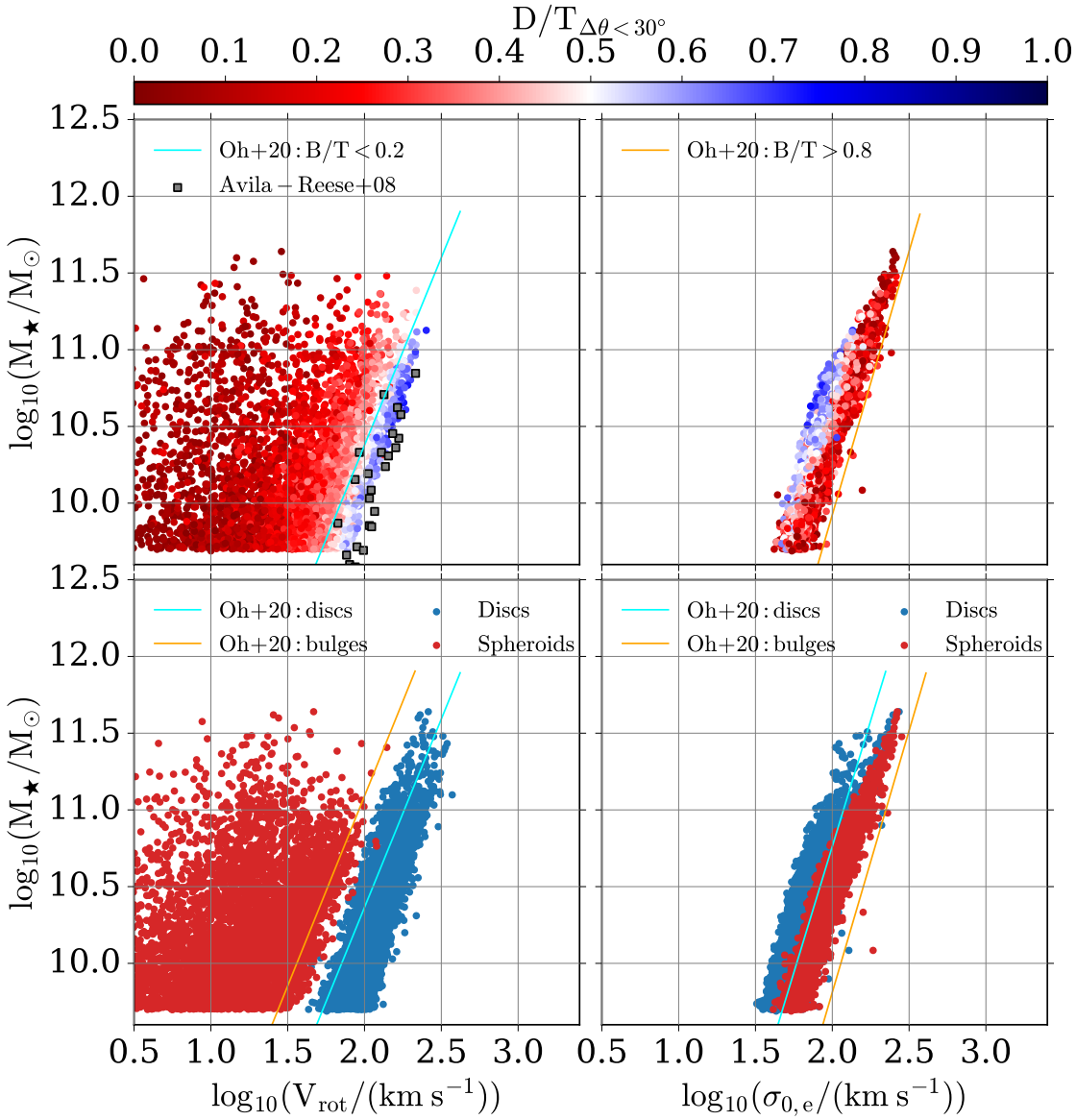

Figure 3.12: The baryonic Tully-Fisher (left-hand column) and Faber-Jackson (right-hand column) relations. *Top left-hand panel:* the galactic stellar mass as a function of the galactic rotational velocity colour-coded by the $D/T_{\Delta\theta<30°}$ ratio. The grey squares and cyan line represent disc-dominated galaxies from Avila-Reese et al. (2008) and Oh et al. (2020), respectively. *Bottom left-hand panel:* the galactic stellar mass as a function of the disc (blue) and spheroid (red) rotational velocity. Cyan and orange lines represent the disc and bulge components, respectively, from Oh et al. (2020). *Top right-hand panel:* The galactic stellar mass as a function of the galactic line-of-sight velocity dispersion colour-coded by the $D/T_{\Delta\theta<30°}$ ratio. The orange line represents bulge-dominated galaxies from Oh et al. (2020). *Bottom right-hand panel:* The galactic stellar mass as a function of the disc (blue) and spheroid (red) line-of-sight velocity dispersion (calcuated within the half-mass redius). The cyan and orange lines represent the disc and bulge components, respectively, from Oh et al. (2020)

and spheroid components (bottom row). We compare our results with the following observational data sets:

(i) Avila-Reese et al. (2008): a sample of non–interacting disc galaxies compiled from the literature (Zavala et al., 2003).

(ii) Oh et al. (2020): a sample of 195 ellipticals, 336 lenticulars, and 295 spirals from the Sydney-AAO Multi-object Integral (SAMI) field spectrograph survey (Croom et al., 2012).

We adopt the method introduced in Thob et al. (2019) to estimate the rotation velocity ($V_{\rm rot.}$) and line-of-sight velocity dispersion ($\sigma_{0,\rm e}$) for the whole galaxy and its components, however we only use particles within one half-mass radius when calculating the latter.

Our galaxies (top left-hand panel) are in great agreement with the observational data of Avila-Reese et al. (2008) and Oh et al. (2020) and show a tight correlation for $D/T_{\Delta\theta<30^\circ}$ values higher than 0.5 (i.e. for disc-dominated galaxies). This correlation appears to vanish as we move to galaxies with a considerable spheroid component (redder colours), as expected. The degree to which each component affects its host galaxy kinematics becomes clear in the bottom left-hand panel which shows the Tully-Fisher relation for the disc (blue) and spheroid (red) component of each galaxy. The disc components follow a well constrained behaviour, while spheroid components' mass and rotational velocity are almost uncorrelated with a significantly larger scatter than the disc, as also found by Oh et al. (2020).

Furthermore, the galactic Faber-Jackson relation reveals a tight correlation between the stellar mass and velocity dispersion where galaxies with higher $D/T_{\Delta\theta<30^\circ}$ have lower $\sigma_{0,\rm e}$ due to their higher degree of ordered rotation. In the bottom right-hand panel we find, in agreement with Du et al. (2020), that discy (spheroidal) structures are formed from dynamically cold (hot) stellar particles. However, we notice that, while our results have similar slope to Oh et al. (2020), they show a slight offset in normalization. A possible explanation can be that Oh et al. (2020) calculated the velocity dispersion as the average flux-weighted velocity dispersion (σ_0) of all spaxels inside the effective radius, where σ_0 of each spaxel was extracted after fitting a Gaussian line-of-sight velocity distribution; whereas we, following Thob

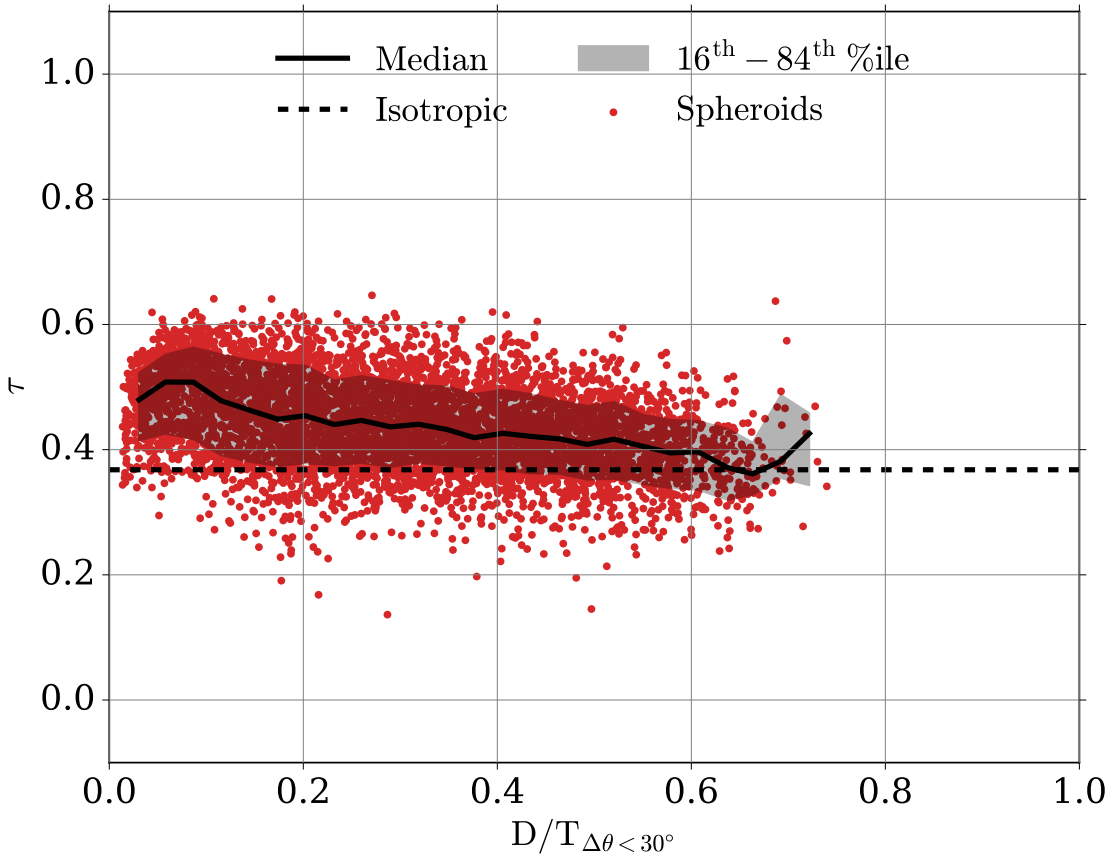

Figure 3.13: Anisotropy parameter for the spheroid components as a function of the $D/T_{\Delta\theta<30^\circ}$ ratio. The black line and shaded region represent the median and 16th-84thpercentile range, respectively. The black dashed horizontal line represents isotropic orbits with $\tau = e^{-1} = 0.367$.

et al. (2019), estimate $\sigma_{0,\mathrm{e}}$ as the remaining motion (after subtracting the ordered corotation component) in the disc plane.

3.4.6 Anisotropy parameter

The anisotropy of stellar orbits within a system (Binney and Tremaine, 2008) can be quantified by the parameter:

$$\beta = 1 - \frac{\overline{u_\theta^2} + \overline{u_\phi^2}}{2\overline{u_r^2}} \,, \tag{3.10}$$

where $\overline{u_\theta}$, $\overline{u_\phi}$, and $\overline{u_r}$ are the average azimuthal, polar, and radial components of the velocity of each stellar particle. Hence, different types of orbits result in different

values of β:

$$\beta = \begin{cases} -\inf, & \text{orbits are circular.} \\ < 0, & \text{orbits are tangentially biased.} \\ = 0, & \text{orbits are isotropic.} \\ > 0, & \text{orbits are radially biased.} \\ 1, & \text{orbits are radial.} \end{cases}$$

In order to study the orbital composition of our spheroids we use a more convenient form of the anisotropy parameter: $\tau \equiv e^{\beta-1}$. Hence, the five cases described above now change to $\tau = 0$, $0 < \tau < 0.367$, $\tau = 0.367$, $0.367 < \tau < 1$ and $\tau = 1$, respectively.

Fig. 3.13 shows τ as a function of the $D/T_{\Delta\theta<30^\circ}$ ratio. Stellar particles which form spheroids have slightly tangentially biased orbits for low $D/T_{\Delta\theta<30^\circ}$ values and gradually move to more isotropic orbits (i.e. τ values closer to the black dashed line) as $D/T_{\Delta\theta<30^\circ}$ increases. In other words spheroid-dominated galaxies consist of stellar particles in tangentially biased orbits while spheroids within disc-dominated galaxies consist of stellar particles in isotropic orbits. This trend while present is quite weak hence agrees with the kinematic similarities between spheroid components and ETGs found by previous studies (see Kormendy, 2016, for a review).

3.4.7 Black-hole spheroid mass relation

Tight relations between black hole and spheroid properties have been revealed in numerous studies and have been linked with the fact that they form in closely associated processes (Kormendy and Gebhardt, 2001; Marconi and Hunt, 2003; Greene et al., 2008; Gadotti and Kauffmann, 2009; Sani et al., 2011; Shankar et al., 2012).

Fig. 3.14 shows the relation between the spheroid and black hole masses[4]. We compare with the Häring and Rix (2004) (sample of 30 nearby galaxies) data set. We find that our spheroids form an almost linear relation (in log-space) between the black hole and spheroid mass which extends to all masses; a behaviour which is in agreement with previous work (Beifiori et al., 2012; Graham, 2012; McConnell

[4]As discussed in McAlpine et al. (2016); The EAGLE team (2017) this is the summed mass of all black holes associated with each subhalo.

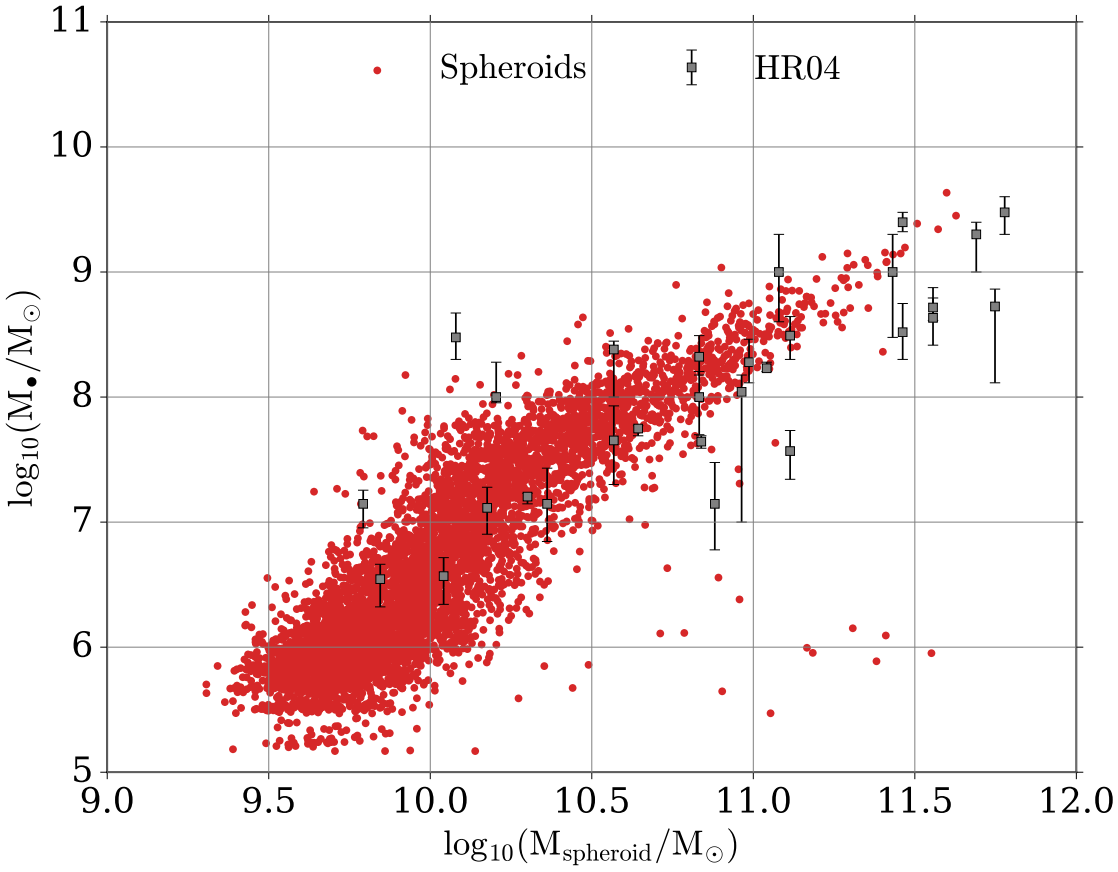

Figure 3.14: The black hole mass as a function of spheroid mass. The grey squares represent Häring and Rix (2004) data.

and Ma, 2013; Barber et al., 2016; Habouzit et al., 2020). Hence, we broadly match the Häring and Rix (2004) relation despite the different definitions and extraction techniques used to estimate the mass of the bulge/spheroid component.

It is worth noting that the free parameters of the EAGLE black hole model have been calibrated to match the black hole-bulge mass relation; however that was performed using both different data sets (i.e. McConnell and Ma (2013) instead of Häring and Rix (2004)) and different masses (i.e. Schaye et al. (2015); Crain et al. (2015) used the total stellar mass instead of the spheroid mass).

3.4.8 Age and metallicity relations

The age and metallicity of galactic components reflect their formation processes and time-scales (Gadotti, 2009; Obreja et al., 2013; Trussler et al., 2020), hence distinct components should follow different relations.

Fig. 3.15 shows the mass-age and mass-metallicity relations for the disc and spheroid components. We use $\overline{\alpha}_{\rm comp.}$ as a proxy for the age of each component, which we define as the average birth (i.e. at the time a stellar particle is born) scale factor for all stellar particles belonging to that component (The EAGLE team, 2017). In addition, the metallicity of each component is defined as the sum of the mass-weighted metallicity Z of all stellar particles belonging to that component, where Z is the mass fraction of elements heavier than helium. At a given component stellar mass, there is a clear trend (based on the median lines) which shows that disc components are younger and more metal-rich than the spheroid components, in agreement with previous simulations (e.g. Naab et al., 2014; Park et al., 2019; Rosito et al., 2019; Wang et al., 2019) and observations (e.g. Bothun and Gregg, 1990; Mancini et al., 2019).

3.5 Discussion

In this work, we follow the method introduced in Section 3.2.2 which decomposes galaxies by identifying kinematically distinct components. This method in order to be in agreement with previous observational and/or theoretical methods assigns to the disc component particles that have angular momenta broadly aligned with the

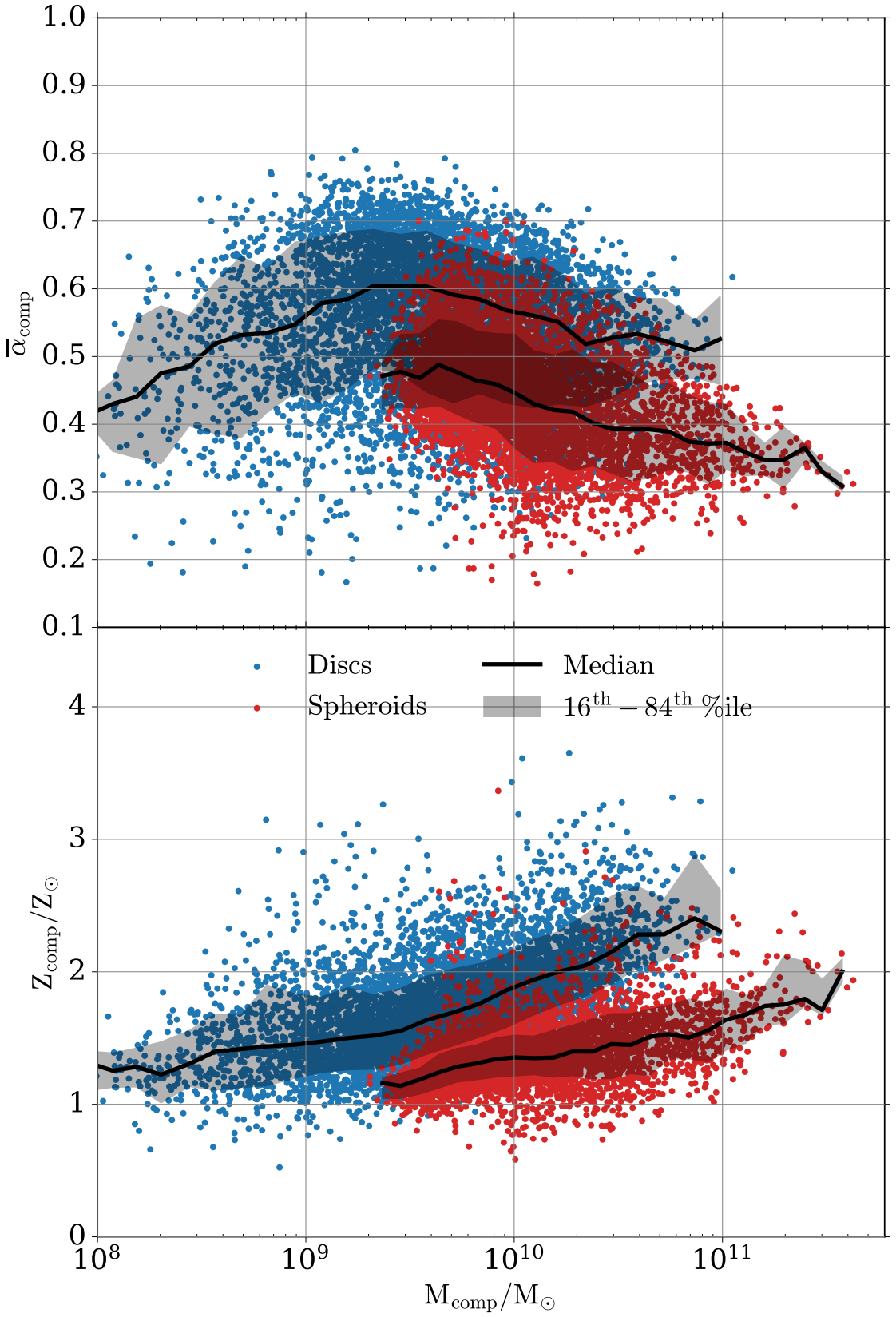

Figure 3.15: The average stellar formation expansion factor (top) and metallicity (bottom) of the disc (blue) and spheroid (red) component as a function of the component stellar mass. The black line and shaded region represent the median and 16th-84th percentile range, respectively.

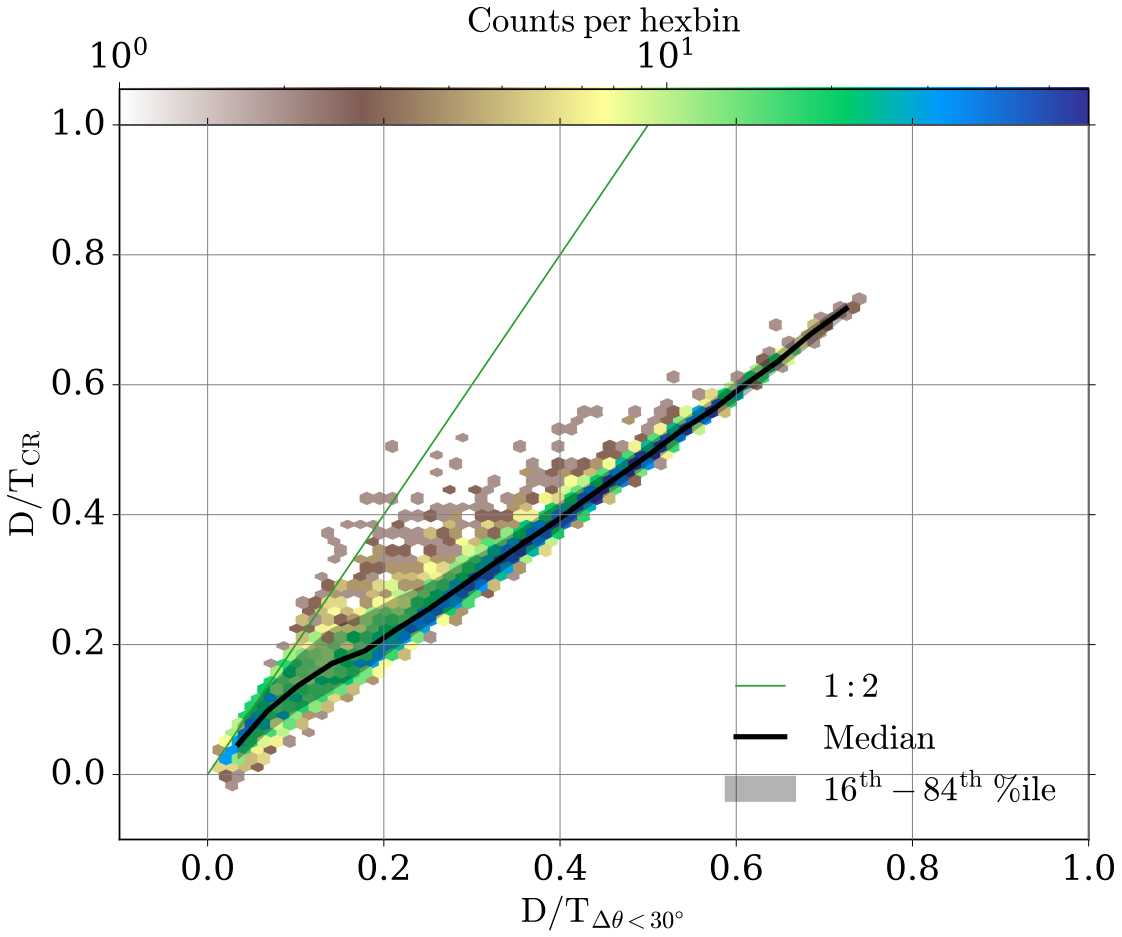

Figure 3.16: The $D/T_{\rm CR}$ ratio as a function of the $D/T_{\Delta\theta<30^\circ}$ ratio. The black line and shaded region represent the median and 16th-84th percentile range, respectively and the green line represents the 1:2 ratio.

galactic one [the angle between the two should not exceed 30°, see equation (3.4)]. However, as discussed in Section 3.3.2 and shown in Fig. 3.9, there are numerous galaxies whose anti-aligned particles also form a component which counter-rotates (with respect to the galactic angular momentum). It is clear that if these particles are also assigned to the disc component that will have a significant impact on the predicted D/T ratio. In this section, we briefly investigate what effect such a method will have on our $D/T_{\Delta\theta<30^\circ}$ ratios.

We follow exactly the same process as the one described in Section 3.2.2 however in step (v) we assign to the disc component particles with

$$\Delta\theta_i < 30^\circ \tag{3.11}$$

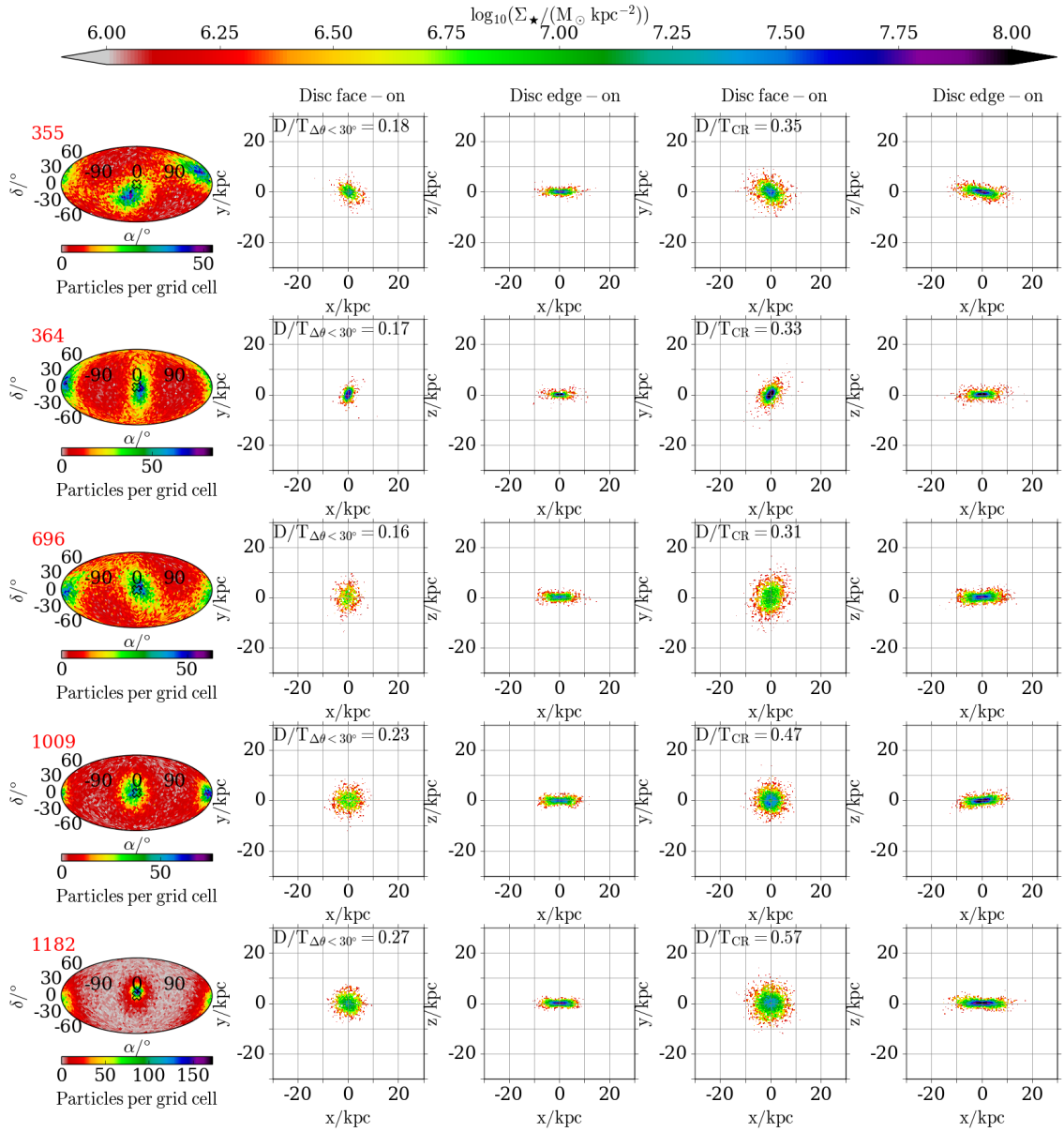

Figure 3.17: A sample of five galaxies selected so that each one has a ratio of $D/T_{\rm CR}$ to $D/T_{\Delta\theta<30^\circ}$ higher than 2. Each galaxy is represented by five panels as described below. The first column displays for each galaxy on a Mollweide projection the angular momentum maps, where the red number on the top left corner in each row refers to each galaxy's group number. As in Fig. 3.1, the galaxies have been rotated so that $\boldsymbol{J}_\star$ (hollow X symbol) points towards the reader. The second and third columns have the face-on and edge-on projections, respectively, for the disc component when it is defined based the method described in Section 3.2.2. The fourth and fifth columns have the same projections, respectively, but when the disc component also includes counter-rotating particles (see the text for more details). The text in the each panel on the second and fourth columns represents the $D/T_{\Delta\theta<30^\circ}$ and $D/T_{\rm CR}$ ratios, respectively, for each galaxy.

and

$$\Delta\theta_i > 150^\circ \ . \tag{3.12}$$

This results in a new D/T ratio which we call $D/T_{\rm CR}$. In addition, we amend step (vi) and we apply to $D/T_{\rm CR}$ a correction with two times χ, to account for the second 30° patch on the angular momentum sphere.

Fig. 3.16 shows $D/T_{\rm CR}$ as a function of $D/T_{\Delta\theta<30^\circ}$. The majority of galaxies, especially the ones with $D/T_{\Delta\theta<30^\circ}$ values higher than 0.2, follow tightly the 1:1 relation as indicated by the median line and 1-σ region. Hence, in cases where there is no significant counter-rotating component the $D/T_{\Delta\theta<30^\circ}$ values are not significantly altered[5]. However, some galaxies, especially the low $D/T_{\Delta\theta<30^\circ}$ ones, have a dramatic change in their D/T ratios that is reflected on their $D/T_{\rm CR}$ values which can be as high as ~ 2.8 times their original $D/T_{\Delta\theta<30^\circ}$ ratios.

Fig. 3.17 shows the angular momentum maps and the face-on and edge-on projections for the two different definitions of the disc component for a sample of five galaxies who display noticeable differences between their $D/T_{\Delta\theta<30^\circ}$ and $D/T_{\rm CR}$ ratios. It becomes apparent from the angular momentum maps of all five galaxies that two structures exist; one well-aligned with the galactic angular momentum and the other counter-rotating with respect to the latter. From the second and third columns, we see that these galaxies have thin rotationally supported discs which they continue to exist (although increase their height and diameter) when particles with $\Delta\theta > 150^\circ$ are included. The most interesting case is galaxy 1182 (fifth row) which has $D/T_{\Delta\theta<30^\circ}$ value of 0.27, while its $D/T_{\rm CR}$ ratio is 0.57. Hence, in with the former definition is classified as a spheroid-dominated galaxy while with the latter a disc-dominated.

3.6 Conclusions

Being able to extract galactic components is vital in studying the galaxy as a whole. In this work, we use the information depicted on angular momentum maps (Sec-

[5]Small fluctuations of order 10^{-2} between the two ratios are also expected due to the smoothing process which finds and uses grid cell centres within 30°. So there are particles within 30° which are not included in the smoothing but are used when estimating the mass of the component.

tion 3.2) to identify kinematically distinct components and study the imprint each component leaves on the properties of their host galaxy. We consider this method a useful addition to the literature since it results in components which are in great agreement with the observed. Our main conclusions are as follows:

(i) We find a clear separation in angular momentum space of distinct components and classify galaxies into several morphological types (Section 3.3).

(ii) We demonstrate that even though we make no assumptions regarding the spatial extent of our components, they follow the expected spatial distribution and surface density profiles (Section 3.3.2).

(iii) We compare with other methods and find, in general, tight relations but also some interesting cases in which our method provides better classification: for example disc-like galaxies with particles on non-circular orbits. (Section 3.4.2).

(iv) Our method identifies a significant population of galaxies with counter-rotating discs embedded within them (Section 3.4.3).

(v) Our components have distinct angular momenta (Section 3.4.4), kinematics (Section 3.4.5 and Section 3.4.6) and ages and chemical compositions (Section 3.4.8). Thus, our morphological classification reproduces the observed properties of such systems.

In a future work, we will use our method to study merging systems and galaxies with counter-rotating discs in order to better understand their formation path and evolution. In addition, we intend to explore possible imprint of other kinematically distinct components, such as bars and pseudo-bulges, on the angular momentum maps.

3.7 Rotation matrix

We rotate the coordinate and velocity vectors of each galaxy's stellar particle by applying to each vector the dot product of following rotation matrices

$$\boldsymbol{R}_{\rm z} = \begin{pmatrix} \cos(\alpha) & \sin(\alpha) & 0 \\ -\sin(\alpha) & \cos(\alpha) & 0 \\ 0 & 0 & 1 \end{pmatrix} \tag{3.13}$$

and

$$\boldsymbol{R}_{\rm y} = \begin{pmatrix} \cos(\delta) & 0 & \sin(\delta) \\ 0 & 1 & 0 \\ -\sin(\delta) & 0 & \cos(\delta) \end{pmatrix} \tag{3.14}$$

where α and δ are the right ascension and elevation from the reference plane of the galactic angular momentum.

3.8 Profiles

The exact value for the term b_n can be obtained by solving

$$\Gamma(2n) = 2\gamma(2n, b) \ , \tag{3.15}$$

where Γ and γ are the complete and incomplete gamma functions, respectively Ciotti (1991). Useful approximations have been proposed by Prugniel and Simien (1997); Ciotti and Bertin (1999), however in this work we follow MacArthur et al. (2003) and use the asymptotic expansion of Ciotti and Bertin (1999) for all $n > 0.36$

$$\begin{aligned} b_n = \ & 2n - \frac{1}{3} + \frac{4}{405n} + \frac{46}{25515n^2} + \frac{131}{1148175n^3} - \frac{2194697}{30690717750n^4} \\ & + O(n^{-5}) \ , \end{aligned} \tag{3.16}$$

and the polynomial expression derived by MacArthur et al. (2003) for $n \leq 0.36$

$$b_n = \sum_{i=0}^{m} \alpha_i n^i \ , \tag{3.17}$$

where m is the order of the polynomial and α_i are the coefficients of the fit which can be written as

$$\begin{aligned} \alpha_0 = 0.01945 \ \alpha_1 = -0.8902 \ , \\ \alpha_2 = 10.95 \ \alpha_3 = -19.67 \ , \alpha_4 = 13.43 \ . \end{aligned} \tag{3.18}$$

Chapter 4

Quantifying the effects of AGN feedback on the structural and dynamical properties of disc galaxies in cosmological simulations

Feedback from active galactic nuclei (AGN) is thought to significantly alter the properties of the most massive galaxies, however its effect on Milky Way mass galaxies is still unclear. In this chapter, we use the Auriga simulations to explore the effects of the radio and quasar AGN feedback modes on the dynamical and structural properties of the bar, bulge, disc, and the galaxy as a whole. We re-simulated three Auriga galaxies using two AGN feedback prescriptions: one without radio mode feedback and one completely without black holes. This allows us to constrain the impact of each mode on galactic properties and bar formation, by comparing the two variants with the original haloes. Since these two AGN feedback modes act differently, they affect the structural and dynamical properties of galaxies in distinct ways. We show that the quasar and radio modes suppress star formation in the inner and outer disc, respectively. Thus, when we turn off the former mode we see more massive central components, while the absence of the latter mode results in cooler haloes. In addition, we find that the complete lack of AGN enhances the bar strength to the point where an originally weakly-barred galaxy is turned into a strongly-barred one. In order to quantify the effects of the AGN feedback modes on

the relative growth of each component, we perform 2D bar/bulge/disc decompositions and we find that AGN plays an important role in shaping the morphology and composition of galaxies. We explain the morphological transformations by showing that in the absence of the quasar mode gas cells survive in the centre resulting in enhanced central star formation. This mechanism is expressed in the formation of stronger but shorter bars. We conclude that the interplay between AGN feedback and bar/bulge formation is more complex than previously reported. AGN feedback can affect the dynamics of galaxies in non-linear ways, hence, how AGN feedback is implemented plays an important role in galaxy formation models.

4.1 Introduction

Numerous studies have identified significant correlations between bars' and their host galaxy's properties, which indicate that there is a causal connection between the two (e.g. Aguerri, 1999; Laurikainen et al., 2002; Kim et al., 2012; Athanassoula et al., 2013). However, bars are not the only central component. In fact, the centre of most late-type barred galaxies is a region where multiple structures, such as bulges, super-massive black holes (SMBH), and nuclear components (rings, discs etc.), coexist (Kormendy and Kennicutt, 2004; Knapen, 2010; Athanassoula, 2013), and each structure affects and is affected by the others in non-linear ways. Despite the rich literature, these interactions need to be further understood as does the effect of different AGN feedback prescriptions on the formation of bars and bulges, and therefore on the galaxy as a whole. This will allow us to understand our models and the non-linear effects they introduce in order to improve our theoretical tools and predictions.

Observational evidence suggests that bars exist in the centres of over half of local spiral galaxies (Aguerri et al., 2009; Nair and Abraham, 2010; Erwin, 2018). From a theoretical perspective, bars can form in isolated galaxies via discs instabilities (Hohl, 1971; Ostriker and Peebles, 1973; Efstathiou et al., 1982) or in interacting discs through tidal forces (Noguchi, 1996; Łokas et al., 2014), and subsequently grow by redistributing angular momentum (Athanassoula, 2003). In general, the bar structure can be supported by a plethora of orbital families (Contopoulos and

Papayannopoulos, 1980; Athanassoula et al., 1983; Skokos et al., 2002; Patsis and Athanassoula, 2019) which shape its properties and morphology.

As mentioned above, bars usually coexist with central bulge components. Athanassoula (2005) split bulges in three distinct types: classical, pseudo/disc-like, and boxy/peanut. Classical bulges form through violent processes such as galaxy mergers (Toomre and Toomre, 1972) or via clumps that spiral into the center and merge together (Noguchi, 1999; Aguerri et al., 2001; Steinmetz and Navarro, 2002; Immeli et al., 2004). On the other hand, pseudo-bulges are linked to secular processes (Kormendy and Kennicutt, 2004). For example, in barred galaxies gas inside the corotation radius loses angular momentum and slowly migrates towards the centre (Athanassoula, 2013). This gradual supply of gas feeds star formation episodes which culminate in the formation of a pseudo-bulge. Hence, due to their diverse formation paths, classical and pseudo-bulges have distinct properties (Wyse et al., 1997; Gadotti, 2009; Fisher and Drory, 2016). The third type of bulge (i.e. the boxy/peanut) does not constitute a distinct physical component on its own as it reflects a part of the bar when the galaxy is viewed edge-on. Burbidge and Burbidge (1959) were one of the first to photograph that central component which they described as *'four bulges of about equal size, coming out of the nucleus itself like a cross'*. These structures were later termed by de Vaucouleurs and de Vaucouleurs (1972) *'peanut-shaped bars'* and have been since observed in numerous galaxies (Jarvis, 1986; Lütticke et al., 2000) including our own (Ness et al., 2012; Wegg et al., 2015). From a theoretical point of view, peanut-shaped bulges naturally arise when bars experience buckling instabilities (Combes et al., 1990a; Raha et al., 1991; Martinez-Valpuesta et al., 2006; Athanassoula, 2016; Łokas, 2020).

Apart from the gaseous and stellar components (i.e. bars and bulges) the central region of most galaxies also harbours supermassive black holes (for a review, see Kormendy and Ho, 2013; Inayoshi et al., 2020). As discussed above, gas that accumulates near the centre forms stars and subsequently pseudo-bulges; however some of that gas can in principle also feed the SMBH (Combes, 2001). In addition to this secular growth, SMBH can rapidly acquire large amounts of gas during gas-rich mergers. In both cases the accretion disc formed around the SMBH results in powerful AGN feedback (Lynden-Bell, 1969; Silk and Rees, 1998; Begelman, 2004;

McNamara and Nulsen, 2012).

Energetic feedback is the natural culprit for shutting down gas supply and eventually the formation of stars (Dekel and Birnboim, 2006; Fabian, 2012). This is the reason why AGN feedback has been considered a mechanism responsible for the quenching and formation of early-type galaxies (ETGs). For example, Dubois et al. (2016); Penoyre et al. (2017); Frigo et al. (2019) showed that AGN feedback is important in order to produce massive slow-rotating ETGs (Emsellem et al., 2007) since it prevents them from developing young fast-rotating stellar discs. However, massive disc-dominated galaxies are also subject to powerful feedback which plays a fundamental role on their properties (see Su et al., 2021, and references therein) and regulates the formation of their constituent stellar components and gas reservoirs (Hani et al., 2019).

Recent studies (Bonoli et al., 2016; Spinoso et al., 2017; Zana et al., 2019) using cosmological zoom-in simulations have shown that AGN feedback can have an effect on bar formation by suppressing the growth of a massive spheroidal component at the centre. Bars grow in mass and size by capturing disc stars (Gadotti et al., 2020). As previously described, while bars evolve they push gas to the centre which fuels the formation of pseudo-bulges (Shlosman et al., 1989; Sellwood and Moore, 1999; Kormendy, 2013; Fanali et al., 2015) but also triggers AGN activity, which in turn suppresses gas inflow (Gavazzi et al., 2015; Fragkoudi et al., 2016) and halts the formation of the pseudo-bulge. This picture becomes more complicated in galaxies which host a classical bulge. As shown by Athanassoula (2003) and Saha et al. (2012), the presence of a classical (non-rotating) bulge alters the amount of angular momentum exchanged between galactic components, since this process depends on the mass distribution and the velocity dispersion of the emitting/absorbing material. Hence, a classical bulge is expected to amplify the transfer of angular momentum from the bar to the bulge which results in the bar losing angular momentum, slowing down, and becoming stronger.

In this work we study the impact of AGN feedback on the formation and evolution of barred galaxies. In particular, we assess to what extent the AGN implementation affects the growth and properties of the disc, bar, and bulge. For that purpose, we selected three Auriga (Grand et al., 2017) galaxies - two strongly and one weakly

barred - and re-simulated each one with two different AGN feedback recipes whilst keeping their initial conditions and physical processes identical to the original. The AURIGA simulations[1] provide an ideal testbed for our analysis, since they produce realistic barred galaxies with prominent boxy/peanut and pseudo-bulges (Gargiulo et al., 2019; Blázquez-Calero et al., 2020; Fragkoudi et al., 2020b,a).

This chapter is organised as follows. In Section 4.2, we briefly describe the AURIGA model and its AGN recipe along with the simulations we use for this study. In Section 4.3, we present the $z = 0$ morphologies and properties (e.g. the stellar-halo mass relation) of the galaxies, and analyse the radial profile of the bar strength and that of the stellar and gaseous distributions. Finally, we estimate the relative contribution of the bar, bulge, and disc component to the total stellar mass by performing photometric 2D decompositions. In Section 4.4, we analyse the temporal evolution of the quasar and radio mode feedback energy rates and their effect on the star formation rate (SFR), bar strength, and gas temperature. Finally, we summarise our results in Section 4.5.

4.2 The AURIGA model

4.2.1 General

The AURIGA project[2] is a suite of cosmological magneto-hydrodynamical zoom-in simulations of isolated Milky-Way mass dark matter haloes (Grand et al., 2017). These were selected from the dark-matter-only EAGLE Ref-L100N1504 cosmological volume (Schaye et al., 2015) and re-simulated at higher resolution with the N-body, magneto-hydrodynamics code AREPO (Springel, 2010; Pakmor et al., 2011, 2016; Weinberger et al., 2020). The simulations incorporate a detailed galaxy formation model which includes primordial and metal-line cooling (Vogelsberger et al., 2013), a hybrid multi-phase star formation model (Springel and Hernquist, 2003), supernova feedback in the form of an effective model for galactic winds and mass and metal return from stellar winds and supernovae (Marinacci et al., 2014; Grand et al.,

[1] https://wwwmpa.mpa-garching.mpg.de/auriga/

[2] AURIGA is a project of the Virgo consortium for cosmological supercomputer simulations http://virgo.dur.ac.uk.

2017), a redshift dependent and spatially uniform UV background (Faucher-Giguère et al., 2009b; Vogelsberger et al., 2013), magnetic fields (Pakmor and Springel, 2013; Pakmor et al., 2014, 2017, 2018), and a black hole formation and feedback model which we describe in more details below.

In this work, we use nine AURIGA haloes: three original runs, first presented in Grand et al. (2017), namely Au-06, Au-17, and Au-18, plus two additional model variants for each one which were simulated for the needs of this study. These variants are as follows:

- the NoR (i.e. no-radio) variants have black hole particles (which grow via gas accretion and mergers) and black hole feedback through the quasar mode, but the radio mode feedback is turned off.
- the NoRNoQ (i.e. no-radio-no-quasar) variants have their black hole particles, and of course both feedback modes, removed.

Throughout this work we use the level-4 resolution (based on the AQUARIUS project nomenclature, Springel et al., 2008) which corresponds to dark matter and baryonic particles masses of 3×10^5 $M_\odot$ and 5×10^4 $M_\odot$, respectively. The gravitational co-moving softening length for stellar and dark matter particles is set to 500 cpc h^{-1}. This is equal to the minimum co-moving softening length allowed for gas cells, while their maximum physical softening length can not exceed 1.85 kpc. For more details on the simulations we refer the reader to Grand et al. (2017). In the following section we describe the AGN feedback prescription in the AURIGA simulations.

4.2.2 Black hole and AGN feedback model

Black holes come into existence by converting the densest gas cell into a collisionless sink particle in Friends-of-Friends (FoF) groups whose mass exceeds 5×10^{10} $M_\odot$ h^{-1}. The initial (seed) mass is set to 10^5 $M_\odot$ h^{-1} which can increase either by acquiring mass from nearby gas cells or by merging with other black hole particles (Springel et al., 2005a; Vogelsberger et al., 2013). The former is described by an Eddington-limited Bondi-Hoyle-Lyttleton accretion (Hoyle and Lyttleton, 1939; Bondi and Hoyle, 1944; Bondi, 1952) along with a term to account for the radio

mode accretion. Hence, the total black hole accretion rate can be expressed by

$$\dot{M}_{\rm BH} = \min\left[\dot{M}_{\rm BHL} + \dot{M}_{\rm radio}, \dot{M}_{\rm Edd.}\right] \ . \tag{4.1}$$

The term $\dot{M}_{\rm Edd.}$ represents the Eddington accretion rate which is defined as

$$\dot{M}_{\rm Edd.} \ = \frac{4\pi \ G \ M_{\rm BH} \ m_{\rm pr.}}{\epsilon_{\rm r} \ \sigma_{\rm T} \ c} \ , \tag{4.2}$$

where G is the gravitational constant, $M_{\rm BH}$ is the black hole mass, $m_{\rm pr.}$ is the proton mass, $\epsilon_{\rm r} = 0.2$ is the black hole radiative efficiency parameter, $\sigma_{\rm T}$ is the Thomson cross section and c is the speed of light.

The term $\dot{M}_{\rm BHL}$ represents the Bondi-Hoyle-Lyttleton accretion rate which is defined as

$$\dot{M}_{\rm BHL} = \frac{4\pi \ G^2 \ M_{\rm BH}^2 \ \rho}{(c_{\rm s}^2 + \upsilon_{\rm BH}^2)^{3/2}} \ , \tag{4.3}$$

where ρ and $c_{\rm s}$ are the density and sound speed, respectively, of the surrounding gas, and $\upsilon_{\rm BH}$ is the velocity of the black hole relative to the gas.

The term $\dot{M}_{\rm radio}$ represents the radio mode accretion rate which is defined as

$$\dot{M}_{\rm radio} = \frac{L_{\rm radio}}{\epsilon_{\rm f} \ \epsilon_{\rm r} \ c^2} \ , \tag{4.4}$$

where $\epsilon_{\rm f} = 0.07$ is the fraction of radiated energy that thermally couples to the gas. This term follows a scheme in which first the X-ray luminosity of the halo ($L_{\rm X}$) is converted to a radio mode luminosity ($L_{\rm radio}$), which is then used to define the radio mode accretion rate. This scheme establishes a self-regulated feedback mechanism by following the process described below.

We first measure the X-ray luminosity on a per FoF halo basis by following the observed X-ray luminosity–temperature relation (Pratt et al., 2009)

$$L_{\rm X} = \frac{H(z)}{H_0} C \left(\frac{T}{T_0}\right)^{2.7} \ , \tag{4.5}$$

where $H(z)$ and H_0 are the Hubble parameter and Hubble constant, respectively, $C = 6 \times 10^{44}$ ergs s^{-1}, and $T_0 = 5$ Kev. Then we follow Nulsen and Fabian (2000) who developed a theory for spherically symmetric accretion of hot gas onto super-massive black holes at the centres of large haloes. This theory connects the accretion rate

back to the state of the gas at large distances away from the black hole based on the formula

$$\dot{M}'_{\rm BH} = \frac{2\pi\ Q(\gamma-1)k_{\rm B}\ T_{\rm vir}}{\mu m_{\rm H}\ \Lambda(T_{\rm vir})} G\ M'_{\rm BH} \left[\frac{\rho^2}{n_{\rm e}\ n_{\rm H}}\right] \mathcal{M}^{3/2}\ , \tag{4.6}$$

where $Q = 2.5$, $\gamma = 5/3$ is the adiabatic index of the gas, $k_{\rm B}$ is the Boltzmann constant, $T_{\rm vir}$ is the virial temperature, $\mu m_{\rm H}$ is the mean mass per gas cell, $\Lambda(T_{\rm vir})$ is the cooling function, ρ, $n_{\rm e}$, and $n_{\rm H}$ are the mean gas, electron number, and hydrogen number densities, respectively, $\mathcal{M} = 0.0075$ is the Mach number of the gas far away from the black hole, and $M'_{\rm BH}$ is derived from the observed $M_{\rm BH}$-σ relation

$$M'_{\rm BH}(\sigma) = M_0 \left(\frac{\sigma}{\sigma_0}\right)^4\ , \tag{4.7}$$

where σ is the velocity dispersion of stars in the galactic bulge. Lastly, we assume a radio power associated with this radio mode accretion which can be written as

$$L_{\rm radio} = R(T_{\rm vir}, z) L_{\rm X}\ , \tag{4.8}$$

where $L_{\rm X}$ is the X-ray luminosity of the halo (calculated using the gas cells) and we define the ratio

$$R(T_{\rm vir}, z) \equiv \frac{\epsilon_{\rm f}\ \epsilon_{\rm r}\ c^2\ \dot{M}'_{\rm BH}}{L_{\rm X}}\ , \tag{4.9}$$

which tends to increase for larger halos and towards later times.

Finally, for both modes the energy ejected from the black hole is given by

$$\dot{E} = \dot{M}_{\rm BH}\ \epsilon_{\rm f}\ \epsilon_{\rm r}\ c^2\ , \tag{4.10}$$

where $\dot{M}_{\rm BH}$ is given by equation (4.1). For the quasar mode this energy is injected isotropically as thermal energy into neighbouring gas cells; while for the radio mode (Sijacki et al., 2007) it takes the form of bubbles (with size 0.1 times the virial radius) which are stochastically inflated at random locations in the halo[3] up to a maximum radius of 0.8 times the virial radius.

4.3 Present day galactic properties

We start this section by presenting the stellar surface densities of the haloes under study (Section 4.3.1) and then investigate the effect of the AGN feedback (or the lack

[3]Following an inverse square distance profile around the black hole.

of it) on bar (Section 4.3.2), stellar (Section 4.3.3, Section 4.3.4, and Section 4.3.5), and gas (Section 4.3.6) properties.

4.3.1 Stellar surface density

Fig. 4.1 shows the stellar surface density projection at $z = 0$. The top, middle, and bottom rows contain results for Au-06, Au-17, and Au-18, respectively. The left-hand, middle, and right-hand columns contain results for the original halo, the NoR, and the NoRNoQ variant, respectively. Each row contains a face-on (top panel) and an edge-on (bottom panel) projection.

The characteristic X-shaped (or peanut) structure (see Laurikainen and Salo, 2016, for a review) is prominent in the centre of many edge-on projections. This feature has been revealed in numerous observed (Whitmore and Bell, 1988; Mihos et al., 1995; Bureau et al., 2006; Laurikainen and Salo, 2017) and simulated galaxies (Combes and Sanders, 1981; Combes et al., 1990b; Pfenniger and Friedli, 1991; Martinez-Valpuesta et al., 2006) and its origin has been connected with either vertical resonance orbits with 2:1[4] or less frequency ratio (Quillen, 2002; Quillen et al., 2014; Parul et al., 2020) or buckling instabilities (Raha et al., 1991; Merritt and Sellwood, 1994).

The peanut bulge is usually described as a part of the bar seen edge-on (Athanassoula, 2005), which is the case for Au-17, Au-18, and their NoR variants where the bar clearly extends beyond the X-shaped structure. It is interesting to note that, as we show below, Au-06 is a weakly barred galaxy which only develops a peanut bulge in the NoRNoQ variant. Even though a significant fraction of galaxies host boxy/peanut bulges (Lütticke et al., 2000; Yoshino and Yamauchi, 2015; Erwin and Debattista, 2017) and they are (from a dynamical perspective) intriguing components, the detailed study of the peanut parameter space (e.g. Ciambur and Graham, 2016) is beyond the scope of this work.

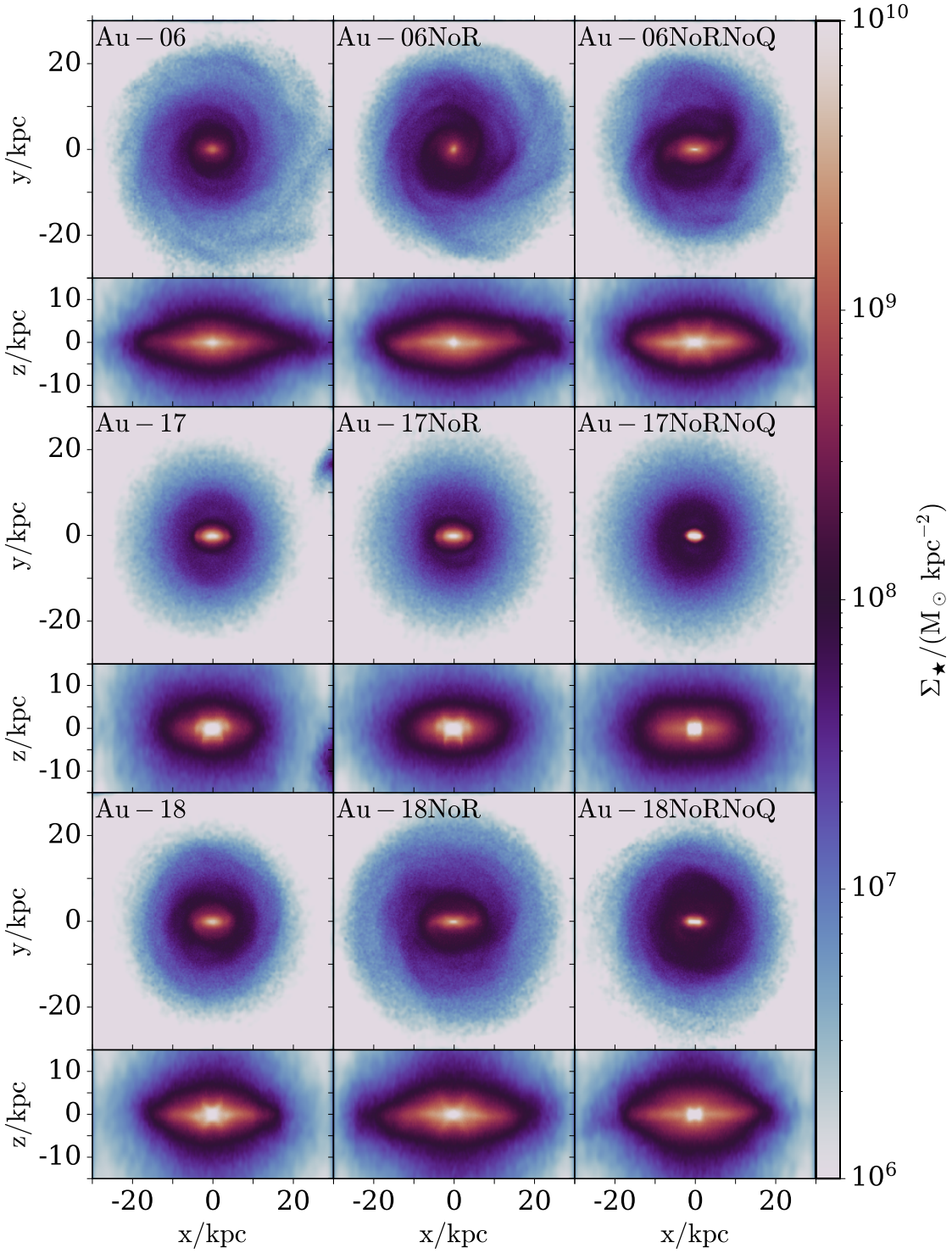

Figure 4.1: Stellar surface density projection at $z = 0$. The top, middle, and bottom rows contain results for Au-06, Au-17, and Au-18, respectively. The left-hand, middle, and right-hand columns contain results for the original halo, the NoR, and the NoRNoQ variant, respectively. Each row contains a face-on (top panel) and an edge-on (bottom panel) projection. Prominent boxy/peanut bulges appear in most edge-on projections.

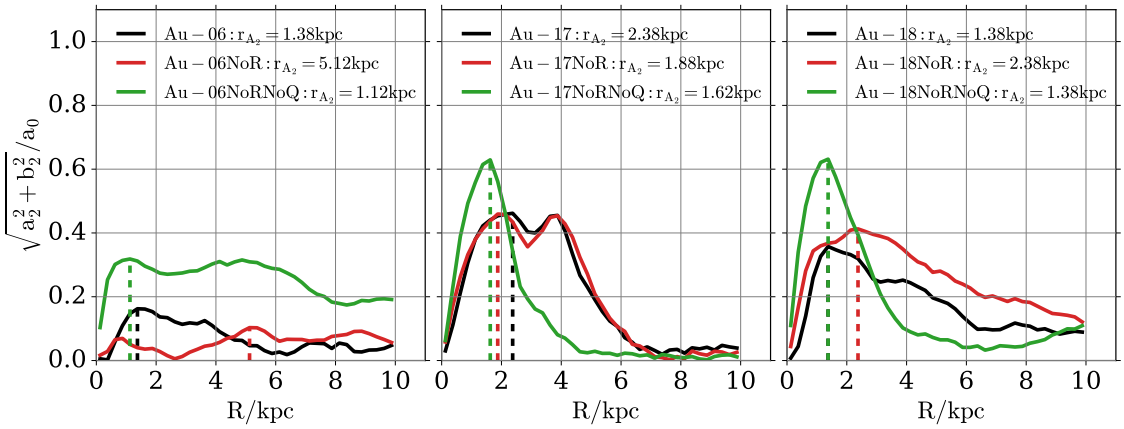

Figure 4.2: Radial profile of the relative amplitude of the $m = 2$ Fourier component at $z = 0$. The left-hand, middle, and right-hand panels contain results for Au-06, Au-17, and Au-18, respectively. The black, red, and green curves show the original halo, the NoR, and the NoRNoQ variant, respectively. The vertical dashed black, red, and green lines show the A_2 radius for the original halo, the NoR, and the NoRNoQ variant, respectively. The complete lack of AGN promotes the formation of stronger and shorter bars.

4.3.2 Bar strength

To obtain the bar strength we follow Athanassoula (2003); Athanassoula et al. (2013) and calculate the Fourier components of the face-on stellar density as

$$a_m(R) = \sum_{i=0}^{N} \mathrm{m}_i \cos(m\theta_i) \ , \quad m = 0, 1, 2, ..., \tag{4.11}$$

$$b_m(R) = \sum_{i=0}^{N} \mathrm{m}_i \sin(m\theta_i) \ , \quad m = 0, 1, 2, ..., \tag{4.12}$$

where R is the cylindrical radius, m_i is the mass and θ_i the azimuthal angle of stellar particle i, and the sum goes over all N stellar particles. Hence, the bar strength is obtained from the maximum value of the $m = 2$ relative Fourier component as

$$A_2 = \max\left(\frac{\sqrt{a_2^2 + b_2^2}}{b_2}\right), \tag{4.13}$$

and in this work we define a strongly-barred galaxy as one having $A_2 > 0.3$ (Fragkoudi et al., 2020a).

Fig. 4.2 shows the radial profile of the relative amplitude of the $m = 2$ Fourier component at $z = 0$. The left-hand, middle, and right-hand panels contain results for Au-06, Au-17, and Au-18, respectively. The black, red, and green curves show

[4]Two vertical oscillations for every revolution in the bar frame.

the original halo, the NoR, and the NoRNoQ variant, respectively. The vertical dashed black, red, and green lines show the A_2 radius for the original halo, the NoR, and the NoRNoQ variant, respectively.

As discussed in Section 4.3.1 Au-06NoRNoQ contains a boxy/peanut bulge when seen edge-on; and this type of bulge is tightly connected to the existence of a bar component. Furthermore, Au-17 and Au-18 – which are both strongly barred galaxies – show a significant increase on their strength when the AGN feedback has been completely turned off (i.e. in their NoRNoQ variants). Hence, Fig. 4.2 suggests that the lack of AGN not only can enhance the strength of a bar (as is the case for Au-17 and Au-18) but it can also turn a weakly-barred galaxy (Au-06) into a strongly-barred one (Au-06NoRNoQ)[5].

Moreover, as mentioned by Athanassoula and Misiriotis (2002) there are several methods one can use to estimate the length of the bar. One of them (e.g. Díaz-García et al., 2016; Rosas-Guevara et al., 2020b) uses as bar length proxy the radii of the maximum relative $m = 2$ Fourier component (A_2), which are shown by the vertical dashed lines in Fig. 4.2. As can been seen by this method, all NoRNoQ runs produce shorter bars than their original and NoR counterparts. However, as discussed by Gadotti (2011) larger galaxies contain larger bars. Hence, in order to check the robustness of this conclusion and any potential dependence of bar length on disc scale length or morphology (Athanassoula and Martinet, 1980; Elmegreen and Elmegreen, 1985; Martin, 1995), in Section 4.3.5 we provide an additional estimate of the bar length (based on photometric decomposition) where we normalise it by the galaxy size.

4.3.3 Stellar-halo mass relation

Fig. 4.3 shows the stellar mass as a function of the halo mass at $z = 0$. The former is defined as the sum over all stellar particles within $0.1R_{200}$ and the latter as the sum over all dark matter particles within R_{200}. The circles, triangles, and squares represent Au-06, Au-17, and Au-18, respectively. The black, red, and green colours represent the original halo, the NoR, and the NoRNoQ variant, respectively. The

[5]We note that the non-vanishing $m = 2$ signal as we move away from the centre results from the strong spiral arm features, which are prominent in e.g. all Au-06 runs and Au-18NoR.

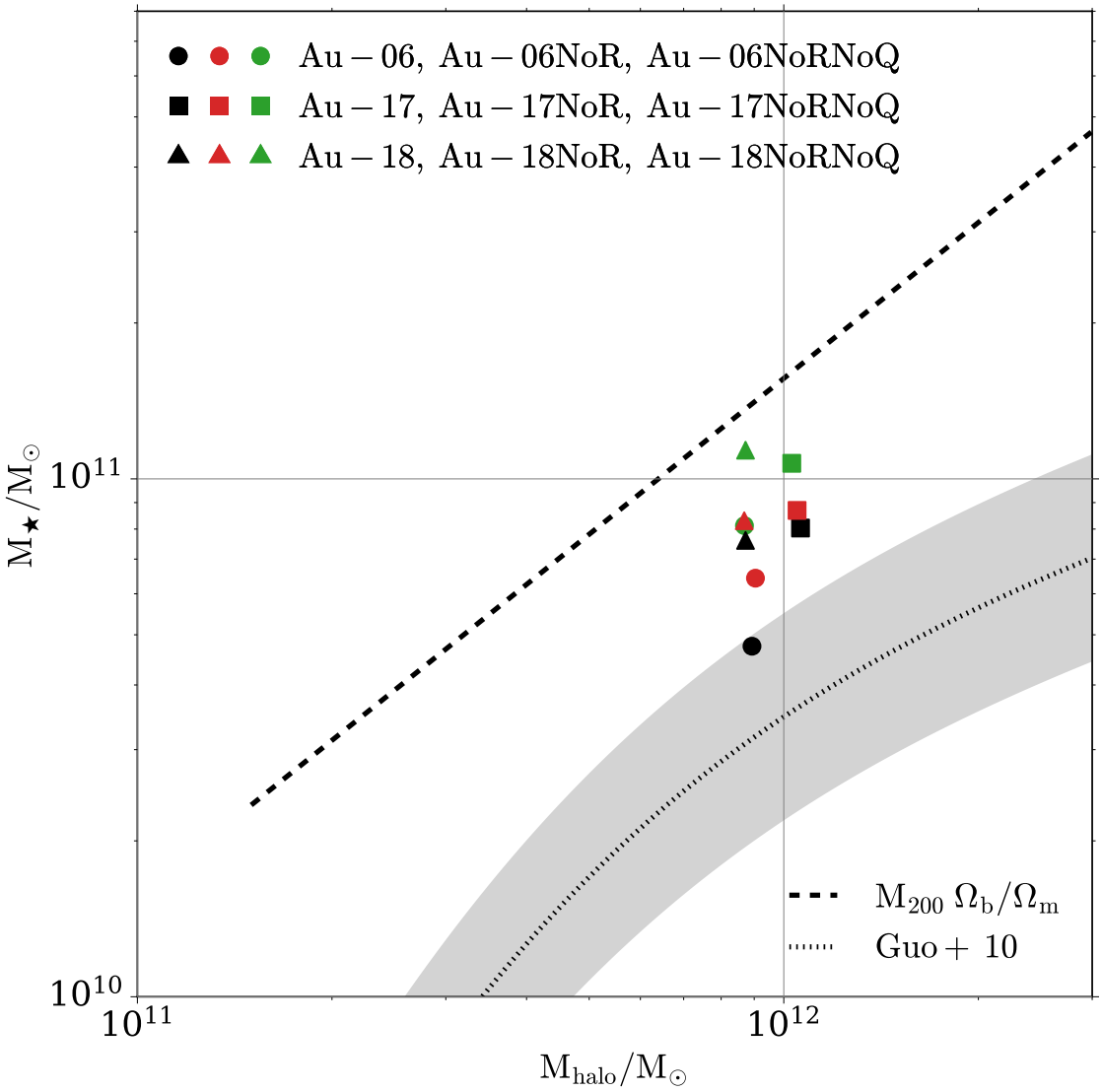

Figure 4.3: Stellar mass as a function of the halo mass at $z = 0$. The former is defined as the sum over all stellar particles within $0.1R_{200}$ and the latter as the sum over all dark matter particles within R_{200}. The circles, triangles, and squares represent Au-06, Au-17, and Au-18, respectively. The black, red, and green colours represent the original halo, the NoR, and the NoRNoQ variant, respectively. The dashed diagonal line shows the baryon conversion efficiency (see the text for more information) and the dotted curve the stellar-halo mass relation from Guo et al. (2010). For all galaxies the NoRNoQ variant has a more massive stellar component than the NoR, which in turn is more massive than the original galaxy.

dashed diagonal line shows the baryon conversion efficiency (Guo et al., 2010; Moster et al., 2013) with $\Omega_{\rm m} = 0.307$ and $\Omega_{\rm b} = 0.048$ (Planck Collaboration et al., 2014b; Grand et al., 2017), and the dotted curve the stellar-halo mass relation from Guo et al. (2010).

There is a clear trend which shows that all original haloes have lower stellar masses than their NoR variants which in turn have lower stellar masses than their NoRNoQ variants. As we discuss in Section 4.4.1.1 such behaviour is expected, since the NoR and NoRNoQ variants have on average higher star formation rates throughout their lifetime, as a consequence of the reduced AGN feedback. This phenomenon is more prominent in the latter variant since the complete lack of AGN feedback allows the gas to cool quicker and form stars more efficiently. Arguably, the NoR and NoRNoQ variants move vertically in the stellar-halo mass plane hence these galaxies end up further away from the abundance matching predictions. It is worth noting that, as has been already reported by Grand et al. (2017) (see their Section 5.3), even the original haloes lie above the abundance matching relation, since the AGN feedback can be insufficient in suppressing early star formation. However, having galaxies more massive than what the abundance matching relation dictates can be beneficial for forming bars with more realistic properties (Fragkoudi et al., 2020c).

Investigating how this additional stellar mass in the NoR and NoRNoQ variants (compared to the original haloes) is distributed in the galaxy is essential in order to understand its dynamical and structural properties. It is well known that massive discs are prone to disc instabilities and bar formation (Efstathiou et al., 1982; Mo et al., 1998; Yurin and Springel, 2015; Irodotou et al., 2019). On the other hand, a substantial central component tends to delay or even suppress bar formation (Athanassoula, 2004, 2013; Kataria and Das, 2019). In order to identify which of the above two mechanisms is the dominant one in our galaxies, we analyse below the distribution of stellar mass (see Section 4.3.4) and calculate the relative contribution of the bar/bulge/disc to the total stellar mass by performing a 2D three component decomposition (see Section 4.3.5).

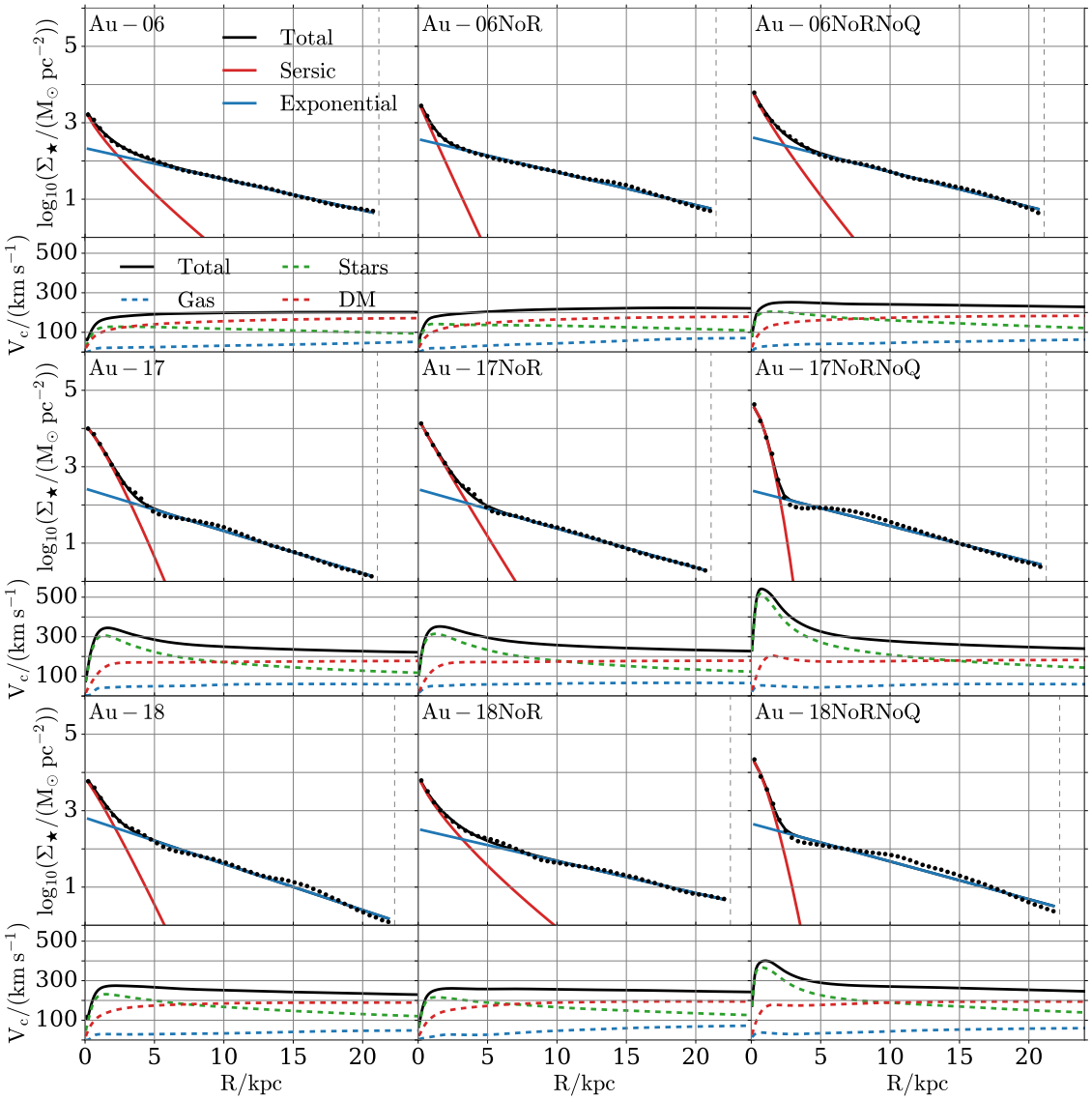

Figure 4.4: Stellar surface density profiles of the face-on projection and circular velocity curves at $z = 0$. The top, middle, and bottom rows contain results for Au-06, Au-17, and Au-18, respectively. The left-hand, middle, and right-hand columns contain results for the original halo, the NoR, and the NoRNoQ variant, respectively. Each row contains a stellar surface density profile (top panel) and a circular velocity curve (bottom panel). The stellar mass is defined as the sum over all stellar particles within $0.1R_{200}$ along the disc plane (vertical dashed grey line) and $\pm$ 5 kpc in the vertical direction. The total fitted profile (black curve) is a combination of a Sersic (red curve) and exponential (blue curve) profile and it was carried out using a non-linear least squares method (Marinacci et al., 2014; Grand et al., 2017). The black, red, green, and blue dashed curves show the total, dark matter, stars, and gas, respectively. NoR and NoRNoQ variants have higher concentration of stellar mass in the central regions compared to their original halo.

Table 4.1: The fitting parameters from Fig. 4.4. The rows represent 1) model names; 2) total stellar mass as defined in Fig. 4.4; 4) Sersic index; 5) effective radius; 6) inferred Sersic mass; 8) scale length; 9) inferred disc mass; 10) disc-to-total stellar mass ratio.

	Au-06	Au-06NoR	Au-06NoRNoQ	Au-17	Au-17NoR	Au-17NoRNoQ	Au-18	Au-18NoR	Au-18NoRNoQ
$M_\star/(10^{10}\ \mathrm{M}_\odot)$	4.57	6.24	7.94	7.38	8.12	11.14	7.77	8.35	10.35
Sersic									
n	1.28	1.02	1.17	0.81	1.05	0.59	0.90	1.35	0.70
$R_{\mathrm{eff.}}/\mathrm{kpc}$	1.74	0.91	1.27	1.16	1.17	0.69	1.15	1.60	0.75
$M_{\mathrm{Sersic}}/(10^{10}\ \mathrm{M}_\odot)$	1.00	0.67	2.24	4.68	5.22	7.53	2.40	3.00	4.36
Exponential									
h/kpc	5.34	5.04	4.78	3.92	4.24	4.68	3.60	5.19	4.39
$M_{\mathrm{d}}/(10^{10}\ \mathrm{M}_\odot)$	3.89	5.95	6.01	2.58	2.89	3.29	5.31	5.58	5.55
D/T	0.80	0.90	0.73	0.36	0.36	0.30	0.70	0.65	0.56

4.3.4 Stellar mass distribution

Fig. 4.4 shows the stellar surface density profiles of the face-on projection and circular velocity curves at $z = 0$. The top, middle, and bottom rows contain results for Au-06, Au-17, and Au-18, respectively. The left-hand, middle, and right-hand columns contain results for the original halo, the NoR, and the NoRNoQ variant, respectively. Each row contains a stellar surface density profile (top panel) and a circular velocity curve (bottom panel). The stellar mass is defined as the sum over all stellar particles within $0.1R_{200}$ along the disc plane (vertical dashed grey line) and ± 5 kpc in the vertical direction. The total fitted profile (black curve) is a combination of a Sersic (red curve) and exponential (blue curve) profile and it was carried out using a non-linear least squares method (Marinacci et al., 2014; Grand et al., 2017). The black, red, green, and blue dashed curves show the total, dark matter, stars, and gas, respectively.

The steepening of the stellar surface density profiles in the very centre as we move from the original to the NoR and NoRNoQ variants indicates the higher concentration of mass in the centre. This is also reflected in the increase of the stellar component's circular velocity in the same variants; while the gas and dark-matter components remain almost unaffected. This behaviour reveals that there is an excess of central mass in these variants which is not present in the original haloes.

The fitting data appearing in Table 4.1 further illustrate this point. As shown in Section 4.3.3, when either the radio mode or both AGN modes are turned off, the resulting galaxy becomes more massive, as expected. This is reflected in the increase of the stellar mass inferred both from the Sersic (sixth row) and the Exponential (ninth row) profiles, respectively. However, the relative contribution of the disc to the total stellar mass (D/T) presented in the last row shows that all NoRNoQ variants' D/T ratios decrease. In other words, their central components (i.e. the ones fitted with a Sersic profile) not only become more massive but also have higher relative contributions to the total stellar mass. At the same time these components also decrease their effective radii. Hence, the lack of AGN feedback results in both more massive and more dense central distributions of mass. A similar conclusion is hard to draw for the NoR runs since they do not seem to have a consistent behaviour (Au-06NoR, Au-17NoR, and Au-18NoR have higher, the same, and lower D/T with

respect to their original haloes).

A few questions that naturally arise are: what dynamical properties do these additional stellar particles have? Are they dynamically hot particles forming a 'classical' bulge or are they part of a bar? It is important to understand what properties these particles have; for that reason in Section 4.3.5 we perform a bar/bulge/disc decomposition and compare the bulge-to-total and bar-to-total ratios between the different runs.

4.3.5 IMFIT decomposition

In this subsection we use IMFIT[6] (Erwin, 2015) to perform a 2D bar/bulge/disc decomposition and quantify the change in the relative contribution of each component between the different variants. Since our intention is to compare the original AURIGA haloes with their NoR and NoRNoQ variants, we use images that accurately represent the mass distribution, not necessarily ones that mimic observations. Therefore, we adopt the following two-step procedure:

(i) Firstly we generate the image and gain a first insight into each galaxy's parameters. In order to do that:

  (i) We rotate all stellar particles such that the bar is along the horizontal axis.

  (ii) We create face-on grey-scaled r-band images.

  (iii) We use a Gaussian filter with FWHM = 2 to blur the images.

  (iv) We use PHOTUTILS (Bradley et al., 2019) to perform isophotal ellipse fitting to the images and estimate the intensity, length, and ellipticity of the bar $(I_0, a_{\rm bar}, ell)$, bulge $(I_{\rm e}, r_{\rm e}, ell)$, and disc (I_0, h, ell) which we provide to IMFIT as an initial set of parameters for the corresponding profiles.

(ii) Then we fit each galaxy with a combinations of following profiles (see Table 4.2):

[6] https://www.mpe.mpg.de/ erwin/code/imfit/

(i) An elliptical 2D exponential function, with the major-axis intensity profile given by

$$I(\alpha) = I_0 \; exp(-\alpha/h) \; , \tag{4.14}$$

where I_0 is the central surface brightness and h is the scale length.

(ii) A 2D analogue of the Ferrers ellipsoid where the intensity profile is given by

$$I(m) = I_0(1 - m^2)^n \; , \tag{4.15}$$

where n controls the sharpness of the truncation and m^2 is defined as

$$m^2 = \left(\frac{|x|}{\alpha}\right)^{c_0+2} \left(\frac{|y|}{b}\right)^{c_0+2} \; , \tag{4.16}$$

where x and y describe the position on the image, α and b are the semi-major and semi-minor axes, respectively, and c_0 defines the shape of the isophotes (zero, negative, and positive values result in pure ellipses, disky, and boxy ellipses, respectively). We note that the intensity is constant on the ellipses and goes to zero outside a specific semi-major axis (sma) value ($a_{\rm bar}$).

(iii) An elliptical 2D Sersic function with the major-axis intensity profile given by

$$I(\alpha) = I_{\rm e} \; exp\left\{-b_{\rm n}\left[\left(\frac{\alpha}{r_{\rm e}}\right)^{1/n} - 1\right]\right\} \; , \tag{4.17}$$

where $I_{\rm e}$ is the surface brightness at the half-light radius ($r_{\rm e}$), n is the Sersic index, and $b_{\rm n}$ is calculated for $n > 0.36$ via the polynomial approximation of Ciotti and Bertin (1999) and the approximation of MacArthur et al. (2003) for $n \leq 0.36$.

The decomposition parameters are presented in Table 4.2 and the corresponding plots in Appendix 4.6. The only galaxy with a prominent round central component (low ellipticity) is Au-06NoR (see Fig. 4.13). Hence, we choose an exponential plus a Sersic profile to accurately model this galaxy. For the remaining galaxies we use an exponential plus one or two Ferrers profiles depending on the model and residual.

Table 4.2: The fitting parameters from IMFIT. The rows represent 1) model names; 3) scale length; 4) disc/total fraction; 6) Sersic index; 7) effective radius; 8) bulge/total fraction; 10) ellipticity; 11) bar length; 12) bar/total fraction. Vertical bar symbols separate the fitting parameters when two Ferrers profiles are used (see the text for more information), while horizontal bar symbols indicate that the corresponding profile was not used in the corresponding galaxy.

	Au-06	Au-06NoR	Au-06NoRNoQ	Au-17	Au-17NoR	Au-17NoRNoQ	Au-18	Au-18NoR	Au-18NoRNoQ
Exponential									
h/kpc	8.20	9.61	9.56	5.36	5.45	5.04	7.03	10.08	7.88
Fraction	0.96	0.98	0.91	0.85	0.81	0.97	0.86	0.94	0.98
Sersic									
n	-	0.79	-	-	-	-	-	-	-
r_e/kpc	-	2.58	-	-	-	-	-	-	-
Fraction	-	0.02	-	-	-	-	-	-	-
FerrersBar2D									
Ellipticity	0.6	-	0.69 | 0.40	0.60 | 0.36	0.69 | 0.40	0.6	0.71 | 0.41	0.69 | 0.7	0.66
$a_{\rm bar}$/kpc	4.69	-	5.83 | 6.41	5.05 | 6.09	5.15 | 5.39	3.63	5.46 | 5.39	3.98 | 7.00	3.98
Fraction	0.04	-	0.02 | 0.07	0.04 | 0.11	0.03 | 0.16	0.03	0.02 | 0.12	0.01 | 0.05	0.02

If there was excess mass around the bar then a second Ferrers profiles with lower ellipticity was added to account for that. This method results in better fits to the ellipticity-sma and intensity-sma plots than a single Ferrers (see bottom leftmost and rightmost panels in each plot in Fig. 4.13, Fig. 4.14, and Fig. 4.15). For these galaxies we quote in the Table 4.2 the values for both Ferrers profiles separated by a vertical bar symbol. In addition, horizontal bar symbols indicate that the corresponding profile was not used in the corresponding galaxy. In general, our results are in agreement with the study of Blázquez-Calero et al. (2020). However, we find systematically larger disc scale lengths due to the different fitting methods followed by each work. Blázquez-Calero et al. (2020) fit all galaxies in their sample with an exponential+Sersic+Ferrers, so the exponential profile in their work was truncating faster since the Sersic profile was reducing its significance.

As already mentioned in Section 4.3.2, Au-06 is a weakly barred galaxy which becomes a strongly barred one when its AGN feedback is absent. This finding is further supported by its 2D decomposition, since we see that Au-06NoRNoQ's bar is longer and has higher contribution to the total compared to Au-06. For Au-17 and Au-18 (which are both strongly barred galaxies) we find that the bar length ($a_{\rm bar}$) of the NoR and NoRNoQ variants is shorter than that of the original haloes when normalised by the corresponding disc scale length (h). In summary, the 2D decompositions support the conclusions drawn so far. When the AGN feedback of our strongly barred galaxies is turned off, they end up having higher central star formation which makes the galaxy more centrally concentrated and the bars stronger and shorter.

4.3.6 AGN effect on the gas

Fig. 4.5 shows the gas temperature as a function of galactocentric distance at $z = 0$ color-coded by the star formation rate of each gas cell (non-star-forming gas cells appear grey). The top, middle, and bottom rows contain results for Au-06, Au-17, and Au-18, respectively. The left-hand, middle, and right-hand columns contain results for the original halo, the NoR, and the NoRNoQ variant, respectively.

The almost complete lack of gas at the very centre ($r/\mathrm{kpc} < 0.4$) of the original haloes is a result of the AGN activity which heats up and expels the cells. On the

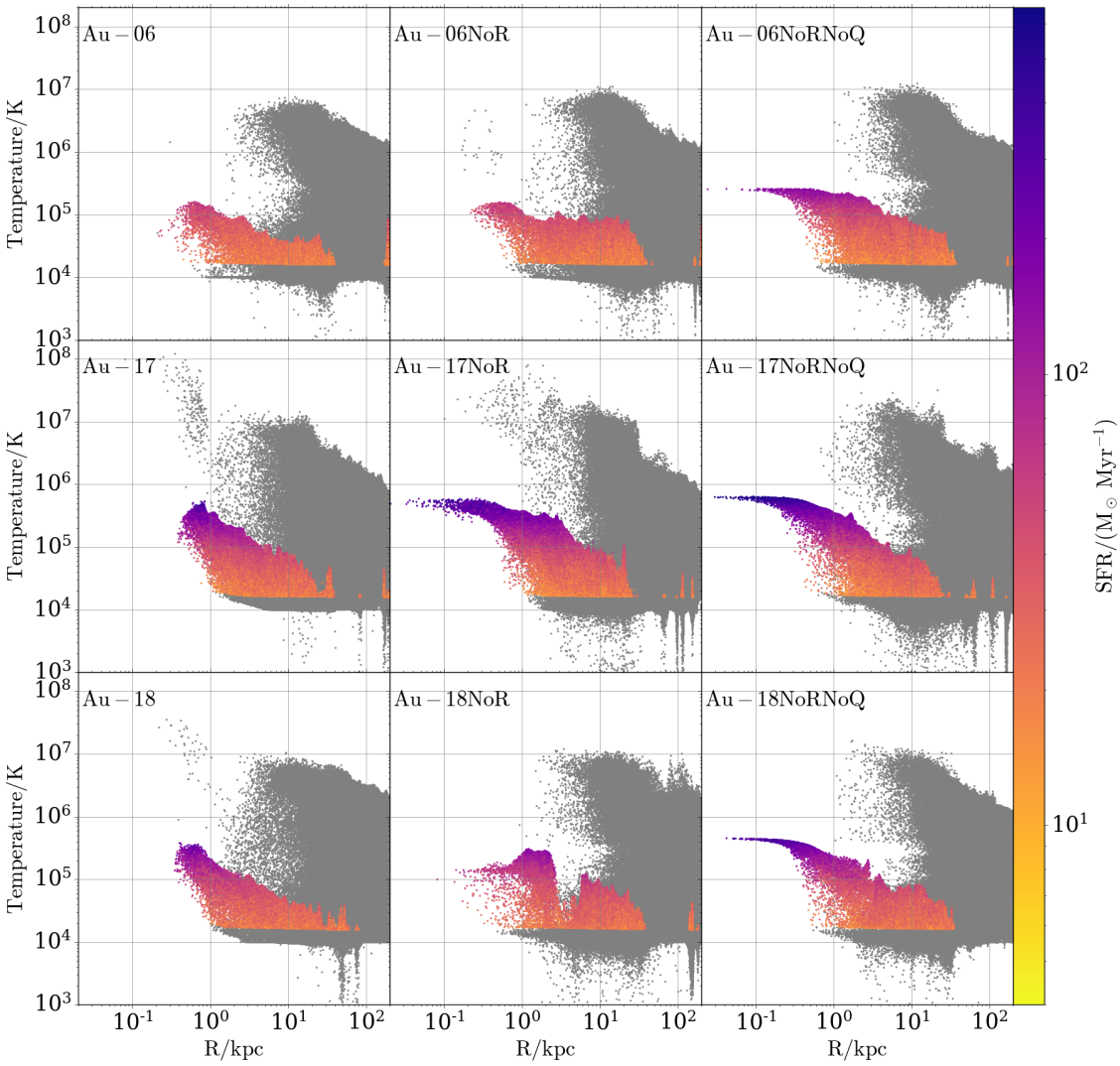

Figure 4.5: Gas temperature as a function of galactocentric distance at $z = 0$ color-coded by the star formation rate of each gas cell (non-star-forming gas cells appear grey). The top, middle, and bottom rows contain results for Au-06, Au-17, and Au-18, respectively. The left-hand, middle, and right-hand columns contain results for the original halo, the NoR, and the NoRNoQ variant, respectively. The AGN feedback expels gas cells and reduces star formation rates in the central regions.

other hand, for all NoR and NoRNoQ variants we see that central gas cells not only exists but in most cases also has a high star formation rate. Hence, the central star formation increases when the AGN feedback is absent (see also Section 4.4.1.1).

Star forming gas cells (Grand et al., 2017) follow an effective equation of state (eEoS) which describes a cell's thermodynamical properties by connecting its pressure to its density (Springel and Hernquist, 2003). A prominent behaviour arises for all NoRNoQ variants (and Au-17NoR) and shows that star forming gas cells' temperatures, which are constrained by the eEoS, form a characteristic horn-like feature. As described in Section 4.2.2 the AGN feedback in the AURIGA simulations has two modes which both inject energy to gas cells. However, this energy will only be absorbed by cells that cool sufficiently slowly, i.e. that are not in the star-forming regime, while cells that are on the eEoS (i.e. have non-zero star forming rates), will not absorb that energy (Weinberger et al., 2018) (see also Section 4.4.1.3).

4.4 Temporal evolution

In the previous section, we explored the present day properties of our galaxies. In this section, we discuss how the quasar (Section 4.4.1) and radio (Section 4.4.2) mode feedback affect the evolution of each variant in order to explains the results we see at $z = 0$.

4.4.1 Quasar mode effects

4.4.1.1 Star formation rate histories

Fig. 4.6 and Fig. 4.7 show the star formation rate histories (top rows) along with the normalised SFR differences between a variant and the original halo (bottom rows) for Au-06, and Au-17 and Au-18, respectively. The left-hand, middle, and right-hand columns contain results inside spherical apertures with radii $0 < r/\mathrm{kpc} \leq 1$, $1 < r/\mathrm{kpc} \leq 5$, and $5 < r/\mathrm{kpc} \leq 15$, respectively. The black, red, and green lines represent the original, the NoR, and the NoRNoQ variant, respectively. The normalised SFR difference is defined as

$$(\delta\mathrm{SFR})_{\mathrm{norm.}} \equiv \frac{\mathrm{SFR}_{\mathrm{original}} - \mathrm{SFR}_{\mathrm{variant}}}{\mathrm{SFR}_{\mathrm{original}}} \,. \tag{4.18}$$

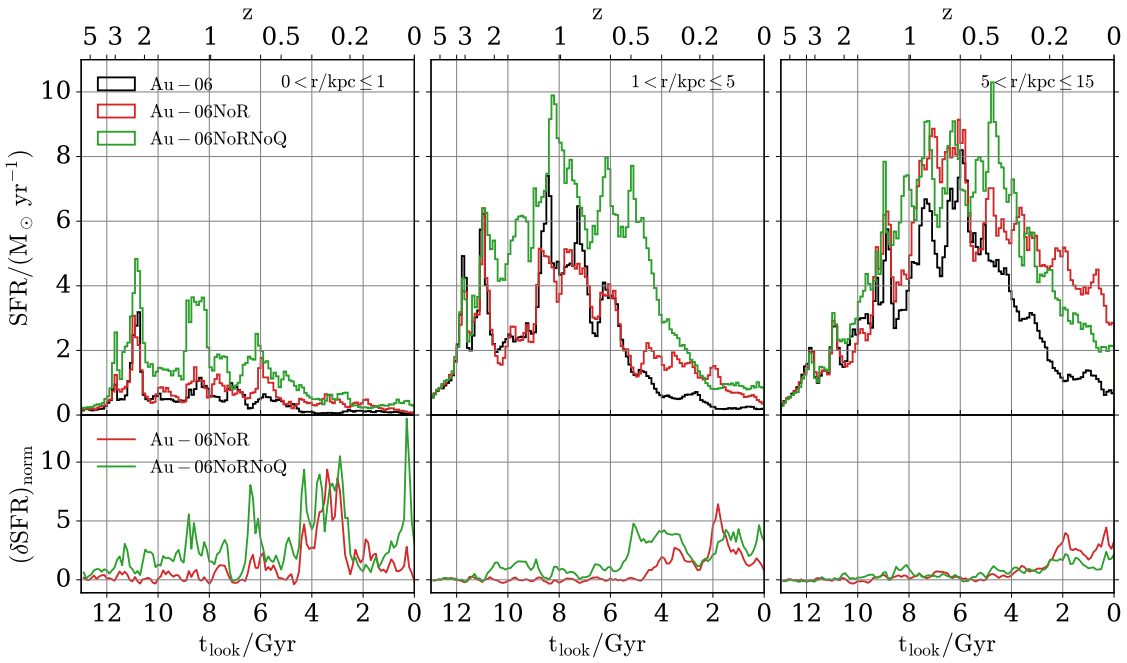

Figure 4.6: Star formation rate histories (top row) along with the normalised SFR difference (see the text for more information) between a variant and the original halo (bottom row) for Au-06. The left-hand, middle, and right-hand columns contain results inside spherical apertures with radii $0 < r/\mathrm{kpc} \leq 1$, $1 < r/\mathrm{kpc} \leq 5$, and $5 < r/\mathrm{kpc} \leq 15$, respectively. The black, red, and green lines represent the original, the NoR, and the NoRNoQ variant, respectively. The AGN feedback suppresses star formation more in the centre than in the disc.

As expected the NoRNoQ variants have on average the highest star-formation rates since the removed AGN feedback allows the gas to cool quicker and form stars more efficiently. This effect is more prominent near the centre ($0 < r/\mathrm{kpc} \leq 1$) for most haloes, which shows that the quasar mode has a significant effect on star formation in the inner regions. Furthermore, the fact that for all haloes and spherical apertures the original halo and the NoR variant follow similar trends while the NoRNoQ variant significantly deviates, suggests that the radio mode has lower impact on the gas than the quasar mode; thus the latter is the dominant (out of the two AGN modes) SF regulator.

4.4.1.2 Bar properties

Fig. 4.8 shows the evolution of the bar strength. The left-hand, middle, and right-hand columns contain results for Au-06, Au-17, and Au-18, respectively. The black, red, and green curves show the original halo, the NoR, and the NoRNoQ variant,

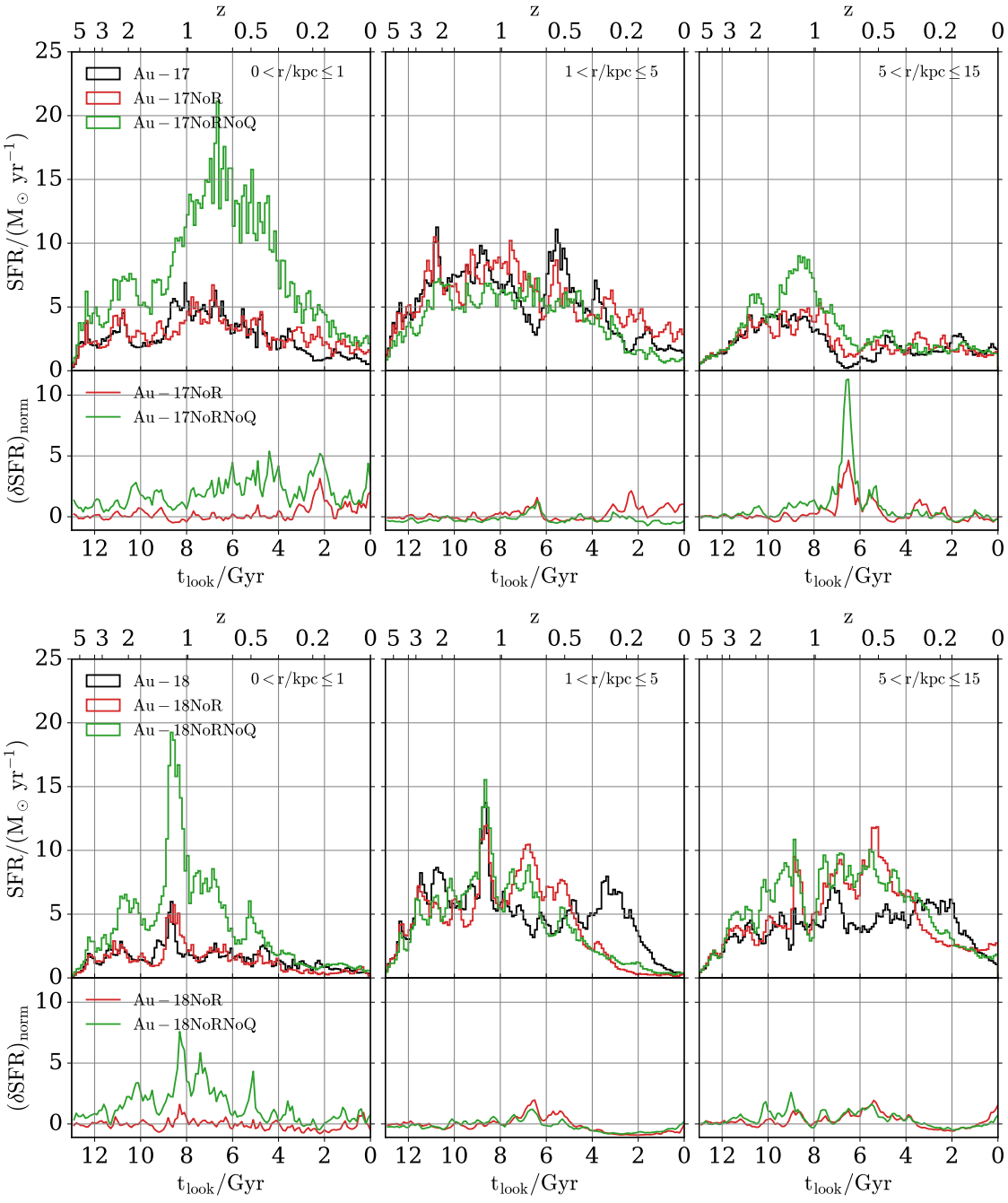

Figure 4.7: Same as Fig. 4.6 but for Au-17 (top plot) and Au-18 (bottom plot).

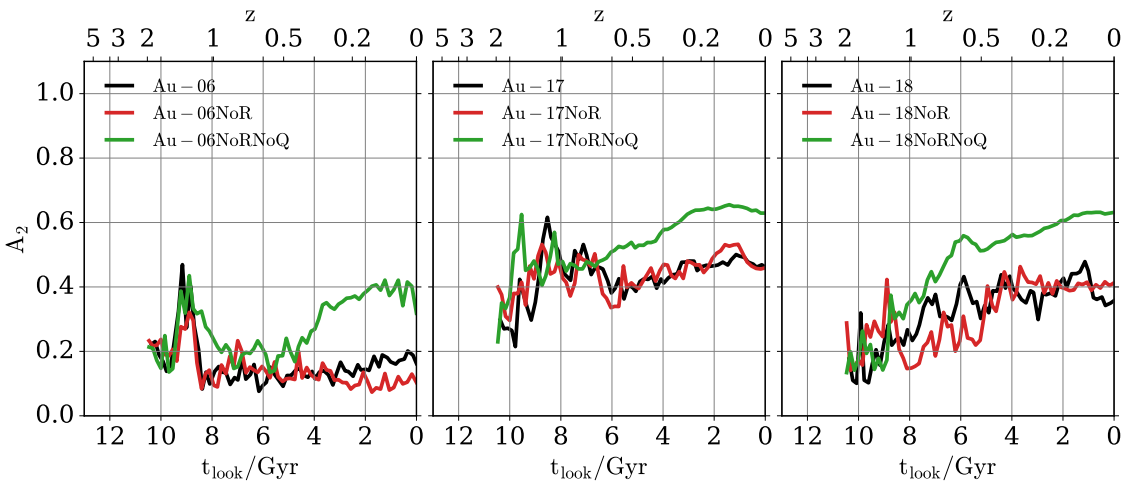

Figure 4.8: Evolution of the bar strength. The left-hand, middle, and right-hand columns contain results for Au-06, Au-17, and Au-18, respectively. The black, red, and green curves show the original halo, the NoR, and the NoRNoQ variant, respectively. All NoRNoQ variants have stronger bars than the original and NoR variants and they develop them earlier.

respectively.

As seen above, all NoR and NoRNoQ variants have on average higher central star formation rates compared to their original haloes. However, the AGN is not the only mechanism that can affect star formation. Multiple studies have analysed the effects of bars on star formation and concluded that (especially strong) bars can have an impact on central star formation (Gavazzi et al., 2015; Fragkoudi et al., 2016; Spinoso et al., 2017; Khoperskov et al., 2018). Bars drive gas towards the centre due to their non-axisymmetric potential which exerts strong torques on the gas (Shlosman et al., 1989; Peeples and Martini, 2006; Cole et al., 2014). As this gas accumulates at the centre it will eventually trigger the formation of stars, and the stronger the bar the more centrally concentrated the star formation (Athanassoula, 1992; Jogee et al., 2005; Wang et al., 2020). This picture is consistent with Fig. 4.8 showing that the NoRNoQ variants develop the strongest bars among our galaxies, and as shown above these variants also have the highest central star formation rates. In addition, we see that all NoRNoQ bars have strengths consistently higher than 0.2 before the corresponding original halo and the NoR variant, hence the NoRNoQ bars not only are stronger but also form earlier.

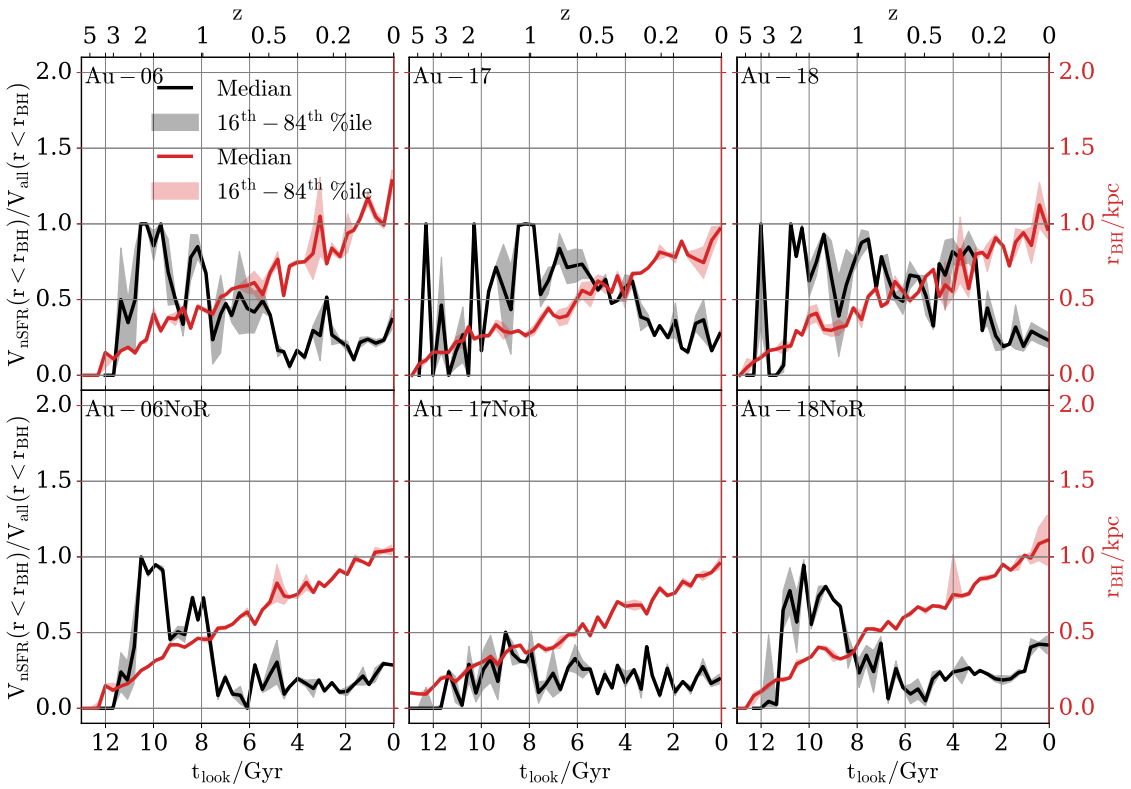

Figure 4.9: Evolution of the ratio between the volume inside the SMBH's sphere of influence (see the text for more information) occupied by all gas cells and that by the non-star-forming ones. The left-hand, middle, and right-hand columns contain results for Au-06, Au-17, and Au-18, respectively. Each column contains on the top and bottom row the original halo and the NoR variant, respectively. The black and red curves and shaded regions show the median and 16th–84th percentile range, respectively. The region around the black hole is populated by more non-star-forming cells when the AGN feedback is present.

4.4.1.3 Energy rate

Fig. 4.9 shows the evolution of the ratio between the volume inside the SMBH's sphere of influence[7] occupied by all gas cells and that by the non-star-forming ones. The left-hand, middle, and right-hand columns contain results for Au-06, Au-17, and Au-18, respectively. Each column contains on the top and bottom row the original halo and the NoR variant, respectively. The black and red curves and shaded regions show the median and 16th–84th percentile range, respectively.

We can see that at various times there is a significant fraction of non-star-forming cells within the black hole's vicinity which allows the quasar mode feedback to be

[7]The radius of the sphere of influence is given by r_{BH} which is the physical radius enclosing the 384 ± 48 nearest gas cells around the black hole.

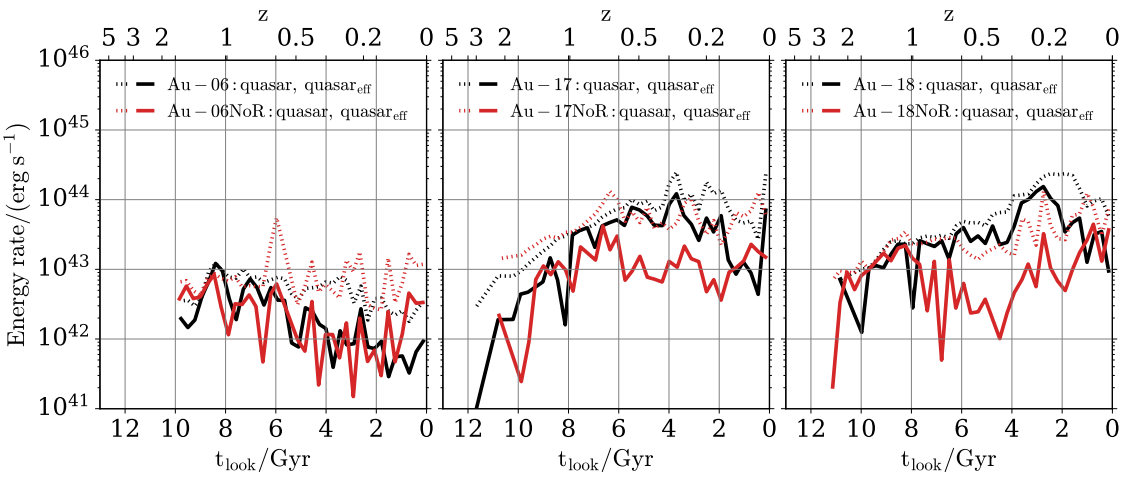

Figure 4.10: Evolution of the quasar mode feedback energy rate. The left-hand, middle, and right-hand columns contain results for Au-06, Au-17, and Au-18, respectively. The black and red curves show results for the original halo and the NoR variant, respectively. The dashed curves show the quasar mode energy and the solid curves show the effective quasar mode energy. For our strongly barred galaxies the quasar mode becomes on average less effective when the radio mode is absent.

effective (i.e. the feedback energy is able to be absorbed). Hence, the ratio between the volume occupied by all gas cells and that by the non-star-forming ones can be used as a proxy to estimate the efficiency of the quasar mode feedback in the AURIGA simulations.

Fig. 4.10 shows the evolution of the quasar mode feedback energy rate. The left-hand, middle, and right-hand columns contain results for Au-06, Au-17, and Au-18, respectively. The black and red curves show results for the original halo and the NoR variant, respectively. The dashed curves show the quasar mode energy and the solid curves show the effective quasar mode energy.

To estimate the efficiency of the quasar mode (i.e. how much of this energy is actually coupled to gas cells and not lost immediately to radiative cooling) we use as a proxy the aforementioned volume ratios. For Au-06 the quasar mode energy rate calculated by the model has an almost flat evolution with time while the effective one decreases for $z < 1$ and becomes roughly an order of magnitude lower than the calculated. This trend holds both for the original halo and the NoR variant. On the other hand, Au-17's and Au-18's quasar mode energy rates increase as we go to lower redshifts and are systematically higher than that of their NoR variants.

Hence, we see that when the radio mode of our strongly barred galaxies is turned off, the quasar mode becomes on average less effective because the volume around the black hole is now occupied more by star forming gas cells (see Fig. 4.9).

In conclusion, we report here that the quasar mode feedback has a significant effect on the gas in the inner regions of Milky Way mass galaxies, contrary to what is commonly found (Somerville and Davé, 2015; Dubois et al., 2016; Rosas-Guevara et al., 2016). Even though it is not capable of fully quenching our galaxies (as it does for massive ETGs, Martig et al., 2009; Rosito et al., 2019), it can impact their morphology and dynamics.

4.4.2 Radio mode effects

4.4.2.1 Gas properties

Fig. 4.11 shows the volume-weighted (top row) and mass-weighted (bottom row) fractional breakdown of gas into different temperature regimes inside the virial radius. In each stacked bar, the blue, green, and red bars represent the cold-to-gas ($T < 2 \times 10^4$ K), warm-to-gas (2×10^4 K $< T < 5 \times 10^5$ K), and hot-to-gas ($T > 5 \times 10^5$ K) ratios, respectively. The height of each bar represents the 1 Gyr time-averaged value of each ratio.

We see that all NoRNoQ variants have lower hot-to-gas mass ratios than the NoR variants while the original haloes have the highest ratios. In addition, the NoRNoQ variants have the highest cold-to-gas volume ratios. These two features reflect the effect of the radio mode feedback on the gas and indicate that the lack of AGN results in cooler haloes. Furthermore, the unexpected decrease in the cold-to-gas mass fractions in some NoR and NoRNoQ variants can be explained by the enhanced star formation rates reported in Fig. 4.6 and Fig. 4.7, which result in more frequent star formation feedback that prevents the gas from cooling.

4.4.2.2 Energy rate

Fig. 4.12 shows the evolution of the radio feedback energy rate. The left-hand, middle, and right-hand columns contain results for Au-06, Au-17, and Au-18, respectively. The black dashed curves shows the radio mode energy calculated by the model.

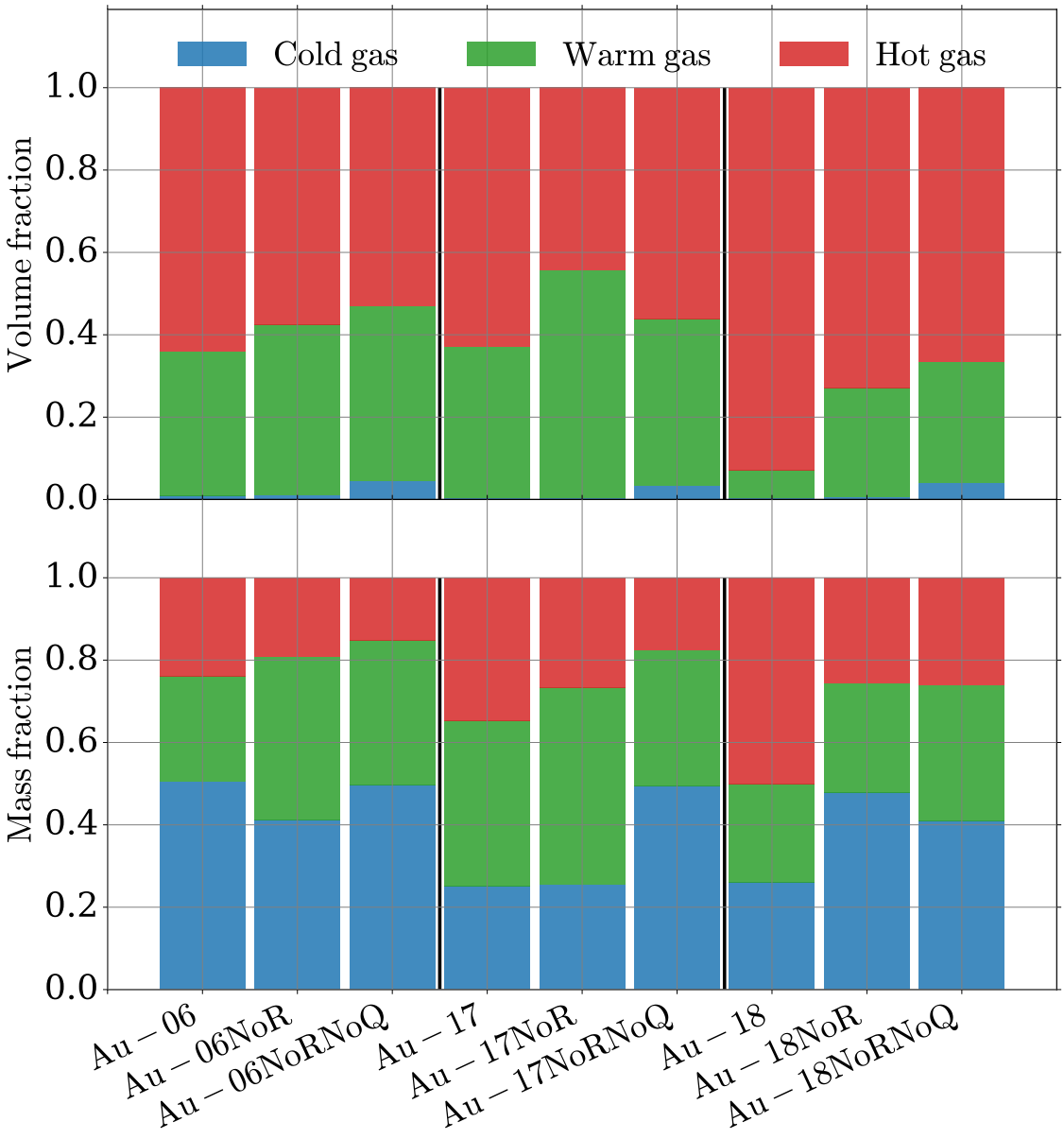

Figure 4.11: Volume-weighted (top row) and mass-weighted (bottom row) fractional breakdown of gas into different temperature regimes inside the virial radius. In each stacked bar, the blue, green, and red bars represent the cold-to-gas ($T < 2 \times 10^4$ K), warm-to-gas (2×10^4 K $< T < 5 \times 10^5$ K), and hot-to-gas ($T > 5 \times 10^5$ K) ratios, respectively. The height of each bar represents the 1 Gyr time-averaged value of each ratio. The lack of AGN feedback reduces the hot-to-gas mass and volume ratios.

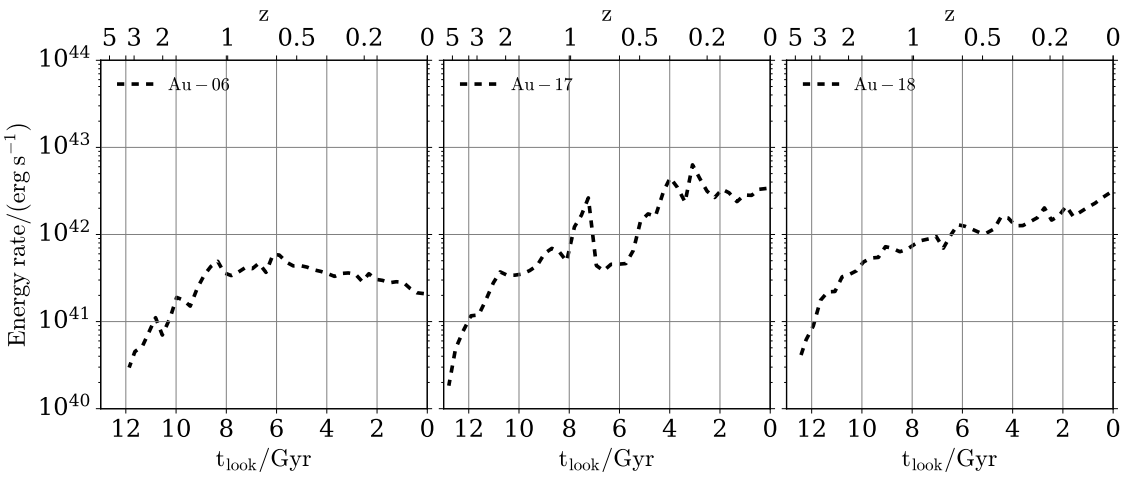

Figure 4.12: Evolution of the radio mode feedback energy rate. The left-hand, middle, and right-hand columns contain results for Au-06, Au-17, and Au-18, respectively. The black dashed curves shows the radio mode energy calculated by the model. The radio mode feedback is responsible for heating up the halo.

We see that Au-06 shows a slightly decreasing trend for $t_{\rm look} < 6$ Gyr. On the other hand, Au-17's and Au-18's radio mode feedback energy rates increase as we go to lower redshifts. In conjunction with the behaviours reported in the previous section (see Fig. 4.11), we argue that the radio mode feedback is responsible for heating up the halo, whilst as discussed in Section 4.4.1.1 the quasar mode mainly affects the star forming gas in the inner disc.

4.5 Conclusions

In this work, we study the impact of the radio and quasar AGN feedback modes on the formation and evolution of barred galaxies. More explicitly, we assess to what extend the Auriga AGN implementation affects the properties of the bar/bulge/disc, and consequently of the galaxy as a whole. For that purpose, we selected three Auriga galaxies - two strongly and one weakly barred - and re-simulated each one with two different AGN feedback variants. Our main conclusions are as follows:

- Different stellar patterns emerge in the central regions of galaxies with different AGN feedback modes. Hence, contrary to what is generally believed, we find that AGN feedback plays a crucial role on the structural and dynamical properties of Milky Way mass galaxies.

- For all galaxies the stellar masses increase as we move from the original haloes to the NoR and NoRNoQ variants. This results from the enhanced star formation rates - especially in the centre - due to the reduced AGN feedback.

- The radio and quasar mode feedback affect the galaxy in different ways. We show that the former heats up the gas in the halo while the latter affects the gas cells in the vicinity of the black hole. Thus, when we turn off the radio mode we find increased star formation in the outer disc and when both modes are absent we see a significant increase in the star formation in the inner regions of the galaxy.

- The radio mode feedback does not have an influential role in the formation and properties of the bar, however it can affect the size of the disc. On the other hand, the quasar mode can have a significant impact on the morphology and dynamical properties of the Auriga galaxies. We find that the NoRNoQ variants develop stronger bars which form earlier than the bars of the original haloes and the NoR variants.

- We conclude that AGN feedback can regulate the structural and dynamical galactic properties both directly (by suppressing central star formation) and indirectly (by heating up the halo). Hence, the way AGN feedback is implemented can play a fundamental role in the properties and morphology of Milky Way mass galaxies.

4.6 2D decompositions

Fig. 4.13, Fig. 4.14, and Fig. 4.15 contain 2D bar/bulge/disc fits for Au-06, Au-17, and Au-18, respectively. In each figure the top, middle, and bottom plot show the original halo, the NoR, and the NoRNoQ variant, respectively. In each plot the top four panels show from left to right the r-band image, model, input/model, and residual produced by Imfit. The bottom four panels show from left to right the ellipticity, position angle, pixel density, and intensity of the r-band image (black) and model (red) as a function of the semi-major axis.

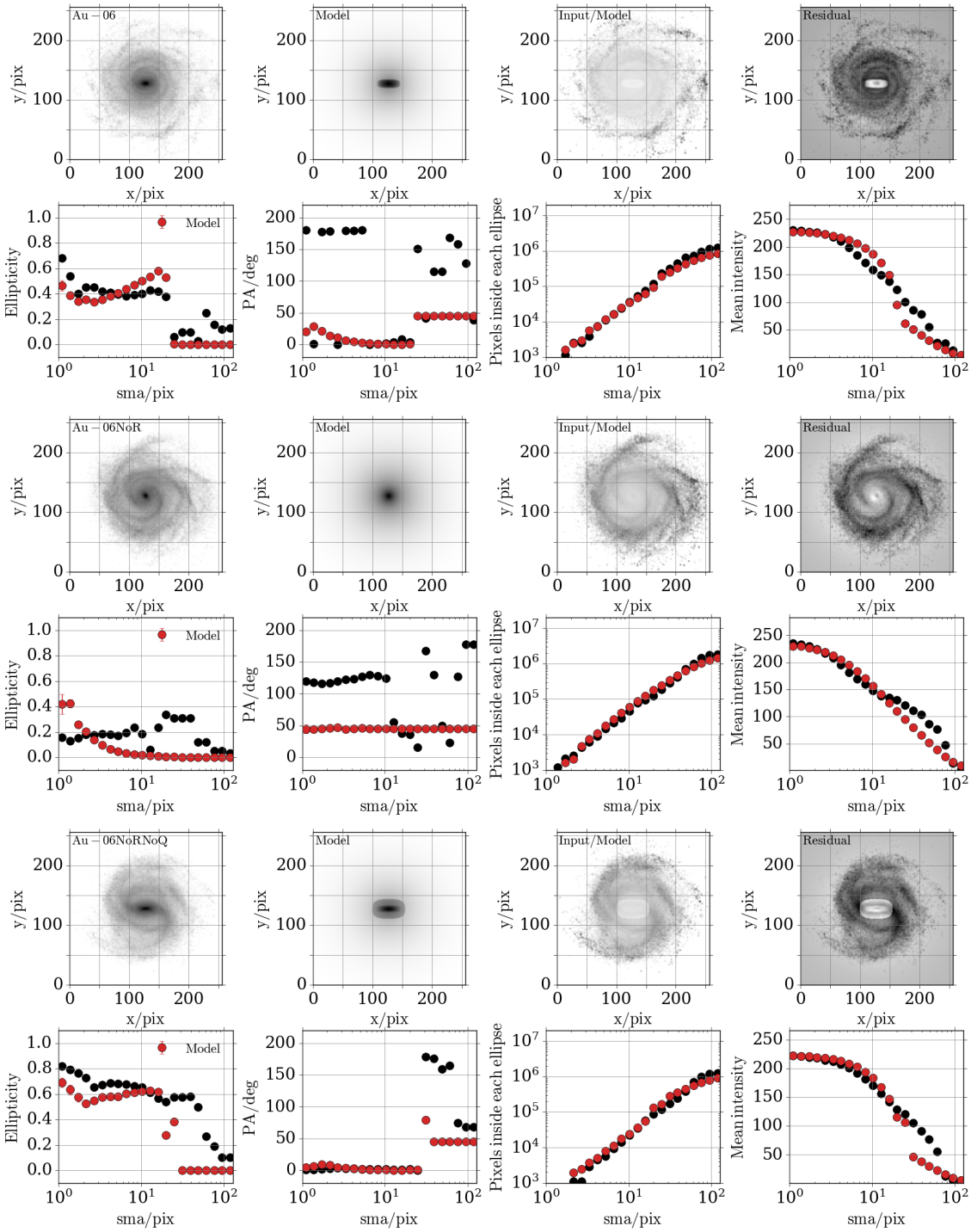

Figure 4.13: 2D bar/bulge/disc decomposition for Au-06. The top, middle, and bottom plot show the original halo, the NoR, and the NoRNoQ variant, respectively. In each plot the top four panels show from left to right the r-band image, model, input/model, and residual produced by Imfit. The bottom four panels show from left to right the ellipticity, position angle, pixel density, and intensity of the r-band image (black) and model (red) as a function of the semi-major axis.

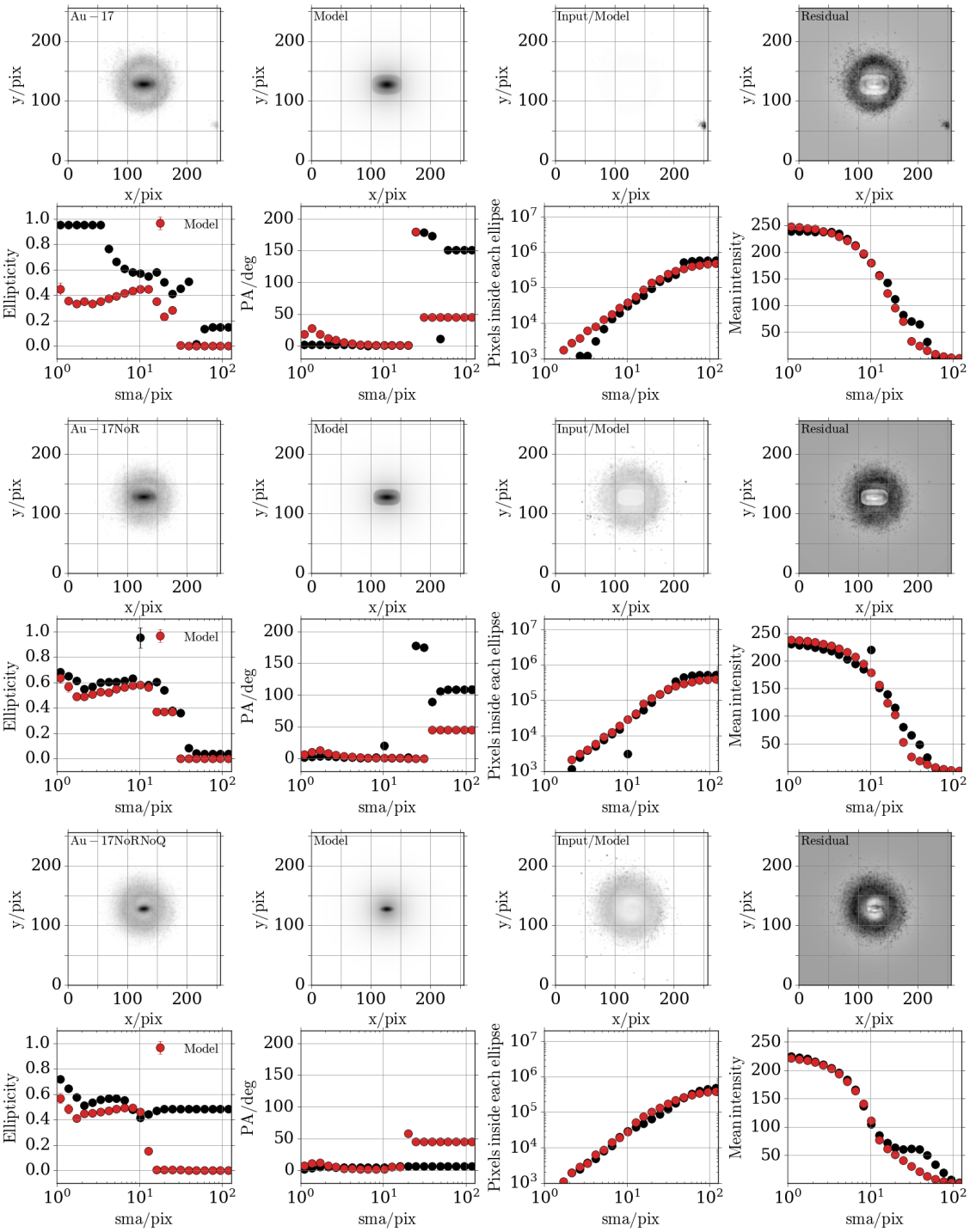

Figure 4.14: Same as Fig. 4.13 but for Au-17.

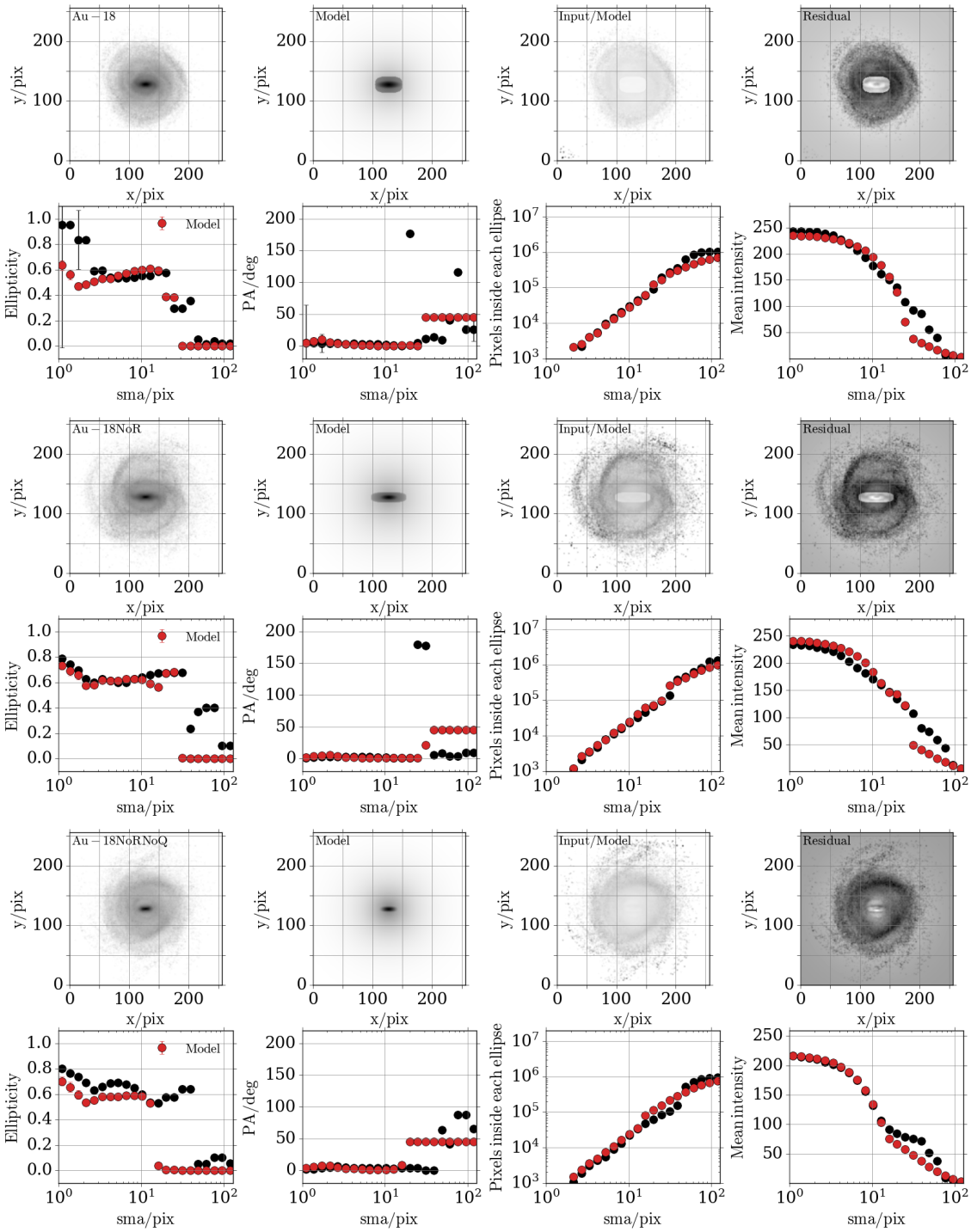

Figure 4.15: Same as Fig. 4.13 but for Au-18.

Chapter 5

Conclusions

5.1 Conclusions

In this thesis, I focus on the characterisation and origin of the morphology of galaxies across multiple scales and epochs. As explained throughout this work, analysing the structural and dynamical properties of galactic components and investigating how they acquired these properties is fundamental in order to understand how galaxies form and evolve. The goal of this thesis is to study this topic by combining observational data with various theoretical tools. Below, I briefly summarise the main achievements.

In Chapter 2, we update the Henriques et al. (2015) version of the L-Galaxies model in order to better follow the formation of bulges (Irodotou et al., 2019). We develop a disc instability method that considers both the gas and the stars, rather than just the latter. The new recipe allows us to be in better agreement than previous work with the observed fraction of different galactic morphologies and the stellar mass functions of different galactic types. Furthermore, we introduce energy dissipation in gas-rich mergers, which results in more compact remnants that match the observed mass-size relation of bulge-dominated galaxies. In addition, due to the reduction of the initial angular momentum of the gas disc, we find that the stellar half-mass radius and specific angular momentum of disc-dominated galaxies is in great agreement with the observed relations.

In Chapter 3, we develop a new method to identify kinematically distinct components by using the information depicted on stellar angular momentum maps

(Irodotou and Thomas, 2021). Our method allows us to extract galactic components and study the imprint each component leaves on the properties of their host galaxy. By comparing with the B/T predictions of other methods we find that even though in general we form tight relations, there are a few cases in which our method provides better classification (e.g. in disc-like galaxies with particles on non-circular orbits or in counter-rotating structures embedded within discs). Our components follow the expected spatial distribution and surface density profiles (i.e. spheroids and discs follow Sersic and exponential profiles, respectively) even though we make no assumptions regarding their spatial extent. Finally, we report that our morphological classification reproduces the observed angular momenta, kinematics, ages, and chemical compositions trends.

In Chapter 4, we study the effect of the radio and quasar AGN feedback modes on the formation and evolution of Milky Way mass galaxies, especially on the properties of their bar, bulge, and disc components. For that purpose, I re-simulated three galaxies - two strongly and one weakly barred - with two different AGN feedback recipes. We find that the Auriga AGN feedback model plays a crucial role on the structural and dynamical properties of barred galaxies, since different stellar structures emerge in the inner disc of the different variants. We show that the total stellar mass increases as we move from the original haloes to the NoR and NoRNoQ variants due to the increased star formation rates which are a consequence of the reduced AGN feedback. More explicitly, the absence of the radio mode results in increased star formation in the outer disc, while when both modes are turned off we see a significant increase in the star formation in the inner regions of the galaxy. Hence, we report that the quasar mode can have a significant impact on the formation and properties of Milky Way mass barred galaxies, since the NoRNoQ variants develop stronger bars which form earlier than the bars of the original haloes and the NoR variants.

5.2 Future work

Below, I summarise a few side projects I worked on during my PhD and I plan on continue working on in the near future, along with new research ideas.

5.2.1 L-Galaxies

As a side project during my PhD, I worked on implementing the disc instability recipe of Irodotou et al. (2019) (see Chapter 2) on the L-Galaxies 2020 SAM (Henriques et al., 2020), as well as on developing a new local instability recipe (Stevens et al., 2016). The L-Galaxies 2020 model resolves the stellar and gaseous discs by splitting them in 12 concentric annuli of fixed radius and width, which allow the migration of stars and gas between them. Hence, in order to study the instability-related formation of pseudo-bulges, a global plus a local (i.e. Toomre Q parameter in each annulus) prescription is needed to calculate the radial migration of stellar and gas clumps.

Furthermore, in collaboration with Rob Yates, I will develop a model to split, apart from the discs, the bulge components in spherical annuli and study the radial gradient of properties in elliptical galaxies and bulges of disc galaxies.

5.2.2 Eagle

The development of the Irodotou and Thomas (2021) decomposition method (see Chapter 3) led to numerous questions regarding the formation of counter-rotating discs in the Eagle simulation. We plan on using the snipshot files, which have smaller time-steps than the snapshots, and create mergers trees in order to link galaxies together and investigate the formation and evolution of counter-rotating particles. This will allow us to identify the processes (i.e. mergers, gas accretion, and/or bar formation) that gave rise to these structures.

In addition, we intend to explore the imprint of pseudo-bulges and bars on the angular momentum maps in order to extend our method and make it able to provide multi-component decompositions.

5.2.3 Flares

In light of the upcoming James Webb Space Telescope, Euclid, and Roman surveys which will observe the formation of the first galaxies, I will lead a project to explore galaxy formation in the most extreme and high-z environments by investigating the effect of intrinsic and environmental processes on structure formation and dynamics.

This study will be carried out as part of the First Light And Reionisation Epoch Simulations (FLARES) project (Lovell et al., 2021) which studies the environmental effect on high-redshift galaxy evolution by performing zoom re-simulations of 40 spherical regions selected from a $(3.2\ \mathrm{cGpc})^3$ dark matter only box at redshift $z \sim 5$. Thus far I co-authored the first two FLARES papers since I got involved in the IC generation process, ran 7 of the regions and provided L-GALAXIES data (Henriques et al., 2015, 2020) which was then used to compare with the evolution of the stellar mass and star formation rate distribution functions predicted by FLARES.

Further Acknowledgements

I thank the developers of Astropy (Astropy Collaboration et al., 2013, 2018), HEALPix/Healpy (Gorski et al., 1999; Górski et al., 2002; Zonca et al., 2019), Matplotlib (Hunter, 2007), NetworkX (Hagberg et al., 2008), NumPy (van der Walt et al., 2011), Pandas (McKinney, 2010), and SciPy (Virtanen et al., 2020).

Part of this work was carried out during the COVID-19 pandemic and would not have been possible without the tireless efforts of the essential workers, who did not have the safety of working from their homes.

This work used the DiRAC@Durham facility managed by the Institute for Computational Cosmology on behalf of the STFC DiRAC HPC Facility (www.dirac.ac.uk). The equipment was funded by BEIS capital funding via STFC capital grants ST/K00042X/1, ST/P002293/1, ST/R002371/1, and ST/S002502/1, Durham University and STFC operations grant ST/R000832/1. DiRAC is part of the National e-Infrastructure.

Data Availability

A Python version of the method introduced in this article can be found at https://github.com/DimitriosIrodotou/Irodotou-Thomas-2021. The EAGLE data is publicly available and accessible at http://icc.dur.ac.uk/Eagle/database.php. The data underlying this article will be shared on reasonable request to the corresponding author.

Bibliography

Abadi, M. G., Navarro, J. F., Steinmetz, M., and Eke, V. R. (2003). Simulations of Galaxy Formation in a Λ Cold Dark Matter Universe. I. Dynamical and Photometric Properties of a Simulated Disk Galaxy. *ApJ*, 591(2):499–514.

Abazajian, K., Adelman-McCarthy, J. K., Agüeros, M. A., Allam, S. S., Anderson, K., Anderson, S. F., Annis, J., Bahcall, N. A., Baldry, I. K., Bastian, S., Berlind, A., Bernardi, M., Blanton, M. R., Bochanski, Jr., J. J., Boroski, W. N., Briggs, J. W., Brinkmann, J., Brunner, R. J., Budavári, T., Carey, L. N., Carliles, S., Castander, F. J., Connolly, A. J., Csabai, I., Doi, M., Dong, F., Eisenstein, D. J., Evans, M. L., Fan, X., Finkbeiner, D. P., Friedman, S. D., Frieman, J. A., Fukugita, M., Gal, R. R., Gillespie, B., Glazebrook, K., Gray, J., Grebel, E. K., Gunn, J. E., Gurbani, V. K., Hall, P. B., Hamabe, M., Harris, F. H., Harris, H. C., Harvanek, M., Heckman, T. M., Hendry, J. S., Hennessy, G. S., Hindsley, R. B., Hogan, C. J., Hogg, D. W., Holmgren, D. J., Ichikawa, S.-i., Ichikawa, T., Ivezić, Ž., Jester, S., Johnston, D. E., Jorgensen, A. M., Kent, S. M., Kleinman, S. J., Knapp, G. R., Kniazev, A. Y., Kron, R. G., Krzesinski, J., Kunszt, P. Z., Kuropatkin, N., Lamb, D. Q., Lampeitl, H., Lee, B. C., Leger, R. F., Li, N., Lin, H., Loh, Y.-S., Long, D. C., Loveday, J., Lupton, R. H., Malik, T., Margon, B., Matsubara, T., McGehee, P. M., McKay, T. A., Meiksin, A., Munn, J. A., Nakajima, R., Nash, T., Neilsen, Jr., E. H., Newberg, H. J., Newman, P. R., Nichol, R. C., Nicinski, T., Nieto-Santisteban, M., Nitta, A., Okamura, S., O'Mullane, W., Ostriker, J. P., Owen, R., Padmanabhan, N., Peoples, J., Pier, J. R., Pope, A. C., Quinn, T. R., Richards, G. T., Richmond, M. W., Rix, H.-W., Rockosi, C. M., Schlegel, D. J., Schneider, D. P., Scranton, R., Sekiguchi, M., Seljak, U., Sergey, G., Sesar, B., Sheldon, E., Shimasaku, K., Siegmund, W. A., Silvestri, N. M., Smith, J. A., Smolčić, V., Snedden, S. A., Stebbins, A., Stoughton, C.,

Strauss, M. A., SubbaRao, M., Szalay, A. S., Szapudi, I., Szkody, P., Szokoly, G. P., Tegmark, M., Teodoro, L., Thakar, A. R., Tremonti, C., Tucker, D. L., Uomoto, A., Vanden Berk, D. E., Vandenberg, J., Vogeley, M. S., Voges, W., Vogt, N. P., Walkowicz, L. M., Wang, S.-i., Weinberg, D. H., West, A. A., White, S. D. M., Wilhite, B. C., Xu, Y., Yanny, B., Yasuda, N., Yip, C.-W., Yocum, D. R., York, D. G., Zehavi, I., Zibetti, S., and Zucker, D. B. (2004). The Second Data Release of the Sloan Digital Sky Survey. *AJ*, 128:502–512.

Adelman-McCarthy, J. K., Agüeros, M. A., Allam, S. S., Anderson, K. S. J., Anderson, S. F., Annis, J., Bahcall, N. A., Bailer-Jones, C. A. L., Baldry, I. K., Barentine, J. C., Beers, T. C., Belokurov, V., Berlind, A., Bernardi, M., Blanton, M. R., Bochanski, J. J., Boroski, W. N., Bramich, D. M., Brewington, H. J., Brinchmann, J., Brinkmann, J., Brunner, R. J., Budavári, T., Carey, L. N., Carliles, S., Carr, M. A., Castander, F. J., Connolly, A. J., Cool, R. J., Cunha, C. E., Csabai, I., Dalcanton, J. J., Doi, M., Eisenstein, D. J., Evans, M. L., Evans, N. W., Fan, X., Finkbeiner, D. P., Friedman, S. D., Frieman, J. A., Fukugita, M., Gillespie, B., Gilmore, G., Glazebrook, K., Gray, J., Grebel, E. K., Gunn, J. E., de Haas, E., Hall, P. B., Harvanek, M., Hawley, S. L., Hayes, J., Heckman, T. M., Hendry, J. S., Hennessy, G. S., Hindsley, R. B., Hirata, C. M., Hogan, C. J., Hogg, D. W., Holtzman, J. A., Ichikawa, S.-i., Ichikawa, T., Ivezić, Ž., Jester, S., Johnston, D. E., Jorgensen, A. M., Jurić, M., Kauffmann, G., Kent, S. M., Kleinman, S. J., Knapp, G. R., Kniazev, A. Y., Kron, R. G., Krzesinski, J., Kuropatkin, N., Lamb, D. Q., Lampeitl, H., Lee, B. C., Leger, R. F., Lima, M., Lin, H., Long, D. C., Loveday, J., Lupton, R. H., Mandelbaum, R., Margon, B., Martínez-Delgado, D., Matsubara, T., McGehee, P. M., McKay, T. A., Meiksin, A., Munn, J. A., Nakajima, R., Nash, T., Neilsen, Jr., E. H., Newberg, H. J., Nichol, R. C., Nieto-Santisteban, M., Nitta, A., Oyaizu, H., Okamura, S., Ostriker, J. P., Padmanabhan, N., Park, C., Peoples, Jr., J., Pier, J. R., Pope, A. C., Pourbaix, D., Quinn, T. R., Raddick, M. J., Re Fiorentin, P., Richards, G. T., Richmond, M. W., Rix, H.-W., Rockosi, C. M., Schlegel, D. J., Schneider, D. P., Scranton, R., Seljak, U., Sheldon, E., Shimasaku, K., Silvestri, N. M., Smith, J. A., Smolčić, V., Snedden, S. A., Stebbins, A., Stoughton, C., Strauss, M. A., SubbaRao, M., Suto, Y., Szalay, A. S., Szapudi, I., Szkody, P., Tegmark, M., Thakar, A. R., Tremonti, C. A., Tucker,

D. L., Uomoto, A., Vanden Berk, D. E., Vandenberg, J., Vidrih, S., Vogeley, M. S., Voges, W., Vogt, N. P., Weinberg, D. H., West, A. A., White, S. D. M., Wilhite, B., Yanny, B., Yocum, D. R., York, D. G., Zehavi, I., Zibetti, S., and Zucker, D. B. (2007). The Fifth Data Release of the Sloan Digital Sky Survey. *ApJS*, 172:634–644.

Agertz, O., Teyssier, R., and Moore, B. (2009). Disc formation and the origin of clumpy galaxies at high redshift. *MNRAS*, 397(1):L64–L68.

Aguerri, J. A. L. (1999). A strong correlation between bar strength and global star forming activity in isolated barred galaxies. *A&A*, 351:43–46.

Aguerri, J. A. L., Balcells, M., and Peletier, R. F. (2001). Growth of galactic bulges by mergers. I. Dense satellites. *A&A*, 367:428–442.

Aguerri, J. A. L., Méndez-Abreu, J., and Corsini, E. M. (2009). The population of barred galaxies in the local universe. I. Detection and characterisation of bars. *A&A*, 495(2):491–504.

Albrecht, A. and Steinhardt, P. J. (1982). Cosmology for Grand Unified Theories with Radiatively Induced Symmetry Breaking. *Phys. Rev. Lett.*, 48(17):1220–1223.

Algorry, D. G., Navarro, J. F., Abadi, M. G., Sales, L. V., Steinmetz, M., and Piontek, F. (2014). Counterrotating stars in simulated galaxy discs. *MNRAS*, 437(4):3596–3602.

Andredakis, Y. C., Peletier, R. F., and Balcells, M. (1995). The Shape of the Luminosity Profiles of Bulges of Spiral Galaxies. *MNRAS*, 275:874.

Andredakis, Y. C. and Sanders, R. H. (1994). Exponential bulges in late-type spirals: an improved description of the light distribution. *MNRAS*, 267:283–296.

Astropy Collaboration, Price-Whelan, A. M., Sipőcz, B. M., Günther, H. M., Lim, P. L., Crawford, S. M., Conseil, S., Shupe, D. L., Craig, M. W., Dencheva, N., Ginsburg, A., Vand erPlas, J. T., Bradley, L. D., Pérez-Suárez, D., de Val-Borro, M., Aldcroft, T. L., Cruz, K. L., Robitaille, T. P., Tollerud, E. J., Ardelean, C.,

Babej, T., Bach, Y. P., Bachetti, M., Bakanov, A. V., Bamford, S. P., Barentsen, G., Barmby, P., Baumbach, A., Berry, K. L., Biscani, F., Boquien, M., Bostroem, K. A., Bouma, L. G., Brammer, G. B., Bray, E. M., Breytenbach, H., Buddelmeijer, H., Burke, D. J., Calderone, G., Cano Rodríguez, J. L., Cara, M., Cardoso, J. V. M., Cheedella, S., Copin, Y., Corrales, L., Crichton, D., D'Avella, D., Deil, C., Depagne, É., Dietrich, J. P., Donath, A., Droettboom, M., Earl, N., Erben, T., Fabbro, S., Ferreira, L. A., Finethy, T., Fox, R. T., Garrison, L. H., Gibbons, S. L. J., Goldstein, D. A., Gommers, R., Greco, J. P., Greenfield, P., Groener, A. M., Grollier, F., Hagen, A., Hirst, P., Homeier, D., Horton, A. J., Hosseinzadeh, G., Hu, L., Hunkeler, J. S., Ivezić, Ž., Jain, A., Jenness, T., Kanarek, G., Kendrew, S., Kern, N. S., Kerzendorf, W. E., Khvalko, A., King, J., Kirkby, D., Kulkarni, A. M., Kumar, A., Lee, A., Lenz, D., Littlefair, S. P., Ma, Z., Macleod, D. M., Mastropietro, M., McCully, C., Montagnac, S., Morris, B. M., Mueller, M., Mumford, S. J., Muna, D., Murphy, N. A., Nelson, S., Nguyen, G. H., Ninan, J. P., Nöthe, M., Ogaz, S., Oh, S., Parejko, J. K., Parley, N., Pascual, S., Patil, R., Patil, A. A., Plunkett, A. L., Prochaska, J. X., Rastogi, T., Reddy Janga, V., Sabater, J., Sakurikar, P., Seifert, M., Sherbert, L. E., Sherwood-Taylor, H., Shih, A. Y., Sick, J., Silbiger, M. T., Singanamalla, S., Singer, L. P., Sladen, P. H., Sooley, K. A., Sornarajah, S., Streicher, O., Teuben, P., Thomas, S. W., Tremblay, G. R., Turner, J. E. H., Terrón, V., van Kerkwijk, M. H., de la Vega, A., Watkins, L. L., Weaver, B. A., Whitmore, J. B., Woillez, J., Zabalza, V., and Astropy Contributors (2018). The Astropy Project: Building an Open-science Project and Status of the v2.0 Core Package. *AJ*, 156(3):123.

Astropy Collaboration, Robitaille, T. P., Tollerud, E. J., Greenfield, P., Droettboom, M., Bray, E., Aldcroft, T., Davis, M., Ginsburg, A., Price-Whelan, A. M., Kerzendorf, W. E., Conley, A., Crighton, N., Barbary, K., Muna, D., Ferguson, H., Grollier, F., Parikh, M. M., Nair, P. H., Unther, H. M., Deil, C., Woillez, J., Conseil, S., Kramer, R., Turner, J. E. H., Singer, L., Fox, R., Weaver, B. A., Zabalza, V., Edwards, Z. I., Azalee Bostroem, K., Burke, D. J., Casey, A. R., Crawford, S. M., Dencheva, N., Ely, J., Jenness, T., Labrie, K., Lim, P. L., Pierfederici, F., Pontzen, A., Ptak, A., Refsdal, B., Servillat, M., and Streicher, O. (2013). Astropy: A community Python package for astronomy. *A&A*, 558:A33.

Athanassoula, E. (1992). The existence and shapes of dust lanes in galactic bars. *MNRAS*, 259:345–364.

Athanassoula, E. (2003). What determines the strength and the slowdown rate of bars? *MNRAS*, 341(4):1179–1198.

Athanassoula, E. (2004). Bars and the connection between dark and visible matter. In Ryder, S., Pisano, D., Walker, M., and Freeman, K., editors, *Dark Matter in Galaxies*, volume 220 of *IAU Symposium*, page 255.

Athanassoula, E. (2005). On the nature of bulges in general and of box/peanut bulges in particular: input from N-body simulations. *MNRAS*, 358(4):1477–1488.

Athanassoula, E. (2008). Disc instabilities and semi-analytic modelling of galaxy formation. *MNRAS*, 390:L69–L72.

Athanassoula, E. (2013). *Bars and secular evolution in disk galaxies: Theoretical input*, page 305.

Athanassoula, E. (2016). *Boxy/Peanut/X Bulges, Barlenses and the Thick Part of Galactic Bars: What Are They and How Did They Form?*, volume 418, page 391.

Athanassoula, E., Bienayme, O., Martinet, L., and Pfenniger, D. (1983). Orbits as building blocks of a barred galaxy model. *A&A*, 127(2):349–360.

Athanassoula, E., Machado, R. E. G., and Rodionov, S. A. (2013). Bar formation and evolution in disc galaxies with gas and a triaxial halo: morphology, bar strength and halo properties. *MNRAS*, 429(3):1949–1969.

Athanassoula, E. and Martinet, L. (1980). A correlation between the lengths of bars and the sizes of bulges. *A&A*, 87(3):L10.

Athanassoula, E. and Misiriotis, A. (2002). Morphology, photometry and kinematics of N -body bars - I. Three models with different halo central concentrations. *MNRAS*, 330(1):35–52.

Aumer, M., White, S. D. M., and Naab, T. (2014). The diverse formation histories of simulated disc galaxies. *MNRAS*, 441(4):3679–3695.

Avila-Reese, V., Zavala, J., Firmani, C., and Hernández-Toledo, H. M. (2008). On the Baryonic, Stellar, and Luminous Scaling Relations of Disk Galaxies. *AJ*, 136:1340–1360.

Baldry, I. K., Driver, S. P., Loveday, J., Taylor, E. N., Kelvin, L. S., Liske, J., Norberg, P., Robotham, A. S. G., Brough, S., Hopkins, A. M., Bamford, S. P., Peacock, J. A., Bland-Hawthorn, J., Conselice, C. J., Croom, S. M., Jones, D. H., Parkinson, H. R., Popescu, C. C., Prescott, M., Sharp, R. G., and Tuffs, R. J. (2012). Galaxy And Mass Assembly (GAMA): the galaxy stellar mass function at z $<$ 0.06. *MNRAS*, 421:621–634.

Baldry, I. K., Glazebrook, K., Brinkmann, J., Ivezić, Ž., Lupton, R. H., Nichol, R. C., and Szalay, A. S. (2004). Quantifying the Bimodal Color-Magnitude Distribution of Galaxies. *ApJ*, 600:681–694.

Bamford, S. P., Nichol, R. C., Baldry, I. K., Land, K., Lintott, C. J., Schawinski, K., Slosar, A., Szalay, A. S., Thomas, D., Torki, M., Andreescu, D., Edmondson, E. M., Miller, C. J., Murray, P., Raddick, M. J., and Vandenberg, J. (2009). Galaxy Zoo: the dependence of morphology and colour on environment*. *MNRAS*, 393:1324–1352.

Barber, C., Schaye, J., Bower, R. G., Crain, R. A., Schaller, M., and Theuns, T. (2016). The origin of compact galaxies with anomalously high black hole masses. *MNRAS*, 460(1):1147–1161.

Barnes, J. and Efstathiou, G. (1987). Angular momentum from tidal torques. *ApJ*, 319:575–600.

Barnes, J. and Hut, P. (1986). A hierarchical O(N log N) force-calculation algorithm. *Nature*, 324(6096):446–449.

Barnes, J. E. and Hernquist, L. (1996). Transformations of Galaxies. II. Gasdynamics in Merging Disk Galaxies. *ApJ*, 471:115.

Barway, S., Saha, K., Vaghmare, K., and Kembhavi, A. K. (2016). Which bulges are favoured by barred S0 galaxies? *MNRAS*, 463:L41–L45.

Baugh, C. M., Cole, S., and Frenk, C. S. (1996). Evolution of the Hubble sequence in hierarchical models for galaxy formation. *MNRAS*, 283:1361–1378.

Begelman, M. C. (2004). AGN Feedback Mechanisms. In Ho, L. C., editor, *Coevolution of Black Holes and Galaxies*, page 374.

Begum, A., Chengalur, J. N., Karachentsev, I. D., and Sharina, M. E. (2008). Baryonic Tully-Fisher relation for extremely low mass Galaxies. *MNRAS*, 386:138–144.

Beifiori, A., Courteau, S., Corsini, E. M., and Zhu, Y. (2012). On the correlations between galaxy properties and supermassive black hole mass. *MNRAS*, 419(3):2497–2528.

Bell, E. F., Phleps, S., Somerville, R. S., Wolf, C., Borch, A., and Meisenheimer, K. (2006). The Merger Rate of Massive Galaxies. *ApJ*, 652:270–276.

Bell, E. F., Wolf, C., Meisenheimer, K., Rix, H.-W., Borch, A., Dye, S., Kleinheinrich, M., Wisotzki, L., and McIntosh, D. H. (2004). Nearly 5000 Distant Early-Type Galaxies in COMBO-17: A Red Sequence and Its Evolution since z˜1. *ApJ*, 608:752–767.

Bender, R. (1988). Rotating and counter-rotating cores in elliptical galaxies. *A&A*, 202:L5–L8.

Bentz, M. C. and Manne-Nicholas, E. (2018). Black Hole-Galaxy Scaling Relationships for Active Galactic Nuclei with Reverberation Masses. *ApJ*, 864(2):146.

Bertin, G. and Romeo, A. B. (1988). Global spiral modes in stellar disks containing gas. *A&A*, 195:105–113.

Bertola, F. and Capaccioli, M. (1975). Dynamics of early type galaxies. I. The rotation curve of the elliptical galaxy NGC 4697. *ApJ*, 200:439–445.

Bertone, S., De Lucia, G., and Thomas, P. A. (2007). The recycling of gas and metals in galaxy formation: predictions of a dynamical feedback model. *MNRAS*, 379:1143–1154.

Binney, J. and Tremaine, S. (2008). *Galactic Dynamics: Second Edition.*

Blanton, M. R., Schlegel, D. J., Strauss, M. A., Brinkmann, J., Finkbeiner, D., Fukugita, M., Gunn, J. E., Hogg, D. W., Ivezić, Ž., Knapp, G. R., Lupton, R. H., Munn, J. A., Schneider, D. P., Tegmark, M., and Zehavi, I. (2005). New York University Value-Added Galaxy Catalog: A Galaxy Catalog Based on New Public Surveys. *AJ*, 129:2562–2578.

Blázquez-Calero, G., Florido, E., Pérez, I., Zurita, A., Grand, R. J. J., Fragkoudi, F., Gómez, F. A., Marinacci, F., and Pakmor, R. (2020). Structural and photometric properties of barred galaxies from the Auriga cosmological simulations. *MNRAS*, 491(2):1800–1819.

Blumenthal, G. R., Faber, S. M., Primack, J. R., and Rees, M. J. (1984). Formation of galaxies and large-scale structure with cold dark matter. *Nature*, 311:517–525.

Bode, P., Ostriker, J. P., and Xu, G. (2000). The Tree Particle-Mesh N-Body Gravity Solver. *ApJS*, 128(2):561–569.

Bondi, H. (1952). On spherically symmetrical accretion. *MNRAS*, 112:195.

Bondi, H. and Hoyle, F. (1944). On the mechanism of accretion by stars. *MNRAS*, 104:273.

Bonoli, S., Mayer, L., Kazantzidis, S., Madau, P., Bellovary, J., and Governato, F. (2016). Black hole starvation and bulge evolution in a Milky Way-like galaxy. *MNRAS*, 459(3):2603–2617.

Booth, C. M. and Schaye, J. (2009). Cosmological simulations of the growth of supermassive black holes and feedback from active galactic nuclei: method and tests. *MNRAS*, 398(1):53–74.

Bothun, G. D. and Gregg, M. D. (1990). The Mean Ages of S0 Disks: Evidence for Star Formation 5 Gigayears Ago. *ApJ*, 350:73.

Bournaud, F. and Combes, F. (2002). Gas accretion on spiral galaxies: Bar formation and renewal. *A&A*, 392:83–102.

Bournaud, F., Jog, C. J., and Combes, F. (2007). Multiple minor mergers: formation of elliptical galaxies and constraints for the growth of spiral disks. *A&A*, 476:1179–1190.

Bower, R. G., Benson, A. J., Malbon, R., Helly, J. C., Frenk, C. S., Baugh, C. M., Cole, S., and Lacey, C. G. (2006). Breaking the hierarchy of galaxy formation. *MNRAS*, 370:645–655.

Boylan-Kolchin, M., Ma, C.-P., and Quataert, E. (2005). Dissipationless mergers of elliptical galaxies and the evolution of the fundamental plane. *MNRAS*, 362(1):184–196.

Bradley, L., Sipocz, B., Robitaille, T., Tollerud, E., Vinícius, Z., Deil, C., Barbary, K., Günther, H. M., Cara, M., Busko, I., Conseil, S., Droettboom, M., Bostroem, A., Bray, E. M., Andersen Bratholm, L., Wilson, T., Craig, M., Barentsen, G., Pascual, S., Donath, A., Greco, J., Perren, G., Lim, P. L., and Kerzendorf, W. (2019). astropy/photutils: v0.6.

Breda, I., Papaderos, P., and Gomes, J.-M. (2020). Indications of the invalidity of the exponentiality of the disk within bulges of spiral galaxies. *A&A*, 640:A20.

Brodie, J. P., Romanowsky, A. J., Strader, J., Forbes, D. A., Foster, C., Jennings, Z. G., Pastorello, N., Pota, V., Usher, C., Blom, C., Kader, J., Roediger, J. C., Spitler, L. R., Villaume, A., Arnold, J. A., Kartha, S. S., and Woodley, K. A. (2014). The SAGES Legacy Unifying Globulars and GalaxieS Survey (SLUGGS): Sample Definition, Methods, and Initial Results. *ApJ*, 796:52.

Brooks, A. and Christensen, C. (2016). *Bulge Formation via Mergers in Cosmological Simulations*, volume 418, page 317.

Bundy, K., Bershady, M. A., Law, D. R., Yan, R., Drory, N., MacDonald, N., Wake, D. A., Cherinka, B., Sánchez-Gallego, J. R., Weijmans, A.-M., Thomas, D., Tremonti, C., Masters, K., Coccato, L., Diamond-Stanic, A. M., Aragón-Salamanca, A., Avila-Reese, V., Badenes, C., Falcón-Barroso, J., Belfiore, F., Bizyaev, D., Blanc, G. A., Bland-Hawthorn, J., Blanton, M. R., Brownstein, J. R., Byler, N., Cappellari, M., Conroy, C., Dutton, A. A., Emsellem, E., Etherington, J., Frinchaboy, P. M., Fu, H., Gunn, J. E., Harding, P., Johnston, E. J., Kauffmann, G., Kinemuchi, K., Klaene, M. A., Knapen, J. H., Leauthaud, A., Li, C., Lin, L., Maiolino, R., Malanushenko, V., Malanushenko, E., Mao, S., Maraston, C., McDermid, R. M., Merrifield, M. R., Nichol, R. C., Oravetz, D., Pan,

K., Parejko, J. K., Sanchez, S. F., Schlegel, D., Simmons, A., Steele, O., Steinmetz, M., Thanjavur, K., Thompson, B. A., Tinker, J. L., van den Bosch, R. C. E., Westfall, K. B., Wilkinson, D., Wright, S., Xiao, T., and Zhang, K. (2015). Overview of the SDSS-IV MaNGA Survey: Mapping nearby Galaxies at Apache Point Observatory. *ApJ*, 798(1):7.

Burbidge, E. M. and Burbidge, G. R. (1959). Three Unusual so Galaxies. *ApJ*, 130:20.

Bureau, M., Aronica, G., Athanassoula, E., Dettmar, R. J., Bosma, A., and Freeman, K. C. (2006). K-band observations of boxy bulges - I. Morphology and surface brightness profiles. *MNRAS*, 370(2):753–772.

Cappellari, M., Emsellem, E., Krajnović, D., McDermid, R. M., Scott, N., Verdoes Kleijn, G. A., Young, L. M., Alatalo, K., Bacon, R., Blitz, L., Bois, M., Bournaud, F., Bureau, M., Davies, R. L., Davis, T. A., de Zeeuw, P. T., Duc, P.-A., Khochfar, S., Kuntschner, H., Lablanche, P.-Y., Morganti, R., Naab, T., Oosterloo, T., Sarzi, M., Serra, P., and Weijmans, A.-M. (2011a). The ATLAS^{3D} project - I. A volume-limited sample of 260 nearby early-type galaxies: science goals and selection criteria. *MNRAS*, 413:813–836.

Cappellari, M., Emsellem, E., Krajnović, D., McDermid, R. M., Serra, P., Alatalo, K., Blitz, L., Bois, M., Bournaud, F., Bureau, M., Davies, R. L., Davis, T. A., de Zeeuw, P. T., Khochfar, S., Kuntschner, H., Lablanche, P.-Y., Morganti, R., Naab, T., Oosterloo, T., Sarzi, M., Scott, N., Weijmans, A.-M., and Young, L. M. (2011b). The ATLAS^{3D} project - VII. A new look at the morphology of nearby galaxies: the kinematic morphology-density relation. *MNRAS*, 416(3):1680–1696.

Cappellari, M., McDermid, R. M., Alatalo, K., Blitz, L., Bois, M., Bournaud, F., Bureau, M., Crocker, A. F., Davies, R. L., Davis, T. A., de Zeeuw, P. T., Duc, P.-A., Emsellem, E., Khochfar, S., Krajnović, D., Kuntschner, H., Morganti, R., Naab, T., Oosterloo, T., Sarzi, M., Scott, N., Serra, P., Weijmans, A.-M., and Young, L. M. (2013). The ATLAS^{3D} project - XX. Mass-size and mass-σ distributions of early-type galaxies: bulge fraction drives kinematics, mass-to-light ratio, molecular gas fraction and stellar initial mass function. *MNRAS*, 432:1862–1893.

Carollo, C. M. (1999). The Centers of Early- to Intermediate-Type Spiral Galaxies: A Structural Analysis. *ApJ*, 523:566–574.

Chabrier, G. (2003). Galactic Stellar and Substellar Initial Mass Function. *PASP*, 115(809):763–795.

Chen, C.-W., Côté, P., West, A. A., Peng, E. W., and Ferrarese, L. (2010). Homogeneous UGRIZ Photometry for ACS Virgo Cluster Survey Galaxies: A Non-parametric Analysis from SDSS Imaging. *ApJS*, 191:1–31.

Christodoulou, D. M., Shlosman, I., and Tohline, J. E. (1995). A new criterion for bar-forming instability in rapidly rotating gaseous and stellar systems. 1: Axisymmetric form. *ApJ*, 443:551–562.

Ciambur, B. C. and Graham, A. W. (2016). Quantifying the (X/peanut)-shaped structure in edge-on disc galaxies: length, strength, and nested peanuts. *MNRAS*, 459(2):1276–1292.

Ciotti, L. (1991). Stellar systems following the R1/m luminosity law. *A&A*, 249:99–106.

Ciotti, L. and Bertin, G. (1999). Analytical properties of the $R^{1/m}$ law. *A&A*, 352:447–451.

Clauwens, B., Schaye, J., Franx, M., and Bower, R. G. (2018). The three phases of galaxy formation. *MNRAS*, 478(3):3994–4009.

Coccato, L., Morelli, L., Pizzella, A., Corsini, E. M., Buson, L. M., and Dalla Bontà, E. (2013). Spectroscopic evidence of distinct stellar populations in the counter-rotating stellar disks of NGC 3593 and NGC 4550. *A&A*, 549:A3.

Cole, D. R., Debattista, V. P., Erwin, P., Earp, S. W. F., and Roškar, R. (2014). The formation of stellar nuclear discs in bar-induced gas inflows. *MNRAS*, 445(4):3352–3369.

Cole, S., Aragon-Salamanca, A., Frenk, C. S., Navarro, J. F., and Zepf, S. E. (1994). A Recipe for Galaxy Formation. *MNRAS*, 271:781.

Cole, S. and Lacey, C. (1996). The structure of dark matter haloes in hierarchical clustering models. *MNRAS*, 281:716.

Cole, S., Lacey, C. G., Baugh, C. M., and Frenk, C. S. (2000). Hierarchical galaxy formation. *MNRAS*, 319:168–204.

Combes, F. (2001). Fueling the AGN. In Aretxaga, I., Kunth, D., and Mújica, R., editors, *Advanced Lectures on the Starburst-AGN*, page 223.

Combes, F., Debbasch, F., Friedli, D., and Pfenniger, D. (1990a). Box and peanut shapes generated by stellar bars. *A&A*, 233:82.

Combes, F., Debbasch, F., Friedli, D., and Pfenniger, D. (1990b). Box and peanut shapes generated by stellar bars. *A&A*, 233:82.

Combes, F. and Sanders, R. H. (1981). Formation and properties of persisting stellar bars. *A&A*, 96:164–173.

Conselice, C. J. (2006). The fundamental properties of galaxies and a new galaxy classification system. *MNRAS*, 373:1389–1408.

Conselice, C. J., Blackburne, J. A., and Papovich, C. (2005). The Luminosity, Stellar Mass, and Number Density Evolution of Field Galaxies of Known Morphology from z = 0.5 to 3. *ApJ*, 620:564–583.

Contopoulos, G. and Papayannopoulos, T. (1980). Orbits in weak and strong bars. *A&A*, 92(1-2):33–46.

Cook, M., Evoli, C., Barausse, E., Granato, G. L., and Lapi, A. (2010). Two phase galaxy formation: the gas content of normal galaxies. *MNRAS*, 402:941–955.

Cook, R. H. W., Cortese, L., Catinella, B., and Robotham, A. S. G. (2020). xGASS: The Role of Bulges Along and Across the Local Star-Forming Main Sequence. *arXiv e-prints*, page arXiv:2003.02464.

Cooper, A. P., Parry, O. H., Lowing, B., Cole, S., and Frenk, C. (2015). Formation of in situ stellar haloes in Milky Way-mass galaxies. *MNRAS*, 454(3):3185–3199.

Correa, C. A., Schaye, J., Clauwens, B., Bower, R. G., Crain, R. A., Schaller, M., Theuns, T., and Thob, A. C. R. (2017). The relation between galaxy morphology and colour in the EAGLE simulation. *MNRAS*, 472(1):L45–L49.

Cortese, L., Fogarty, L. M. R., Bekki, K., van de Sand e, J., Couch, W., Catinella, B., Colless, M., Obreschkow, D., Taranu, D., Tescari, E., Barat, D., Bland-Hawthorn, J., Bloom, J., Bryant, J. J., Cluver, M., Croom, S. M., Drinkwater, M. J., d'Eugenio, F., Konstantopoulos, I. S., Lopez-Sanchez, A., Mahajan, S., Scott, N., Tonini, C., Wong, O. I., Allen, J. T., Brough, S., Goodwin, M., Green, A. W., Ho, I. T., Kelvin, L. S., Lawrence, J. S., Lorente, N. P. F., Medling, A. M., Owers, M. S., Richards, S., Sharp, R., and Sweet, S. M. (2016). The SAMI Galaxy Survey: the link between angular momentum and optical morphology. *MNRAS*, 463(1):170–184.

Courteau, S., de Jong, R. S., and Broeils, A. H. (1996). Evidence for Secular Evolution in Late-Type Spirals. *ApJ*, 457:L73.

Covington, M., Dekel, A., Cox, T. J., Jonsson, P., and Primack, J. R. (2008). Predicting the properties of the remnants of dissipative galaxy mergers. *MNRAS*, 384:94–106.

Covington, M. D., Primack, J. R., Porter, L. A., Croton, D. J., Somerville, R. S., and Dekel, A. (2011). The role of dissipation in the scaling relations of cosmological merger remnants. *MNRAS*, 415:3135–3152.

Crain, R. A., McCarthy, I. G., Frenk, C. S., Theuns, T., and Schaye, J. (2010). X-ray coronae in simulations of disc galaxy formation. *MNRAS*, 407(3):1403–1422.

Crain, R. A., Schaye, J., Bower, R. G., Furlong, M., Schaller, M., Theuns, T., Dalla Vecchia, C., Frenk, C. S., McCarthy, I. G., Helly, J. C., Jenkins, A., Rosas-Guevara, Y. M., White, S. D. M., and Trayford, J. W. (2015). The EAGLE simulations of galaxy formation: calibration of subgrid physics and model variations. *MNRAS*, 450(2):1937–1961.

Crain, R. A., Theuns, T., Dalla Vecchia, C., Eke, V. R., Frenk, C. S., Jenkins, A., Kay, S. T., Peacock, J. A., Pearce, F. R., Schaye, J., Springel, V., Thomas,

P. A., White, S. D. M., and Wiersma, R. P. C. (2009). Galaxies-intergalactic medium interaction calculation - I. Galaxy formation as a function of large-scale environment. *MNRAS*, 399(4):1773–1794.

Croom, S. M., Lawrence, J. S., Bland-Hawthorn, J., Bryant, J. J., Fogarty, L., Richards, S., Goodwin, M., Farrell, T., Miziarski, S., Heald, R., Jones, D. H., Lee, S., Colless, M., Brough, S., Hopkins, A. M., Bauer, A. E., Birchall, M. N., Ellis, S., Horton, A., Leon-Saval, S., Lewis, G., López-Sánchez, Á. R., Min, S.-S., Trinh, C., and Trowland, H. (2012). The Sydney-AAO Multi-object Integral field spectrograph. *MNRAS*, 421(1):872–893.

Croton, D. J., Springel, V., White, S. D. M., De Lucia, G., Frenk, C. S., Gao, L., Jenkins, A., Kauffmann, G., Navarro, J. F., and Yoshida, N. (2006). The many lives of active galactic nuclei: cooling flows, black holes and the luminosities and colours of galaxies. *MNRAS*, 365(1):11–28.

Croton, D. J., Stevens, A. R. H., Tonini, C., Garel, T., Bernyk, M., Bibiano, A., Hodkinson, L., Mutch, S. J., Poole, G. B., and Shattow, G. M. (2016). Semi-Analytic Galaxy Evolution (SAGE): Model Calibration and Basic Results. *ApJS*, 222:22.

Dalcanton, J. J., Spergel, D. N., and Summers, F. J. (1997). The Formation of Disk Galaxies. *ApJ*, 482:659–676.

Dalla Vecchia, C. and Schaye, J. (2012). Simulating galactic outflows with thermal supernova feedback. *MNRAS*, 426(1):140–158.

Danovich, M., Dekel, A., Hahn, O., Ceverino, D., and Primack, J. (2015). Four phases of angular-momentum buildup in high-z galaxies: from cosmic-web streams through an extended ring to disc and bulge. *MNRAS*, 449:2087–2111.

Davies, R. L., Efstathiou, G., Fall, S. M., Illingworth, G., and Schechter, P. L. (1983). The kinematic properties of faint elliptical galaxies. *ApJ*, 266:41–57.

Davis, M., Efstathiou, G., Frenk, C. S., and White, S. D. M. (1985). The evolution of large-scale structure in a universe dominated by cold dark matter. *ApJ*, 292:371–394.

De Lucia, G. and Helmi, A. (2008). The Galaxy and its stellar halo: insights on their formation from a hybrid cosmological approach. *MNRAS*, 391:14–31.

De Lucia, G., Kauffmann, G., and White, S. D. M. (2004). Chemical enrichment of the intracluster and intergalactic medium in a hierarchical galaxy formation model. *MNRAS*, 349(3):1101–1116.

De Lucia, G., Springel, V., White, S. D. M., Croton, D., and Kauffmann, G. (2006). The formation history of elliptical galaxies. *MNRAS*, 366:499–509.

de Souza, R. E., Gadotti, D. A., and dos Anjos, S. (2004). BUDDA: A New Two-dimensional Bulge/Disk Decomposition Code for Detailed Structural Analysis of Galaxies. *ApJS*, 153(2):411–427.

de Vaucouleurs, G. (1948). Recherches sur les Nebuleuses Extragalactiques. *Annales d'Astrophysique*, 11:247.

de Vaucouleurs, G. and de Vaucouleurs, A. (1972). Integrated magnitudes and colours of bright galaxies in the UBV system. *Mem. RAS*, 77:1.

Debattista, V. P., Mayer, L., Carollo, C. M., Moore, B., Wadsley, J., and Quinn, T. (2006). The Secular Evolution of Disk Structural Parameters. *ApJ*, 645:209–227.

Deibel, A. T., Valluri, M., and Merritt, D. (2011). The Orbital Structure of Triaxial Galaxies with Figure Rotation. *ApJ*, 728(2):128.

Dekel, A. and Birnboim, Y. (2006). Galaxy bimodality due to cold flows and shock heating. *MNRAS*, 368(1):2–20.

Dekel, A. and Cox, T. J. (2006). The dissipative merger progenitors of elliptical galaxies. *MNRAS*, 370:1445–1453.

del P. Lagos, C., Tobar, R. J., Robotham, A. S. G., Obreschkow, D., Mitchell, P. D., Power, C., and Elahi, P. J. (2018). Shark: introducing an open source, free, and flexible semi-analytic model of galaxy formation. *MNRAS*, 481:3573–3603.

Díaz-García, S., Salo, H., Laurikainen, E., and Herrera-Endoqui, M. (2016). Characterization of galactic bars from 3.6 μm S^{4}G imaging. *A&A*, 587:A160.

Dimauro, P., Huertas-Company, M., Daddi, E., Pérez-González, P. G., Bernardi, M., Barro, G., Buitrago, F., Caro, F., Cattaneo, A., Dominguez-Sánchez, H., Faber, S. r. M., Häußler, B., Kocevski, D. D., Koekemoer, A. M., Koo, D. C., Lee, C. T., Mei, S., Margalef-Bentabol, B., Primack, J., Rodriguez-Puebla, A., Salvato, M., Shankar, F., and Tuccillo, D. (2018). A catalog of polychromatic bulge-disc decompositions of ∼17.600 galaxies in CANDELS. *MNRAS*, 478(4):5410–5426.

Domínguez Sánchez, H., Huertas-Company, M., Bernardi, M., Tuccillo, D., and Fischer, J. L. (2018). Improving galaxy morphologies for SDSS with Deep Learning. *MNRAS*, 476(3):3661–3676.

Driver, S. P., Hill, D. T., Kelvin, L. S., Robotham, A. S. G., Liske, J., Norberg, P., Baldry, I. K., Bamford, S. P., Hopkins, A. M., Loveday, J., Peacock, J. A., Andrae, E., Bland-Hawthorn, J., Brough, S., Brown, M. J. I., Cameron, E., Ching, J. H. Y., Colless, M., Conselice, C. J., Croom, S. M., Cross, N. J. G., de Propris, R., Dye, S., Drinkwater, M. J., Ellis, S., Graham, A. W., Grootes, M. W., Gunawardhana, M., Jones, D. H., van Kampen, E., Maraston, C., Nichol, R. C., Parkinson, H. R., Phillipps, S., Pimbblet, K., Popescu, C. C., Prescott, M., Roseboom, I. G., Sadler, E. M., Sansom, A. E., Sharp, R. G., Smith, D. J. B., Taylor, E., Thomas, D., Tuffs, R. J., Wijesinghe, D., Dunne, L., Frenk, C. S., Jarvis, M. J., Madore, B. F., Meyer, M. J., Seibert, M., Staveley-Smith, L., Sutherland, W. J., and Warren, S. J. (2011). Galaxy and Mass Assembly (GAMA): survey diagnostics and core data release. *MNRAS*, 413:971–995.

Drory, N., MacDonald, N., Bershady, M. A., Bundy, K., Gunn, J., Law, D. R., Smith, M., Stoll, R., Tremonti, C. A., Wake, D. A., Yan, R., Weijmans, A. M., Byler, N., Cherinka, B., Cope, F., Eigenbrot, A., Harding, P., Holder, D., Huehnerhoff, J., Jaehnig, K., Jansen, T. C., Klaene, M., Paat, A. M., Percival, J., and Sayres, C. (2015). The MaNGA Integral Field Unit Fiber Feed System for the Sloan 2.5 m Telescope. *AJ*, 149(2):77.

Du, M., Ho, L. C., Debattista, V. P., Pillepich, A., Nelson, D., Zhao, D., and Hernquist, L. (2020). Kinematic decomposition of IllustrisTNG disk galaxies: morphology and relation with morphological structures. *arXiv e-prints*, page arXiv:2002.04182.

Dubois, Y., Peirani, S., Pichon, C., Devriendt, J., Gavazzi, R., Welker, C., and Volonteri, M. (2016). The HORIZON-AGN simulation: morphological diversity of galaxies promoted by AGN feedback. *MNRAS*, 463(4):3948–3964.

Duckworth, C., Tojeiro, R., and Kraljic, K. (2020). Decoupling the rotation of stars and gas - I. The relationship with morphology and halo spin. *MNRAS*, 492(2):1869–1886.

Dutton, A. A. and van den Bosch, F. C. (2012). The angular momentum of disc galaxies: implications for gas accretion, outflows, and dynamical friction. *MNRAS*, 421(1):608–620.

Efstathiou, G., Lake, G., and Negroponte, J. (1982). The stability and masses of disc galaxies. *MNRAS*, 199:1069–1088.

Eliche-Moral, M. C., Balcells, M., Aguerri, J. A. L., and González-García, A. C. (2006). Growth of galactic bulges by mergers. II. Low-density satellites. *A&A*, 457:91–108.

Eliche-Moral, M. C., González-García, A. C., Balcells, M., Aguerri, J. A. L., Gallego, J., Zamorano, J., and Prieto, M. (2011). A minor merger origin for stellar inner discs and rings in spiral galaxies. *A&A*, 533:A104.

Elmegreen, B. G. (1995). An effective Q parameter for two-fluid instabilities in spiral galaxies. *MNRAS*, 275:944–950.

Elmegreen, B. G. and Elmegreen, D. M. (1985). Properties of barred spiral galaxies. *ApJ*, 288:438–455.

Emsellem, E., Cappellari, M., Krajnović, D., Alatalo, K., Blitz, L., Bois, M., Bournaud, F., Bureau, M., Davies, R. L., Davis, T. A., de Zeeuw, P. T., Khochfar, S., Kuntschner, H., Lablanche, P.-Y., McDermid, R. M., Morganti, R., Naab, T., Oosterloo, T., Sarzi, M., Scott, N., Serra, P., van de Ven, G., Weijmans, A.-M., and Young, L. M. (2011). The ATLAS^{3D} project - III. A census of the stellar angular momentum within the effective radius of early-type galaxies: unveiling the distribution of fast and slow rotators. *MNRAS*, 414(2):888–912.

Emsellem, E., Cappellari, M., Krajnović, D., van de Ven, G., Bacon, R., Bureau, M., Davies, R. L., de Zeeuw, P. T., Falcón-Barroso, J., Kuntschner, H., McDermid, R., Peletier, R. F., and Sarzi, M. (2007). The SAURON project - IX. A kinematic classification for early-type galaxies. *MNRAS*, 379(2):401–417.

Englmaier, P. and Shlosman, I. (2004). Dynamical Decoupling of Nested Bars: Self-gravitating Gaseous Nuclear Bars. *ApJ*, 617:L115–L118.

Epinat, B., Amram, P., and Marcelin, M. (2008a). GHASP: an Hα kinematic survey of 203 spiral and irregular galaxies - VII. Revisiting the analysis of Hα data cubes for 97 galaxies. *MNRAS*, 390:466–504.

Epinat, B., Amram, P., Marcelin, M., Balkowski, C., Daigle, O., Hernandez, O., Chemin, L., Carignan, C., Gach, J.-L., and Balard, P. (2008b). GHASP: an Hα kinematic survey of spiral and irregular galaxies - VI. New Hα data cubes for 108 galaxies. *MNRAS*, 388:500–550.

Erwin, P. (2015). IMFIT: A Fast, Flexible New Program for Astronomical Image Fitting. *ApJ*, 799(2):226.

Erwin, P. (2018). The dependence of bar frequency on galaxy mass, colour, and gas content - and angular resolution - in the local universe. *MNRAS*, 474(4):5372–5392.

Erwin, P. and Debattista, V. P. (2017). The frequency and stellar-mass dependence of boxy/peanut-shaped bulges in barred galaxies. *MNRAS*, 468(2):2058–2080.

Faber, S. M. and Jackson, R. E. (1976). Velocity dispersions and mass-to-light ratios for elliptical galaxies. *ApJ*, 204:668–683.

Fabian, A. C. (2012). Observational Evidence of Active Galactic Nuclei Feedback. *ARA&A*, 50:455–489.

Falcón-Barroso, J., Lyubenova, M., van de Ven, G., Mendez-Abreu, J., Aguerri, J. A. L., García-Lorenzo, B., Bekeraité, S., Sánchez, S. F., Husemann, B., García-Benito, R., Mast, D., Walcher, C. J., Zibetti, S., Barrera-Ballesteros, J. K., Galbany, L., Sánchez-Blázquez, P., Singh, R., van den Bosch, R. C. E., Wild, V.,

Zhu, L., Bland-Hawthorn, J., Cid Fernandes, R., de Lorenzo-Cáceres, A., Gallazzi, A., González Delgado, R. M., Marino, R. A., Márquez, I., Pérez, E., Pérez, I., Roth, M. M., Rosales-Ortega, F. F., Ruiz-Lara, T., Wisotzki, L., Ziegler, B., and Califa Collaboration (2017). Stellar kinematics across the Hubble sequence in the CALIFA survey: general properties and aperture corrections. *A&A*, 597:A48.

Fall, S. M. (1983). Galaxy formation - Some comparisons between theory and observation. In Athanassoula, E., editor, *Internal Kinematics and Dynamics of Galaxies*, volume 100 of *IAU Symposium*, pages 391–398.

Fall, S. M. and Efstathiou, G. (1980). Formation and rotation of disc galaxies with haloes. *MNRAS*, 193:189–206.

Fall, S. M. and Romanowsky, A. J. (2013). Angular Momentum and Galaxy Formation Revisited: Effects of Variable Mass-to-light Ratios. *ApJ*, 769(2):L26.

Fall, S. M. and Romanowsky, A. J. (2018). Angular Momentum and Galaxy Formation Revisited: Scaling Relations for Disks and Bulges. *ApJ*, 868(2):133.

Fanali, R., Dotti, M., Fiacconi, D., and Haardt, F. (2015). Bar formation as driver of gas inflows in isolated disc galaxies. *MNRAS*, 454(4):3641–3652.

Faucher-Giguère, C.-A., Lidz, A., Zaldarriaga, M., and Hernquist, L. (2009a). A New Calculation of the Ionizing Background Spectrum and the Effects of He II Reionization. *ApJ*, 703(2):1416–1443.

Faucher-Giguère, C.-A., Lidz, A., Zaldarriaga, M., and Hernquist, L. (2009b). A New Calculation of the Ionizing Background Spectrum and the Effects of He II Reionization. *ApJ*, 703(2):1416–1443.

Ferland, G. J., Korista, K. T., Verner, D. A., Ferguson, J. W., Kingdon, J. B., and Verner, E. M. (1998). CLOUDY 90: Numerical Simulation of Plasmas and Their Spectra. *PASP*, 110(749):761–778.

Fisher, D. B. (2006). Central Star Formation and PAH Profiles in Pseudobulges and Classical Bulges. *ApJ*, 642:L17–L20.

Fisher, D. B. and Drory, N. (2008). The Structure of Classical Bulges and Pseudobulges: the Link Between Pseudobulges and SÉRSIC Index. *AJ*, 136:773–839.

Fisher, D. B. and Drory, N. (2016). *An Observational Guide to Identifying Pseudobulges and Classical Bulges in Disc Galaxies*, volume 418 of *Astrophysics and Space Science Library*, page 41.

Fisher, D. B., Drory, N., and Fabricius, M. H. (2009). Bulges of Nearby Galaxies with Spitzer: The Growth of Pseudobulges in Disk Galaxies and its Connection to Outer Disks. *ApJ*, 697:630–650.

Forbes, D. A., Sinpetru, L., Savorgnan, G., Romanowsky, A. J., Usher, C., and Brodie, J. (2017). The SLUGGS Survey: stellar masses and effective radii of early-type galaxies from Spitzer Space Telescope 3.6 μm imaging. *MNRAS*, 464:4611–4623.

Forbes, J. C., Krumholz, M. R., Burkert, A., and Dekel, A. (2014). Balance among gravitational instability, star formation and accretion determines the structure and evolution of disc galaxies. *MNRAS*, 438(2):1552–1576.

Fragkoudi, F., Athanassoula, E., and Bosma, A. (2016). A close look at secular evolution: boxy/peanut bulges reduce gas inflow to the central kiloparsec. *MNRAS*, 462(1):L41–L45.

Fragkoudi, F., Athanassoula, E., Bosma, A., and Iannuzzi, F. (2015). The effects of Boxy/Peanut bulges on galaxy models. *MNRAS*, 450:229–245.

Fragkoudi, F., Grand, R. J. J., Pakmor, R., Blázquez-Calero, G., Gargiulo, I., Gomez, F., Marinacci, F., Monachesi, A., Ness, M. K., Perez, I., Tissera, P., and White, S. D. M. (2020a). Chemodynamics of barred galaxies in cosmological simulations: On the Milky Way's quiescent merger history and in-situ bulge. *MNRAS*, 494(4):5936–5960.

Fragkoudi, F., Grand, R. J. J., Pakmor, R., Springel, V., White, S. D. M., Marinacci, F., Gomez, F. A., and Navarro, J. F. (2020b). Fast-rotating bars in the ΛCDM cosmological paradigm. *arXiv e-prints*, page arXiv:2011.13942.

Fragkoudi, F., Grand, R. J. J., Pakmor, R., Springel, V., White, S. D. M., Marinacci, F., Gomez, F. A., and Navarro, J. F. (2020c). Fast-rotating bars in the ΛCDM cosmological paradigm. *arXiv e-prints*, page arXiv:2011.13942.

Friedli, D. and Benz, W. (1995). Secular evolution of isolated barred galaxies. II. Coupling between stars and interstellar medium via star formation. *A&A*, 301:649.

Frigo, M., Naab, T., Hirschmann, M., Choi, E., Somerville, R. S., Krajnovic, D., Davé, R., and Cappellari, M. (2019). The impact of AGN on stellar kinematics and orbits in simulated massive galaxies. *MNRAS*, 489(2):2702–2722.

Fujii, M. S., Bédorf, J., Baba, J., and Portegies Zwart, S. (2018). The dynamics of stellar discs in live dark-matter haloes. *MNRAS*, 477:1451–1471.

Fukugita, M., Nakamura, O., Okamura, S., Yasuda, N., Barentine, J. C., Brinkmann, J., Gunn, J. E., Harvanek, M., Ichikawa, T., Lupton, R. H., Schneider, D. P., Strauss, M. A., and York, D. G. (2007). A Catalog of Morphologically Classified Galaxies from the Sloan Digital Sky Survey: North Equatorial Region. *AJ*, 134:579–593.

Gadotti, D. A. (2009). Structural properties of pseudo-bulges, classical bulges and elliptical galaxies: a Sloan Digital Sky Survey perspective. *MNRAS*, 393(4):1531–1552.

Gadotti, D. A. (2011). Secular evolution and structural properties of stellar bars in galaxies. *MNRAS*, 415(4):3308–3318.

Gadotti, D. A. (2012). Galaxy Bulges and Elliptical Galaxies - Lecture Notes. *arXiv e-prints*, page arXiv:1208.2295.

Gadotti, D. A., Bittner, A., Falcón-Barroso, J., Méndez-Abreu, J., Kim, T., Fragkoudi, F., de Lorenzo-Cáceres, A., Leaman, R., Neumann, J., Querejeta, M., Sánchez-Blázquez, P., Martig, M., Martín-Navarro, I., Pérez, I., Seidel, M. K., and van de Ven, G. (2020). Kinematic signatures of nuclear discs and bar-driven secular evolution in nearby galaxies of the MUSE TIMER project. *A&A*, 643:A14.

Gadotti, D. A. and Kauffmann, G. (2009). The growth of supermassive black holes in pseudo-bulges, classical bulges and elliptical galaxies. *MNRAS*, 399(2):621–627.

Gargiulo, I. D., Cora, S. A., Padilla, N. D., Muñoz Arancibia, A. M., Ruiz, A. N., Orsi, A. A., Tecce, T. E., Weidner, C., and Bruzual, G. (2015). Chemoarchaeological downsizing in a hierarchical universe: impact of a top-heavy IGIMF. *MNRAS*, 446(4):3820–3841.

Gargiulo, I. D., Cora, S. A., Vega-Martínez, C. A., Gonzalez, O. A., Zoccali, M., González, R., Ruiz, A. N., and Padilla, N. D. (2017). Stellar Populations in a semi-analytic model I: Bulges of Milky Way-like galaxies. *MNRAS*, 472:4133–4143.

Gargiulo, I. D., Monachesi, A., Gómez, F. A., Grand, R. J. J., Marinacci, F., Pakmor, R., White, S. D. M., Bell, E. F., Fragkoudi, F., and Tissera, P. (2019). The prevalence of pseudo-bulges in the Auriga simulations. *MNRAS*, 489(4):5742–5763.

Garrison-Kimmel, S., Hopkins, P. F., Wetzel, A., El-Badry, K., Sanderson, R. E., Bullock, J. S., Ma, X., van de Voort, F., Hafen, Z., Faucher-Giguère, C.-A., Hayward, C. C., Quataert, E., Kereš, D., and Boylan-Kolchin, M. (2018). The origin of the diverse morphologies and kinematics of Milky Way-mass galaxies in the FIRE-2 simulations. *MNRAS*, 481(3):4133–4157.

Gavazzi, G., Consolandi, G., Dotti, M., Fanali, R., Fossati, M., Fumagalli, M., Viscardi, E., Savorgnan, G., Boselli, A., Gutiérrez, L., Hernández Toledo, H., Giovanelli, R., and Haynes, M. P. (2015). Hα3: an Hα imaging survey of HI selected galaxies from ALFALFA. VI. The role of bars in quenching star formation from z = 3 to the present epoch. *A&A*, 580:A116.

Gingold, R. A. and Monaghan, J. J. (1977). Smoothed particle hydrodynamics: theory and application to non-spherical stars. *MNRAS*, 181:375–389.

Gnedin, N. Y. (2000). Effect of Reionization on Structure Formation in the Universe. *ApJ*, 542(2):535–541.

Górski, K. M., Banday, A. J., Hivon, E., and Wand elt, B. D. (2002). HEALPix — a Framework for High Resolution, Fast Analysis on the Sphere. In *Astronomical Data Analysis Software and Systems XI*, volume 281 of *Astronomical Society of the Pacific Conference Series*, page 107.

Gorski, K. M., Wandelt, B. D., Hansen, F. K., Hivon, E., and Banday, A. J. (1999). The HEALPix Primer. *arXiv e-prints*, pages astro–ph/9905275.

Governato, F., Brook, C. B., Brooks, A. M., Mayer, L., Willman, B., Jonsson, P., Stilp, A. M., Pope, L., Christensen, C., Wadsley, J., and Quinn, T. (2009). Forming a large disc galaxy from a z $<$ 1 major merger. *MNRAS*, 398:312–320.

Graham, A. W. (2012). Breaking the Law: The M $_{bh}$-M $_{spheroid}$ Relations for Core-Sérsic and Sérsic Galaxies. *ApJ*, 746(1):113.

Grand, R. J. J., Gómez, F. A., Marinacci, F., Pakmor, R., Springel, V., Campbell, D. J. R., Frenk, C. S., Jenkins, A., and White, S. D. M. (2017). The Auriga Project: the properties and formation mechanisms of disc galaxies across cosmic time. *MNRAS*, 467(1):179–207.

Greene, J. E., Ho, L. C., and Barth, A. J. (2008). Black Holes in Pseudobulges and Spheroidals: A Change in the Black Hole-Bulge Scaling Relations at Low Mass. *ApJ*, 688(1):159–179.

Guedes, J., Mayer, L., Carollo, M., and Madau, P. (2013). Pseudobulge Formation as a Dynamical Rather than a Secular Process. *ApJ*, 772:36.

Guo, Q., White, S., Boylan-Kolchin, M., De Lucia, G., Kauffmann, G., Lemson, G., Li, C., Springel, V., and Weinmann, S. (2011). From dwarf spheroidals to cD galaxies: simulating the galaxy population in a ΛCDM cosmology. *MNRAS*, 413:101–131.

Guo, Q., White, S., Li, C., and Boylan-Kolchin, M. (2010). How do galaxies populate dark matter haloes? *MNRAS*, 404(3):1111–1120.

Guth, A. H. (1981). Inflationary universe: A possible solution to the horizon and flatness problems. *Phys. Rev. D*, 23(2):347–356.

Habouzit, M., Li, Y., Somerville, R. S., Genel, S., Pillepich, A., Volonteri, M., Davé, R., Rosas-Guevara, Y., McAlpine, S., Peirani, S., Hernquist, L., Anglés-Alcázar, D., Reines, A., Bower, R., Dubois, Y., Nelson, D., Pichon, C., and Vogelsberger, M. (2020). Supermassive black holes in cosmological simulations I: M_BH-M_star relation and black hole mass function. *arXiv e-prints*, page arXiv:2006.10094.

Hagberg, A. A., Schult, D. A., and Swart, P. J. (2008). Exploring network structure, dynamics, and function using networkx. In *Proceedings of the 7th Python in Science Conference*, pages 11 – 15, Pasadena, CA USA.

Hani, M. H., Ellison, S. L., Sparre, M., Grand , R. J. J., Pakmor, R., Gomez, F. A., and Springel, V. (2019). The diversity of the circumgalactic medium around z = 0 Milky Way-mass galaxies from the Auriga simulations. *MNRAS*, 488(1):135–152.

Häring, N. and Rix, H.-W. (2004). On the Black Hole Mass-Bulge Mass Relation. *ApJ*, 604(2):L89–L92.

Hawarden, T. G., Mountain, C. M., Leggett, S. K., and Puxley, P. J. (1986). Enhanced star formation - The importance of bars in spiral galaxies. *MNRAS*, 221:41P–45P.

Heckman, T. M. and Thompson, T. A. (2017). Galactic Winds and the Role Played by Massive Stars. *arXiv e-prints*, page arXiv:1701.09062.

Henriques, B. M. B., White, S. D. M., Thomas, P. A., Angulo, R., Guo, Q., Lemson, G., Springel, V., and Overzier, R. (2015). Galaxy formation in the Planck cosmology - I. Matching the observed evolution of star formation rates, colours and stellar masses. *MNRAS*, 451:2663–2680.

Henriques, B. M. B., Yates, R. M., Fu, J., Guo, Q., Kauffmann, G., Srisawat, C., Thomas, P. A., and White, S. D. M. (2020). L-GALAXIES 2020: Spatially resolved cold gas phases, star formation, and chemical enrichment in galactic discs. *MNRAS*, 491(4):5795–5814.

Hohl, F. (1971). Numerical Experiments with a Disk of Stars. *ApJ*, 168:343.

Holmes, L., Spekkens, K., Sánchez, S. F., Walcher, C. J., García-Benito, R., Mast, D., Cortijo-Ferrero, C., Kalinova, V., Marino, R. A., Mendez-Abreu, J., and Barrera-Ballesteros, J. K. (2015). The incidence of bar-like kinematic flows in CALIFA galaxies. *MNRAS*, 451:4397–4411.

Hopkins, P. F. (2013). A general class of Lagrangian smoothed particle hydrodynamics methods and implications for fluid mixing problems. *MNRAS*, 428(4):2840–2856.

Hopkins, P. F., Bundy, K., Croton, D., Hernquist, L., Keres, D., Khochfar, S., Stewart, K., Wetzel, A., and Younger, J. D. (2010a). Mergers and Bulge Formation in ΛCDM: Which Mergers Matter? *ApJ*, 715(1):202–229.

Hopkins, P. F., Bundy, K., Hernquist, L., Wuyts, S., and Cox, T. J. (2010b). Discriminating between the physical processes that drive spheroid size evolution. *MNRAS*, 401:1099–1117.

Hopkins, P. F., Cox, T. J., Younger, J. D., and Hernquist, L. (2009a). How do Disks Survive Mergers? *ApJ*, 691:1168–1201.

Hopkins, P. F., Cox, T. J., Younger, J. D., and Hernquist, L. (2009b). How do Disks Survive Mergers? *ApJ*, 691(2):1168–1201.

Hopkins, P. F., Hernquist, L., Cox, T. J., Di Matteo, T., Robertson, B., and Springel, V. (2006). A Unified, Merger-driven Model of the Origin of Starbursts, Quasars, the Cosmic X-Ray Background, Supermassive Black Holes, and Galaxy Spheroids. *ApJS*, 163(1):1–49.

Hopkins, P. F., Hernquist, L., Cox, T. J., Keres, D., and Wuyts, S. (2009c). Dissipation and Extra Light in Galactic Nuclei. IV. Evolution in the Scaling Relations of Spheroids. *ApJ*, 691:1424–1458.

Hoyle, F. (1951). The Origin of the Rotations of the Galaxies. In *Problems of Cosmical Aerodynamics*, page 195.

Hoyle, F. and Lyttleton, R. A. (1939). The effect of interstellar matter on climatic variation. *Proceedings of the Cambridge Philosophical Society*, 35(3):405.

Hubble, E. (1929). A Relation between Distance and Radial Velocity among Extra-Galactic Nebulae. *Proceedings of the National Academy of Science*, 15(3):168–173.

Hubble, E. P. (1936). *Realm of the Nebulae*.

Hunter, D. A., Ficut-Vicas, D., Ashley, T., Brinks, E., Cigan, P., Elmegreen, B. G., Heesen, V., Herrmann, K. A., Johnson, M., Oh, S.-H., Rupen, M. P., Schruba, A., Simpson, C. E., Walter, F., Westpfahl, D. J., Young, L. M., and Zhang, H.-X. (2012). Little Things. *AJ*, 144(5):134.

Hunter, J. D. (2007). Matplotlib: A 2D Graphics Environment. *Computing in Science and Engineering*, 9(3):90–95.

Ilbert, O., Salvato, M., Le Floc'h, E., Aussel, H., Capak, P., McCracken, H. J., Mobasher, B., Kartaltepe, J., Scoville, N., Sanders, D. B., Arnouts, S., Bundy, K., Cassata, P., Kneib, J.-P., Koekemoer, A., Le Fèvre, O., Lilly, S., Surace, J., Taniguchi, Y., Tasca, L., Thompson, D., Tresse, L., Zamojski, M., Zamorani, G., and Zucca, E. (2010). Galaxy Stellar Mass Assembly Between $0.2 < z < 2$ from the S-COSMOS Survey. *ApJ*, 709:644–663.

Immeli, A., Samland, M., Gerhard, O., and Westera, P. (2004). Gas physics, disk fragmentation, and bulge formation in young galaxies. *A&A*, 413:547–561.

Inayoshi, K., Visbal, E., and Haiman, Z. (2020). The Assembly of the First Massive Black Holes. *ARA&A*, 58:27–97.

Irodotou, D. and Thomas, P. A. (2021). Using angular momentum maps to detect kinematically distinct galactic components. *MNRAS*, 501(2):2182–2197.

Irodotou, D., Thomas, P. A., Henriques, B. M., Sargent, M. T., and Hislop, J. M. (2019). Morphological evolution and galactic sizes in the L-Galaxies SA model. *MNRAS*, 489(3):3609–3624.

Jackson, R. A., Martin, G., Kaviraj, S., Laigle, C., Devriendt, J. E. G., Dubois, Y., and Pichon, C. (2020). Why do extremely massive disc galaxies exist today? *MNRAS*, 494(4):5568–5575.

Jarvis, B. J. (1986). A search for box- and peanut-shaped bulges. *AJ*, 91:65–69.

Jeans, J. H. (1902). The Stability of a Spherical Nebula. *Philosophical Transactions of the Royal Society of London Series A*, 199:1–53.

Jenkins, A. (2010). Second-order Lagrangian perturbation theory initial conditions for resimulations. *MNRAS*, 403(4):1859–1872.

Jenkins, A. (2013). A new way of setting the phases for cosmological multiscale Gaussian initial conditions. *MNRAS*, 434(3):2094–2120.

Jiang, F., Dekel, A., Kneller, O., Lapiner, S., Ceverino, D., Primack, J. R., Faber, S. M., Macciò, A. V., Dutton, A., Genel, S., and Somerville, R. S. (2018). Is the dark-matter halo spin a predictor of galaxy spin and size? *arXiv e-prints*, page arXiv:1804.07306.

Jog, C. J. (1996). Local stability criterion for stars and gas in a galactic disc. *MNRAS*, 278:209–218.

Jog, C. J. and Solomon, P. M. (1984a). A galactic disk as a two-fluid system - Consequences for the critical stellar velocity dispersion and the formation of condensations in the gas. *ApJ*, 276:127–134.

Jog, C. J. and Solomon, P. M. (1984b). Two-fluid gravitational instabilities in a galactic disk. *ApJ*, 276:114–126.

Jogee, S. (2006). The Fueling and Evolution of AGN: Internal and External Triggers. In Alloin, D., editor, *Physics of Active Galactic Nuclei at all Scales*, volume 693 of *Lecture Notes in Physics, Berlin Springer Verlag*, page 143.

Jogee, S., Scoville, N., and Kenney, J. D. P. (2005). The Central Region of Barred Galaxies: Molecular Environment, Starbursts, and Secular Evolution. *ApJ*, 630(2):837–863.

Johansson, P. H., Naab, T., and Burkert, A. (2009). Equal- and Unequal-Mass Mergers of Disk and Elliptical Galaxies with Black Holes. *ApJ*, 690:802–821.

Joshi, G. D., Pillepich, A., Nelson, D., Marinacci, F., Springel, V., Rodriguez-Gomez, V., Vogelsberger, M., and Hernquist, L. (2020). The fate of disk galaxies in IllustrisTNG clusters. *arXiv e-prints*, page arXiv:2004.01191.

Kalinova, V., Colombo, D., Rosolowsky, E., Kannan, R., Galbany, L., García-Benito, R., González Delgado, R., Sánchez, S. F., Ruiz-Lara, T., Méndez-Abreu, J., Catalán-Torrecilla, C., Sánchez-Menguiano, L., de Lorenzo-Cáceres, A., Costantin, L., Florido, E., Kodaira, K., Marino, R. A., Läsker, R., and Bland-Hawthorn, J. (2017). Towards a new classification of galaxies: principal component analysis of CALIFA circular velocity curves. *MNRAS*, 469:2539–2594.

Kataria, S. K. and Das, M. (2019). The Effect of Bulge Mass on Bar Pattern Speed in Disk Galaxies. *ApJ*, 886(1):43.

Katz, N. and Gunn, J. E. (1991). Dissipational galaxy formation. I - Effects of gasdynamics. *ApJ*, 377:365–381.

Kauffmann, G., Charlot, S., and White, S. D. M. (1996). Detection of strong evolution in the population of early-type galaxies. *MNRAS*, 283(4):L117–L122.

Kauffmann, G., Colberg, J. M., Diaferio, A., and White, S. D. M. (1999). Clustering of galaxies in a hierarchical universe - I. Methods and results at z=0. *MNRAS*, 303(1):188–206.

Kauffmann, G., White, S. D. M., and Guiderdoni, B. (1993). The Formation and Evolution of Galaxies Within Merging Dark Matter Haloes. *MNRAS*, 264:201.

Kaufmann, T., Mayer, L., Wadsley, J., Stadel, J., and Moore, B. (2007). Angular momentum transport and disc morphology in smoothed particle hydrodynamics simulations of galaxy formation. *MNRAS*, 375:53–67.

Kelvin, L. S., Driver, S. P., Robotham, A. S. G., Taylor, E. N., Graham, A. W., Alpaslan, M., Baldry, I., Bamford, S. P., Bauer, A. E., Bland-Hawthorn, J., Brown, M. J. I., Colless, M., Conselice, C. J., Holwerda, B. W., Hopkins, A. M., Lara-López, M. A., Liske, J., López-Sánchez, Á. R., Loveday, J., Norberg, P., Phillipps, S., Popescu, C. C., Prescott, M., Sansom, A. E., and Tuffs, R. J. (2014). Galaxy And Mass Assembly (GAMA): stellar mass functions by Hubble type. *MNRAS*, 444:1647–1659.

Kennicutt, Robert C., J. (1998). The Global Schmidt Law in Star-forming Galaxies. *ApJ*, 498(2):541–552.

Kent, S. M. (1986). Dark matter in spiral galaxies. I - Galaxies with optical rotation curves. *AJ*, 91:1301–1327.

Kent, S. M. (1987). Dark matter in spiral galaxies. II - Galaxies with H I rotation curves. *AJ*, 93:816–832.

Kent, S. M. (1988). Dark matter in spiral galaxies. III - The SA galaxies. *AJ*, 96:514–527.

Khoperskov, S., Haywood, M., Di Matteo, P., Lehnert, M. D., and Combes, F. (2018). Bar quenching in gas-rich galaxies. *A&A*, 609:A60.

Kim, W.-T., Seo, W.-Y., and Kim, Y. (2012). Gaseous Structures in Barred Galaxies: Effects of the Bar Strength. *ApJ*, 758(1):14.

Kimm, T., Devriendt, J., Slyz, A., Pichon, C., Kassin, S. A., and Dubois, Y. (2011). The angular momentum of baryons and dark matter halos revisited. *ArXiv e-prints*.

Knapen, J. H. (2010). Rings and Bars: Unmasking Secular Evolution of Galaxies. In Block, D. L., Freeman, K. C., and Puerari, I., editors, *Galaxies and their Masks*, page 201.

Koribalski, B. S., Wang, J., Kamphuis, P., Westmeier, T., Staveley-Smith, L., Oh, S. H., López-Sánchez, Á. R., Wong, O. I., Ott, J., de Blok, W. J. G., and Shao, L. (2018). The Local Volume H I Survey (LVHIS). *MNRAS*, 478(2):1611–1648.

Kormendy, J. (2013). *Secular Evolution in Disk Galaxies*, page 1.

Kormendy, J. (2016). *Elliptical Galaxies and Bulges of Disc Galaxies: Summary of Progress and Outstanding Issues*, volume 418, page 431.

Kormendy, J. and Bender, R. (1996). A Proposed Revision of the Hubble Sequence for Elliptical Galaxies. *ApJ*, 464:L119.

Kormendy, J. and Cornell, M. E. (2004). Secular Evolution And The Growth of Pseudobulges In Disk Galaxies. In Block, D. L., Puerari, I., Freeman, K. C., Groess, R., and Block, E. K., editors, *Penetrating Bars Through Masks of Cosmic Dust*, volume 319 of *Astrophysics and Space Science Library*, page 261.

Kormendy, J. and Gebhardt, K. (2001). Supermassive black holes in galactic nuclei. In Wheeler, J. C. and Martel, H., editors, *20th Texas Symposium on relativistic astrophysics*, volume 586 of *American Institute of Physics Conference Series*, pages 363–381.

Kormendy, J. and Ho, L. C. (2013). Coevolution (Or Not) of Supermassive Black Holes and Host Galaxies. *ARA&A*, 51(1):511–653.

Kormendy, J. and Illingworth, G. (1982). Rotation of the bulge components of disk galaxies. *ApJ*, 256:460.

Kormendy, J. and Kennicutt, Robert C., J. (2004). Secular Evolution and the Formation of Pseudobulges in Disk Galaxies. *ARA&A*, 42(1):603–683.

Krajnović, D., Weilbacher, P. M., Urrutia, T., Emsellem, E., Carollo, C. M., Shirazi, M., Bacon, R., Contini, T., Epinat, B., Kamann, S., Martinsson, T., and Steinmetz, M. (2015). Unveiling the counter-rotating nature of the kinematically distinct core in NGC 5813 with MUSE. *MNRAS*, 452(1):2–18.

Lacey, C. and Cole, S. (1993). Merger rates in hierarchical models of galaxy formation. *MNRAS*, 262:627–649.

Lagos, C. D. P., Cora, S. A., and Padilla, N. D. (2008). Effects of AGN feedback on ΛCDM galaxies. *MNRAS*, 388(2):587–602.

Lagos, C. d. P., Schaye, J., Bahé, Y., Van de Sande, J., Kay, S. T., Barnes, D., Davis, T. A., and Dalla Vecchia, C. (2018a). The connection between mass, environment, and slow rotation in simulated galaxies. *MNRAS*, 476(4):4327–4345.

Lagos, C. d. P., Stevens, A. R. H., Bower, R. G., Davis, T. A., Contreras, S., Padilla, N. D., Obreschkow, D., Croton, D., Trayford, J. W., Welker, C., and Theuns, T. (2018b). Quantifying the impact of mergers on the angular momentum of simulated galaxies. *MNRAS*, 473(4):4956–4974.

Lange, R., Driver, S. P., Robotham, A. S. G., Kelvin, L. S., Graham, A. W., Alpaslan, M., Andrews, S. K., Baldry, I. K., Bamford, S., Bland-Hawthorn, J., Brough, S., Cluver, M. E., Conselice, C. J., Davies, L. J. M., Haeussler, B., Konstantopoulos, I. S., Loveday, J., Moffett, A. J., Norberg, P., Phillipps, S., Taylor, E. N., López-Sánchez, Á. R., and Wilkins, S. M. (2015). Galaxy And Mass Assembly (GAMA): mass-size relations of z $<$ 0.1 galaxies subdivided by Sérsic index, colour and morphology. *MNRAS*, 447:2603–2630.

Laurikainen, E. and Salo, H. (2016). *Observed Properties of Boxy/Peanut/Barlens Bulges*, volume 418 of *Astrophysics and Space Science Library*, page 77.

Laurikainen, E. and Salo, H. (2017). Barlenses and X-shaped features compared: two manifestations of boxy/peanut bulges. *A&A*, 598:A10.

Laurikainen, E., Salo, H., and Buta, R. (2005). Multicomponent decompositions for a sample of S0 galaxies. *MNRAS*, 362:1319–1347.

Laurikainen, E., Salo, H., Buta, R., Knapen, J. H., and Comerón, S. (2010). Photometric scaling relations of lenticular and spiral galaxies. *MNRAS*, 405:1089–1118.

Laurikainen, E., Salo, H., and Rautiainen, P. (2002). Comparison of bar strengths in active and non-active galaxies. *MNRAS*, 331(4):880–892.

Le Fèvre, O., Abraham, R., Lilly, S. J., Ellis, R. S., Brinchmann, J., Schade, D., Tresse, L., Colless, M., Crampton, D., Glazebrook, K., Hammer, F., and Broadhurst, T. (2000). Hubble Space Telescope imaging of the CFRS and LDSS redshift surveys - IV. Influence of mergers in the evolution of faint field galaxies from z˜1. *MNRAS*, 311:565–575.

Lelli, F., McGaugh, S. S., and Schombert, J. M. (2016). SPARC: Mass Models for 175 Disk Galaxies with Spitzer Photometry and Accurate Rotation Curves. *AJ*, 152(6):157.

Lifshitz, E. M. (1946). On the gravitational stability of the expanding universe. *Zhurnal Eksperimentalnoi i Teoreticheskoi Fiziki*, 16:587–602.

Liller, M. H. (1966). The Distribution of Intensity in Elliptical Galaxies of the Virgo Cluster. II. *ApJ*, 146:28.

Linde, A. D. (1982). A new inflationary universe scenario: A possible solution of the horizon, flatness, homogeneity, isotropy and primordial monopole problems. *Physics Letters B*, 108(6):389–393.

Lingard, T. K., Masters, K. L., Krawczyk, C., Lintott, C., Kruk, S., Simmons, B., Simpson, R., Bamford, S., Nichol, R. C., and Baeten, E. (2020). Galaxy Zoo

Builder: Four Component Photometric decomposition of Spiral Galaxies Guided by Citizen Science. *arXiv e-prints*, page arXiv:2006.10450.

Liske, J., Baldry, I. K., Driver, S. P., Tuffs, R. J., Alpaslan, M., Andrae, E., Brough, S., Cluver, M. E., Grootes, M. W., Gunawardhana, M. L. P., Kelvin, L. S., Loveday, J., Robotham, A. S. G., Taylor, E. N., Bamford, S. P., Bland-Hawthorn, J., Brown, M. J. I., Drinkwater, M. J., Hopkins, A. M., Meyer, M. J., Norberg, P., Peacock, J. A., Agius, N. K., Andrews, S. K., Bauer, A. E., Ching, J. H. Y., Colless, M., Conselice, C. J., Croom, S. M., Davies, L. J. M., De Propris, R., Dunne, L., Eardley, E. M., Ellis, S., Foster, C., Frenk, C. S., Häußler, B., Holwerda, B. W., Howlett, C., Ibarra, H., Jarvis, M. J., Jones, D. H., Kafle, P. R., Lacey, C. G., Lange, R., Lara-López, M. A., López-Sánchez, Á. R., Maddox, S., Madore, B. F., McNaught-Roberts, T., Moffett, A. J., Nichol, R. C., Owers, M. S., Palamara, D., Penny, S. J., Phillipps, S., Pimbblet, K. A., Popescu, C. C., Prescott, M., Proctor, R., Sadler, E. M., Sansom, A. E., Seibert, M., Sharp, R., Sutherland, W., Vázquez-Mata, J. A., van Kampen, E., Wilkins, S. M., Williams, R., and Wright, A. H. (2015). Galaxy And Mass Assembly (GAMA): end of survey report and data release 2. *MNRAS*, 452:2087–2126.

Łokas, E. L. (2020). The effect of warm gas on the buckling instability in galactic bars. *A&A*, 634:A122.

Łokas, E. L., Athanassoula, E., Debattista, V. P., Valluri, M., Pino, A. d., Semczuk, M., Gajda, G., and Kowalczyk, K. (2014). Adventures of a tidally induced bar. *MNRAS*, 445(2):1339–1350.

Łokas, E. L., Ebrová, I., del Pino, A., Sybilska, A., Athanassoula, E., Semczuk, M., Gajda, G., and Fouquet, S. (2016). Tidally Induced Bars of Galaxies in Clusters. *ApJ*, 826:227.

Lotz, J. M., Davis, M., Faber, S. M., Guhathakurta, P., Gwyn, S., Huang, J., Koo, D. C., Le Floc'h, E., Lin, L., Newman, J., Noeske, K., Papovich, C., Willmer, C. N. A., Coil, A., Conselice, C. J., Cooper, M., Hopkins, A. M., Metevier, A., Primack, J., Rieke, G., and Weiner, B. J. (2008). The Evolution of Galaxy Mergers and Morphology at z $<$ 1.2 in the Extended Groth Strip. *ApJ*, 672:177–197.

Lovell, C. C., Vijayan, A. P., Thomas, P. A., Wilkins, S. M., Barnes, D. J., Irodotou, D., and Roper, W. (2021). First Light And Reionization Epoch Simulations (FLARES) - I. Environmental dependence of high-redshift galaxy evolution. *MNRAS*, 500(2):2127–2145.

Lütticke, R., Dettmar, R. J., and Pohlen, M. (2000). Box- and peanut-shaped bulges. I. Statistics. *A&AS*, 145:405–414.

Lynden-Bell, D. (1969). Galactic Nuclei as Collapsed Old Quasars. *Nature*, 223(5207):690–694.

MacArthur, L. A., Courteau, S., and Holtzman, J. A. (2003). Structure of Disk-dominated Galaxies. I. Bulge/Disk Parameters, Simulations, and Secular Evolution. *ApJ*, 582(2):689–722.

Mancera Piña, P. E., Posti, L., Fraternali, F., Adams, E. A. K., and Oosterloo, T. (2020). The baryonic specific angular momentum of disc galaxies. *arXiv e-prints*, page arXiv:2009.06645.

Mancini, C., Daddi, E., Juneau, S., Renzini, A., Rodighiero, G., Cappellari, M., Rodríguez-Muñoz, L., Liu, D., Pannella, M., Baronchelli, I., Franceschini, A., Bergamini, P., D'Eugenio, C., and Puglisi, A. (2019). Rejuvenated galaxies with very old bulges at the origin of the bending of the main sequence and of the 'green valley'. *MNRAS*, 489(1):1265–1290.

Marconi, A. and Hunt, L. K. (2003). The Relation between Black Hole Mass, Bulge Mass, and Near-Infrared Luminosity. *ApJ*, 589(1):L21–L24.

Marinacci, F., Pakmor, R., and Springel, V. (2014). The formation of disc galaxies in high-resolution moving-mesh cosmological simulations. *MNRAS*, 437(2):1750–1775.

Martig, M., Bournaud, F., Teyssier, R., and Dekel, A. (2009). Morphological Quenching of Star Formation: Making Early-Type Galaxies Red. *ApJ*, 707(1):250–267.

Martin, P. (1995). Quantitative Morphology of Bars in Spiral Galaxies. *AJ*, 109:2428.

Martinez-Valpuesta, I., Shlosman, I., and Heller, C. (2006). Evolution of Stellar Bars in Live Axisymmetric Halos: Recurrent Buckling and Secular Growth. *ApJ*, 637(1):214–226.

Masters, K. L. and Galaxy Zoo Team (2020). Twelve years of Galaxy Zoo. In Valluri, M. and Sellwood, J. A., editors, *IAU Symposium*, volume 353 of *IAU Symposium*, pages 205–212.

McAlpine, S., Helly, J. C., Schaller, M., Trayford, J. W., Qu, Y., Furlong, M., Bower, R. G., Crain, R. A., Schaye, J., Theuns, T., Dalla Vecchia, C., Frenk, C. S., McCarthy, I. G., Jenkins, A., Rosas-Guevara, Y., White, S. D. M., Baes, M., Camps, P., and Lemson, G. (2016). The EAGLE simulations of galaxy formation: Public release of halo and galaxy catalogues. *Astronomy and Computing*, 15:72–89.

McConnell, N. J. and Ma, C.-P. (2013). Revisiting the Scaling Relations of Black Hole Masses and Host Galaxy Properties. *ApJ*, 764(2):184.

McGaugh, S. S. (2012). The Baryonic Tully-Fisher Relation of Gas-rich Galaxies as a Test of ΛCDM and MOND. *AJ*, 143:40.

McGaugh, S. S., Schombert, J. M., Bothun, G. D., and de Blok, W. J. G. (2000). The Baryonic Tully-Fisher Relation. *ApJ*, 533:L99–L102.

McKinney, W. (2010). Data Structures for Statistical Computing in Python. In *Proceedings of the 9th Python in Science Conference*, pages 56–61.

McNamara, B. R. and Nulsen, P. E. J. (2012). Mechanical feedback from active galactic nuclei in galaxies, groups and clusters. *New Journal of Physics*, 14(5):055023.

Merritt, D. and Sellwood, J. A. (1994). Bending Instabilities in Stellar Systems. *ApJ*, 425:551.

Mihos, J. C. and Hernquist, L. (1994). Triggering of starbursts in galaxies by minor mergers. *ApJ*, 425:L13–L16.

Mihos, J. C., Walker, I. R., Hernquist, L., Mendes de Oliveira, C., and Bolte, M. (1995). A Merger Origin for X Structures in S0 Galaxies. *ApJ*, 447:L87.

Minchev, I. and Famaey, B. (2010). A New Mechanism for Radial Migration in Galactic Disks: Spiral-Bar Resonance Overlap. *ApJ*, 722:112–121.

Mo, H., van den Bosch, F. C., and White, S. (2010). *Galaxy Formation and Evolution*.

Mo, H. J., Mao, S., and White, S. D. M. (1998). The formation of galactic discs. *MNRAS*, 295(2):319–336.

Moffett, A. J., Ingarfield, S. A., Driver, S. P., Robotham, A. S. G., Kelvin, L. S., Lange, R., Meštrić, U., Alpaslan, M., Baldry, I. K., Bland-Hawthorn, J., Brough, S., Cluver, M. E., Davies, L. J. M., Holwerda, B. W., Hopkins, A. M., Kafle, P. R., Kennedy, R., Norberg, P., and Taylor, E. N. (2016a). Galaxy And Mass Assembly (GAMA): the stellar mass budget by galaxy type. *MNRAS*, 457:1308–1319.

Moffett, A. J., Lange, R., Driver, S. P., Robotham, A. S. G., Kelvin, L. S., Alpaslan, M., Andrews, S. K., Bland-Hawthorn, J., Brough, S., Cluver, M. E., Colless, M., Davies, L. J. M., Holwerda, B. W., Hopkins, A. M., Kafle, P. R., Liske, J., and Meyer, M. (2016b). Galaxy and Mass Assembly (GAMA): the stellar mass budget of galaxy spheroids and discs. *MNRAS*, 462(4):4336–4348.

Monachesi, A., Gómez, F. A., Grand , R. J. J., Simpson, C. M., Kauffmann, G., Bustamante, S., Marinacci, F., Pakmor, R., Springel, V., Frenk, C. S., White, S. D. M., and Tissera, P. B. (2019). The Auriga stellar haloes: connecting stellar population properties with accretion and merging history. *MNRAS*, 485(2):2589–2616.

Monaco, P., Fontanot, F., and Taffoni, G. (2007). The MORGANA model for the rise of galaxies and active nuclei. *MNRAS*, 375:1189–1219.

Moster, B. P., Naab, T., and White, S. D. M. (2013). Galactic star formation and accretion histories from matching galaxies to dark matter haloes. *MNRAS*, 428(4):3121–3138.

Naab, T., Oser, L., Emsellem, E., Cappellari, M., Krajnović, D., McDermid, R. M., Alatalo, K., Bayet, E., Blitz, L., Bois, M., Bournaud, F., Bureau, M., Crocker, A., Davies, R. L., Davis, T. A., de Zeeuw, P. T., Duc, P. A., Hirschmann, M., Johansson, P. H., Khochfar, S., Kuntschner, H., Morganti, R., Oosterloo, T., Sarzi, M., Scott, N., Serra, P., van de Ven, G., Weijmans, A., and Young, L. M. (2014). The ATLAS^{3D} project - XXV. Two-dimensional kinematic analysis of simulated galaxies and the cosmological origin of fast and slow rotators. *MNRAS*, 444(4):3357–3387.

Nair, P. B. and Abraham, R. G. (2010). On the Fraction of Barred Spiral Galaxies. *ApJ*, 714(2):L260–L264.

Navarro, J. F., Frenk, C. S., and White, S. D. M. (1995). The assembly of galaxies in a hierarchically clustering universe. *MNRAS*, 275:56–66.

Navarro, J. F. and Steinmetz, M. (1997). The Effects of a Photoionizing Ultraviolet Background on the Formation of Disk Galaxies. *ApJ*, 478:13–28.

Navarro, J. F. and White, S. D. M. (1993). Simulations of Dissipative Galaxy Formation in Hierarchically Clustering Universes - Part One - Tests of the Code. *MNRAS*, 265:271.

Navarro, J. F. and White, S. D. M. (1994). Simulations of dissipative galaxy formation in hierarchically clustering universes-2. Dynamics of the baryonic component in galactic haloes. *MNRAS*, 267:401–412.

Ness, M., Freeman, K., Athanassoula, E., Wylie-De-Boer, E., Bland-Hawthorn, J., Lewis, G. F., Yong, D., Asplund, M., Lane, R. R., Kiss, L. L., and Ibata, R. (2012). The Origin of the Split Red Clump in the Galactic Bulge of the Milky Way. *ApJ*, 756(1):22.

Noguchi, M. (1996). Barred Galaxies: Intrinsic or Extrinsic? *ApJ*, 469:605.

Noguchi, M. (1999). Early Evolution of Disk Galaxies: Formation of Bulges in Clumpy Young Galactic Disks. *ApJ*, 514(1):77–95.

Nulsen, P. E. J. and Fabian, A. C. (2000). Fuelling quasars with hot gas. *MNRAS*, 311(2):346–356.

Obreja, A., Domínguez-Tenreiro, R., Brook, C., Martínez-Serrano, F. J., Doménech-Moral, M., Serna, A., Mollá, M., and Stinson, G. (2013). A Two-phase Scenario for Bulge Assembly in ΛCDM Cosmologies. *ApJ*, 763(1):26.

Obreja, A., Macciò, A. V., Moster, B., Dutton, A. A., Buck, T., Stinson, G. S., and Wang, L. (2018). Introducing galactic structure finder: the multiple stellar kinematic structures of a simulated Milky Way mass galaxy. *MNRAS*, 477(4):4915–4930.

Obreschkow, D., Elahi, P. J., Lagos, C. d. P., Poulton, R. J. J., and Ludlow, A. D. (2020). Characterizing the structure of halo merger trees using a single parameter: the tree entropy. *MNRAS*, 493(3):4551–4569.

Obreschkow, D. and Glazebrook, K. (2014). Fundamental Mass-Spin-Morphology Relation Of Spiral Galaxies. *ApJ*, 784(1):26.

Oh, S., Colless, M., Barsanti, S., Casura, S., Cortese, L., van de Sande, J., Owers, M. S., Scott, N., D'Eugenio, F., Bland-Hawthorn, J., Brough, S., Bryant, J. J., Croom, S. M., Foster, C., Groves, B., Lawrence, J. S., Richards, S. N., and Sweet, S. M. (2020). The SAMI Galaxy Survey: decomposed stellar kinematics of galaxy bulges and disks. *MNRAS*, 495(4):4638–4658.

Okamoto, T., Frenk, C. S., Jenkins, A., and Theuns, T. (2010). The properties of satellite galaxies in simulations of galaxy formation. *MNRAS*, 406(1):208–222.

Okamoto, T., Gao, L., and Theuns, T. (2008). Mass loss of galaxies due to an ultraviolet background. *MNRAS*, 390(3):920–928.

Ostriker, J. P. and Peebles, P. J. E. (1973). A Numerical Study of the Stability of Flattened Galaxies: or, can Cold Galaxies Survive? *ApJ*, 186:467–480.

Ott, J., Stilp, A. M., Warren, S. R., Skillman, E. D., Dalcanton, J. J., Walter, F., de Blok, W. J. G., Koribalski, B., and West, A. A. (2012). VLA-ANGST: A High-resolution H I Survey of Nearby Dwarf Galaxies. *AJ*, 144(4):123.

Pakmor, R., Bauer, A., and Springel, V. (2011). Magnetohydrodynamics on an unstructured moving grid. *MNRAS*, 418(2):1392–1401.

Pakmor, R., Gómez, F. A., Grand , R. J. J., Marinacci, F., Simpson, C. M., Springel, V., Campbell, D. J. R., Frenk, C. S., Guillet, T., Pfrommer, C., and White, S. D. M. (2017). Magnetic field formation in the Milky Way like disc galaxies of the Auriga project. *MNRAS*, 469(3):3185–3199.

Pakmor, R., Guillet, T., Pfrommer, C., Gómez, F. A., Grand, R. J. J., Marinacci, F., Simpson, C. M., and Springel, V. (2018). Faraday rotation maps of disc galaxies. *MNRAS*, 481(4):4410–4418.

Pakmor, R., Marinacci, F., and Springel, V. (2014). Magnetic Fields in Cosmological Simulations of Disk Galaxies. *ApJ*, 783(1):L20.

Pakmor, R. and Springel, V. (2013). Simulations of magnetic fields in isolated disc galaxies. *MNRAS*, 432(1):176–193.

Pakmor, R., Springel, V., Bauer, A., Mocz, P., Munoz, D. J., Ohlmann, S. T., Schaal, K., and Zhu, C. (2016). Improving the convergence properties of the moving-mesh code AREPO. *MNRAS*, 455(1):1134–1143.

Park, M.-J., Yi, S. K., Dubois, Y., Pichon, C., Kimm, T., Devriendt, J., Choi, H., Volonteri, M., Kaviraj, S., and Peirani, S. (2019). New Horizon: On the Origin of the Stellar Disk and Spheroid of Field Galaxies at z = 0.7. *ApJ*, 883(1):25.

Parul, H. D., Smirnov, A. A., and Sotnikova, N. Y. (2020). Orbital Ingredients for Cooking X-structures in Edge-on Galaxies. *ApJ*, 895(1):12.

Patsis, P. A. and Athanassoula, E. (2019). The orbital content of bars: the origin of 'non-x1-tree', bar-supporting orbits. *MNRAS*, 490(2):2740–2759.

Paturel, G., Petit, C., Prugniel, P., Theureau, G., Rousseau, J., Brouty, M., Dubois, P., and Cambrésy, L. (2003). HYPERLEDA. I. Identification and designation of galaxies. *A&A*, 412:45–55.

Pedrosa, S. E. and Tissera, P. B. (2015). Angular momentum evolution for galaxies in a Λ-CDM scenario. *A&A*, 584:A43.

Peebles, P. J. and Ratra, B. (2003). The cosmological constant and dark energy. *Reviews of Modern Physics*, 75(2):559–606.

Peebles, P. J. E. (1969). Origin of the Angular Momentum of Galaxies. *ApJ*, 155:393.

Peebles, P. J. E. (1984). Dark matter and the origin of galaxies and globular star clusters. *ApJ*, 277:470–477.

Peebles, P. J. E. (2020). Formation of the Large Nearby Galaxies. *arXiv e-prints*, page arXiv:2005.07588.

Peeples, M. S. and Martini, P. (2006). The Connection between Bar Strength and Circumnuclear Dust Structure. *ApJ*, 652(2):1097–1111.

Peng, C. Y., Ho, L. C., Impey, C. D., and Rix, H.-W. (2002). Detailed Structural Decomposition of Galaxy Images. *AJ*, 124(1):266–293.

Penoyre, Z., Moster, B. P., Sijacki, D., and Genel, S. (2017). The origin and evolution of fast and slow rotators in the Illustris simulation. *MNRAS*, 468(4):3883–3906.

Penzias, A. A. and Wilson, R. W. (1965). A Measurement of Excess Antenna Temperature at 4080 Mc/s. *ApJ*, 142:419–421.

Peschken, N. and Łokas, E. L. (2019). Tidally induced bars in Illustris galaxies. *MNRAS*, 483:2721–2735.

Pfenniger, D. and Friedli, D. (1991). Structure and dynamics of 3D N-body barred galaxies. *A&A*, 252:75–93.

Pfenniger, D. and Norman, C. (1990). Dissipation in barred galaxies - The growth of bulges and central mass concentrations. *ApJ*, 363:391–410.

Pillepich, A., Madau, P., and Mayer, L. (2015). Building Late-type Spiral Galaxies by In-situ and Ex-situ Star Formation. *ApJ*, 799(2):184.

Planck Collaboration, Ade, P. A. R., Aghanim, N., Alves, M. I. R., Armitage-Caplan, C., Arnaud, M., Ashdown, M., Atrio-Barandela, F., Aumont, J., Aussel, H., Baccigalupi, C., Banday, A. J., Barreiro, R. B., Barrena, R., Bartelmann, M., Bartlett, J. G., Bartolo, N., Basak, S., Battaner, E., Battye, R., Benabed, K., Benoît, A., Benoit-Lévy, A., Bernard, J. P., Bersanelli, M., Bertincourt, B., Bethermin, M., Bielewicz, P., Bikmaev, I., Blanchard, A., Bobin, J., Bock, J. J.,

Böhringer, H., Bonaldi, A., Bonavera, L., Bond, J. R., Borrill, J., Bouchet, F. R., Boulanger, F., Bourdin, H., Bowyer, J. W., Bridges, M., Brown, M. L., Bucher, M., Burenin, R., Burigana, C., Butler, R. C., Calabrese, E., Cappellini, B., Cardoso, J. F., Carr, R., Carvalho, P., Casale, M., Castex, G., Catalano, A., Challinor, A., Chamballu, A., Chary, R. R., Chen, X., Chiang, H. C., Chiang, L. Y., Chon, G., Christensen, P. R., Churazov, E., Church, S., Clemens, M., Clements, D. L., Colombi, S., Colombo, L. P. L., Combet, C., Comis, B., Couchot, F., Coulais, A., Crill, B. P., Cruz, M., Curto, A., Cuttaia, F., Da Silva, A., Dahle, H., Danese, L., Davies, R. D., Davis, R. J., de Bernardis, P., de Rosa, A., de Zotti, G., Déchelette, T., Delabrouille, J., Delouis, J. M., Démoclès, J., Désert, F. X., Dick, J., Dickinson, C., Diego, J. M., Dolag, K., Dole, H., Donzelli, S., Doré, O., Douspis, M., Ducout, A., Dunkley, J., Dupac, X., Efstathiou, G., Elsner, F., Enßlin, T. A., Eriksen, H. K., Fabre, O., Falgarone, E., Falvella, M. C., Fantaye, Y., Fergusson, J., Filliard, C., Finelli, F., Flores-Cacho, I., Foley, S., Forni, O., Fosalba, P., Frailis, M., Fraisse, A. A., Franceschi, E., Freschi, M., Fromenteau, S., Frommert, M., Gaier, T. C., Galeotta, S., Gallegos, J., Galli, S., Gandolfo, B., Ganga, K., Gauthier, C., Génova-Santos, R. T., Ghosh, T., Giard, M., Giardino, G., Gilfanov, M., Girard, D., Giraud-Héraud, Y., Gjerløw, E., González-Nuevo, J., Górski, K. M., Gratton, S., Gregorio, A., Gruppuso, A., Gudmundsson, J. E., Haissinski, J., Hamann, J., Hansen, F. K., Hansen, M., Hanson, D., Harrison, D. L., Heavens, A., Helou, G., Hempel, A., Henrot-Versillé, S., Hernández-Monteagudo, C., Herranz, D., Hildebrandt, S. R., Hivon, E., Ho, S., Hobson, M., Holmes, W. A., Hornstrup, A., Hou, Z., Hovest, W., Huey, G., Huffenberger, K. M., Hurier, G., Ilić, S., Jaffe, A. H., Jaffe, T. R., Jasche, J., Jewell, J., Jones, W. C., Juvela, M., Kalberla, P., Kangaslahti, P., Keihänen, E., Kerp, J., Keskitalo, R., Khamitov, I., Kiiveri, K., Kim, J., Kisner, T. S., Kneissl, R., Knoche, J., Knox, L., Kunz, M., Kurki-Suonio, H., Lacasa, F., Lagache, G., Lähteenmäki, A., Lamarre, J. M., Langer, M., Lasenby, A., Lattanzi, M., Laureijs, R. J., Lavabre, A., Lawrence, C. R., Le Jeune, M., Leach, S., Leahy, J. P., Leonardi, R., León-Tavares, J., Leroy, C., Lesgourgues, J., Lewis, A., Li, C., Liddle, A., Liguori, M., Lilje, P. B., Linden-Vørnle, M., Lindholm, V., López-Caniego, M., Lowe, S., Lubin, P. M., Macías-Pérez, J. F., MacTavish, C. J., Maf-

fei, B., Maggio, G., Maino, D., Mandolesi, N., Mangilli, A., Marcos-Caballero, A., Marinucci, D., Maris, M., Marleau, F., Marshall, D. J., Martin, P. G., Martínez-González, E., Masi, S., Massardi, M., Matarrese, S., Matsumura, T., Matthai, F., Maurin, L., Mazzotta, P., McDonald, A., McEwen, J. D., McGehee, P., Mei, S., Meinhold, P. R., Melchiorri, A., Melin, J. B., Mendes, L., Menegoni, E., Mennella, A., Migliaccio, M., Mikkelsen, K., Millea, M., Miniscalco, R., Mitra, S., Miville-Deschênes, M. A., Molinari, D., Moneti, A., Montier, L., Morgante, G., Morisset, N., Mortlock, D., Moss, A., Munshi, D., Murphy, J. A., Naselsky, P., Nati, F., Natoli, P., Negrello, M., Nesvadba, N. P. H., Netterfield, C. B., Nørgaard-Nielsen, H. U., North, C., Noviello, F., Novikov, D., Novikov, I., O'Dwyer, I. J., Orieux, F., Osborne, S., O'Sullivan, C., Oxborrow, C. A., Paci, F., Pagano, L., Pajot, F., Paladini, R., Pandolfi, S., Paoletti, D., Partridge, B., Pasian, F., Patanchon, G., Paykari, P., Pearson, D., Pearson, T. J., Peel, M., Peiris, H. V., Perdereau, O., Perotto, L., Perrotta, F., Pettorino, V., Piacentini, F., Piat, M., Pierpaoli, E., Pietrobon, D., Plaszczynski, S., Platania, P., Pogosyan, D., Pointecouteau, E., Polenta, G., Ponthieu, N., Popa, L., Poutanen, T., Pratt, G. W., Prézeau, G., Prunet, S., Puget, J. L., Pullen, A. R., Rachen, J. P., Racine, B., Rahlin, A., Räth, C., Reach, W. T., Rebolo, R., Reinecke, M., Remazeilles, M., Renault, C., Renzi, A., Riazuelo, A., Ricciardi, S., Riller, T., Ringeval, C., Ristorcelli, I., Robbers, G., Rocha, G., Roman, M., Rosset, C., Rossetti, M., Roudier, G., Rowan-Robinson, M., Rubiño-Martín, J. A., Ruiz-Granados, B., Rusholme, B., Salerno, E., Sandri, M., Sanselme, L., Santos, D., Savelainen, M., Savini, G., Schaefer, B. M., Schiavon, F., Scott, D., Seiffert, M. D., Serra, P., Shellard, E. P. S., Smith, K., Smoot, G. F., Souradeep, T., Spencer, L. D., Starck, J. L., Stolyarov, V., Stompor, R., Sudiwala, R., Sunyaev, R., Sureau, F., Sutter, P., Sutton, D., Suur-Uski, A. S., Sygnet, J. F., Tauber, J. A., Tavagnacco, D., Taylor, D., Terenzi, L., Texier, D., Toffolatti, L., Tomasi, M., Torre, J. P., Tristram, M., Tucci, M., Tuovinen, J., Türler, M., Tuttlebee, M., Umana, G., Valenziano, L., Valiviita, J., Van Tent, B., Varis, J., Vibert, L., Viel, M., Vielva, P., Villa, F., Vittorio, N., Wade, L. A., Wandelt, B. D., Watson, C., Watson, R., Wehus, I. K., Welikala, N., Weller, J., White, M., White, S. D. M., Wilkinson, A., Winkel, B., Xia, J. Q., Yvon, D., Zacchei, A., Zibin, J. P., and Zonca, A. (2014a). Planck 2013 results. I. Overview

of products and scientific results. *A&A*, 571:A1.

Planck Collaboration, Ade, P. A. R., Aghanim, N., Armitage-Caplan, C., Arnaud, M., Ashdown, M., Atrio-Barand ela, F., Aumont, J., Baccigalupi, C., Banday, A. J., Barreiro, R. B., Bartlett, J. G., Battaner, E., Benabed, K., Benoît, A., Benoit-Lévy, A., Bernard, J. P., Bersanelli, M., Bielewicz, P., Bobin, J., Bock, J. J., Bonaldi, A., Bond, J. R., Borrill, J., Bouchet, F. R., Bridges, M., Bucher, M., Burigana, C., Butler, R. C., Calabrese, E., Cappellini, B., Cardoso, J. F., Catalano, A., Challinor, A., Chamballu, A., Chary, R. R., Chen, X., Chiang, H. C., Chiang, L. Y., Christensen, P. R., Church, S., Clements, D. L., Colombi, S., Colombo, L. P. L., Couchot, F., Coulais, A., Crill, B. P., Curto, A., Cuttaia, F., Danese, L., Davies, R. D., Davis, R. J., de Bernardis, P., de Rosa, A., de Zotti, G., Delabrouille, J., Delouis, J. M., Désert, F. X., Dickinson, C., Diego, J. M., Dolag, K., Dole, H., Donzelli, S., Doré, O., Douspis, M., Dunkley, J., Dupac, X., Efstathiou, G., Elsner, F., Enßlin, T. A., Eriksen, H. K., Finelli, F., Forni, O., Frailis, M., Fraisse, A. A., Franceschi, E., Gaier, T. C., Galeotta, S., Galli, S., Ganga, K., Giard, M., Giardino, G., Giraud-Héraud, Y., Gjerløw, E., González-Nuevo, J., Górski, K. M., Gratton, S., Gregorio, A., Gruppuso, A., Gudmundsson, J. E., Haissinski, J., Hamann, J., Hansen, F. K., Hanson, D., Harrison, D., Henrot-Versillé, S., Hernández-Monteagudo, C., Herranz, D., Hildebrand t, S. R., Hivon, E., Hobson, M., Holmes, W. A., Hornstrup, A., Hou, Z., Hovest, W., Huffenberger, K. M., Jaffe, A. H., Jaffe, T. R., Jewell, J., Jones, W. C., Juvela, M., Keihänen, E., Keskitalo, R., Kisner, T. S., Kneissl, R., Knoche, J., Knox, L., Kunz, M., Kurki-Suonio, H., Lagache, G., Lähteenmäki, A., Lamarre, J. M., Lasenby, A., Lattanzi, M., Laureijs, R. J., Lawrence, C. R., Leach, S., Leahy, J. P., Leonardi, R., León-Tavares, J., Lesgourgues, J., Lewis, A., Liguori, M., Lilje, P. B., Linden-Vørnle, M., López-Caniego, M., Lubin, P. M., Macías-Pérez, J. F., Maffei, B., Maino, D., Mand olesi, N., Maris, M., Marshall, D. J., Martin, P. G., Martínez-González, E., Masi, S., Massardi, M., Matarrese, S., Matthai, F., Mazzotta, P., Meinhold, P. R., Melchiorri, A., Melin, J. B., Mendes, L., Menegoni, E., Mennella, A., Migliaccio, M., Millea, M., Mitra, S., Miville-Deschênes, M. A., Moneti, A., Montier, L., Morgante, G., Mortlock, D., Moss, A., Munshi, D., Murphy, J. A., Naselsky, P., Nati, F., Natoli, P., Netterfield, C. B., Nørgaard-Nielsen, H. U.,

Noviello, F., Novikov, D., Novikov, I., O'Dwyer, I. J., Osborne, S., Oxborrow, C. A., Paci, F., Pagano, L., Pajot, F., Paladini, R., Paoletti, D., Partridge, B., Pasian, F., Patanchon, G., Pearson, D., Pearson, T. J., Peiris, H. V., Perdereau, O., Perotto, L., Perrotta, F., Pettorino, V., Piacentini, F., Piat, M., Pierpaoli, E., Pietrobon, D., Plaszczynski, S., Platania, P., Pointecouteau, E., Polenta, G., Ponthieu, N., Popa, L., Poutanen, T., Pratt, G. W., Prézeau, G., Prunet, S., Puget, J. L., Rachen, J. P., Reach, W. T., Rebolo, R., Reinecke, M., Remazeilles, M., Renault, C., Ricciardi, S., Riller, T., Ristorcelli, I., Rocha, G., Rosset, C., Roudier, G., Rowan-Robinson, M., Rubiño-Martín, J. A., Rusholme, B., Sandri, M., Santos, D., Savelainen, M., Savini, G., Scott, D., Seiffert, M. D., Shellard, E. P. S., Spencer, L. D., Starck, J. L., Stolyarov, V., Stompor, R., Sudiwala, R., Sunyaev, R., Sureau, F., Sutton, D., Suur-Uski, A. S., Sygnet, J. F., Tauber, J. A., Tavagnacco, D., Terenzi, L., Toffolatti, L., Tomasi, M., Tristram, M., Tucci, M., Tuovinen, J., Türler, M., Umana, G., Valenziano, L., Valiviita, J., Van Tent, B., Vielva, P., Villa, F., Vittorio, N., Wade, L. A., Wandelt, B. D., Wehus, I. K., White, M., White, S. D. M., Wilkinson, A., Yvon, D., Zacchei, A., and Zonca, A. (2014b). Planck 2013 results. XVI. Cosmological parameters. *A&A*, 571:A16.

Planck Collaboration, Ade, P. A. R., Aghanim, N., Armitage-Caplan, C., Arnaud, M., Ashdown, M., Atrio-Barandela, F., Aumont, J., Baccigalupi, C., Banday, A. J., Barreiro, R. B., Bartlett, J. G., Battaner, E., Benabed, K., Benoît, A., Benoit-Lévy, A., Bernard, J. P., Bersanelli, M., Bielewicz, P., Bobin, J., Bock, J. J., Bonaldi, A., Bond, J. R., Borrill, J., Bouchet, F. R., Bridges, M., Bucher, M., Burigana, C., Butler, R. C., Calabrese, E., Cappellini, B., Cardoso, J. F., Catalano, A., Challinor, A., Chamballu, A., Chary, R. R., Chen, X., Chiang, H. C., Chiang, L. Y., Christensen, P. R., Church, S., Clements, D. L., Colombi, S., Colombo, L. P. L., Couchot, F., Coulais, A., Crill, B. P., Curto, A., Cuttaia, F., Danese, L., Davies, R. D., Davis, R. J., de Bernardis, P., de Rosa, A., de Zotti, G., Delabrouille, J., Delouis, J. M., Désert, F. X., Dickinson, C., Diego, J. M., Dolag, K., Dole, H., Donzelli, S., Doré, O., Douspis, M., Dunkley, J., Dupac, X., Efstathiou, G., Elsner, F., Enßlin, T. A., Eriksen, H. K., Finelli, F., Forni, O., Frailis, M., Fraisse, A. A., Franceschi, E., Gaier, T. C., Galeotta, S., Galli, S., Ganga, K., Giard, M., Giardino, G., Giraud-Héraud, Y., Gjerløw, E., Gonzá lez-

Nuevo, J., Górski, K. M., Gratton, S., Gregorio, A., Gruppuso, A., Gudmundsson, J. E., Haissinski, J., Hamann, J., Hansen, F. K., Hanson, D., Harrison, D., Henrot-Versillé, S., Hernández-Monteagudo, C., Herranz, D., Hildebrandt, S. R., Hivon, E., Hobson, M., Holmes, W. A., Hornstrup, A., Hou, Z., Hovest, W., Huffenberger, K. M., Jaffe, A. H., Jaffe, T. R., Jewell, J., Jones, W. C., Juvela, M., Keihänen, E., Keskitalo, R., Kisner, T. S., Kneissl, R., Knoche, J., Knox, L., Kunz, M., Kurki-Suonio, H., Lagache, G., Lähteenmäki, A., Lamarre, J. M., Lasenby, A., Lattanzi, M., Laureijs, R. J., Lawrence, C. R., Leach, S., Leahy, J. P., Leonardi, R., León-Tavares, J., Lesgourgues, J., Lewis, A., Liguori, M., Lilje, P. B., Linden-Vørnle, M., López-Caniego, M., Lubin, P. M., Macías-Pérez, J. F., Maffei, B., Maino, D., Mandolesi, N., Maris, M., Marshall, D. J., Martin, P. G., Martínez-González, E., Masi, S., Massardi, M., Matarrese, S., Matthai, F., Mazzotta, P., Meinhold, P. R., Melchiorri, A., Melin, J. B., Mendes, L., Menegoni, E., Mennella, A., Migliaccio, M., Millea, M., Mitra, S., Miville- Deschênes, M. A., Moneti, A., Montier, L., Morgante, G., Mortlock, D., Moss, A., Munshi, D., Murphy, J. A., Naselsky, P., Nati, F., Natoli, P., Netterfield, C. B., Nørgaard-Nielsen, H. U., Noviello, F., Novikov, D., Novikov, I., O'Dwyer, I. J., Osborne, S., Oxborrow, C. A., Paci, F., Pagano, L., Pajot, F., Paladini, R., Paoletti, D., Partridge, B., Pasian, F., Patanchon, G., Pearson, D., Pearson, T. J., Peiris, H. V., Perdereau, O., Perotto, L., Perrotta, F., Pettorino, V., Piacentini, F., Piat, M., Pierpaoli, E., Pietrobon, D., Plaszczynski, S., Platania, P., Pointecouteau, E., Polenta, G., Ponthieu, N., Popa, L., Poutanen, T., Pratt, G. W., Prézeau, G., Prunet, S., Puget, J. L., Rachen, J. P., Reach, W. T., Rebolo, R., Reinecke, M., Remazeilles, M., Renault, C., Ricciardi, S., Riller, T., Ristorcelli, I., Rocha, G., Rosset, C., Roudier, G., Rowan-Robinson, M., Rubiño-Martín, J. A., Rusholme, B., Sandri, M., Santos, D., Savelainen, M., Savini, G., Scott, D., Seiffert, M. D., Shellard, E. P. S., Spencer, L. D., Starck, J. L., Stolyarov, V., Stompor, R., Sudiwala, R., Sunyaev, R., Sureau, F., Sutton, D., Suur-Uski, A. S., Sygnet, J. F., Tauber, J. A., Tavagnacco, D., Terenzi, L., Toffolatti, L., Tomasi, M., Tristram, M., Tucci, M., Tuovinen, J., Türler, M., Umana, G., Valenziano, L., Valiviita, J., Van Tent, B., Vielva, P., Villa, F., Vittorio, N., Wade, L. A., Wandelt, B. D., Wehus, I. K., White, M., White, S. D. M., Wilkinson, A., Yvon, D., Zacchei, A., and Zonca, A.

(2014c). Planck 2013 results. XVI. Cosmological parameters. *A&A*, 571:A16.

Ponomareva, A. A., Verheijen, M. A. W., and Bosma, A. (2016). Detailed H I kinematics of Tully-Fisher calibrator galaxies. *MNRAS*, 463(4):4052–4067.

Porter, L. A., Somerville, R. S., Primack, J. R., and Johansson, P. H. (2014). Understanding the structural scaling relations of early-type galaxies. *MNRAS*, 444:942–960.

Posti, L., Fraternali, F., Di Teodoro, E. M., and Pezzulli, G. (2018a). The angular momentum-mass relation: a fundamental law from dwarf irregulars to massive spirals. *A&A*, 612:L6.

Posti, L., Fraternali, F., Di Teodoro, E. M., and Pezzulli, G. (2018b). The angular momentum-mass relation: a fundamental law from dwarf irregulars to massive spirals. *A&A*, 612:L6.

Posti, L., Pezzulli, G., Fraternali, F., and Di Teodoro, E. M. (2018c). Galaxy spin as a formation probe: the stellar-to-halo specific angular momentum relation. *MNRAS*, 475(1):232–243.

Pratt, G. W., Croston, J. H., Arnaud, M., and Böhringer, H. (2009). Galaxy cluster X-ray luminosity scaling relations from a representative local sample (REXCESS). *A&A*, 498(2):361–378.

Prugniel, P. and Simien, F. (1997). The fundamental plane of early-type galaxies: non-homology of the spatial structure. *A&A*, 321:111–122.

Quillen, A. C. (2002). Growth of a Peanut-shaped Bulge via Resonant Trapping of Stellar Orbits in the Vertical Inner Lindblad Resonances. *AJ*, 124(2):722–732.

Quillen, A. C., Minchev, I., Sharma, S., Qin, Y.-J., and Di Matteo, P. (2014). A vertical resonance heating model for X- or peanut-shaped galactic bulges. *MNRAS*, 437(2):1284–1307.

Rafikov, R. R. (2001). The local axisymmetric instability criterion in a thin, rotating, multicomponent disc. *MNRAS*, 323:445–452.

Raha, N., Sellwood, J. A., James, R. A., and Kahn, F. D. (1991). A dynamical instability of bars in disk galaxies. *Nature*, 352(6334):411–412.

Rees, M. J. and Ostriker, J. P. (1977). Cooling, dynamics and fragmentation of massive gas clouds: clues to the masses and radii of galaxies and clusters. *MNRAS*, 179:541–559.

Robertson, B., Bullock, J. S., Cox, T. J., Di Matteo, T., Hernquist, L., Springel, V., and Yoshida, N. (2006a). A Merger-driven Scenario for Cosmological Disk Galaxy Formation. *ApJ*, 645:986–1000.

Robertson, B., Cox, T. J., Hernquist, L., Franx, M., Hopkins, P. F., Martini, P., and Springel, V. (2006b). The Fundamental Scaling Relations of Elliptical Galaxies. *ApJ*, 641:21–40.

Romanowsky, A. J. and Fall, S. M. (2012). Angular Momentum and Galaxy Formation Revisited. *ApJS*, 203(2):17.

Romeo, A. B. and Wiegert, J. (2011). The effective stability parameter for two-component galactic discs: is 1/Q 1/Qstars + 1/Qgas? *MNRAS*, 416:1191–1196.

Rosas-Guevara, Y., Bonoli, S., Dotti, M., Zana, T., Nelson, D., Pillepich, A., Ho, L. C., Izquierdo-Villalba, D., Hernquist, L., and Pakmor, R. (2020a). The buildup of strongly barred galaxies in the TNG100 simulation. *MNRAS*, 491(2):2547–2564.

Rosas-Guevara, Y., Bonoli, S., Dotti, M., Zana, T., Nelson, D., Pillepich, A., Ho, L. C., Izquierdo-Villalba, D., Hernquist, L., and Pakmor, R. (2020b). The buildup of strongly barred galaxies in the TNG100 simulation. *MNRAS*, 491(2):2547–2564.

Rosas-Guevara, Y., Bower, R. G., Schaye, J., McAlpine, S., Dalla Vecchia, C., Frenk, C. S., Schaller, M., and Theuns, T. (2016). Supermassive black holes in the EAGLE Universe. Revealing the observables of their growth. *MNRAS*, 462(1):190–205.

Rosas-Guevara, Y. M., Bower, R. G., Schaye, J., Furlong, M., Frenk, C. S., Booth, C. M., Crain, R. A., Dalla Vecchia, C., Schaller, M., and Theuns, T. (2015). The impact of angular momentum on black hole accretion rates in simulations of galaxy formation. *MNRAS*, 454(1):1038–1057.

Rosito, M. S., Pedrosa, S. E., Tissera, P. B., Avila-Reese, V., Lacerna, I., Bignone, L. A., Ibarra-Medel, H. J., and Varela, S. (2018). Field spheroid-dominated galaxies in a Λ-CDM Universe. *A&A*, 614:A85.

Rosito, M. S., Tissera, P. B., Pedrosa, S. E., and Rosas-Guevara, Y. (2019). Assembly of spheroid-dominated galaxies in the EAGLE simulation. *A&A*, 629:A37.

Ruiz, A. N., Cora, S. A., Padilla, N. D., Domínguez, M. J., Vega-Martínez, C. A., Tecce, T. E., Orsi, Á., Yaryura, Y., García Lambas, D., Gargiulo, I. D., and Muñoz Arancibia, A. M. (2015). Calibration of Semi-analytic Models of Galaxy Formation Using Particle Swarm Optimization. *ApJ*, 801:139.

Sachdeva, S. and Saha, K. (2018). Bright compact bulges at intermediate redshifts. *MNRAS*, 478(1):41–49.

Saha, K. and Cortesi, A. (2018). Forming Lenticular Galaxies via Violent Disk Instability. *ApJ*, 862(1):L12.

Saha, K., Martinez-Valpuesta, I., and Gerhard, O. (2012). Spin-up of low-mass classical bulges in barred galaxies. *MNRAS*, 421(1):333–345.

Sales, L. V., Navarro, J. F., Theuns, T., Schaye, J., White, S. D. M., Frenk, C. S., Crain, R. A., and Dalla Vecchia, C. (2012). The origin of discs and spheroids in simulated galaxies. *MNRAS*, 423(2):1544–1555.

Sánchez, S. F., Kennicutt, R. C., Gil de Paz, A., van de Ven, G., Vílchez, J. M., Wisotzki, L., Walcher, C. J., Mast, D., Aguerri, J. A. L., Albiol-Pérez, S., Alonso-Herrero, A., Alves, J., Bakos, J., Bartáková, T., Bland-Hawthorn, J., Boselli, A., Bomans, D. J., Castillo-Morales, A., Cortijo-Ferrero, C., de Lorenzo-Cáceres, A., Del Olmo, A., Dettmar, R. J., Díaz, A., Ellis, S., Falcón-Barroso, J., Flores, H., Gallazzi, A., García-Lorenzo, B., González Delgado, R., Gruel, N., Haines, T., Hao, C., Husemann, B., Iglésias-Páramo, J., Jahnke, K., Johnson, B., Jungwiert, B., Kalinova, V., Kehrig, C., Kupko, D., López-Sánchez, Á. R., Lyubenova, M., Marino, R. A., Mármol-Queraltó, E., Márquez, I., Masegosa, J., Meidt, S., Mendez-Abreu, J., Monreal-Ibero, A., Montijo, C., Mourão, A. M., Palacios-Navarro, G., Papaderos, P., Pasquali, A., Peletier, R., Pérez, E., Pérez,

I., Quirrenbach, A., Relaño, M., Rosales-Ortega, F. F., Roth, M. M., Ruiz-Lara, T., Sánchez-Blázquez, P., Sengupta, C., Singh, R., Stanishev, V., Trager, S. C., Vazdekis, A., Viironen, K., Wild, V., Zibetti, S., and Ziegler, B. (2012). CALIFA, the Calar Alto Legacy Integral Field Area survey. I. Survey presentation. *A&A*, 538:A8.

Sani, E., Marconi, A., Hunt, L. K., and Risaliti, G. (2011). The Spitzer/IRAC view of black hole-bulge scaling relations. *MNRAS*, 413(2):1479–1494.

Scannapieco, C., White, S. D. M., Springel, V., and Tissera, P. B. (2009). The formation and survival of discs in a ΛCDM universe. *MNRAS*, 396(2):696–708.

Schaller, M., Dalla Vecchia, C., Schaye, J., Bower, R. G., Theuns, T., Crain, R. A., Furlong, M., and McCarthy, I. G. (2015). The EAGLE simulations of galaxy formation: the importance of the hydrodynamics scheme. *MNRAS*, 454(3):2277–2291.

Schaye, J. (2004). Star Formation Thresholds and Galaxy Edges: Why and Where. *ApJ*, 609(2):667–682.

Schaye, J., Crain, R. A., Bower, R. G., Furlong, M., Schaller, M., Theuns, T., Dalla Vecchia, C., Frenk, C. S., McCarthy, I. G., Helly, J. C., Jenkins, A., Rosas-Guevara, Y. M., White, S. D. M., Baes, M., Booth, C. M., Camps, P., Navarro, J. F., Qu, Y., Rahmati, A., Sawala, T., Thomas, P. A., and Trayford, J. (2015). The EAGLE project: simulating the evolution and assembly of galaxies and their environments. *MNRAS*, 446(1):521–554.

Schaye, J. and Dalla Vecchia, C. (2008). On the relation between the Schmidt and Kennicutt-Schmidt star formation laws and its implications for numerical simulations. *MNRAS*, 383(3):1210–1222.

Schaye, J., Dalla Vecchia, C., Booth, C. M., Wiersma, R. P. C., Theuns, T., Haas, M. R., Bertone, S., Duffy, A. R., McCarthy, I. G., and van de Voort, F. (2010). The physics driving the cosmic star formation history. *MNRAS*, 402(3):1536–1560.

Scorza, C. and Bender, R. (1995). The internal structure of disky elliptical galaxies. *A&A*, 293:20–43.

Sellwood, J. A. (2014a). Secular evolution in disk galaxies. *Reviews of Modern Physics*, 86(1):1–46.

Sellwood, J. A. (2014b). Secular evolution in disk galaxies. *Reviews of Modern Physics*, 86:1–46.

Sellwood, J. A. and Moore, E. M. (1999). On the Formation of Disk Galaxies and Massive Central Objects. *ApJ*, 510(1):125–135.

Seo, W.-Y., Kim, W.-T., Kwak, S., Hsieh, P.-Y., Han, C., and Hopkins, P. F. (2019). Effects of Gas on Formation and Evolution of Stellar Bars and Nuclear Rings in Disk Galaxies. *ApJ*, 872(1):5.

Sersic, J. L. (1968). *Atlas de Galaxias Australes*.

Shankar, F., Marulli, F., Bernardi, M., Dai, X., Hyde, J. B., and Sheth, R. K. (2010). Sizes and ages of SDSS ellipticals: comparison with hierarchical galaxy formation models. *MNRAS*, 403:117–128.

Shankar, F., Marulli, F., Bernardi, M., Mei, S., Meert, A., and Vikram, V. (2013). Size evolution of spheroids in a hierarchical Universe. *MNRAS*, 428:109–128.

Shankar, F., Marulli, F., Mathur, S., Bernardi, M., and Bournaud, F. (2012). Black holes in pseudobulges: demography and models. *A&A*, 540:A23.

Shen, S., Mo, H. J., White, S. D. M., Blanton, M. R., Kauffmann, G., Voges, W., Brinkmann, J., and Csabai, I. (2003). The size distribution of galaxies in the Sloan Digital Sky Survey. *MNRAS*, 343:978–994.

Shlosman, I., Frank, J., and Begelman, M. C. (1989). Bars within bars: a mechanism for fuelling active galactic nuclei. *Nature*, 338(6210):45–47.

Sijacki, D., Springel, V., Di Matteo, T., and Hernquist, L. (2007). A unified model for AGN feedback in cosmological simulations of structure formation. *MNRAS*, 380(3):877–900.

Silk, J. (1977). On the fragmentation of cosmic gas clouds. I - The formation of galaxies and the first generation of stars. *ApJ*, 211:638–648.

Silk, J. and Rees, M. J. (1998). Quasars and galaxy formation. *A&A*, 331:L1–L4.

Simard, L., Willmer, C. N. A., Vogt, N. P., Sarajedini, V. L., Phillips, A. C., Weiner, B. J., Koo, D. C., Im, M., Illingworth, G. D., and Faber, S. M. (2002). The DEEP Groth Strip Survey. II. Hubble Space Telescope Structural Parameters of Galaxies in the Groth Strip. *ApJS*, 142(1):1–33.

Skokos, C., Patsis, P. A., and Athanassoula, E. (2002). Orbital dynamics of three-dimensional bars - I. The backbone of three-dimensional bars. A fiducial case. *MNRAS*, 333(4):847–860.

Smith, R. E. (2012). How covariant is the galaxy luminosity function? *MNRAS*, 426(1):531–548.

Somerville, R. S. and Davé, R. (2015). Physical Models of Galaxy Formation in a Cosmological Framework. *ARA&A*, 53:51–113.

Somerville, R. S. and Primack, J. R. (1999). Semi-analytic modelling of galaxy formation: the local Universe. *MNRAS*, 310:1087–1110.

Somerville, R. S., Primack, J. R., and Faber, S. M. (2000). The Nature of High-Redshift Galaxies. *ArXiv Astrophysics e-prints*.

Spinoso, D., Bonoli, S., Dotti, M., Mayer, L., Madau, P., and Bellovary, J. (2017). Bar-driven evolution and quenching of spiral galaxies in cosmological simulations. *MNRAS*, 465(3):3729–3740.

Springel, V. (2005). The cosmological simulation code GADGET-2. *MNRAS*, 364(4):1105–1134.

Springel, V. (2010). E pur si muove: Galilean-invariant cosmological hydrodynamical simulations on a moving mesh. *MNRAS*, 401(2):791–851.

Springel, V., Di Matteo, T., and Hernquist, L. (2005a). Modelling feedback from stars and black holes in galaxy mergers. *MNRAS*, 361(3):776–794.

Springel, V. and Hernquist, L. (2003). Cosmological smoothed particle hydrodynamics simulations: a hybrid multiphase model for star formation. *MNRAS*, 339(2):289–311.

Springel, V., Wang, J., Vogelsberger, M., Ludlow, A., Jenkins, A., Helmi, A., Navarro, J. F., Frenk, C. S., and White, S. D. M. (2008). The Aquarius Project: the subhaloes of galactic haloes. *MNRAS*, 391(4):1685–1711.

Springel, V., White, S. D. M., Jenkins, A., Frenk, C. S., Yoshida, N., Gao, L., Navarro, J., Thacker, R., Croton, D., Helly, J., Peacock, J. A., Cole, S., Thomas, P., Couchman, H., Evrard, A., Colberg, J., and Pearce, F. (2005b). Simulations of the formation, evolution and clustering of galaxies and quasars. *Nature*, 435:629–636.

Springel, V., White, S. D. M., Tormen, G., and Kauffmann, G. (2001a). Populating a cluster of galaxies - I. Results at [formmu2]z=0. *MNRAS*, 328(3):726–750.

Springel, V., Yoshida, N., and White, S. D. M. (2001b). GADGET: a code for collisionless and gasdynamical cosmological simulations. *New Astron.*, 6:79–117.

Stark, D. V., McGaugh, S. S., and Swaters, R. A. (2009). A First Attempt to Calibrate the Baryonic Tully-Fisher Relation with Gas-Dominated Galaxies. *AJ*, 138:392–401.

Starobinsky, A. A. (1982). Dynamics of phase transition in the new inflationary universe scenario and generation of perturbations. *Physics Letters B*, 117(3-4):175–178.

Steinmetz, M. and Navarro, J. F. (2002). The hierarchical origin of galaxy morphologies. *New Astron.*, 7(4):155–160.

Stevens, A. R. H., Croton, D. J., and Mutch, S. J. (2016). Building disc structure and galaxy properties through angular momentum: the DARK SAGE semi-analytic model. *MNRAS*, 461(1):859–876.

Stevens, A. R. H., Lagos, C. d. P., Contreras, S., Croton, D. J., Padilla, N. D., Schaller, M., Schaye, J., and Theuns, T. (2017). How to get cool in the heat: comparing analytic models of hot, cold, and cooling gas in haloes and galaxies with EAGLE. *MNRAS*, 467:2066–2084.

Stewart, K. R., Bullock, J. S., Wechsler, R. H., and Maller, A. H. (2009). Gas-rich Mergers in LCDM: Disk Survivability and the Baryonic Assembly of Galaxies. *ApJ*, 702:307–317.

Stewart, K. R., Bullock, J. S., Wechsler, R. H., Maller, A. H., and Zentner, A. R. (2008). Merger Histories of Galaxy Halos and Implications for Disk Survival. *ApJ*, 683(2):597–610.

Su, K.-Y., Hopkins, P. F., Bryan, G. L., Somerville, R. S., Hayward, C. C., Anglés-Alcázar, D., Faucher-Giguère, C.-A., Wellons, S., Stern, J., Terrazas, B. A., Chan, T. K., Orr, M. E., Hummels, C., Feldmann, R., and Kereš, D. (2021). Which AGN Jets Quench Star Formation in Massive Galaxies? *arXiv e-prints*, page arXiv:2102.02206.

Sweet, S. M., Fisher, D., Glazebrook, K., Obreschkow, D., Lagos, C., and Wang, L. (2018). Revisiting the Stellar Mass-Angular Momentum-Morphology Relation: Extension to Higher Bulge Fraction and the Effect of Bulge Type. *ApJ*, 860(1):37.

Tabor, M., Merrifield, M., Aragón-Salamanca, A., Fraser-McKelvie, A., Peterken, T., Smethurst, R., Drory, N., and Lane, R. R. (2019). SDSS-IV MaNGA: full spectroscopic bulge-disc decomposition of MaNGA early-type galaxies. *MNRAS*, 485(2):1546–1558.

Tacchella, S., Diemer, B., Hernquist, L., Genel, S., Marinacci, F., Nelson, D., Pillepich, A., Rodriguez-Gomez, V., Sales, L. V., Springel, V., and Vogelsberger, M. (2019). Morphology and star formation in IllustrisTNG: the build-up of spheroids and discs. *MNRAS*, 487(4):5416–5440.

Teklu, A. F., Remus, R.-S., Dolag, K., Beck, A. M., Burkert, A., Schmidt, A. S., Schulze, F., and Steinborn, L. K. (2015). Connecting Angular Momentum and Galactic Dynamics: The Complex Interplay between Spin, Mass, and Morphology. *ApJ*, 812(1):29.

Thanjavur, K., Simard, L., Bluck, A. F. L., and Mendel, T. (2016). Stellar mass functions of galaxies, discs and spheroids at z $\sim$ 0.1. *MNRAS*, 459(1):44–69.

The EAGLE team (2017). The EAGLE simulations of galaxy formation: Public release of particle data. *arXiv e-prints*, page arXiv:1706.09899.

Thob, A. C. R., Crain, R. A., McCarthy, I. G., Schaller, M., Lagos, C. D. P., Schaye, J., Talens, G. J. J., James, P. A., Theuns, T., and Bower, R. G. (2019). The relationship between the morphology and kinematics of galaxies and its dependence on dark matter halo structure in EAGLE. *MNRAS*, 485(1):972–987.

Tissera, P. B., Rosas-Guevara, Y., Bower, R. G., Crain, R. A., del P Lagos, C., Schaller, M., Schaye, J., and Theuns, T. (2019). The oxygen abundance gradients in the gas discs of galaxies in the EAGLE simulation. *MNRAS*, 482(2):2208–2221.

Tissera, P. B., White, S. D. M., Pedrosa, S., and Scannapieco, C. (2010). Dark matter response to galaxy formation. *MNRAS*, 406:922–935.

Tissera, P. B., White, S. D. M., and Scannapieco, C. (2012). Chemical signatures of formation processes in the stellar populations of simulated galaxies. *MNRAS*, 420(1):255–270.

Tonini, C., Mutch, S. J., Croton, D. J., and Wyithe, J. S. B. (2016). The growth of discs and bulges during hierarchical galaxy formation - I. Fast evolution versus secular processes. *MNRAS*, 459:4109–4129.

Toomre, A. (1964). On the gravitational stability of a disk of stars. *ApJ*, 139:1217–1238.

Toomre, A. (1977). Mergers and Some Consequences. In Tinsley, B. M. and Larson, Richard B. Gehret, D. C., editors, *Evolution of Galaxies and Stellar Populations*, page 401.

Toomre, A. and Toomre, J. (1972). Galactic Bridges and Tails. *ApJ*, 178:623–666.

Torres-Flores, S., Epinat, B., Amram, P., Plana, H., and Mendes de Oliveira, C. (2011). GHASP: an Hα kinematic survey of spiral and irregular galaxies - IX. The near-infrared, stellar and baryonic Tully-Fisher relations. *MNRAS*, 416:1936–1948.

Trachternach, C., de Blok, W. J. G., McGaugh, S. S., van der Hulst, J. M., and Dettmar, R.-J. (2009). The baryonic Tully-Fisher relation and its implication for dark matter halos. *A&A*, 505:577–587.

Trayford, J. W., Frenk, C. S., Theuns, T., Schaye, J., and Correa, C. (2019). The star formation rate and stellar content contributions of morphological components in the EAGLE simulations. *MNRAS*, 483(1):744–766.

Trussler, J., Maiolino, R., Maraston, C., Peng, Y., Thomas, D., Goddard, D., and Lian, J. (2020). The weak imprint of environment on the stellar populations of galaxies. *arXiv e-prints*, page arXiv:2006.01154.

Tully, R. B. and Fisher, J. R. (1977). Reprint of 1977A&A....54..661T. A new method of determining distance to galaxies. *A&A*, 500:105–117.

Vaghmare, K., Barway, S., and Kembhavi, A. (2013). A Spitzer Study of Pseudobulges in S0 Galaxies: Secular Evolution of Disks. *ApJ*, 767:L33.

Valluri, M. and Merritt, D. (1998). Regular and Chaotic Dynamics of Triaxial Stellar Systems. *ApJ*, 506(2):686–711.

van den Bergh, S. (1976). A new classification system for galaxies. *ApJ*, 206:883–887.

van der Hulst, J. M., van Albada, T. S., and Sancisi, R. (2001). The Westerbork HI Survey of Irregular and Spiral Galaxies, WHISP. In Hibbard, J. E., Rupen, M., and van Gorkom, J. H., editors, *Gas and Galaxy Evolution*, volume 240 of *Astronomical Society of the Pacific Conference Series*, page 451.

van der Walt, S., Colbert, S. C., and Varoquaux, G. (2011). The NumPy Array: A Structure for Efficient Numerical Computation. *Computing in Science and Engineering*, 13(2):22–30.

van Dokkum, P. G. (2005). The Recent and Continuing Assembly of Field Elliptical Galaxies by Red Mergers. *AJ*, 130:2647–2665.

Vergani, D., Pizzella, A., Corsini, E. M., van Driel, W., Buson, L. M., Dettmar, R. J., and Bertola, F. (2007). NGC 5719/13: interacting spirals forming a counter-rotating stellar disc. *A&A*, 463(3):883–892.

Virtanen, P., Gommers, R., Oliphant, T. E., Haberland, M., Reddy, T., Cournapeau, D., Burovski, E., Peterson, P., Weckesser, W., Bright, J., van der Walt, S. J., Brett, M., Wilson, J., Millman, K. J., Mayorov, N., Nelson, A. R. J., Jones, E., Kern, R., Larson, E., Carey, C. J., Polat, İ., Feng, Y., Moore, E. W., Vand erPlas, J., Laxalde, D., Perktold, J., Cimrman, R., Henriksen, I., Quintero, E. A., Harris, C. R., Archibald, A. M., Ribeiro, A. H., Pedregosa, F., van Mulbregt, P., and SciPy 1. 0 Contributors (2020). SciPy 1.0: fundamental algorithms for scientific computing in Python. *Nature Methods*, 17:261–272.

Vogelsberger, M., Genel, S., Sijacki, D., Torrey, P., Springel, V., and Hernquist, L. (2013). A model for cosmological simulations of galaxy formation physics. *MNRAS*, 436(4):3031–3067.

Vogelsberger, M., Marinacci, F., Torrey, P., and Puchwein, E. (2020). Cosmological simulations of galaxy formation. *Nature Reviews Physics*, 2(1):42–66.

Walter, F., Brinks, E., de Blok, W. J. G., Bigiel, F., Kennicutt, Robert C., J., Thornley, M. D., and Leroy, A. (2008a). THINGS: The H I Nearby Galaxy Survey. *AJ*, 136(6):2563–2647.

Walter, F., Brinks, E., de Blok, W. J. G., Bigiel, F., Kennicutt, Jr., R. C., Thornley, M. D., and Leroy, A. (2008b). THINGS: The H I Nearby Galaxy Survey. *AJ*, 136:2563–2647.

Wang, B. and Silk, J. (1994). Gravitational Instability and Disk Star Formation. *ApJ*, 427:759.

Wang, J., Athanassoula, E., Yu, S.-Y., Wolf, C., Shao, L., Gao, H., and Randriamampandry, T. H. (2020). Suppressed or Enhanced Central Star Formation Rates in Late-type Barred Galaxies. *ApJ*, 893(1):19.

Wang, L., Obreschkow, D., Lagos, C. d. P., Sweet, S. M., Fisher, D., Glazebrook, K., Macciò, A. V., Dutton, A. A., and Kang, X. (2019). Angular momentum evolution of bulge stars in disc galaxies in NIHAO. *MNRAS*, 482(4):5477–5491.

Wegg, C., Gerhard, O., and Portail, M. (2015). The structure of the Milky Way's bar outside the bulge. *MNRAS*, 450(4):4050–4069.

Weinberger, R., Springel, V., and Pakmor, R. (2020). The AREPO Public Code Release. *ApJS*, 248(2):32.

Weinberger, R., Springel, V., Pakmor, R., Nelson, D., Genel, S., Pillepich, A., Vogelsberger, M., Marinacci, F., Naiman, J., Torrey, P., and Hernquist, L. (2018). Supermassive black holes and their feedback effects in the IllustrisTNG simulation. *MNRAS*, 479(3):4056–4072.

Weinzirl, T., Jogee, S., Khochfar, S., Burkert, A., and Kormendy, J. (2009). Bulge n and B/T in High-Mass Galaxies: Constraints on the Origin of Bulges in Hierarchical Models. *ApJ*, 696(1):411–447.

White, S. D. M. (1984). Angular momentum growth in protogalaxies. *ApJ*, 286:38–41.

White, S. D. M. and Frenk, C. S. (1991). Galaxy Formation through Hierarchical Clustering. *ApJ*, 379:52.

White, S. D. M. and Rees, M. J. (1978). Core condensation in heavy halos - A two-stage theory for galaxy formation and clustering. *MNRAS*, 183:341–358.

Whitmore, B. C. and Bell, M. (1988). IC 4767 (the "X-Galaxy"): The Missing Link for Understanding Galaxies with Peanut-shaped Bulges? *ApJ*, 324:741.

Wiersma, R. P. C., Schaye, J., and Smith, B. D. (2009). The effect of photoionization on the cooling rates of enriched, astrophysical plasmas. *MNRAS*, 393(1):99–107.

Willett, K. W., Lintott, C. J., Bamford, S. P., Masters, K. L., Simmons, B. D., Casteels, K. R. V., Edmondson, E. M., Fortson, L. F., Kaviraj, S., Keel, W. C., Melvin, T., Nichol, R. C., Raddick, M. J., Schawinski, K., Simpson, R. J., Skibba, R. A., Smith, A. M., and Thomas, D. (2013). Galaxy Zoo 2: detailed morphological classifications for 304 122 galaxies from the Sloan Digital Sky Survey. *MNRAS*, 435(4):2835–2860.

Wilman, D. J. and Erwin, P. (2012). The Relation between Galaxy Morphology and Environment in the Local Universe: An RC3-SDSS Picture. *ApJ*, 746:160.

Wyse, R. F. G., Gilmore, G., and Franx, M. (1997). Galactic Bulges. *ARA&A*, 35:637–675.

Xu, G. (1995). A New Parallel N-Body Gravity Solver: TPM. *ApJS*, 98:355.

York, D. G., Adelman, J., Anderson, Jr., J. E., Anderson, S. F., Annis, J., Bahcall, N. A., Bakken, J. A., Barkhouser, R., Bastian, S., Berman, E., Boroski, W. N., Bracker, S., Briegel, C., Briggs, J. W., Brinkmann, J., Brunner, R., Burles, S., Carey, L., Carr, M. A., Castander, F. J., Chen, B., Colestock, P. L., Connolly, A. J., Crocker, J. H., Csabai, I., Czarapata, P. C., Davis, J. E., Doi, M., Dombeck, T., Eisenstein, D., Ellman, N., Elms, B. R., Evans, M. L., Fan, X., Federwitz, G. R., Fiscelli, L., Friedman, S., Frieman, J. A., Fukugita, M., Gillespie, B., Gunn, J. E., Gurbani, V. K., de Haas, E., Haldeman, M., Harris, F. H., Hayes, J., Heckman, T. M., Hennessy, G. S., Hindsley, R. B., Holm, S., Holmgren, D. J., Huang, C.-h., Hull, C., Husby, D., Ichikawa, S.-I., Ichikawa, T., Ivezić, Ž., Kent, S., Kim, R. S. J., Kinney, E., Klaene, M., Kleinman, A. N., Kleinman, S., Knapp, G. R., Korienek, J., Kron, R. G., Kunszt, P. Z., Lamb, D. Q., Lee, B., Leger, R. F., Limmongkol, S., Lindenmeyer, C., Long, D. C., Loomis, C., Loveday, J., Lucinio, R., Lupton, R. H., MacKinnon, B., Mannery, E. J., Mantsch, P. M., Margon, B., McGehee, P., McKay, T. A., Meiksin, A., Merelli, A., Monet, D. G., Munn, J. A., Narayanan, V. K., Nash, T., Neilsen, E., Neswold, R., Newberg, H. J., Nichol, R. C., Nicinski, T., Nonino, M., Okada, N., Okamura, S., Ostriker, J. P., Owen, R., Pauls, A. G., Peoples, J., Peterson, R. L., Petravick, D., Pier, J. R., Pope, A., Pordes, R., Prosapio, A., Rechenmacher, R., Quinn, T. R., Richards, G. T., Richmond, M. W., Rivetta, C. H., Rockosi, C. M., Ruthmansdorfer, K., Sandford, D., Schlegel, D. J., Schneider, D. P., Sekiguchi, M., Sergey, G., Shimasaku, K., Siegmund, W. A., Smee, S., Smith, J. A., Snedden, S., Stone, R., Stoughton, C., Strauss, M. A., Stubbs, C., SubbaRao, M., Szalay, A. S., Szapudi, I., Szokoly, G. P., Thakar, A. R., Tremonti, C., Tucker, D. L., Uomoto, A., Vanden Berk, D., Vogeley, M. S., Waddell, P., Wang, S.-i., Watanabe, M., Weinberg, D. H., Yanny, B., Yasuda, N., and SDSS Collaboration (2000). The Sloan Digital Sky Survey: Technical Summary. *AJ*, 120:1579–1587.

Yoshino, A. and Yamauchi, C. (2015). Box/peanut and bar structures in edge-on and

face-on nearby galaxies in the Sloan Digital Sky Survey - I. Catalogue. *MNRAS*, 446(4):3749–3767.

Yurin, D. and Springel, V. (2015). The stability of stellar discs in Milky Way-sized dark matter haloes. *MNRAS*, 452(3):2367–2387.

Zana, T., Capelo, P. R., Dotti, M., Mayer, L., Lupi, A., Haardt, F., Bonoli, S., and Shen, S. (2019). Barred galaxies in cosmological zoom-in simulations: the importance of feedback. *MNRAS*, 488(2):1864–1877.

Zanisi, L., Shankar, F., Lapi, A., Menci, N., Bernardi, M., Duckworth, C., Huertas-Company, M., Grylls, P., and Salucci, P. (2020). Galaxy sizes and the galaxy-halo connection - I. The remarkable tightness of the size distributions. *MNRAS*, 492(2):1671–1690.

Zavala, J., Avila-Reese, V., Hernández-Toledo, H., and Firmani, C. (2003). The luminous and dark matter content of disk galaxies. *A&A*, 412:633–650.

Zavala, J., Okamoto, T., and Frenk, C. S. (2008). Bulges versus discs: the evolution of angular momentum in cosmological simulations of galaxy formation. *MNRAS*, 387:364–370.

Zhang, Y.-C. and Yang, X.-H. (2019). Size distribution of galaxies in SDSS DR7: weak dependence on halo environment. *Research in Astronomy and Astrophysics*, 19(1):006.

Zhu, L., van de Ven, G., van den Bosch, R., Rix, H.-W., Lyubenova, M., Falcón-Barroso, J., Martig, M., Mao, S., Xu, D., Jin, Y., Obreja, A., Grand , R. J. J., Dutton, A. A., Macciò, A. V., Gómez, F. A., Walcher, J. C., García-Benito, R., Zibetti, S., and Sánchez, S. F. (2018). The stellar orbit distribution in present-day galaxies inferred from the CALIFA survey. *Nature Astronomy*, 2:233–238.

Zoldan, A., De Lucia, G., Xie, L., Fontanot, F., and Hirschmann, M. (2018). Structural and dynamical properties of galaxies in a hierarchical Universe: sizes and specific angular momenta. *MNRAS*, 481:1376–1400.

Zonca, A., Singer, L., Lenz, D., Reinecke, M., Rosset, C., Hivon, E., and Gorski, K. (2019). healpy: equal area pixelization and spherical harmonics transforms for data on the sphere in Python. *The Journal of Open Source Software*, 4(35):1298.